

265059

NASA CR-144037

HEAO-S-73-943

# HEAO

HIGH ENERGY

ASTRONOMY OBSERVATORY

3 DECEMBER 1973

## STUDY OF HEAO ATTITUDE CONTROL USING WHEELS/MAGNETICS/COLD GAS

REPRODUCED BY  
NATIONAL TECHNICAL  
INFORMATION SERVICE  
U. S. DEPARTMENT OF COMMERCE  
SPRINGFIELD, VA. 22161

(NASA-CF-144037) STUDY OF HEAO ATTITUDE  
CONTROL USING WHEELS/MAGNETICS/COLD GAS  
Final Report (TRW Systems Group) 205 p

247

N75-78141

00/98

Unclas  
01498

Prepared for

NASA GEORGE C. MARSHALL SPACE FLIGHT CENTER

Under

Contract No. NAS8-28300

**TRW**  
SYSTEMS GROUP

ONE SPACE PARK • REDONDO BEACH, CALIFORNIA 90278

01/98

# HEAO

HIGH ENERGY

ASTRONOMY OBSERVATORY

3 DECEMBER 1973

## STUDY OF HEAO ATTITUDE CONTROL USING WHEELS/MAGNETICS/COLD GAS

Prepared for

NASA GEORGE C. MARSHALL SPACE FLIGHT CENTER

Under

Contract No. NAS8-28300


**TRW**  
SYSTEMS GROUP


STUDY OF HEAO ATTITUDE CONTROL  
USING WHEELS/MAGNETICS/COLD GAS

Prepared by:

  
E. P. Todosiev  
Study Manager

Approved by:

  
R. Zacharias, Deputy APM  
System Engineering

  
E. G. Wheeler, Acting Manager  
HEAO Project

## CONTENTS

	Page
1. Introduction	1-1
2. Summary	2-1
3. System Engineering	3-1
4. Attitude Control Subsystem	4-1
5. Reaction Control Subsystem (Cold Gas Option)	5-1
6. Mechanical Design Integration	6-1
7. Electrical Design Integration	7-1
8. Electrical Subsystem	8-1
9. Experiment Integration	9-1
10. Communications and Tape Recorder Subsystem	10-1
11. Thermal Design Integration	11-1
12. Reliability	12-1
13. Verification and Mission Operations	13-1



## 1. INTRODUCTION

The initial Phase A studies for the HEAO program baselined a magnetic controller as part of the observatory attitude control system. Later when an orbit adjust system was added to the observatory, the magnetic controller was deleted since the RCS subsystem required to supply the attitude control torques during  $\Delta V$  orbital adjustments could be used for on-orbit control as well. When the  $\Delta V$  requirement was dropped in the restructured HEAO program, use of magnetics in the attitude control system again became worthy of consideration. Two possible control configurations using magnetics were defined; one would employ reaction wheels and magnetics for both acquisition and normal on-orbit control, the other would use a small cold gas system for acquisition and reaction wheels plus magnetics for the normal cruise modes.

Preliminary trade studies between the alternate control systems employing magnetics and the baseline hydrazine reaction control subsystem (RCS), indicated a number of attractive advantages for the alternate control approaches. Listed in order of significance, the identifiable potential advantages were:

- A significant program cost saving
- A common attitude control design for all HEAO missions
- Life no longer limited by expendables
- Smoother attitude control performance for Missions A and C
- Elimination of wheel unloading transients for Mission B

These potential advantages provided the impetus for conducting a comprehensive study to firmly establish the feasibility of using magnetics in the attitude control system for all the HEAO missions.

This document reports the results of that study and includes: 1) an assessment of concept feasibility, 2) a definition of concept implementation and 3) performance comparisons between the baseline and alternate systems.

## 2. SUMMARY

Evaluation of study results indicates that attitude control using reaction wheels, electromagnets, and cold gas is technically feasible for all the HEAO missions. Acquisition is effected by a cold gas system; during the cruise modes, attitude control is achieved with reaction wheels and electromagnets. Implementation of this control approach involves replacement of the RCS subsystem on HEAO-A, -B, and -C, with magnetic and cold gas systems and the addition of reaction wheels to HEAO-A and -C. This control approach permits rapid sun acquisitions and operation of the reaction wheels at a small fraction of their total momentum capacity. The use of a control approach employing only reaction wheels and magnetics cannot be recommended at this time primarily because of the long periods required for spacecraft acquisition or reacquisition of the sun line.

Table 2-1 represents a weight/power/reliability tradeoff between the wheels/magnetics/cold gas system and the RCS baseline. Use of the new system would impose a weight penalty of 85 to 315 pounds and a power penalty of 54 watts on HEAO-A and -C. The weight change on HEAO-B would range between a savings of 117 pounds to a penalty of 113 pounds; 8 watts of power would be saved. For all HEAO missions, the reliability of this system is better than the current baseline.

Table 2-1. Weight/Power/Reliability Trade

	Weight (lbs)		Power (watts)		Spacecraft Reliability	
	HEAO-A/C	HEAO-B	HEAO-A/C	HEAO-B	HEAO-A/C	HEAO-B
Wheels/ Magnetics/Cold Gas System	432 to 662	230 to 343	58	-4	.929	.823
Reaction Control System (RCS)	347	347	4	4	.925	.809
Weight Delta	+85 to +315	-117 to +113	--	--		
Power Delta	--	--	+54	-8		
Current Weight Margin	960	720*	--	--		
Current Power Margin	--	--	Inadequate - Must add Extra Array Module	No signi- ficant change		

\* May change significantly as result of new experiment configuration

### 3. SYSTEM ENGINEERING

#### 3.1 Selected Magnetic Configuration

The selected attitude control configuration employs reaction wheels together with a magnetic controller and a small cold gas system for all three HEAO missions. With this control configuration, initial sun acquisition is effected with a cold gas system. Attitude control during the cruise modes (celestial scan or celestial point) is accomplished with reaction wheels and a magnetic controller. In the cruise modes, the wheels provide primary attitude control and the magnetic controller is employed solely for continuous desaturation of the reaction wheels. Sun reacquisitions and control during backup operation would be effected with the cold gas system.

Selection of the cold gas system for acquisition, rather than the magnetic controller, was based on the following considerations:

- a) The study has shown that the magnetic controller could permit sun acquisition within three orbits. However, it was also found that the acquisition process was sensitive to magnetic coupling between the electro-magnets and the magnetometer as well as to stray residual magnetic fields on the observatory. Both of these effects result in longer acquisition periods. This has a significant impact on the depth of discharge in the battery if the spacecraft is not tumbling in a random manner. Since it is not possible to accurately predict the dynamic behavior of the spacecraft for all booster tipoff conditions and the ensuing motion during acquisition, it then becomes technically attractive to choose an acquisition system which is capable of performing sun acquisition rapidly. The cold gas system selected will permit sun acquisition within ten minutes.
- b) Due to the study scope, a backup approach was not developed. Preliminary considerations indicate that the design of a suitable backup mode is greatly simplified if continuous control authority is available upon demand about each spacecraft axis. This is the case if a cold gas system is employed. With the magnetic controller and no active reaction wheels, it is only possible to generate torques in that specific spacecraft plane which is instantaneously normal to the earth's magnetic field vector. Since this fact will significantly impact the design of a practical backup system using only the magnetic controller, it was concluded at this time that significant design problems could be avoided by using a cold gas system.

### 3.2 Implementation

Implementation of the control configuration consisting of reaction wheels, magnetic controller, and the cold gas system, involves the following major design changes to the spacecraft:

- o Removal of the current RCS system and all associated equipment from HEAO-A, -B and -C.
- o Addition of electromagnets, electromagnet electronics, magnetometers, and interface electronics to HEAO-A, -B and -C
- o Addition of reaction wheels and reaction wheel drivers to HEAO-A and -C only
- o Addition of a cold gas system to HEAO-A, -B and -C
- o Additional solar array module for HEAO-A

The magnetic controller employs three electromagnets which consist of dual-wound aluminum coils on a vanadium permendur core. Each electromagnet is capable of generating a magnetic moment of  $2000 \text{ amp-turn-m}^2$  and weighs 51 pounds. During the cruise modes the electromagnets would operate with maximum moments between 200 and  $400 \text{ amp-turn-m}^2$ . The electromagnets are located at the base of the spacecraft. The earth's field is sensed by a magnetometer located at the top of the spacecraft on the array structure.

The cold gas system would employ six thrusters with a nominal thrust in the 0.1 to 1 pound range. For the purpose of this study, the propellant capacity was based on the amount required to effect three worst case sun acquisitions (i.e., acquisition with maximum tip-off rates of 1 degree per second about each axis and the HEAO-B growth inertias). The required propellant weight is 4.3 pounds. Two flight qualified tanks, each 7.6 inches in diameter, were selected as the storage vessels with capacity closest to the requirement. Together, they have a 4.6 lb capacity. The total cold gas system weight is 30 pounds.

Propellant capacity was parameterized as a function of flight qualified tanks (Section 5). The largest tank that could be accommodated within the equipment module is the 20.5 inch diameter tank which has a capacity of 43.8 pounds. These tanks would give a maximum propellant

capacity of 88 pounds. The total weight delta of this maximum capacity system over the 4.6 pound system is 230 pounds which includes the additional support structure. Should the system under consideration be selected in lieu of the present baseline, we would recommend that the specification of the propellant capacity remain open until the HEAO-B experiment module configuration is better defined and meaningful evaluation of weight margin is established. Weight permitting, tanks larger than the 4.6 lbs. discussed above could then be selected. The impact on system cost will be minimal as the larger tanks are not significantly more expensive than the small baseline tanks.

### 3.3 Weight/Power Trade

Table 3-1 illustrates the trade-off in weight and power between the wheels/magnetics/cold gas system and the baseline RCS subsystem. For Missions A and C, the weight of the wheels/magnetics components is 402 pounds of which 53 pounds (15%) is contingency. Note that this includes the weight of the additional solar array module. Addition of the cold gas system (5 pound capacity) gives a total weight of 432 pounds. Therefore the weight penalty of using the recommended system on Missions A and C is 85 pounds. If 88 pounds of nitrogen gas was carried instead of 5 pounds, then the weight penalty would increase to 315 pounds.

For Mission B, only the magnetics and cold gas systems must be added to implement the recommended system. This represents a weight saving of 117 pounds relative to the RCS baseline. Increasing the nitrogen gas capacity from 5 to the 88 pounds maximum, yields a weight penalty of 113 pounds.

The power penalty of implementing the recommended system for Mission A and C is 54 watts which includes a 15% contingency of 8 watts. For Mission B there is a power saving of 8 watts.

### 3.4 Magnetic Field Assessment

A principal concern in the design of any magnetic control system is the effect of the magnetic fields produced by the electromagnets on spacecraft components which are sensitive to magnetic fields. These

Table 3-1 WEIGHT/POWER TRADE

<u>WHEELS/MAGNETICS COMPONENTS</u>	<u>TOTAL WEIGHT (LBS)</u>		<u>TOTAL POWER (WATTS)</u>	
	<u>HEAO-A/C</u>	<u>HEAO-B</u>	<u>HEAO-A/C</u>	<u>HEAO-B</u>
MAGNETIC CONTROL SYSTEM	174	174	5(22*)	7(33*)
REACTION WHEELS & ELECTRONICS	148	-	45(46*)	-11(90*)
ADDITION TO DIGITAL PROCESSOR	5	-	-	-
ADDITIONAL SOLAR ARRAY	22	0	-	-
CONTINGENCY (15%)	<u>53</u>	<u>26</u>	<u>8(10*)</u>	<u>-(18*)</u>
SUBTOTAL	402	200	58(78*)	-4(141*)
<u>COLD GAS SYSTEM (5 LB CAPACITY)</u>	<u>30</u>	<u>30</u>	<u>0</u>	<u>0</u>
<u>TOTAL SYSTEM</u>	432	230	58	-4
<u>RCS SUBSYSTEM</u>	347	347	4	4
<u>WEIGHT DELTA</u>	+85	-117	-	-
<u>POWER DELTA</u>	-	-	+54	-8

\* ACQUISITION WITH MAGNETICS

8<

components include star trackers, rate gyros, tape recorders, memories in digital computers, and photomultiplier tubes in experiments.

The field produced by each electromagnet was derived using a distributed source model (Section 9). This model gives an accurate measure of the near-field of the electromagnet where the simple dipole model is not valid. The model also applies to intermediate and far-field regions of the electromagnet. This model was employed in the evaluation of the magnetic fields at each of the component locations. The total field was obtained by root-sum-squaring the field contributions from each electromagnet. This gives a conservative result as there will be some cancellation where the fields are summed vectorially. Table 3-2 summarizes the results of the mapping analysis

The allowable field for the star tracker of 3 gauss was based on a state-of-the-art shield enclosing the photomultiplier tube within the tracker. The allowable field for the rate gyro of 20 gauss was based on a TRW test performed during the HEAO proposal phase. A recent test on the tape recorder (Section 10) indicated the recorder could tolerate fields as high as 5 gauss without generating any bit errors. Similarly, existing test data was used in selecting the allowable fields for the transponder, digital processor (plated wire memory), and the cold gas thrusters. For all those components for which an allowable field has been specified, the peak field from the electromagnets is less than the allowable operating limit.

The field coupled into the magnetometer is a key parameter in the magnetic controller design. The worst coupling occurs in Mission B where the peak coupled field is 4% relative to the maximum earth's field. The coupling effect was analyzed in Section 4 where it is shown that a 5% coupling factor can be readily accommodated by the magnetic controller.

It was concluded that the current location of the electromagnets is satisfactory as far as the resultant peak field on the observatory is concerned.



Table 3-2 PEAK ELECTROMAGNET FIELD (GAUSS)

<u>COMPONENT</u>	<u>ALLOWABLE FIELD</u>	<u>ACTUAL FIELD</u>	
		<u>CRUISE(A)</u>	<u>CRUISE(B)</u>
MAGNETOMETER	-	.0065	.013
STAR TRACKER	3	.41	.82
RATE GYROS	20	.32	.65
TAPE RECORDER	5	.17	.33
TRANSPONDER	25	.082	.16
DIGITAL PROCESSOR	13	.70	1.4
COLD GAS THRUSTERS	500	3.2	6.4
A-3 TRACKER	-	.048	-
A-1 EXPERIMENT	-	.46	-
A-4 EXPERIMENT	-	.18	-
TELESCOPE FOCUS	-	-	.44

#### 4. ACDS

##### 4.1 Introduction and Summary

The ACDS portion of the magnetic torquing study considered the implementation feasibility of using a magnetic controller on the observatory in lieu of a reaction control system. This requires the electromagnets, acting in concert with the reaction wheels, to provide control during sun acquisition and normal modes of operation for both HEAO-A/C and HEAO-B configurations. The gross effect on the spacecraft design is the deletion of the RCS from all configurations, the addition of reaction wheels and drive electronics to the HEAO-A/C configurations and the addition of magnetometers, electromagnetic torquers and electromagnetics to all configurations.

The scope of the study encompassed preliminary design and analysis of the subsystem from the standpoint of analytical development of control laws, electronic circuit design and component sizing. The analytical development was followed by a performance analysis effort using a digital simulation which included the pertinent dynamic, kinematic and geometric models for the spacecraft, torquers, wheels, gravity gradient disturbances, earth's magnetic field, etc. The performance analysis considered the development/verification of the hardware characteristics and the sensitivity to their variations. The sun acquisition mode was analyzed for the case of acquisition from a worst case booster separation (max tipoff rates). The normal modes of celestial scan (HEAO-A/C) and celestial point (HEAO-B) were analyzed to verify wheel unloading performance under worst case conditions. The mass properties used throughout are those of Table 4-1, which were projected on the basis of payload growth limits for the Atlas/Centaur launch vehicle. Spacecraft attitudes, seasons, time of day, and other geometrical conditions were selected to approximate worst case conditions.

The magnetic control configuration studied is shown schematically in Figure 4-1. It consists of an orthogonal triad of electromagnets in the equipment module, which are activated to interact with the earth's magnetic field to produce control torques. Magnetic field sensing is accomplished via a three-axis magnetometer array located at the top of the observatory. The other ACDS equipment is located as in the current baselines in or on

Table 4-1. Mass Properties for Magnetic Torquing Study  
(Beginning of Life On-Orbit Conditions)

	HEAO-A	HEAO-B
WEIGHT (LBS)	6936.	6436.
MASS CENTER LOCATION		
$\bar{X}$ (IN FROM SEP PLANE)	76.5	100.3
$\bar{Y}$ (IN FROM S/C CL)	5.1	- 0.5
$\bar{Z}$ (IN FROM S/C CL)	- 1.2	0.7
MOMENTS OF INERTIA		
$I_{xx}$ (SLUG-FT <sup>2</sup> )	1750.	1520.
$I_{yy}$ (SLUG-FT <sup>2</sup> )	4030.	7970.
$I_{zz}$ (SLUG-FT <sup>2</sup> )	4300.	7920.
$I_{xy}$ (SLUG-FT <sup>2</sup> )	96.	47.
$I_{xz}$ (SLUG-FT <sup>2</sup> )	14.	359.
$I_{yz}$ (SLUG-FT <sup>2</sup> )	17.	4.

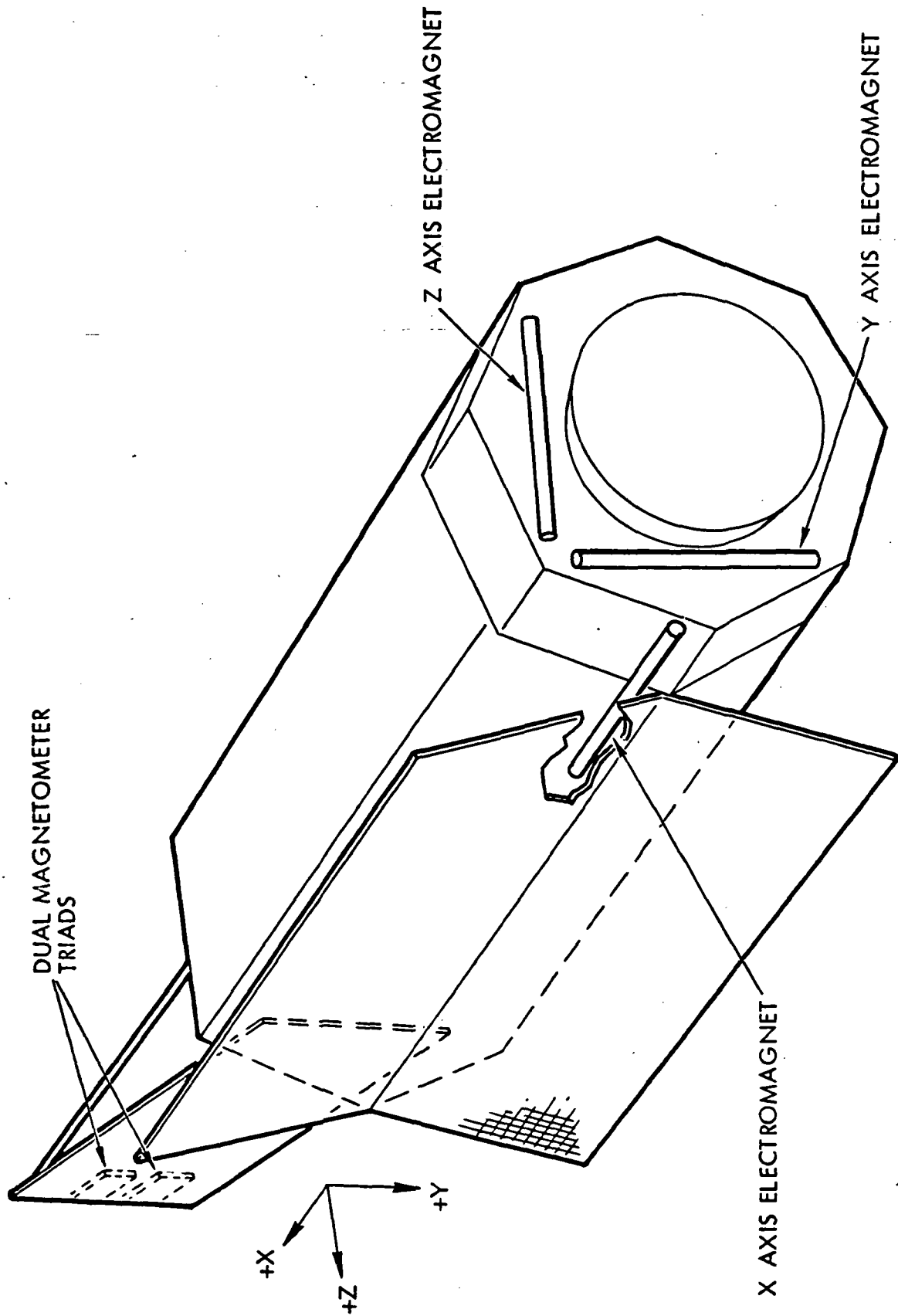


Figure 4-1. Magnetic Attitude Control Component Layout

the equipment module. The functional block diagram of the ACDS is shown in Figure 4-2. The computational functions indicated are performed by the digital processor (DPA) with sensor and actuator interfacing provided through the transfer assembly (TA).

The operating control modes for the ACDS are shown in Figure 4-3 for both the scanning and pointing observatories. The normal sun acquisition mode has two submodes (phases) in the magnetics implementation. The initial phase activates the torquers to reduce the spacecraft body momenta, as measured by the angular rate data from the gyros. During the initial phase, the reaction wheels are inoperative. As the momentum is reduced to a level compatible with the reaction wheel storage capability ( $\approx 50\%$  of capacity), reaction wheel control is activated based upon sun sensor position data and gyro rate data. At this transition, which is accomplished automatically based upon angular rate thresholds and sun presence information, the magnetic control law is changed to exert torques as required to unload the reaction wheels. This results in the wheels providing primary attitude control actuation and the magnetics providing an outer loop for momentum dumping to maintain the wheels in an unloaded state. The same unloading control concept is used during the other normal modes of point, scan, and maneuver.

The study has shown that the combined wheel/magnetics attitude control design using electromagnets with a moment of  $2000 \text{ amp-turn-m}^2$  is feasible. The design allows sun acquisitions to be accomplished using rate gyro and sun sensor data. The acquisition time is dependent upon the conditions at the start of the sequence. For a predicted worst case representation of booster separation with maximum tipoff rates, the acquisition time is on the order of 2-3 orbits. Normal mode performance using  $300\text{-}400 \text{ amp-turn-m}^2$  magnetic moment (of the available 2000) results in maintaining the reaction wheels below 3-4 ft-lb-sec in celestial scan and 7-8 ft-lb-sec in celestial point. This provides margins for maneuvering, which can probably be increased after more detailed design. The ACDS weight and power requirements for the wheel/magnetics configuration are estimated to be 349.9 lbs/109.1 watts for HEAO-A/C and 388.4 lbs/140.8 watts for HEAO-B.

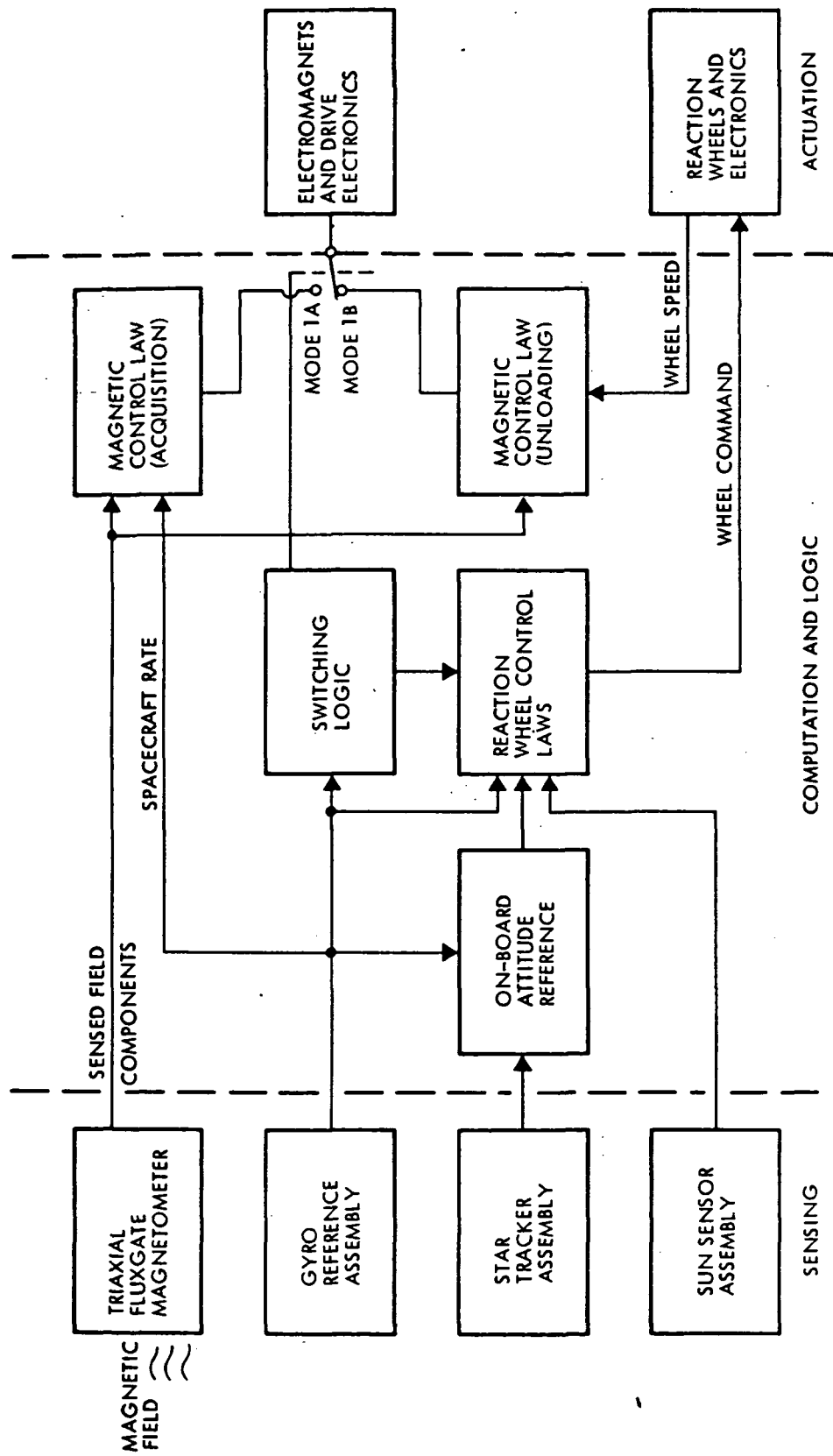
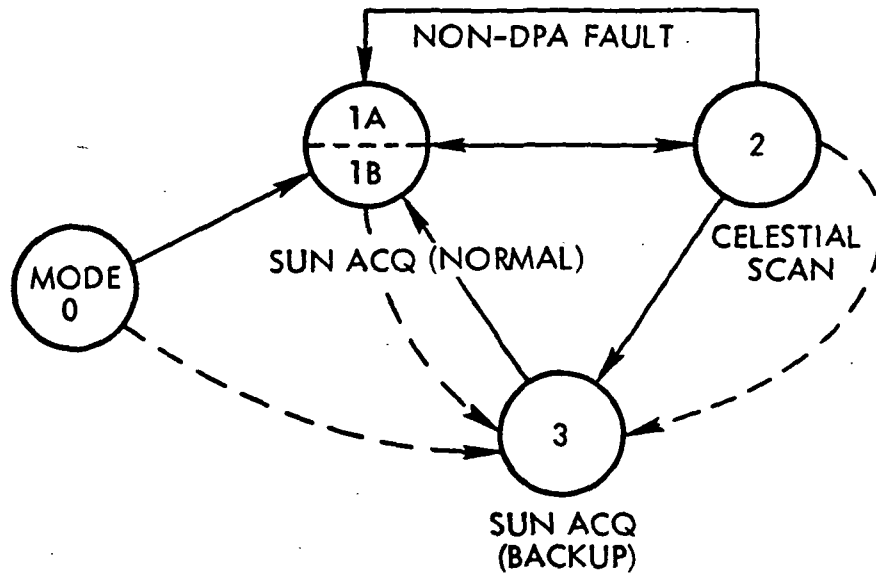
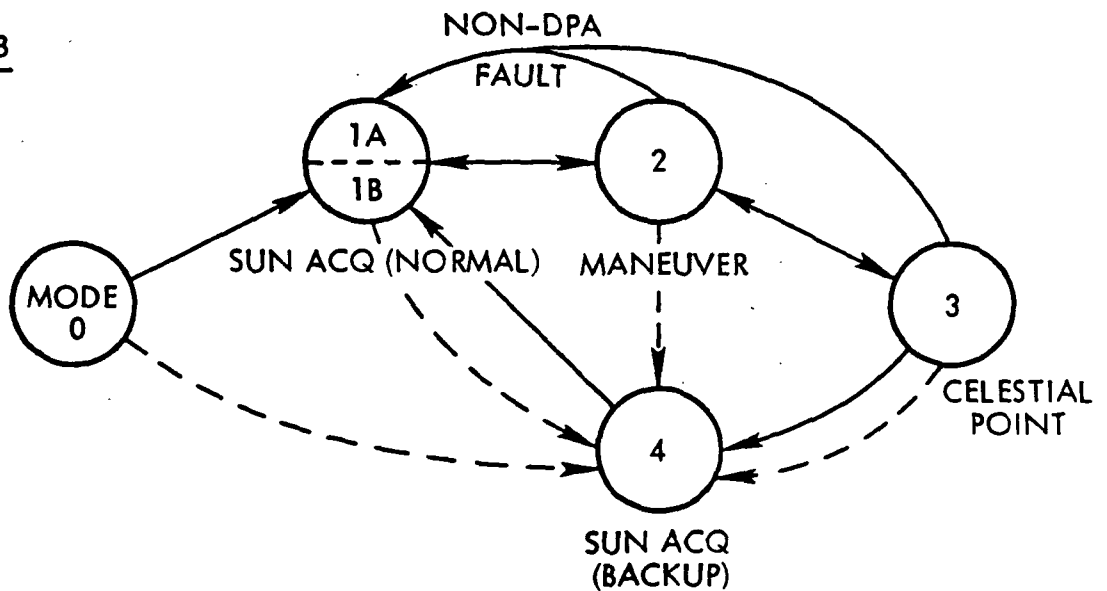


Figure 4-2. Wheel Magnetics Attitude Control Block Diagram

HEAO-A/C



HEAO-B



- INDICATES GROUND CONTROL TRANSFER
- - - - INDICATES ON-BOARD TRANSFER

Figure 4-3. ACDS Operating Mode Flow

## 4.2 Subsystem Design

The initial phase of the ACDS study effort on magnetic torquing addressed the aspects of conceptual design from the standpoint of control law analysis and development, and hardware design feasibility and sizing. The control law work utilized the results from previous magnetic control studies conducted on other programs and in support of HEAO. The hardware design bases were primarily the requirements established by earlier HEAO magnetics studies. The electromagnet design and sizing characteristics drew from the experience gained in the SESP 72-1 spacecraft attitude control work which utilized electromagnets for control. The analysis and hardware designs are discussed in this section.

### 4.2.1 Magnetic Control Laws

Two candidate magnetic control laws were evaluated during the study. For reasons which will later become apparent, they will be denoted as the  $\bar{B}$  and the  $B \times H$  control laws.

The first control law was derived on the basis of kinetic energy. During sun acquisition, the magnetic system must monotonically reduce the spacecraft rotational kinetic energy. The rate of change of kinetic energy equals the rate at which work is done on the spacecraft, which in turn is a function of the applied torque and the inertial rate. Mathematically, this relation is expressed as:

$$\frac{dW}{dt} = \bar{T} \cdot \bar{\omega} \quad (4-1)$$

where  $W$  is the work done on the spacecraft,  $\bar{T}$  is the torque applied to the spacecraft, and  $\bar{\omega}$  is the angular rate of the spacecraft. Obviously, the despin torque should assure that the above expression always remains negative, thereby guaranteeing removal of energy from the spacecraft at all times.

A control torque ( $\bar{T}$ ) is applied to the spacecraft when the magnetic moment ( $\bar{M}$ ) of the electromagnets interacts with the earth's field ( $\bar{B}$ ) according to the following vector cross product law:

$$\bar{T} = \bar{M} \times \bar{B} \quad (4-2)$$



Hence,

$$\frac{d\bar{W}}{dt} = (\bar{M} \times \bar{B}) \cdot \bar{\omega} \quad (4-3)$$

Using appropriate vector identities

$$\frac{d\bar{W}}{dt} = -\bar{M} \cdot (\bar{\omega} \times \bar{B}) \quad (4-4)$$

Assuming that the inertial rate of change of  $\bar{B}$  is negligible relative to the spacecraft tumble rate ( $\bar{\omega}$ ), then

$$\bar{\omega} \times \bar{B} \approx -\dot{\bar{B}} \quad (4-5)$$

The expression for the rate of work under this approximation becomes

$$\frac{d}{dt} (W) = \bar{M} \cdot \dot{\bar{B}} \quad (4-6)$$

In order to assure that

$$\bar{M} \cdot \dot{\bar{B}} = M_x \dot{B}_x + M_y \dot{B}_y + M_z \dot{B}_z < 0, \quad (4-7)$$

it is sufficient to provide that

$$M_i \dot{B}_i < 0 \quad i = x, y \text{ and } z \quad (4-8)$$

Hence, each of the components of the spacecraft field must have opposite polarity to the corresponding component of  $\dot{\bar{B}}$ . The magnetic control law reflecting this characteristic becomes

$$\bar{M} = -K_D \dot{\bar{B}} \quad (4-9)$$

and is denoted the  $\dot{B}$  control law. The control gain magnitude ( $K_D$ ) is selected primarily on the basis of experimental iteration for a given design. The range of values used in this study using this approach was 1-10 ft-lb-sec/gauss<sup>2</sup>.

The  $\dot{B}$  control law is applicable only during the acquisition mode before activation of the reaction wheels and while the spacecraft rates are relatively high. After wheel activation, when the spacecraft momentum is transferred to the wheels, the  $\dot{B}$  law must be dropped in favor of the  $B \times H$  control law.

The alternate magnetic control law was derived from momentum considerations and will be recognizable as the conventional control law normally proposed for momentum removal. The total spacecraft momentum may be defined as:

$$\bar{H} = [I] \bar{\omega} + \bar{h} \quad (4-10)$$

where

$\bar{\omega}$  = spacecraft inertial rate vector

$\bar{h}$  = wheel momentum vector

$[I]$  = spacecraft inertia matrix

Now consider the task of finding a magnetic control law which will always command the control torque to oppose the momentum and thereby guarantee reduction of spacecraft momentum. In general, the control torque produced by the electromagnets is

$$\bar{T} = \bar{M} \times \bar{B} \quad (4-11)$$

and in accordance with the proposed control law

$$\bar{T} = K\bar{H} + \bar{e} \quad (4-12)$$

where  $K$  is the control gain and  $\bar{e}$  is an unavoidable error torque. The error torque results when  $\bar{H}$  is not perpendicular to  $\bar{B}$ , which is generally the case. The three vectors  $\bar{T}$ ,  $\bar{H}$  and  $\bar{e}$  all lie in the same plane, but it can be shown that the error torque  $\bar{e}$ , will be minimized if this plane also contains the field vector ( $\bar{B}$ ). If this constraint is imposed, then the error torque will be perpendicular to  $\bar{B}$ , and it follows from Equations (4-11) and (4-12) that:

$$\bar{B} \times \bar{e} = \bar{B} \times (\bar{M} \times \bar{B}) + K\bar{B} \times \bar{H} = 0 \quad (4-13)$$

Therefore,

$$M\bar{B}^2 - (\bar{B} \cdot \bar{M})\bar{B} + K\bar{B} \times \bar{H} = 0 \quad (4-14)$$

where

$$B^2 = B_x^2 + B_y^2 + B_z^2 \quad (4-15)$$

If a torque efficiency constraint is imposed whereby the magnetic moment is restricted to be normal to the earth's field to maximize the magnetic torque produced, then

$$\vec{M} \cdot \vec{B} = 0 \quad (4-16)$$

and the required magnetic moment from the electromagnets is obviously

$$\vec{M} = -\frac{K}{B^2} (\vec{B} \times \vec{H}) \quad (4-17)$$

The above expression represents the BxH control law and can be employed for both acquisition and unloading by appropriate definition of the  $\vec{H}$  vector.

#### 4.2.2 Reaction Wheel Control Laws

The reaction wheels are the primary means of providing attitude maneuvering, stabilization, and control during the final sun acquisition phase and in normal modes. The wheels produce torques on the spacecraft which are functions of the spacecraft attitude errors and rates. Control error signals for the roll, pitch and yaw axis are formed as follows:

$$\epsilon_x = K_{px} (\phi^L + K_{rx} \omega_x) \quad (4-18)$$

$$\epsilon_y = K_{py} (\theta^L + K_{ry} \omega_y) \quad (4-19)$$

$$\epsilon_z = K_{pz} (\psi^L + K_{rz} \omega_z) \quad (4-20)$$

where  $K_{pi}$  and  $K_{ri}$  are the respective position and rate gains;  $\phi^L$ ,  $\theta^L$  and  $\psi^L$  are the limited attitude errors for the attitude reference; and  $\omega_i$  are the respective spacecraft rates as sensed by the rate gyros. The error signals,  $\epsilon_x$ ,  $\epsilon_y$ , and  $\epsilon_z$  are the actuating signals to the motor drivers. Torques equal and opposite to the motor torques are applied to spacecraft body in response to these error signals. A block diagram of the reaction wheel attitude control system is shown in Figure 4-4. This form of controller is a typical rate plus position servo loop closed around the spacecraft dynamics to provide attitude control through momentum management. These control laws are of the same form as those currently

baselined for HEAO-B.

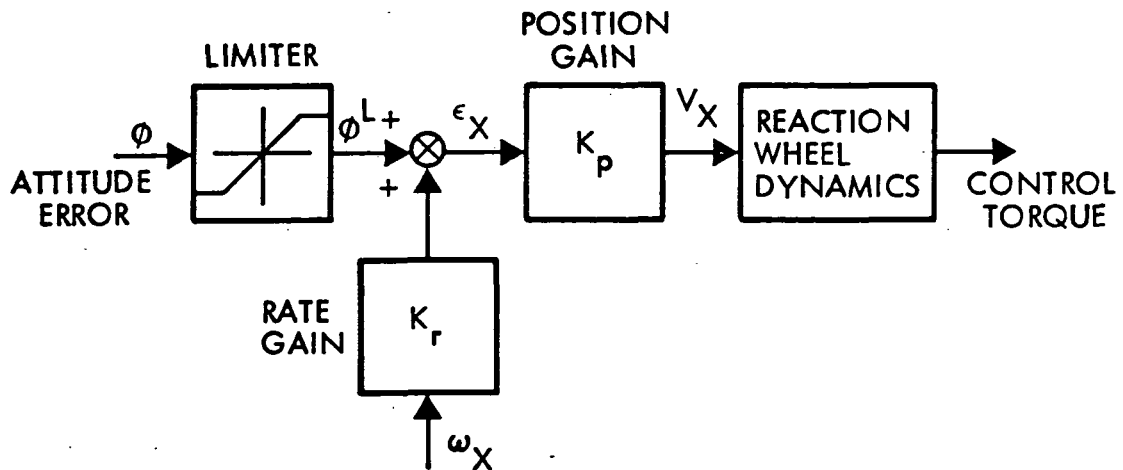


Figure 4-4. Block Diagram of Reaction Wheel Attitude Control System (Roll Axis Only)

#### 4.2.3 Control Law Parameter Selection

##### 4.2.3.1 Sun Acquisition

During sun acquisition, the magnetic controller provides external torques to reduce the initial angular rates (momentum) of the observatory to levels compatible with reaction wheel activation. The magnetic control laws evaluated in the study were:

$$\vec{M} = -K/B^2 (\vec{B} \times \vec{H})$$

$\vec{B} \times \vec{H}$  law

$$\vec{M} = -K_D \dot{\vec{B}}$$

$\dot{\vec{B}}$  law

The control parameters requiring specification are  $K$  and  $K_D$ . In this study,  $B^2$  was considered as constant in the BxH law so that the effective control parameter was the  $K/B^2$  quotient. Previous preliminary simulation studies on HEAO had developed the desirable gain value for the BxH law as  $0.5 (\text{sec-gauss}^2)^{-1}$ . The specification of this parameter was therefore accomplished experimentally. The  $\dot{B}$  control law gain can be roughly related to the BxH gain through the inertia properties of the spacecraft. From Equation (4-5):

$$-\dot{\bar{B}} = \bar{\omega} \times \bar{B}$$

Therefore, the  $\dot{B}$  law can be rewritten as

$$\begin{aligned} M &= K_D (\bar{\omega} \times \bar{B}) \\ &= \frac{K_D}{I} (I \bar{\omega} \times \bar{B}) \approx \frac{K_D}{I} (\bar{H} \times \bar{B}) \end{aligned}$$

The latter expansion assumes  $I$  is an "inertia" of the spacecraft such that  $I \bar{\omega} = \bar{H}$  in some sense. By similarity with the BxH control law, then:

$$K_D = \frac{K}{B^2} I$$

which associates the gain range for the  $\dot{B}$  law with that of the BxH law. Through experimental studies using this relation as a starting point, it was found that values of  $K_D \approx 1$  provided satisfactory performance. As a result of comparative studies of the two control laws, however, it was found that the  $\dot{B}$  law was slightly inferior to the BxH law and thus the emphasis of the study was on performance using the BxH law.

The selection of the control parameters employed by the reaction wheels during the final phase of sun acquisition was based on obtaining deadbeat response for a simple single axis maneuver. The phase plane trajectory for such a maneuver is shown in Figure 4-5. A deadbeat response characteristic is desirable from the standpoint of convergence time and power efficiency as the null condition is achieved without appreciable oscillatory motion.

The idealized gain for this condition can be computed as follows. The average deceleration required is given by:

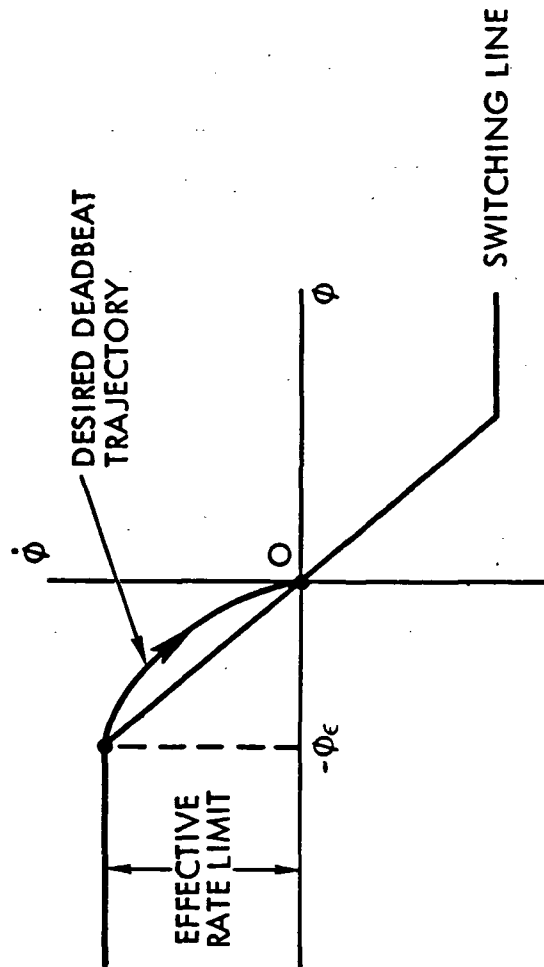


Figure 4-5. Phase Plane Trajectory for Deadbeat Response

$$\ddot{\phi} = \frac{T_{ave}}{I_{xx}} \quad (4-21)$$

where

$$\begin{aligned} \ddot{\phi} &= \text{deceleration along the desired trajectory} \\ T_{ave} &= \text{torque available from the wheel} \\ I_{xx} &= \text{moment of inertia} \end{aligned}$$

The time for deceleration to the origin is

$$t = \frac{\dot{\phi}^L}{\ddot{\phi}} \quad (4-22)$$

where  $t$  is the time to decelerate to zero rate and  $\dot{\phi}^L$  is the effective rate limit. The error angle limit  $\phi_\epsilon$  is given by

$$\phi_\epsilon = 1/2 \ddot{\phi} t^2 \quad (4-23)$$

The slope of the switching line is  $K_r$  (the rate gain) and is related to  $\dot{\phi}^L$  and  $\phi_\epsilon$  by:

$$K_r = \frac{\dot{\phi}^L}{\phi_\epsilon} \quad (4-24)$$

The position error limit  $\phi_\epsilon$  is determined by the reaction wheel controller voltage characteristics. A saturation level ( $V_{sat}$ ) of 17.1 volts was selected for the reaction wheel controller design. The position gain is given by

$$K_{pi} = \frac{V_{sat}}{\phi_\epsilon} \quad (4-25)$$

where the  $K_{pi}$  have dimensions of volts per radians and are the effective position gains.

For HEAO-B the values shown in Table 4-2 were used as preliminary design values. These values provide the gain and limits also shown in the table. These preliminary values were changed for pitch and yaw to the

Table 4-2. Reaction Wheel Control Parameters

ACQUISITION MODEDESIGN PARAMETERS

- MOMENTS OF INERTIA (SEE TABLE 4-1)
- MANEUVER RATE LIMITS 0.1 DEG/SEC (EACH AXIS)
- AVERAGE WHEEL TORQUE 0.117 FT-LB (EACH AXIS)

WHEEL CONTROLLER GAINS

	<u>POSITION GAIN</u>	<u>ERROR LIMIT</u>	<u>RATE GAIN</u>
HEAO-A:			
ROLL	865 VOLTS/RAD	0.0196 RAD	11.2 SEC
PITCH	162 VOLTS/RAD	0.105 RAD	60.0 SEC
YAW	162 VOLTS/RAD	0.105 RAD	60.0 SEC
HEAO-B:			
ROLL	684 VOLTS/RAD	0.025 RAD	14.3 SEC
PITCH	300 VOLTS/RAD	0.057 RAD	32.6 SEC
YAW	300 VOLTS/RAD	0.057 RAD	32.6 SEC

NORMAL MODEWHEEL CONTROLLER GAINS

	<u>POSITION GAIN</u>	<u>RATE GAIN</u>
ROLL	$3.64 \times 10^4$ VOLTS/RAD	11.7 SEC
PITCH	$2.16 \times 10^5$ VOLTS/RAD	5.65 SEC
YAW	$2.16 \times 10^5$ VOLTS/RAD	5.65 SEC



following values to improve control performance, based upon simulation results:

$$K_{py} = K_{pz} = 97 \text{ volts/rad}$$

$$K_{ry} = K_{rz} = 100 \text{ sec}$$

$$\theta^L = \psi^L = .075 \text{ radians}$$

These values provided improved response in both pitch and yaw and were used throughout the final studies.

#### 4.2.3.2 Normal Mode

The magnetic control law during normal mode must be the BxH law, as the B law is not applicable. The momentum reference (H) in the control law in this case, however, is the wheel momenta rather than the spacecraft body momenta. This results in an effective gain reduction as the maximum body momentum is of the order of 200 ft-lb-sec, while the maximum wheel momentum is of the order of 40 ft-lb-sec. Thus to get loop gain equivalent to the acquisition case, one would have to increase the control gain by a factor of approximately 5. However, it is desired that a lower maximum magnetic moment be utilized during normal mode for power conservation. To achieve this characteristic, the control gain would be reduced by approximately an order of magnitude (equivalent to  $\approx 200 \text{ amp-turn-m}^2$  maximum moment command). The net effect is a gain reduction of about two relative to the acquisition magnetic gain. By experimentation, using this preliminary estimate, a value of  $0.01 (\text{sec-gauss}^2)^{-1}$  was found to provide the most satisfactory performance.

The wheel control parameters used in the study of normal mode were taken directly from the current HEAO-B study results in which attitude control is via wheels. These control parameters are also shown in Table 4-2. For the celestial scan mode, the yaw control channel must be modified to provide scan rate control. The control law employed was

$$\epsilon_z = K_{pz} K_{rz} (\omega_z - \omega_{z0}) \quad (4-26)$$

where  $\omega_{z0}$  is the desired scan rate. The gains have the same value as for the pointing mode above.

#### 4.2.4 Electromagnet Design

Three electromagnets arranged in an orthogonal configuration are necessary for generation of the required attitude control torques. The electromagnets must be designed to operate in two basic modes, namely sun acquisition (and reacquisition) and normal mode (celestial scan or celestial point). During acquisition, the electromagnets must generate a large torque to permit efficient removal of tipoff momentum, while during the normal cruise mode, a much smaller torque is required as the electromagnets are employed only for momentum unloading of the reaction wheels. The required control torques on a per axis basis are 10 in-oz for acquisition, and 1 to 2 in-oz for normal mode. Generation of a 10 in-oz torque with an electromagnet at the HEAO orbital altitudes, requires an electromagnet with a magnetic moment of 2,000 amp-turn-m<sup>2</sup>. During the cruise modes, the required magnetic moment decreases to a value between 200 and 400 amp-turn-m<sup>2</sup>. Magnetic moment is the primary parameter in the electromagnet design.

After selection of the magnetic moment, the core volume, length and material must be chosen. To minimize the demagnetization effects of the core (which is inversely proportional to the core length to diameter ratio), it is necessary to select the maximum core length practically possible. For the current HEAO configuration and the proposed electromagnet locations, an overall electromagnet length of 5 feet is appropriate. As the magnetic moment generated is a function of the core flux density, it is imperative that the core material be able to sustain a high saturation induction (24,500 gauss) and a high incremental permeability. The high incremental permeability is necessary because the electromagnet drivers operate in a pulsed manner and this forces the core magnetization to cycle in a minor hysteresis loop about a bias value. For good overall linearity, the maximum core flux density was limited to 20,000 gauss.

The maximum input power to the electromagnet was set at 16 watts for a minimum voltage of 22 volts. A computer program (previously developed for the SESP electromagnet design) was then used to select the required wire size, number of turns and coil current. Aluminum wire was chosen over copper for weight reasons. The resultant coil design employs 6,545 turns of No. 17 AWG heavy Poly-thermalize wire wound on an epoxy

glass coil form. Each coil form is 1.650 inches inner diameter and 2.734 inches outer diameter by 58.2 inches in length. The core is 1.500 inches in diameter and 58.200 inches long. Each electromagnet has a redundant winding and is enclosed in a fiberglass case filled with silastic potting compound. Table 4-3 lists the key magnetic, electrical and mechanical parameters of the electromagnet design.

#### 4.2.5 Electromagnet Driver Design

The electromagnet driver electronics generates a drive current ( $I_c$ ) with the magnitude and polarity determined by the magnetic moment command ( $M$ ) received through the transfer assembly (TA). Two complete drivers and electromagnet windings are required for each control axis. These two separate systems (per axis) are operated in an active/standby mode with the mode controlled by the TA. The two drivers are cross-strapped with the two TA's to satisfy system reliability requirements.

The principal design requirements established for the driver electronics was that coil current must be proportional to the magnetic moment command, and the driver circuit must operate efficiently. After evaluating different circuit configurations which included linear power amplifiers and variable voltage dc-to-dc converters, it was found that a pulsed transistor bridge switch could best satisfy these design requirements.

A block diagram of the selected electromagnet driver is presented in Figure 4-6. As indicated in this diagram, the driver consists of five separate functional circuits.

The absolute value detector converts the bipolar magnetic moment command received from the TA into an absolute value voltage and a sign voltage. The absolute voltage determines the coil winding current ( $I_c$ ) magnitude (and thus the magnetic moment magnitude) while the sign voltage controls the coil current direction (magnetic moment sense). The sign voltage also controls the feedback voltage  $e_f$  such that this voltage is always positive at the comparator circuit input.

The signal  $e_f$  is compared to  $|M|$  at the comparator and if it is less than an allowable percentage of  $|M|$ , then the coil current is increased. If  $e_f$  exceeds  $|M|$  by the same percentage, then the coil current is

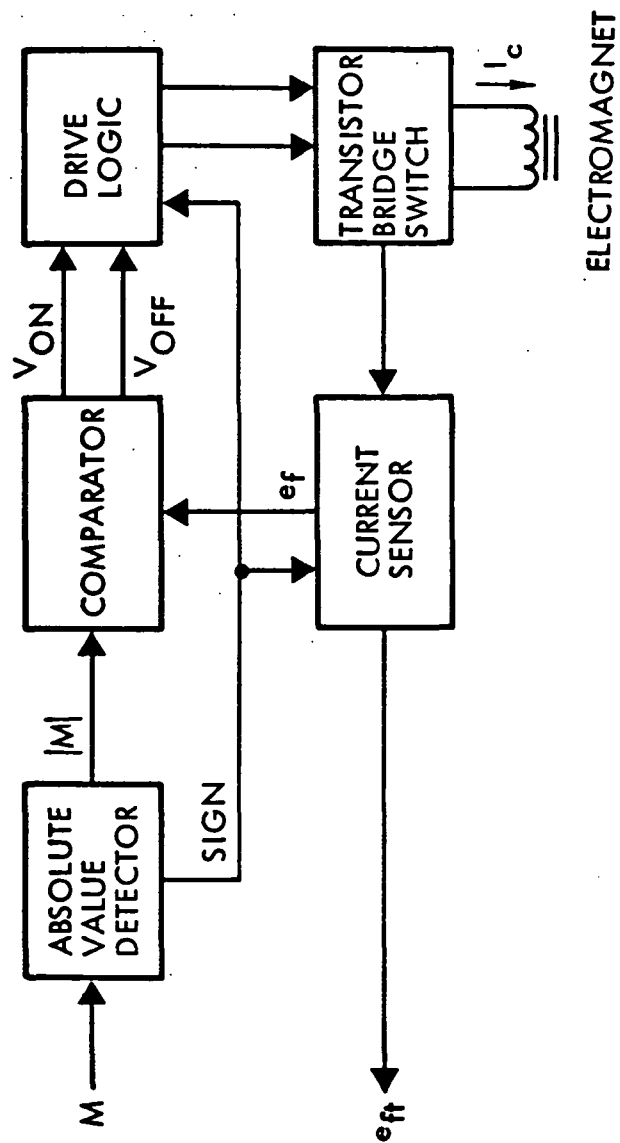


Figure 4-6. Block Diagram of the Electromagnet Drive Electronics

Table 4-3. Electromagnet Design Parameters

<u>MAGNETIC PARAMETERS</u>	
MAGNETIC MOMENT (MAX)	2,062 Amp-turn-m <sup>2</sup>
CORE FLUX DENSITY (MAX)	19,751 Gauss
EFFECTIVE PERMEABILITY	564 Gauss/Oersted
LENGTH/DIAMETER RATIO	38.8
<u>ELECTRICAL PARAMETERS</u>	
POWER (MAX)	16 Watts
CURRENT (MAX)	.727 Amperes
VOLTAGE	22 Volts
RESISTANCE	30.3 Ohms
INDUCTANCE	20.3 Henries
<u>MECHANICAL PARAMETERS</u>	
SIZE	2.85 In. Dia. x 60.0 In.
WEIGHT	51.1 Lbs
CORE	(30.1) Lbs
CONDUCTOR	(13.7) Lbs
POTTING COMPOUND	( 5.8) Lbs
CASE	( 1.5) Lbs

decreased. This logic allows duty cycling of the control current.

The drive logic circuit decodes the comparator output voltage ( $V_{on}$  and  $V_{off}$ ) to ensure correct pulsing of the bridge switch. Also included in the drive logic circuit is an analog switch controlled by the sign voltage. This switch connects the logic output to the correct transistors and thus determines the coil current direction.

The transistor bridge switch consists of switching, amplifying, and power transistors. The four power transistors are arranged in a bridge circuit with the electromagnet between the two sides of the bridge. This arrangement is illustrated in the figure below. As indicated in the figure, the coil current direction and magnitude can be controlled by pulsing the correct pair of transistors.

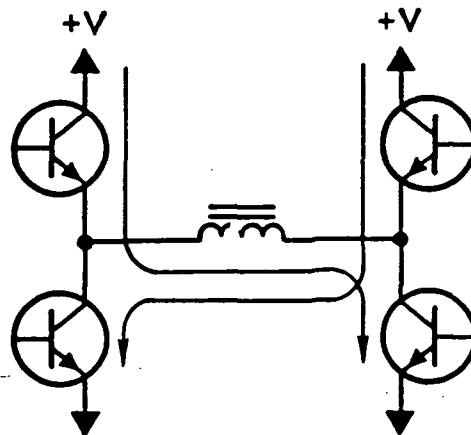


Figure 4-7. Transistor Bridge Circuit

The current sensor circuit constantly senses the current  $I_c$  and generates a voltage  $e_f$ , which is proportional to the current. This voltage is used to compare the current with the magnetic moment command. An additional output from the sensor circuit is  $e_{ft}$ . This voltage is the same as  $e_f$ , except that it contains current magnitude and direction for monitoring via telemetry.

The use of a bridge switch arrangement for controlling the coil current requires a variable duty cycle (as a function of coil current magnitude) and a constant dc mode when new current magnitudes are required. The technique selected to control the current through the coil is to sense the coil current level and to maintain this level within a current band of  $\pm \epsilon$ , as illustrated below.

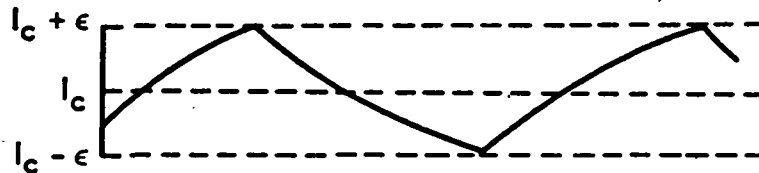


Figure 4-8. Electromagnet Coil Current Characteristic

This method will maintain the current within a small "error" band and allow a pulsed mode of operation. When a new current level is required, the on transistors of the bridge switch remain on until the  $I_c + \epsilon$  level is sensed, and then the transistors are turned off. When the current drops to  $I_c - \epsilon$ , the transistors are turned on again.

The method of establishing the limits of the current band can be more easily understood by referring to the more detailed block diagram of Figure 4-9. In this block diagram, the comparator section consists of operational amplifiers  $A_1$  and  $A_2$  and the two comparators. The  $A_1$  and  $A_2$  gains determine the range  $\pm \epsilon$  within which the coil current is maintained. If an  $\epsilon$  of .01 (1%) were chosen, then the gain of  $A_1$  would equal 1.01 and the gain of  $A_2$  would be 0.99. When the current flowing through the coil causes a voltage ( $e_f$ ) to be less than 0.99 M,  $Q_1$  and  $Q_2$  of the

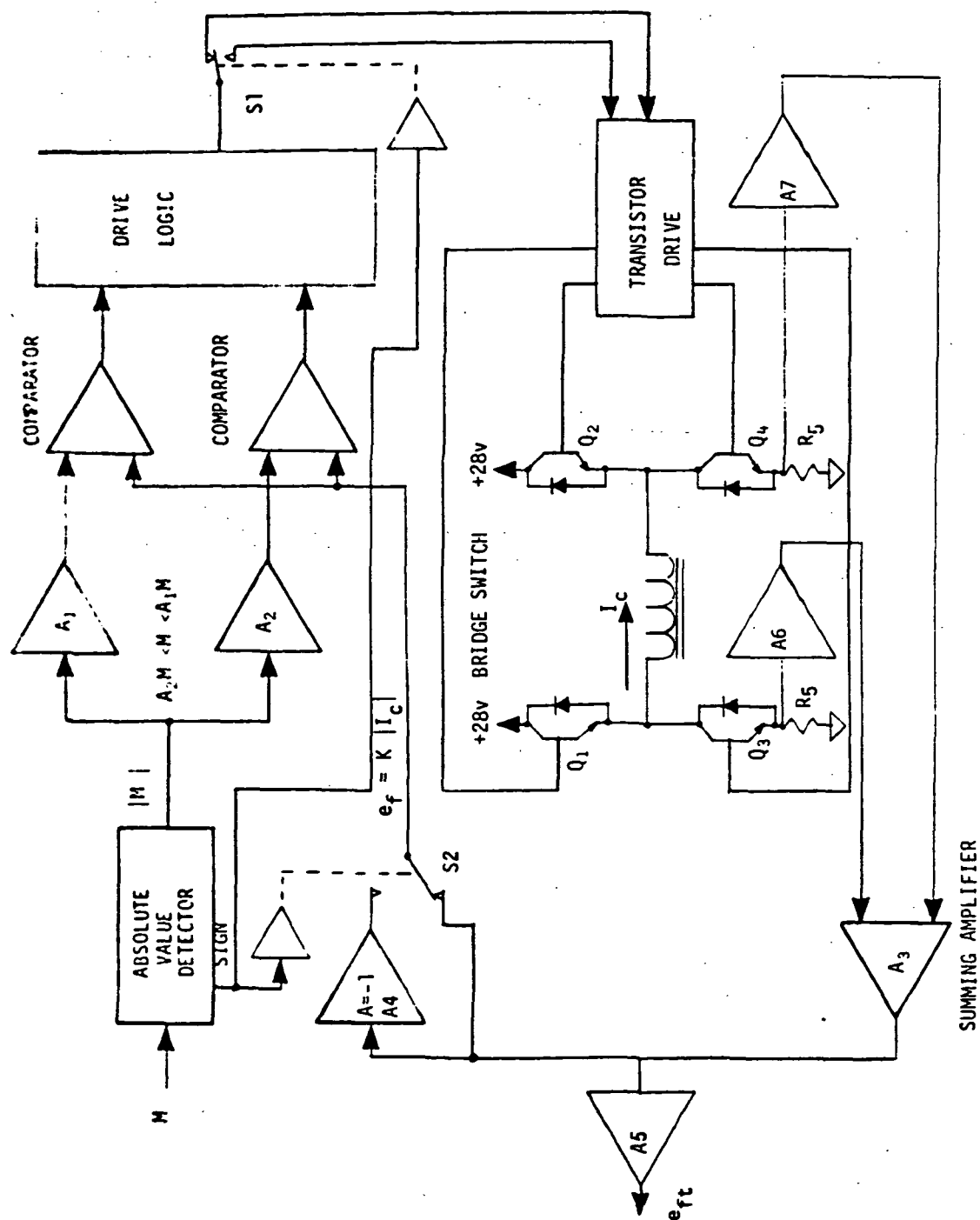


Figure 4-9. Block Diagram - Electromagnet Drive



bridge switch would remain on for the current direction shown in Figure 4-9 until  $e_f = 1.01M$ . When this voltage is reached,  $Q_1$  and  $Q_2$  will be turned off and remain off until  $e_f$  decreases to  $.99M$  again.

The duty cycle for this circuit is a function of the coil current magnitude. This is because the current path for the on and off portions of the duty cycle are different (i.e., different time constants), and this difference has more effect at large currents than at lesser currents. When  $Q_1$  and  $Q_2$  in Figure 4-9 are turned on, the current flows through these transistors and the load consisting of  $L$ ,  $R_L$  (coil resistance), and  $R_5$ . When  $Q_1$  and  $Q_2$  are turned off, the diodes across  $Q_2$  and  $Q_3$  provide a low resistance path for current to flow and thus prevent large induced voltages across the transistors caused by the coil inductance. However, this "off" current path differs from the "on" current path and accounts for the duty cycle variation. If we define  $T_{on}$  and  $T_{off}$  to be the on and off time constants, we can see that  $T_{off}$  is smaller than  $T_{on}$ , because the diode voltage drop ( $V_{diode}$ ) is greater than the transistor saturation voltage ( $V_{cesat}$ ). Or,  $R_{diode} > R_{sat}$  and since  $T = \frac{L}{R}$ ,  $T_{on} (= \frac{L}{R_{on}})$  is greater than  $T_{off} (= \frac{L}{R_{off}})$  where  $R_{on}$  and  $R_{off}$  are the path resistances during on and off conditions and are equal to  $R_{sat} + R_{coil}$  and  $R_{diode} + R_{coil}$ , respectively. This discussion can be proven by determining the time required for increasing and decreasing current between the levels  $I_c \pm \epsilon$  during pulsed operation and then determining the duty cycle by the equation,

$$\text{Duty Cycle (\%)} = \frac{100 \times t_{on}}{t_{on} \times t_{off}} \quad (4-27)$$

where

$t_{on}$  is the time to increase the current from  $I_c - \epsilon$  to  $I_c + \epsilon$

$t_{off}$  is the time to decrease the current from  $I_c + \epsilon$  to  $I_c - \epsilon$

The equation relating duty cycle and the required coil current,  $I_c$ , is given by the relation:

$$\text{Duty Cycle (\%)} = \frac{100}{1 + \frac{\ln A}{\ln B}} \quad (4-28)$$

where:

$$A = \frac{(1-\epsilon)I_c + (E+2ED)/R}{(1+\epsilon)I_c + (E+2ED)/R}$$

$$B = \frac{(1+\epsilon)I_c - (E-2V_{ces})/R}{(1+\epsilon)I_c - (E-2V_{ces})/R}$$

where:

$E$  = voltage applied to the bridge switch

$V_{ces}$  = transistor saturation voltage

$R$  = coil resistance (since  $R_s \ll R_L$ )

$ED$  = diode forward voltage drop

If we assume that  $V_{ces}$  and  $ED$  are constant, then the duty cycle is a function of  $I_c$  only. A plot of duty cycle versus  $I_c$  can be made if we substitute values for the constants in Equation (4-28). This plot is shown in Figure 4-10, with the following constant values:

$E$  = 28 VDC

$V_{ces}$  = 0.35 VDC

$R_L$  = 30 Ohms

$ED$  = 0.6 VDC

$\epsilon$  = 0.01

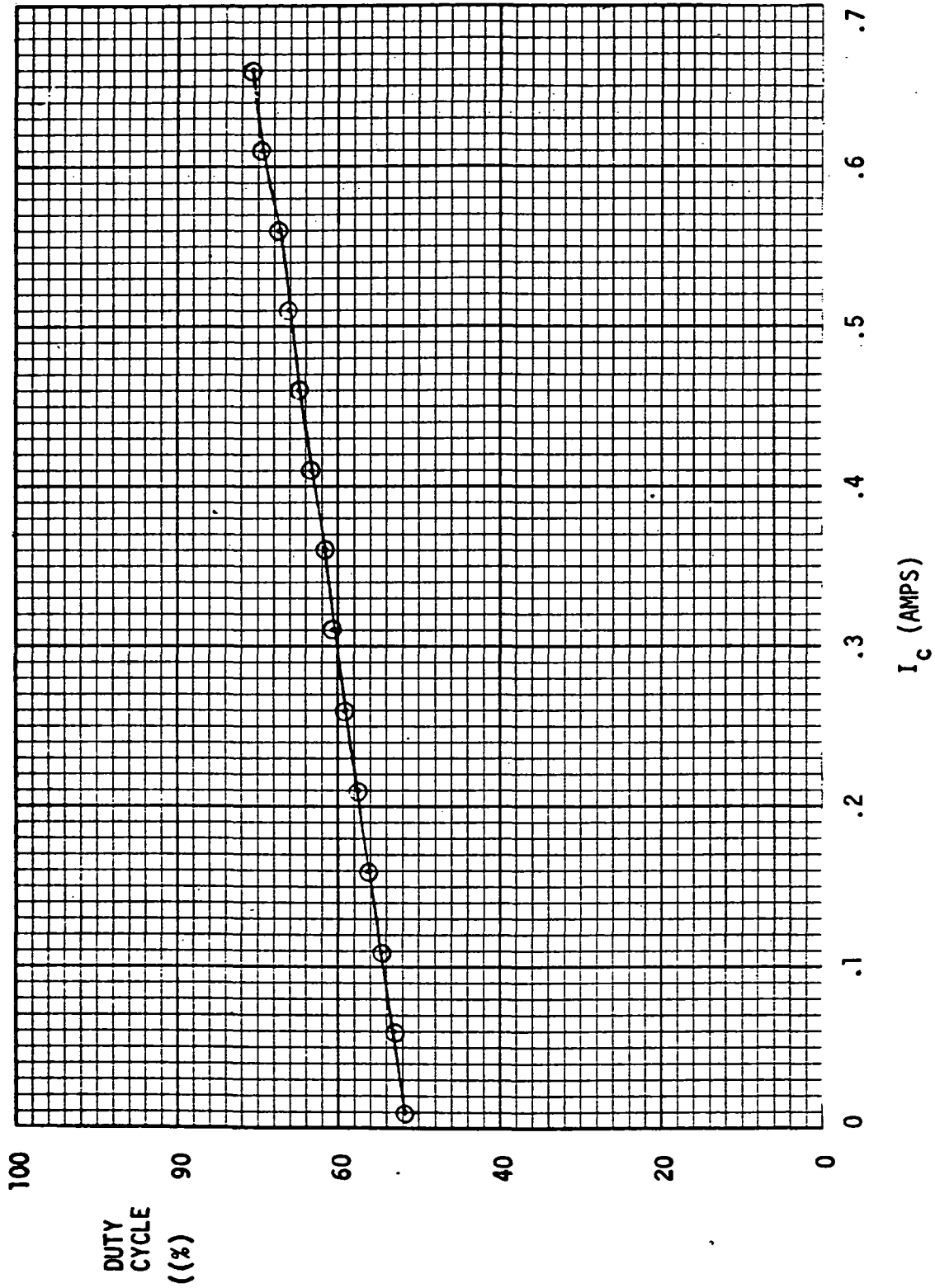


Figure 4-10. Electromagnet Driver Duty Cycle vs. Coil Current

The peak power required for both acquisition and unloading is given below in Table 4-4 for the drive electronics (bridge switch and transistor drive) and the processing electronics (amplifiers and drive logic).

Table 4-4. Peak Power Requirements

	<u>ACQUISITION</u>	<u>UNLOADING</u>
PROCESSING ELECTRONICS (SECONDARY VOLTAGE)	0.9	0.7
DRIVE ELECTRONICS (PRIMARY BUS VOLTAGE)	1.1	0.4
TOTAL	2.0	1.1

The output signal  $e_{ft}$  is transmitted to the TA to provide status of the electromagnet driver via the telemetry link. If the active electromagnet drive electronics fails, this signal, when compared with the magnetic moment command will indicate a failure, and the standby electromagnet driver and coil can be placed in operation.

In addition to the sections of the driver electronics discussed above, the circuit will require filtering of the power bus because of the transistor bridge switching. Filtering will ensure compliance with HEAO EMC Specification EV2-32A. Short circuit protection for the power bus will also be required in the final design. Neither of the above requirements however, present an extreme design problem or cause significant additional power requirements.

#### 4.2.6 Magnetometer Requirements

The magnetometer to be used in the magnetic control system to measure the magnetic field at the spacecraft will be a Triaxial Fluxgate Magnetometer Assembly. The assembly consists of a sensor unit, an electronic unit, and the interface cable between these units. There will be two magnetometer assemblies aboard each spacecraft operating in an active/standby mode.

The sensor units will be mounted on the extended solar arrays (possibly on a mechanical support assembly on HEAO-A). The maximum size of these units will be 5 inches x 3 inches x 3 inches. The maximum weight of each sensor unit and interfacing cable will be 4.0 lbs. Maximum power required by the Magnetometer Assembly will be 1.0 watt.

The electronic unit will be mounted in the equipment module. The maximum size of each electronics package will be 7 inches x 5.5 inches x 3 inches. The maximum weight of these units will be 2 lbs each.

The Magnetometer Assembly must be capable of measuring the earth's magnetic field, which is approximately 0.35 gauss at HEAO spacecraft altitudes. It must measure the field present with the resolution and accuracy to meet system design requirements. The magnetometer range will permit measurement of fields greater than the earth's field and will allow biasing out any static fields present due to fields generated by either the experiments or spacecraft equipment.

The performance requirements for the Magnetometer Assembly are listed below in Table 4-5.

Table 4-5. Magnetometer Assembly Performance Requirements (Per Axis)

OUTPUT SIGNAL CHARACTERISTICS	0 + 5 VDC
RANGE	$\pm 1$ Gauss
LINEARITY	THE NONLINEARITY OF THE READING SHALL NOT EXCEED + 1% OF 2.5 VOLTS/GAUSS OVER THE ENTIRE RANGE.
RESOLUTION	0.004 Gauss
ACCURACY	$\pm 0.1\%$ OF FULL SCALE

A bias voltage of 2.5 VDC corresponding to a zero magnetic field will be provided as an output of the magnetometer. A change in this bias voltage would be an erroneous indication of the magnetic field. Therefore, this bias voltage output and each axis field voltage output will be buffered in the transfer assembly for ground monitoring via the telemetry link.

#### 4.2.7 Interface Electronics

Each Magnetometer Assembly (active and standby) interfaces with one transfer assembly (TA). The block diagram below illustrates the signal and power interface between the magnetometer and the TA.

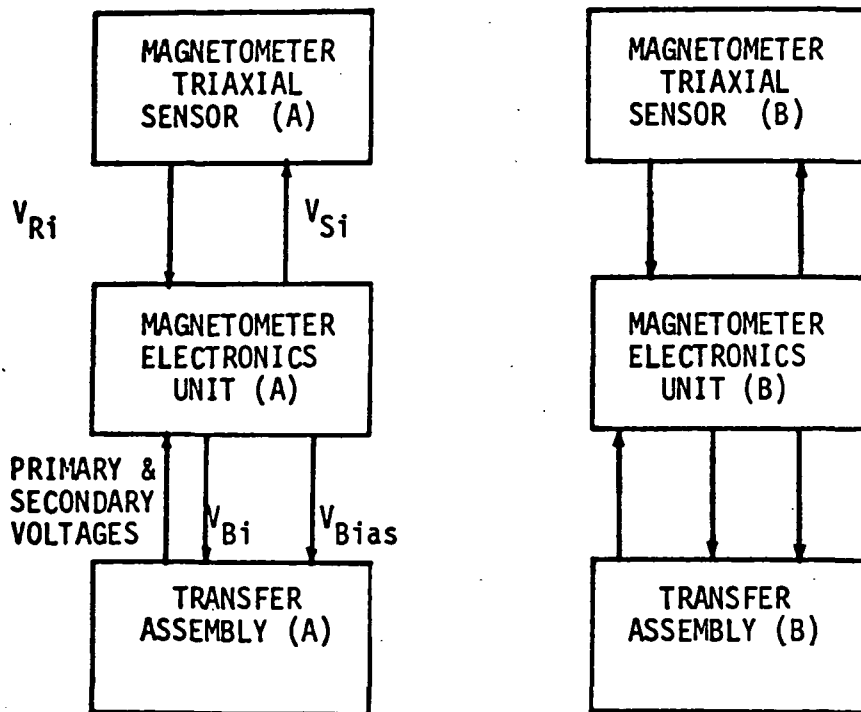


Figure 4-11. Block Diagram - Magnetometer to Transfer Assy. Interface

In this block diagram,  $V_{Si}$  and  $V_{Ri}$  are the input and output signals per axis ( $i = X, Y, Z$ ), which are used to measure the ambient magnetic fields.  $V_{Bi}$  and  $V_{Bias}$  are the field measurement voltages and the zero magnetic field bias voltages, respectively.

The electromagnet driver electronics also interface with the transfer assembly, as shown in the block diagram below. The signals  $M_i$  and  $e_{fti}$  were defined in the electromagnet driver design discussion of Section 4.2.5. The power for the driver electronics provided through and controlled by the TA. This enables each TA to control each driver, as illustrated symbolically by paralleling the voltage and signal lines in the block diagram. In this manner, the TA selects which of the drivers is active and which is in standby.

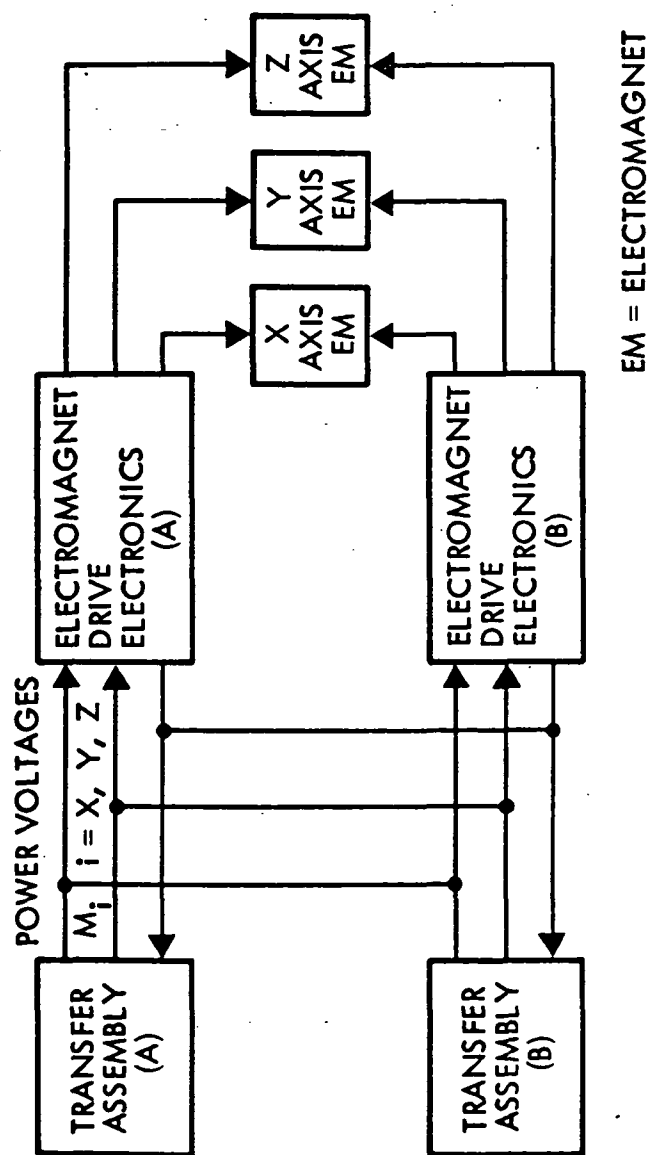


Figure 4-12. Transfer Assembly/Electromagnet Electronics Interface

### 4.3 Subsystem Performance

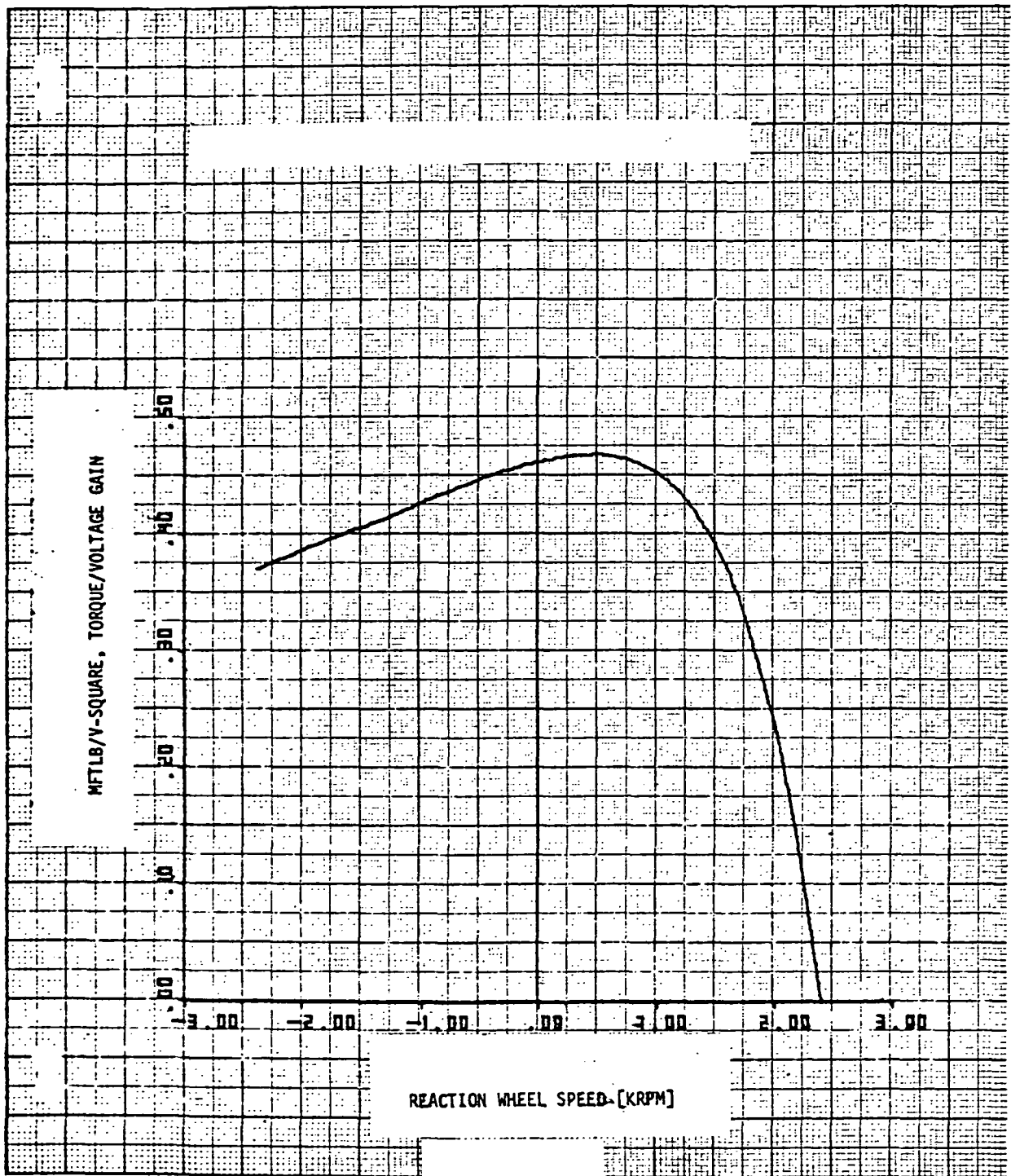
The design feasibility of magnetics in the ACDS implementation is dependent upon two general aspects of performance:

- The ability to accomplish sun acquisition
- The ability to maintain the reaction wheels in an unloaded condition during normal mode

These two aspects of performance were addressed separately in the study. The results will similarly be discussed separately in this section.

The performance analysis work was performed with the aid of a common digital computer simulation, which modeled the three-degree-of-freedom rigid body angular equations of motion. The earth's magnetic field was modeled as a tilted dipole, inclined  $11^\circ$  with respect to the earth's spin axis and offset  $20^\circ$  from the Greenwich meridian. The magnetometers, sun sensor and rate gyros were modeled as ideal sensors. Gravity gradient disturbance torque equations were included in the simulation for long and short term performance assessment. The reaction wheel model used featured some unique characteristics of special note. For simplification, only three reaction wheels were modeled - one for each axis. The torque-speed characteristics of a typical wheel are shown in Figure 4-13. The torque is proportional to the square of the impressed voltage (Figure 4-13 ordinates), whereas the voltage is directly proportional to the attitude error signal (see reaction wheel control laws). Thus, the error to torque transfer is a square law relation. The inertia assumed for each wheel was based on either the three or four wheel model of HEAO-B, to provide a total momentum capability for each axis, as shown in Table 4-6.





TQSP1 090673

Figure 4-13. Reaction Wheel Torque Gain Constant Characteristic

Table 4-6. Reaction Wheel Momentum Characteristics

	<u>4 WHEELS ACTIVE</u>	<u>3 WHEELS ACTIVE</u>
$H_x$	$0.684 H_w$	$0.342 H_w$
$H_y$	$1.328 H_w$	$0.664 H_w$
$H_z$	$1.328 H_w$	$0.664 H_w$

where:

- $H_x$  = momentum storage capability for x-axis
- $H_y$  = momentum storage capability for y-axis
- $H_z$  = momentum storage capability for z-axis
- $H_w$  = momentum storage capability for one HEAO-B wheel

These characteristics were used throughout the individual studies discussed in the following sections.

#### 4.3.1 Sun Acquisition Performance

The goals of this portion of the study were to determine the conditions under which sun acquisition could be performed satisfactorily and to assess the sensitivity of the nominal performance to the following types of effects:

- Mass properties (HEAO-A/C or B, see Table 4-1)
- Initial body rates (maximum of  $1^\circ/\text{sec}$  about each axis due to separation)
- Initial magnetic field/momentum geometry
- Maximum electromagnet moment capability
- Magnetics to wheels transition criteria
- Magnetic field biases

- Magnetic control coupling between electromagnetics and magnetometers
- Reaction wheel configuration

The relevant comparison criteria used in the performance assessment consisted of the following parameters:

- Total time required for sun acquisition
- Amount of time under magnetic control alone
- Amount of time under combined wheel and magnetic control
- Momentum stored in wheels at time of acquisition capture

The numerical values of these parameters resulting from the simulations are summarized in Table 4-7 for the various perturbation conditions studied. As indicated in the footnote in the table, the specific value of total time to acquisition capture is quantized to +0, -10 minutes, due to manner in which the completion criteria logic was implemented. Thus, differences of the order of 10 minutes are not significant for comparison purposes. The time to combined wheel/magnetic transition was more precisely defined and thus not subject to the same quantization. This parameter indicates the effectiveness of the magnetic controllers. The last column in the table indicates the final composite magnitude of the momentum stored in the wheels after sun acquisition is complete.

The basic philosophy used in the development of the acquisition control sequence was that the reaction wheel control system would remain off until the magnetic torquers had reduced all three body rates below some threshold. At this switching point (Mode 1A to 1B transition), the magnetic control law would be changed to the unloading law, and the position loop closed via the sun sensor for wheel control. Thus true acquisition only began at transition to wheel control.

A perturbation to this sequence in which the reaction wheels are activated immediately upon separation and the magnetic control system activated to unload wheel momentum was also considered. This technique allowed earlier acquisition, but requires relatively long unloading periods.

Table 4-7. Acquisition Performance Summary

CASE	DESCRIPTION	OPERATING TIME ON MAGNETICS ONLY (MINUTES)	OPERATING TIME ON WHEELS + MAGNETICS (MINUTES)*	ACQUISITION TIME (MINUTES)*	FINAL MAGNITUDE OF STORED WHEEL MOMENTUM (FT-LB-SEC)
1	BASILINE (HEAO-B)	186	14	200	17.5
2	HEAO-A	22	43	65	42.1
3	BASILINE WITH LOWER INERTIA (2/3)	193	7	200	7.1
4	BASILINE WITH ADVERSE INITIAL ALIGNMENT ( $B \times H$ ) $t = t_0 = 0$	212	28	240	22.3
5	BASILINE WITH HIGHER RATES FOR WHEEL TRANSITION	92	58	150	24.7
6	BASILINE WITH INITIAL WHEEL ACTIVATION	0	150	150	30.3
7	BASILINE WITH REDUCED MAXIMUM MAGNETIC MOMENT (1000 amp-turn-m <sup>2</sup> )	241	19	260	3.9
8	BASILINE WITH INCREASED MAXIMUM MAGNETIC MOMENT (3000 amp-turn-m <sup>2</sup> )	197	33	230	7.6
9	BASILINE WITH RESIDUAL FIELD BIAS (1%)	250	20	270	20.3
10	BASILINE WITH MAGNETIC COUPLING (5%)	239	41**	280	NOT AVAILABLE
11	BASILINE WITH MAGNETIC COUPLING (5%) AND REDUCED INITIAL RATES	190	10	200	13.8

\*TIMES QUANTIZED TO +0, -10 MINUTES DUE TO SIMULATION TERMINATION LOGIC

\*\*ESTIMATE BASED UPON ACQUISITION PERFORMANCE FROM OTHER SIMULATED CASES

### Baseline Performance

A performance baseline was established which reflected operation from the following set of conditions:

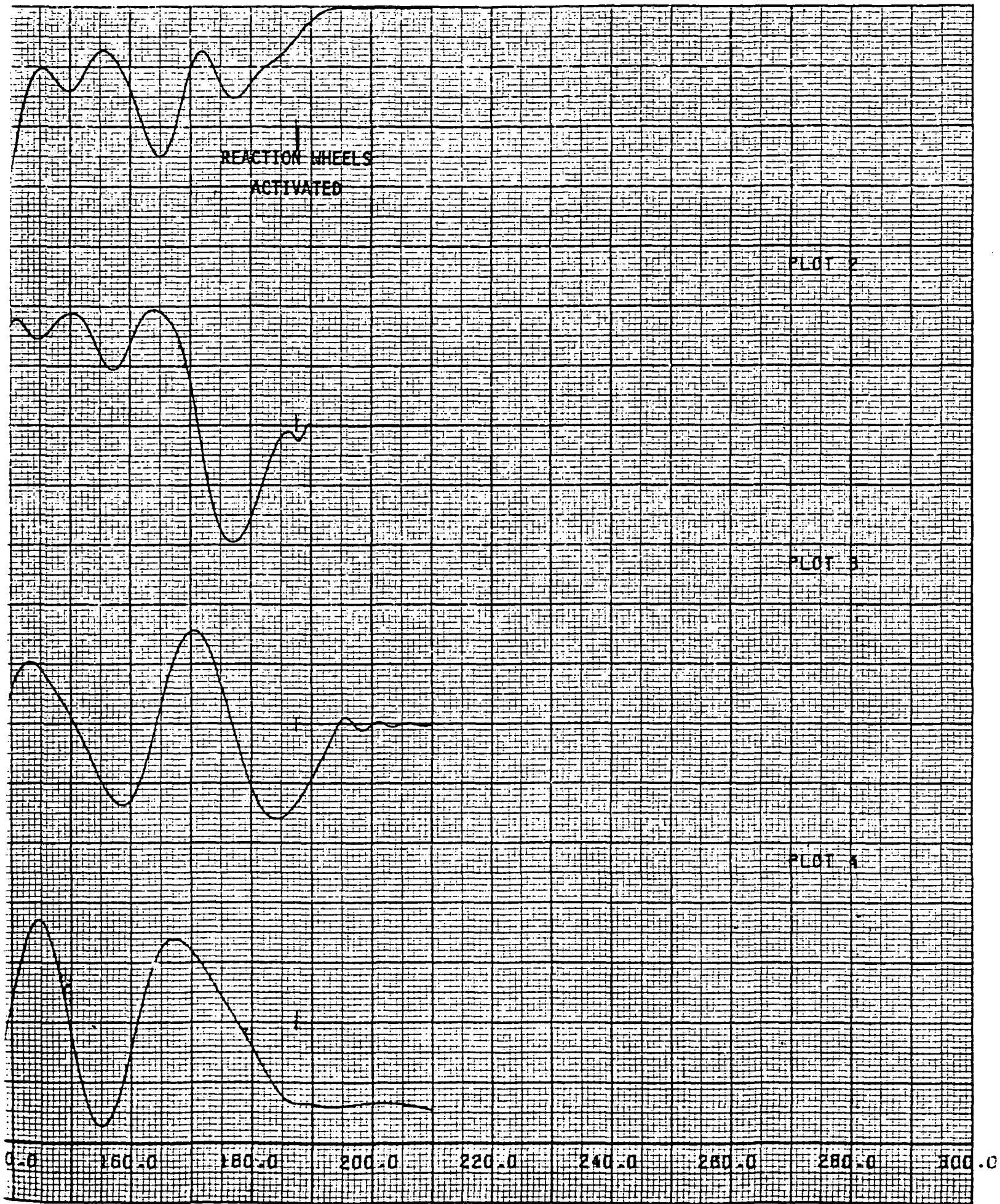
- HEAO-B mass properties (see Table 4-1)
- Gravity gradient disturbance torques active
- 22.5° orbit inclination
- 225 nautical mile orbital altitude
- 2000 amp-turn-m<sup>2</sup> magnetic moment capability per axis
- Initial body rates of 1°/sec about each axis
- Wheel activation at  $\omega_x = 0.573^\circ/\text{sec}$ ,  $\omega_y = \omega_z = 0.115^\circ/\text{sec}$

Figures 4-14 through 4-18 illustrate the performance for the baseline conditions of Case 1 (Table 4-7).

Figure 4-14 illustrates the attitude of the spacecraft during the acquisition phase in relationship to the sun. The direction cosine, B33, which is plotted at the top of the figure, is representative of the angular deviation of the spacecraft z-body axis from the sun vector. The next three plots on Figure 4-14 represent attitude errors with respect to the quasi-inertial (sun pointed) coordinate system. That system is defined by a z-vector being sun pointing, the y-vector in the ecliptic plane and the x-vector completing the right-hand set. Direction cosine B23 represents the roll error and B13 represents the negative of the pitch error. The requirements for acquisition are that B33 approach +1, and that B13 and B23 both go to zero. The value of B12 is not controlled, because it represents the angle of rotation about the z-body or sun pointing axis. However, the z-body rate is nulled by the action of the control system.

Figures 4-15, 4-16 and 4-17 illustrate the attitude control performance about the x, y, and z axes of the spacecraft, respectively. Note that the electromagnet associated with a given axis (bottom variable) actually exerts control about the other two axes due to the cross product characteristic of the magnetic interaction. Wheel control activation is indicated in the figures at 187.5 seconds.

POSITION (HXB) K=.05



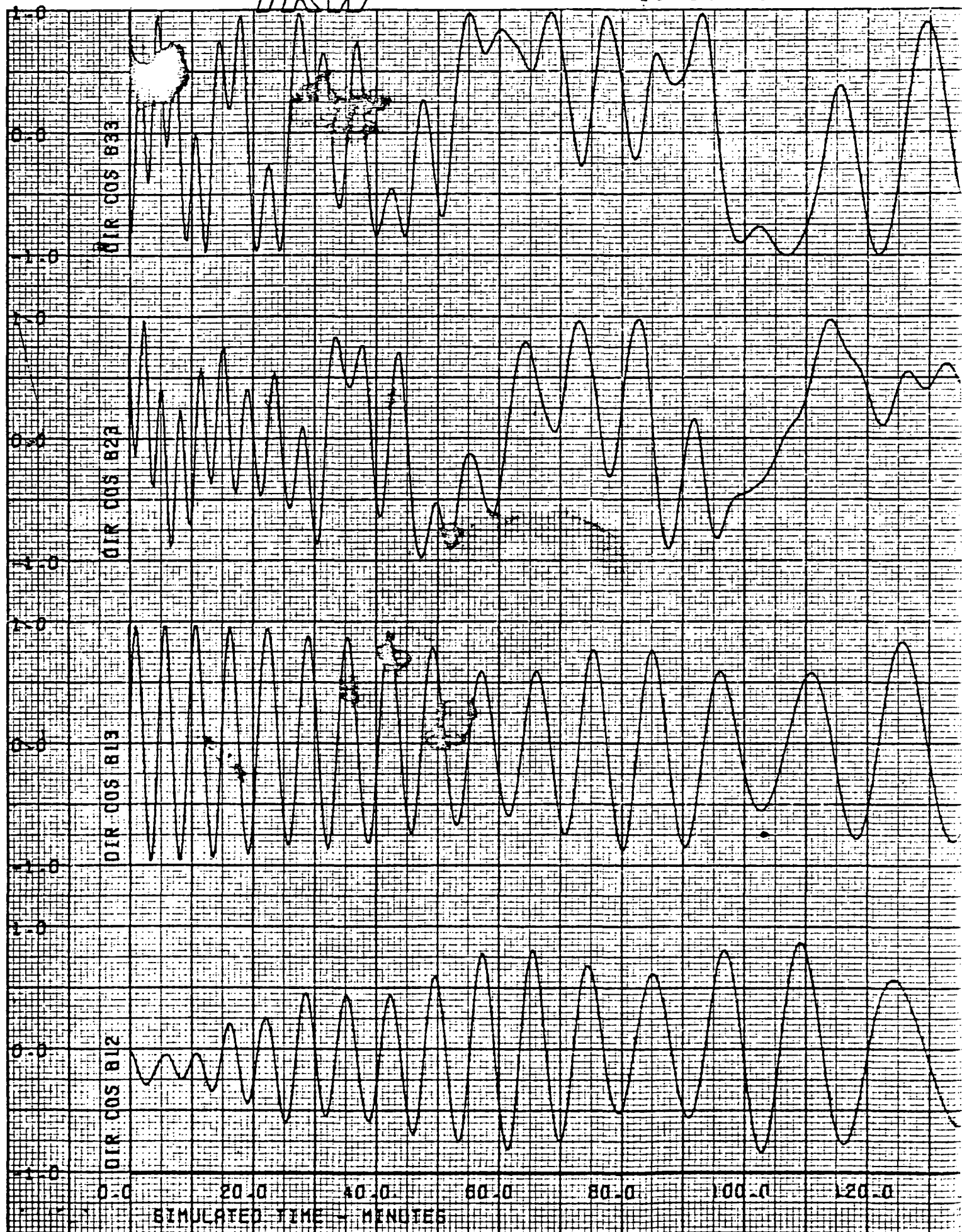
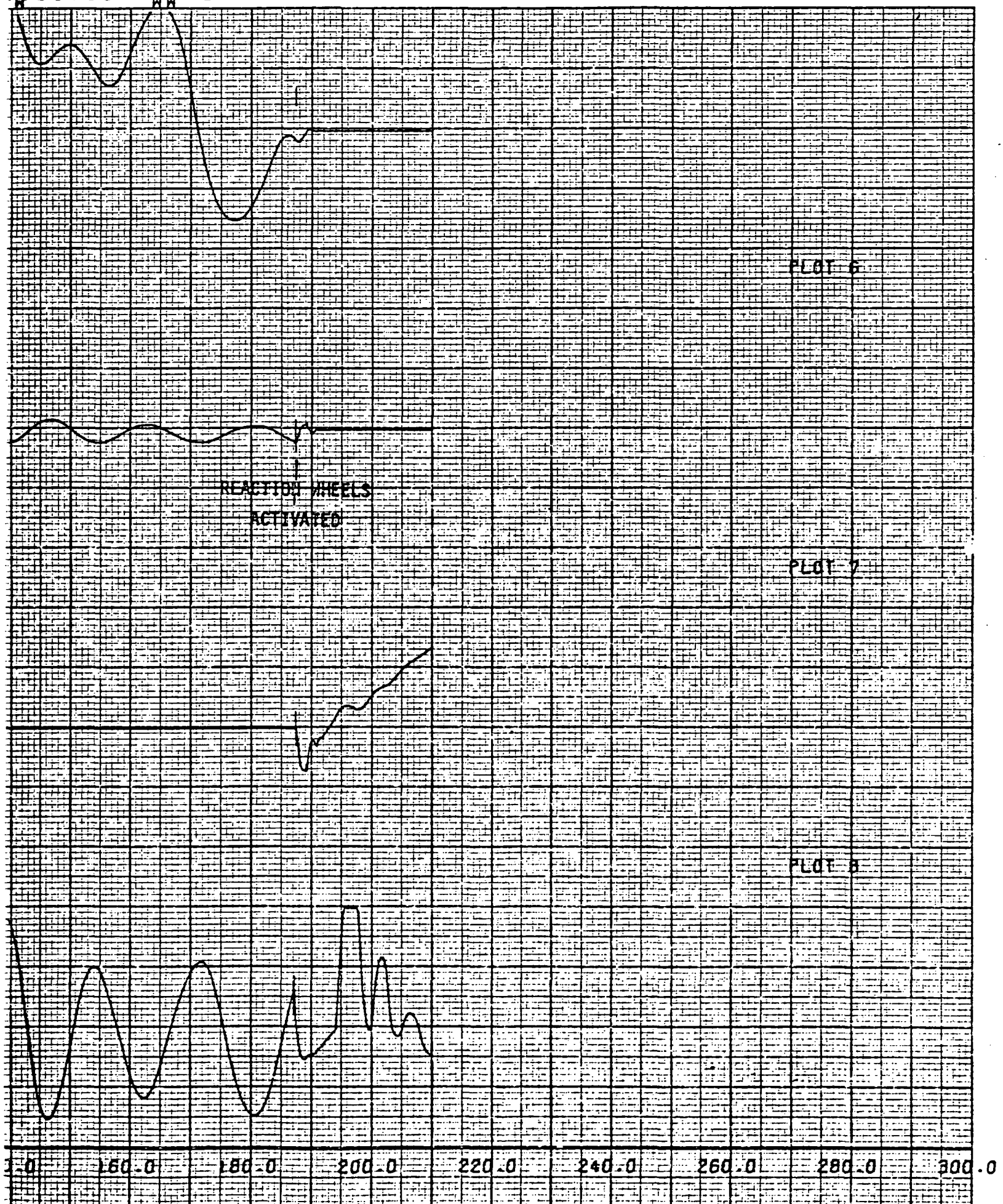


Figure 4-14. HEAD-B







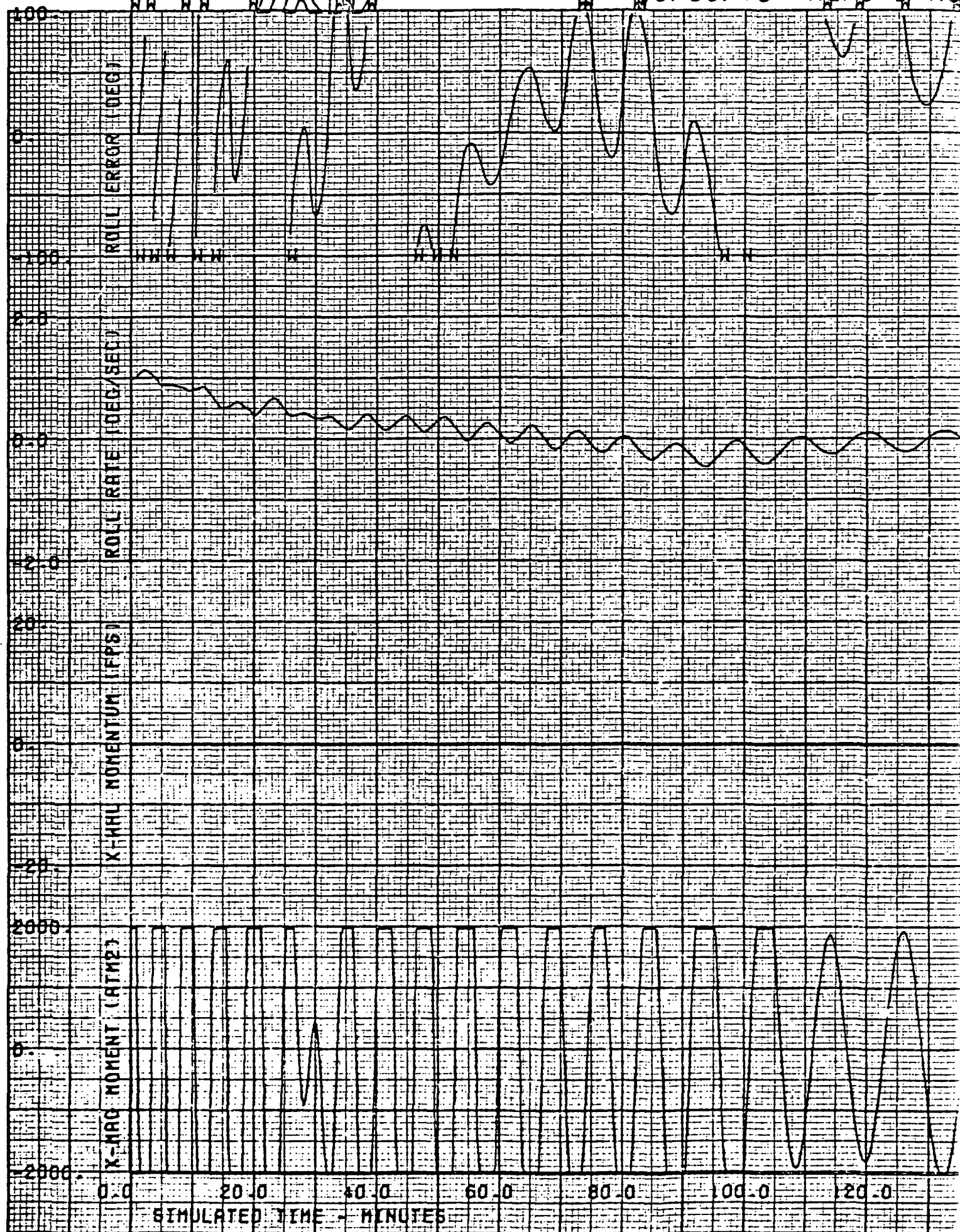
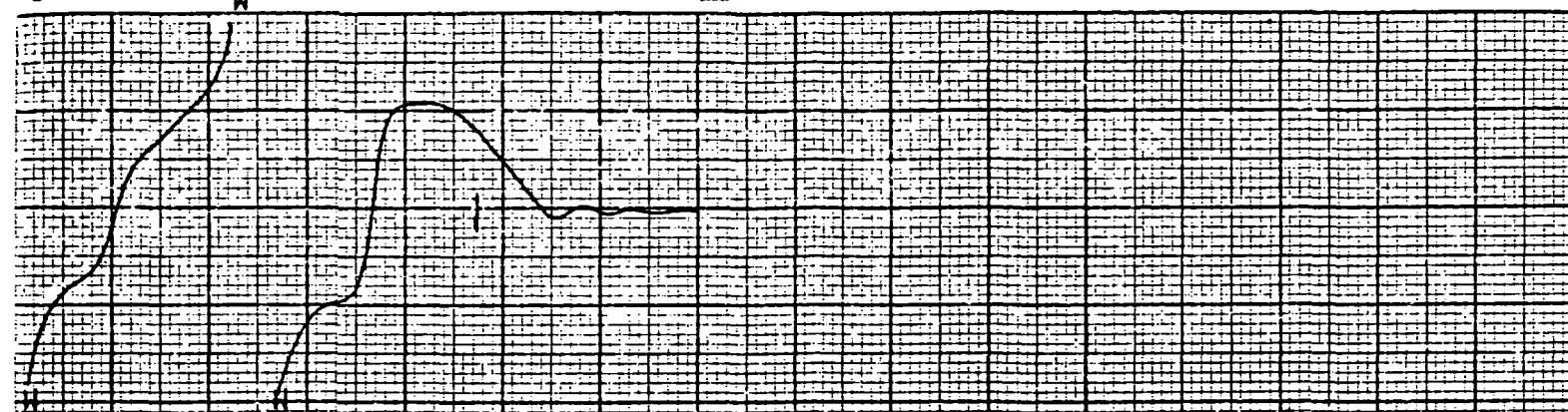
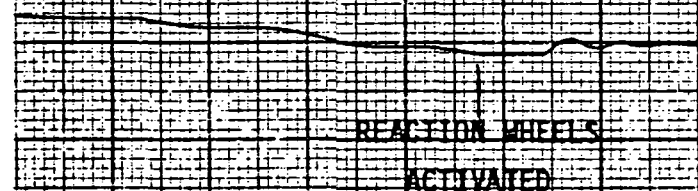


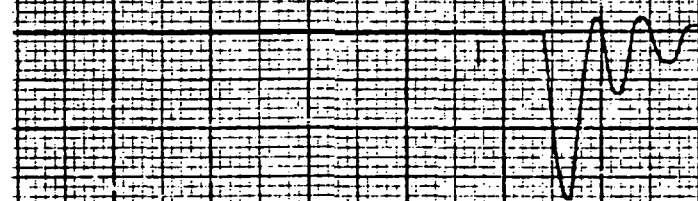
Figure 4-15. Roll Responses



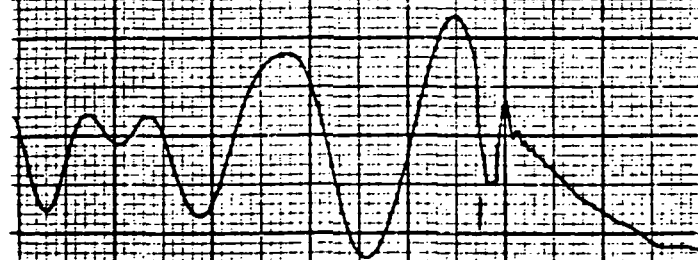
PLOT 10



PLOT 11



PLOT 12



-0.0 160.0 180.0 200.0 220.0 240.0 260.0 280.0 300.0

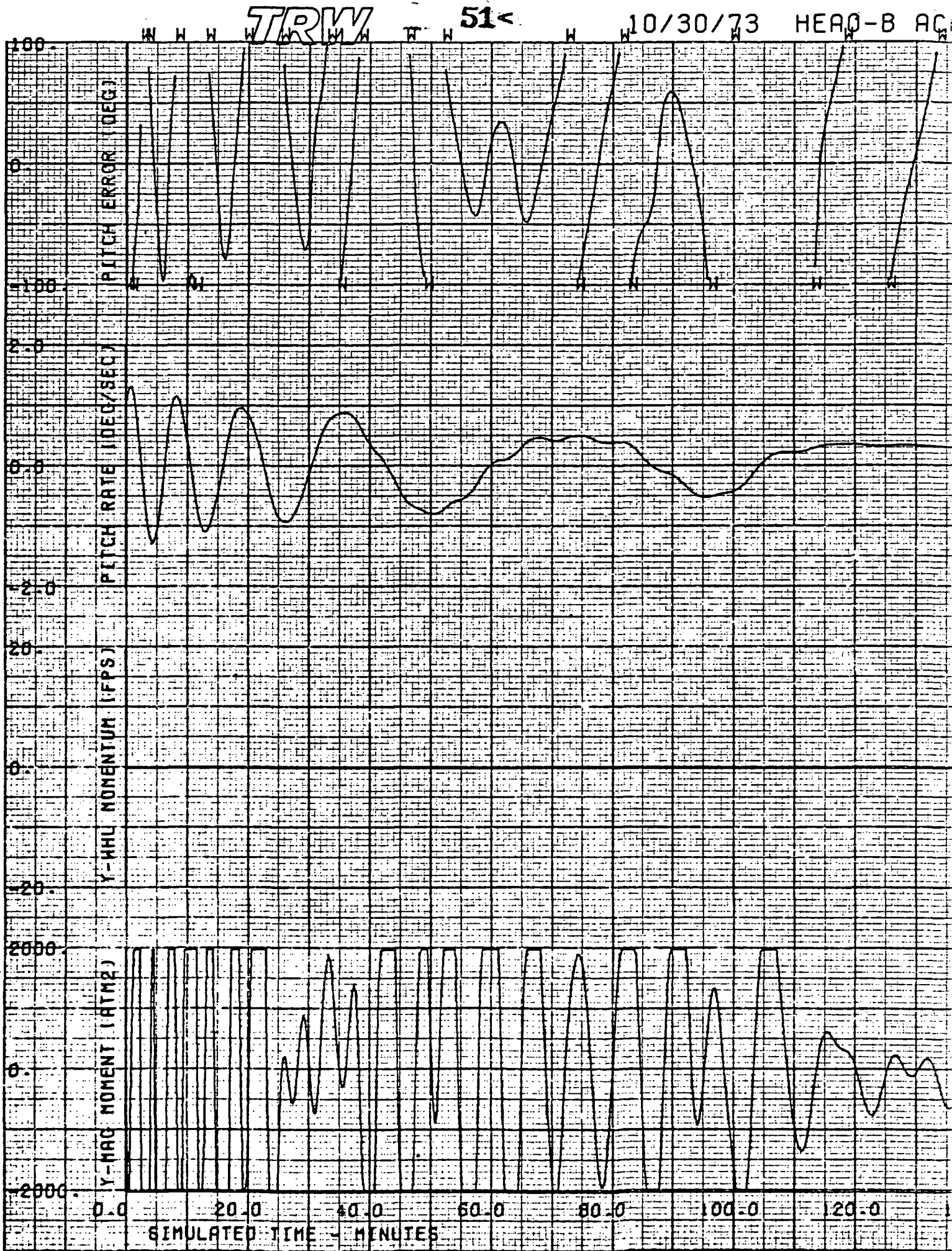
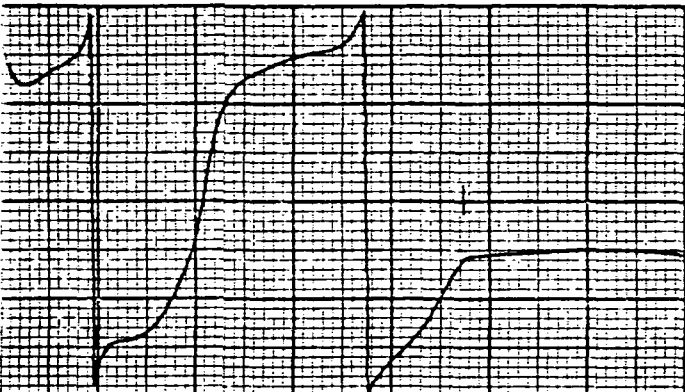
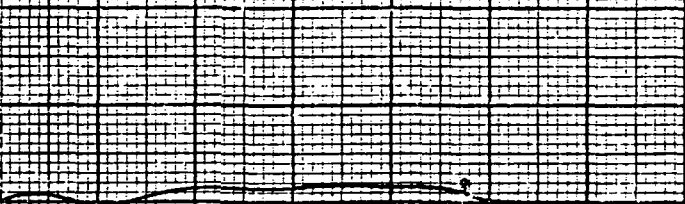


Figure 4-16. Pi



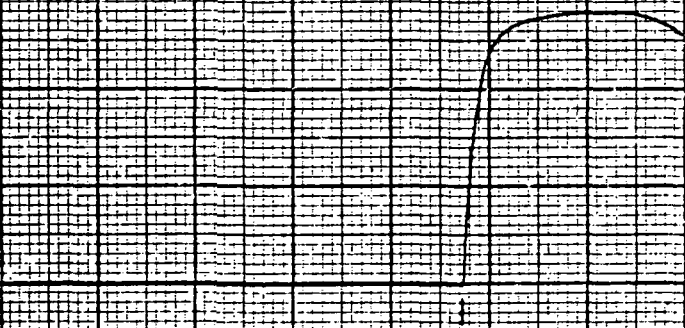


PLOT 14



REACTION WHEELS  
ACTIVATED

PLOT 15



PLOT 16



0.0 160.0 180.0 200.0 220.0 240.0 260.0 280.0 300.0

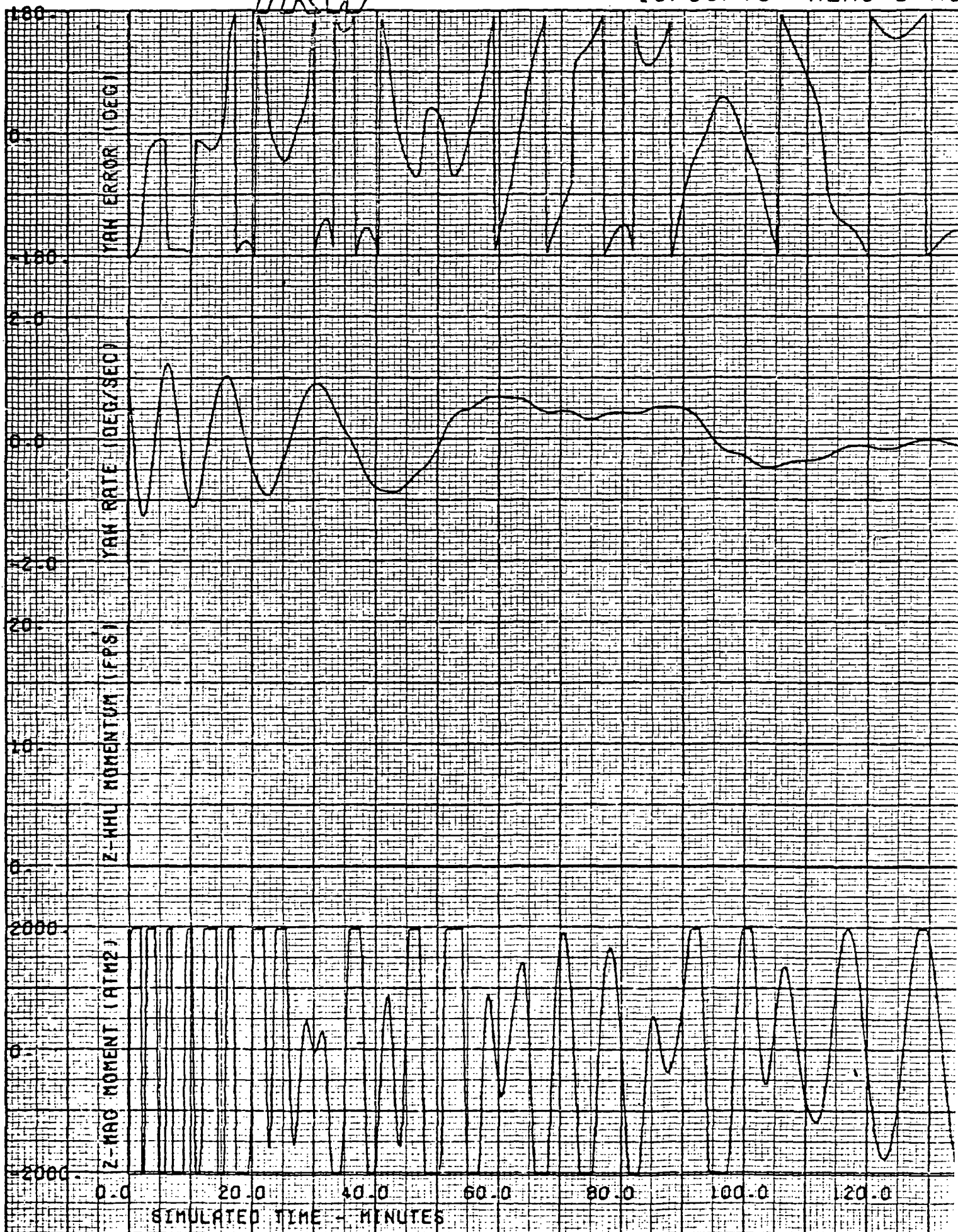


Figure 4-17. Yaw Responses

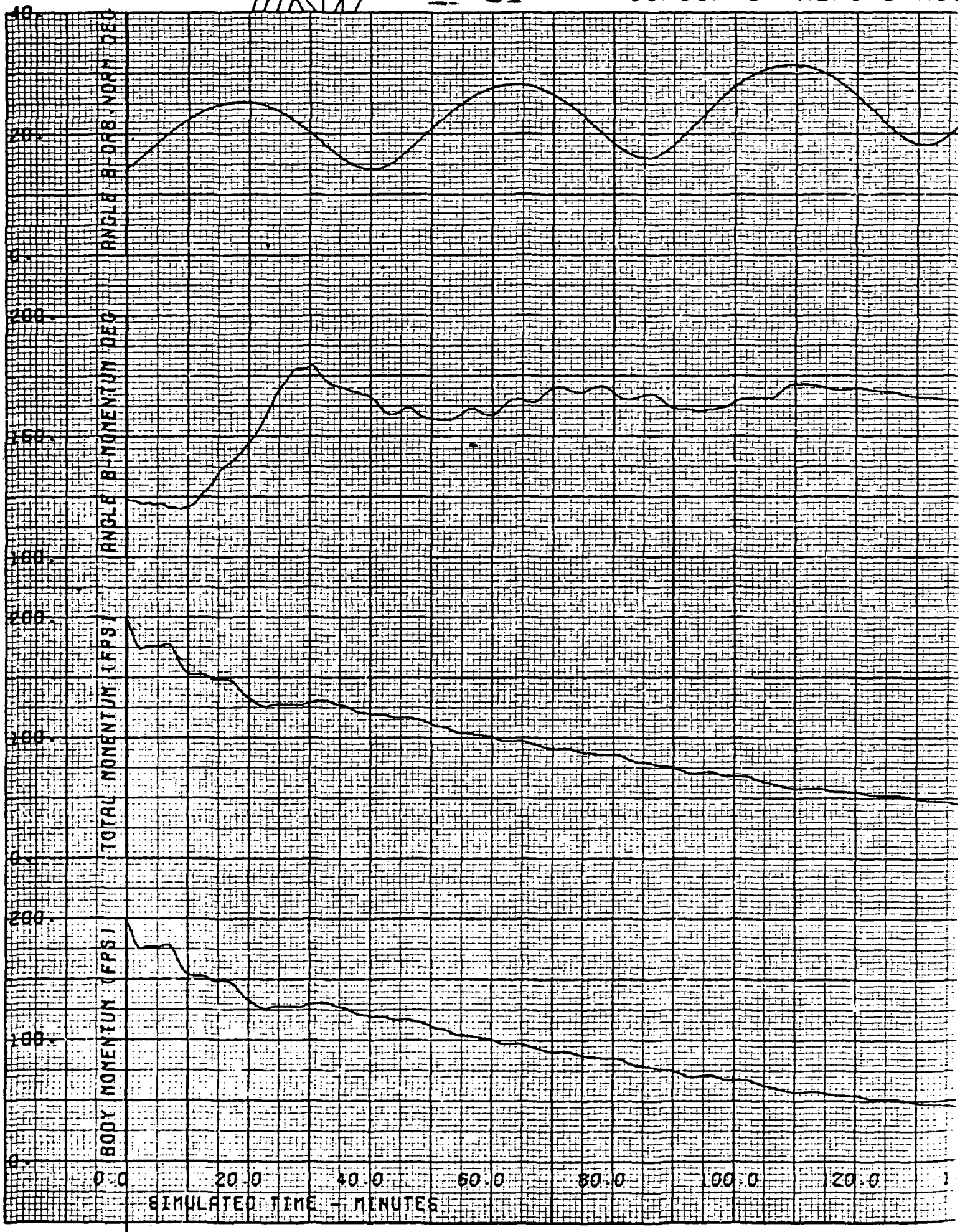
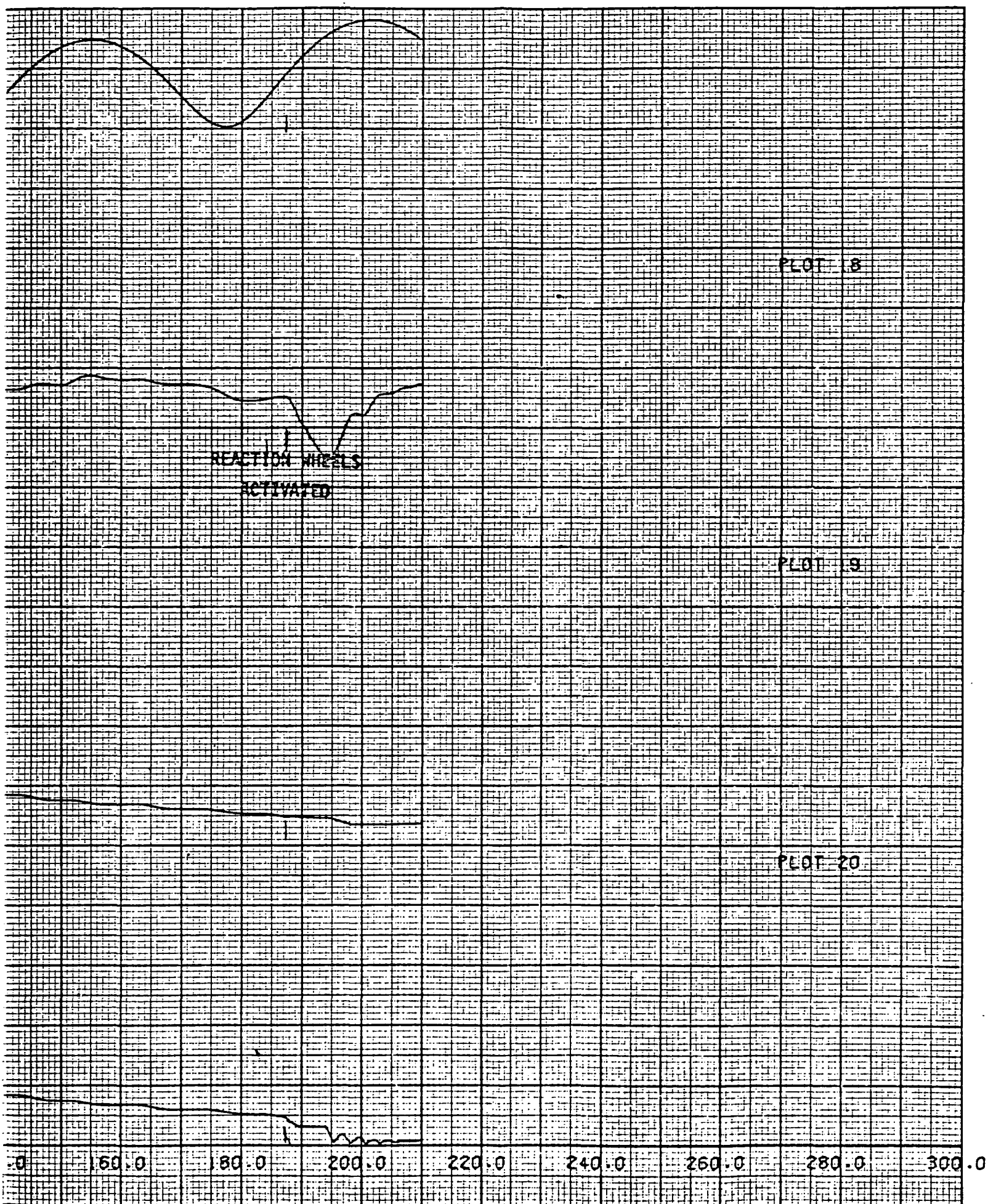


Figure 4-18. Magnetic





The trace second from the top of Figure 4-18 shows the relationship between the earth's magnetic field ( $\vec{B}$ ) and the spacecraft momentum vector. The two vectors are colinear when the angle shown is  $180^\circ$ . The field/momentum vector geometry is significant, since the magnetic controller can produce no torque along the field vector. For the baseline, Case 1, the wheels were activated after 187.5 minutes of operation, with acquisition (less than  $10^\circ$  error) occurring approximately 10 minutes later, as seen from Figure 4-14.

The momentum removal of the magnetic system is dependent upon the angle between the momentum vector and the earth's field (second parameter in Figure 4-18). During the initial portion (0-20 minutes) of acquisition, the momentum removal rate is approximately 3.5 ft-lb-sec per minute, and the angle varies from 55 to 30 degrees. During the rest of the acquisition period, the separation angle is approximately 20 degrees, and the momentum removal rate drops to about 0.7 ft-lb-sec per minute, due to this geometrical effect.

The performance of the reaction wheel attitude control system during acquisition is generally satisfactory, although the pitch channel exhibits an underdamped characteristic. This characteristic could be reduced by a more extensive analysis of the required gains for the pitch wheel control loop. A deadbeat response of the pitch control loop would shorten the total acquisition time by approximately five minutes. Since wheel performance was not the emphasis of this study however, no attempt was made to iterate the wheel controller parameter selection once satisfactory response was obtained.

A second baseline case, applicable to HEAO-A, was also simulated with the results as shown in Table 4-7 (Case 2). The same worst case tipoff rates were used as initial conditions; however, due to the smaller moments of inertia of HEAO-A, the initial momentum existing in the spacecraft is smaller than for the corresponding HEAO-B case. Similarly, the momentum transition condition for wheel activation allows transition at higher spacecraft rates. These two effects cause the acquisition to be completed in about  $1/3$  the time for HEAO-B (65 minutes). The HEAO-B baseline, Case 1, was carried as the primary comparison for the other perturbations due to its worst case characteristics.



### Mass Property Influences

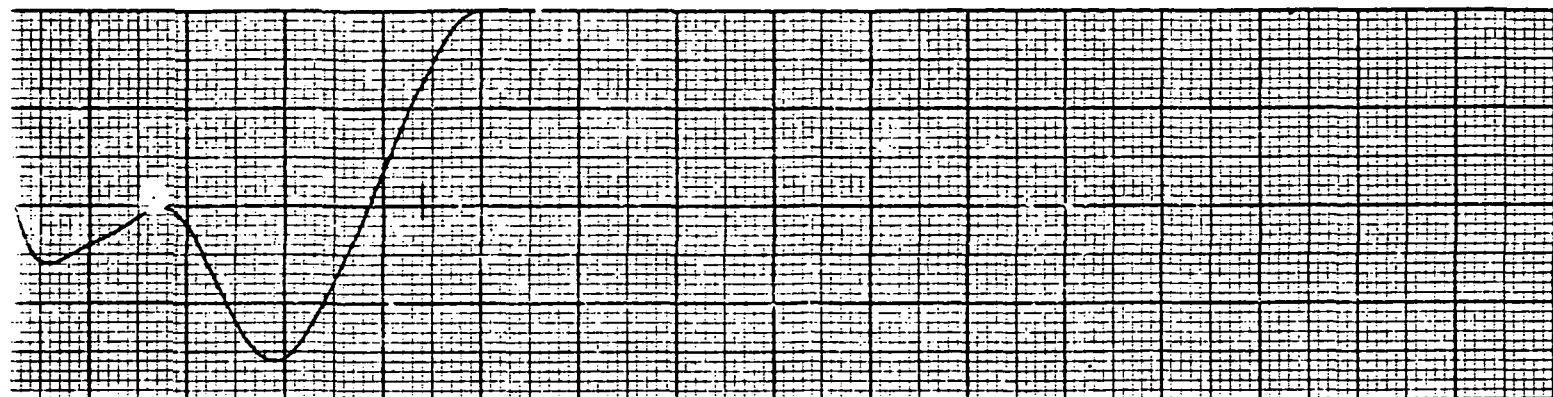
The most pertinent change to mass property characteristics occurs as a result of the differences between the HEAO-A/C and HEAO-B spacecraft themselves. The magnetics design is to be common to all three observatory configurations. Therefore, to assess the effect of mass property changes on acquisition, the inertia properties of HEAO-A/C from Table 4-1 were used in the simulation. Figures 4-19 through 4-23 show the simulation time histories resulting from Case 3. The acquisition capture time is approximately 200 minutes, or about the same as for the baseline case (HEAO-B). This is somewhat misleading, in that the criteria used for wheel control transition was based upon body rates, not momentum. Since the mass properties are reduced from the baseline case, the same rates embody a reduced momentum. The wheel capability, however, is in terms of momentum. Therefore, if the transition criteria were made to a common momentum bases, it is estimated that the acquisition time could be reduced to the order of 100 minutes on the basis of the momentum characteristics of Figure 4-23. This prediction is born out by the results from Case 2, noted previously.

The overall characteristics of the acquisition performance, as indicated in the figures for Case 3 are quite similar to those of the baseline, shown previously (Case 1). Therefore, no critical sensitivity to mass properties is indicated by these studies.

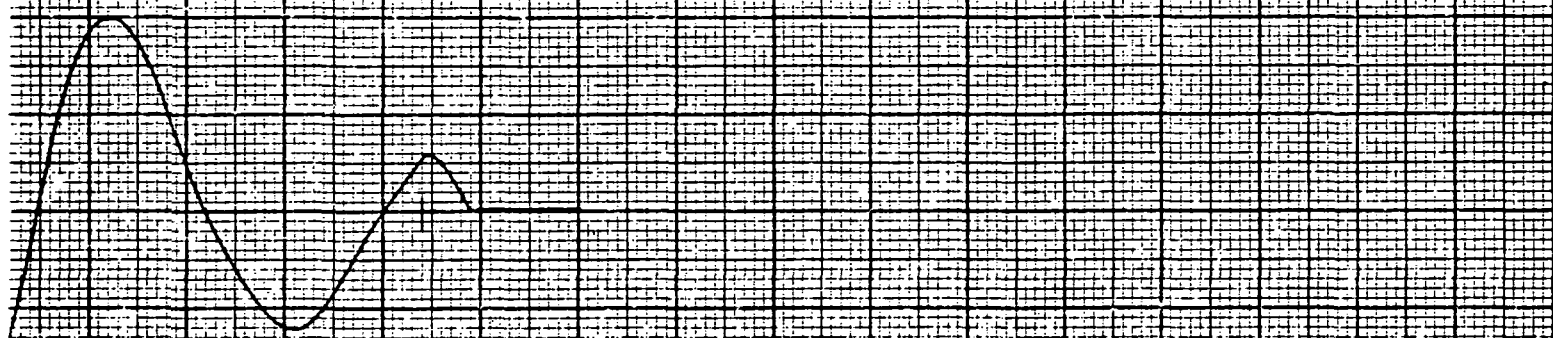
### Initial Field/Momentum Orientation

The magnetic torque available from the electromagnets is a function of the relative angular separation between the spacecraft momentum vector and the instantaneous earth magnetic field vector. When the two vectors are colinear, the cross-product goes to zero and therefore, no torque can be produced in the field direction to reduce the momentum. This worst case condition was evaluated with the results as shown in Figure 4-24. In Case 4, although the initial alignment was unfavorable, within 20 minutes the orbital and control dynamics have caused the momentum to rotate to an angle of  $20^\circ$  with respect to the field vector, as shown in the second time history in the figure. This angular separation allows the magnetic controller to become sufficiently effective to reduce the

POSITION (HXB) K=.05 2K ATM2 58<

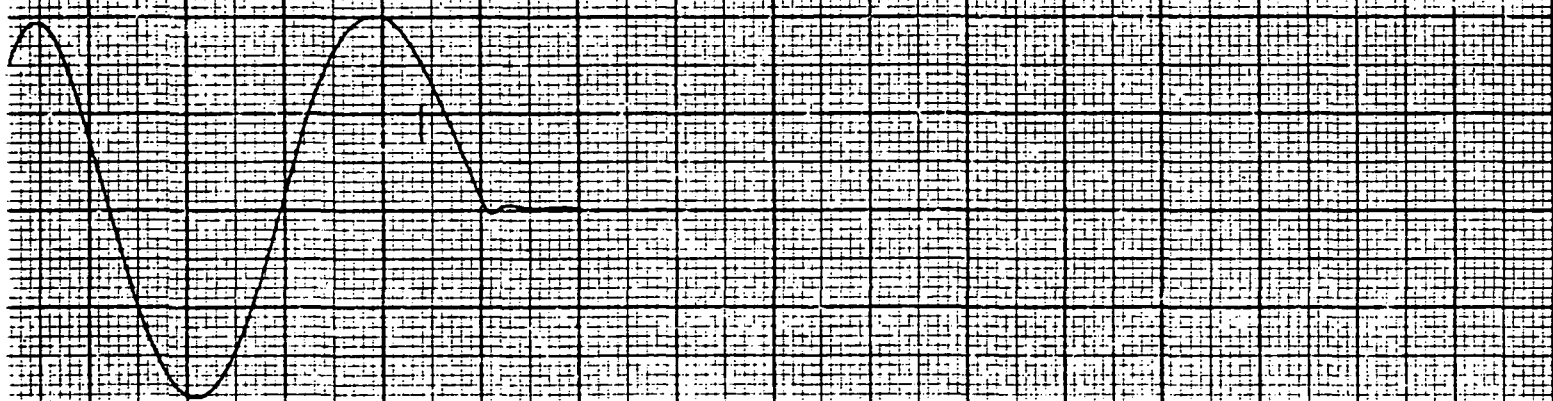


PLOT 2

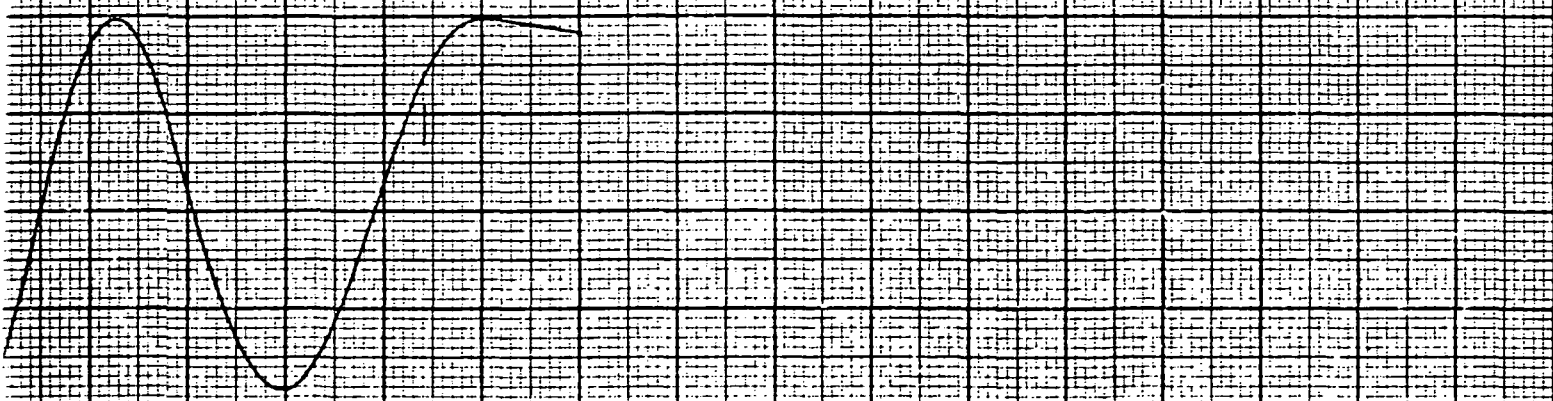


REACTION WHEELS  
ACTIVATED

PLOT 3



PLOT 4



0 160.0 180.0 200.0 220.0 240.0 260.0 280.0 300.0

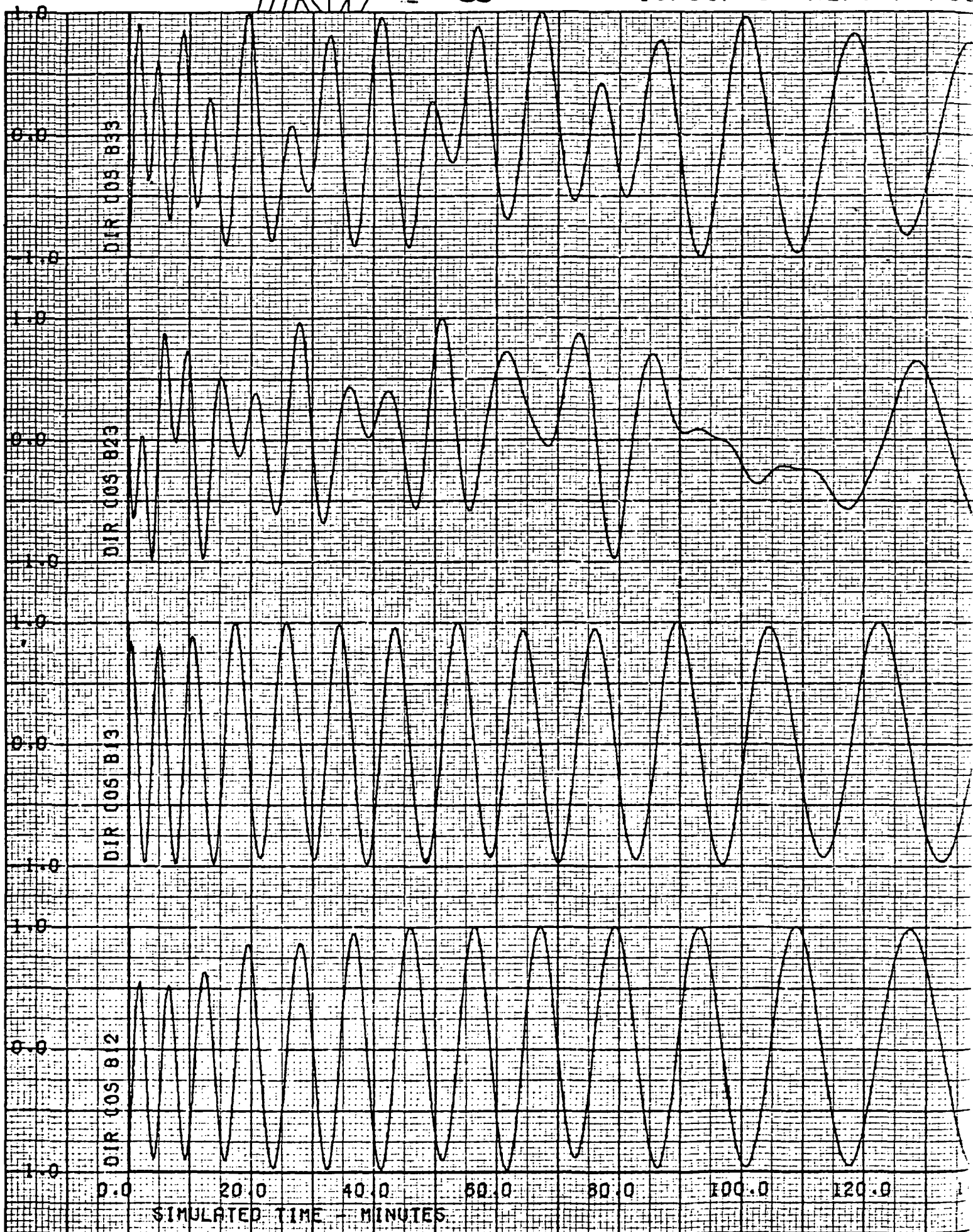
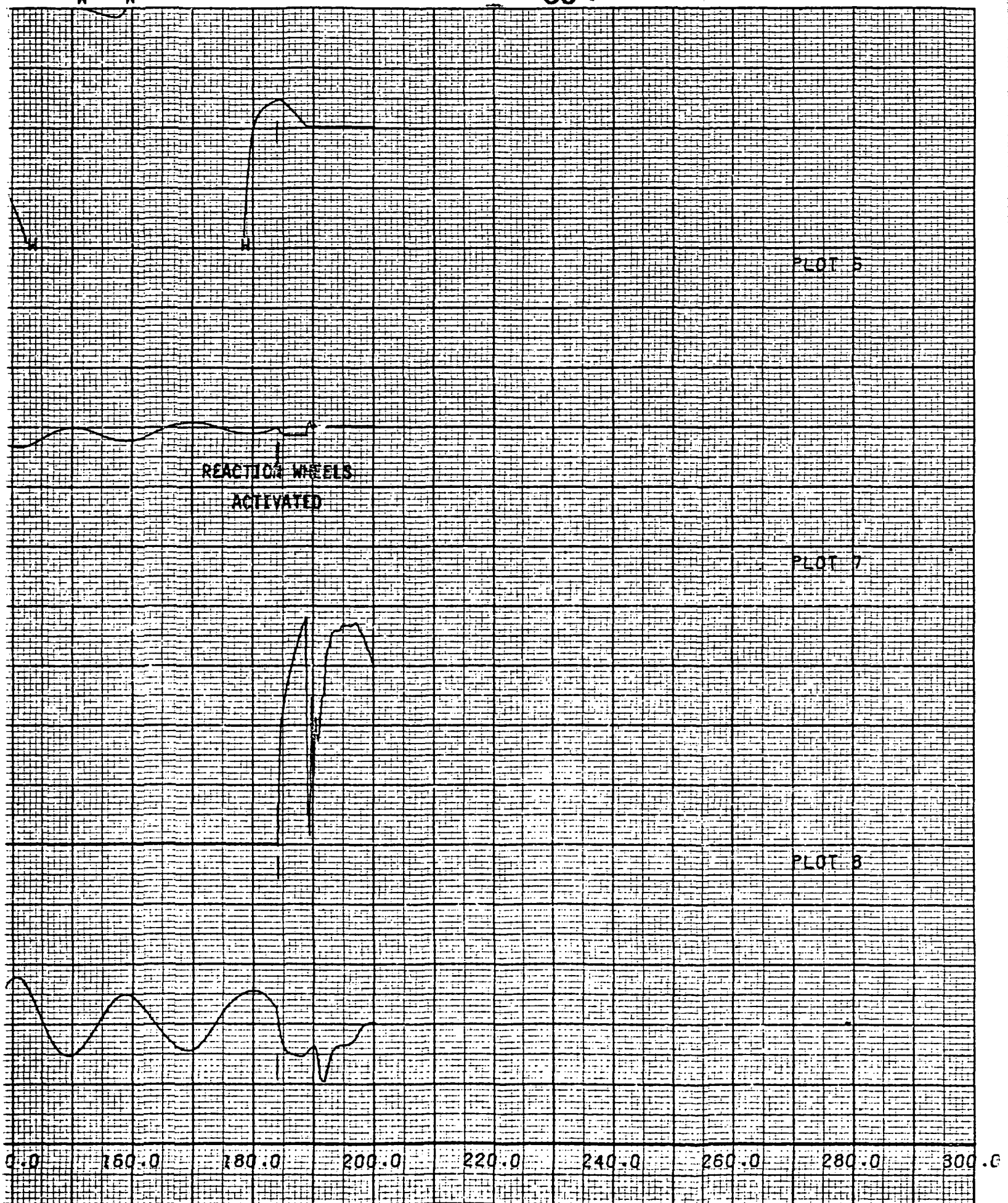


Figure 4-19. Attitude Respon

POSITION (HXB) K=.05 2K ATM2

60&lt;





TRW 61<

10/31/73

HEAD-A AC

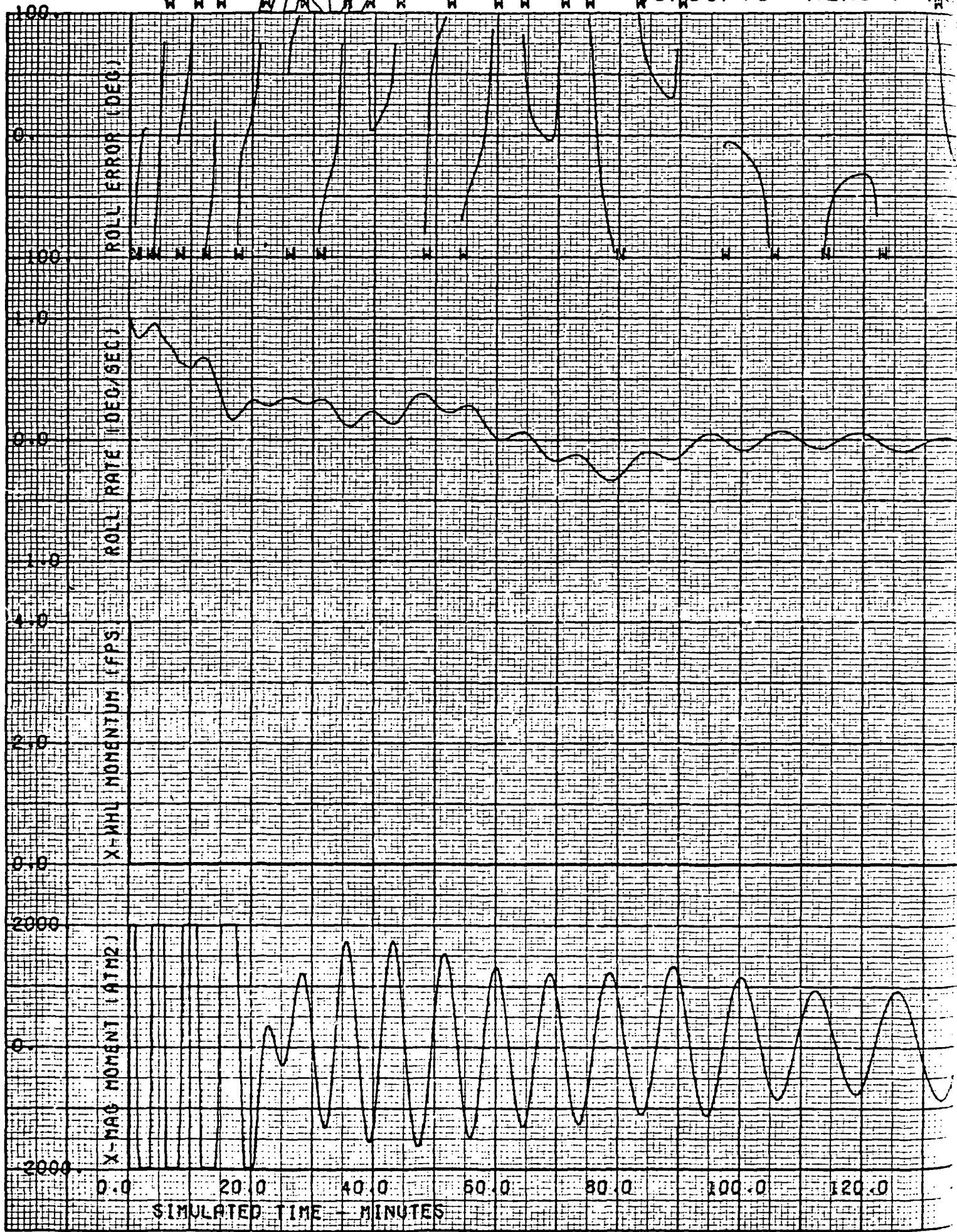
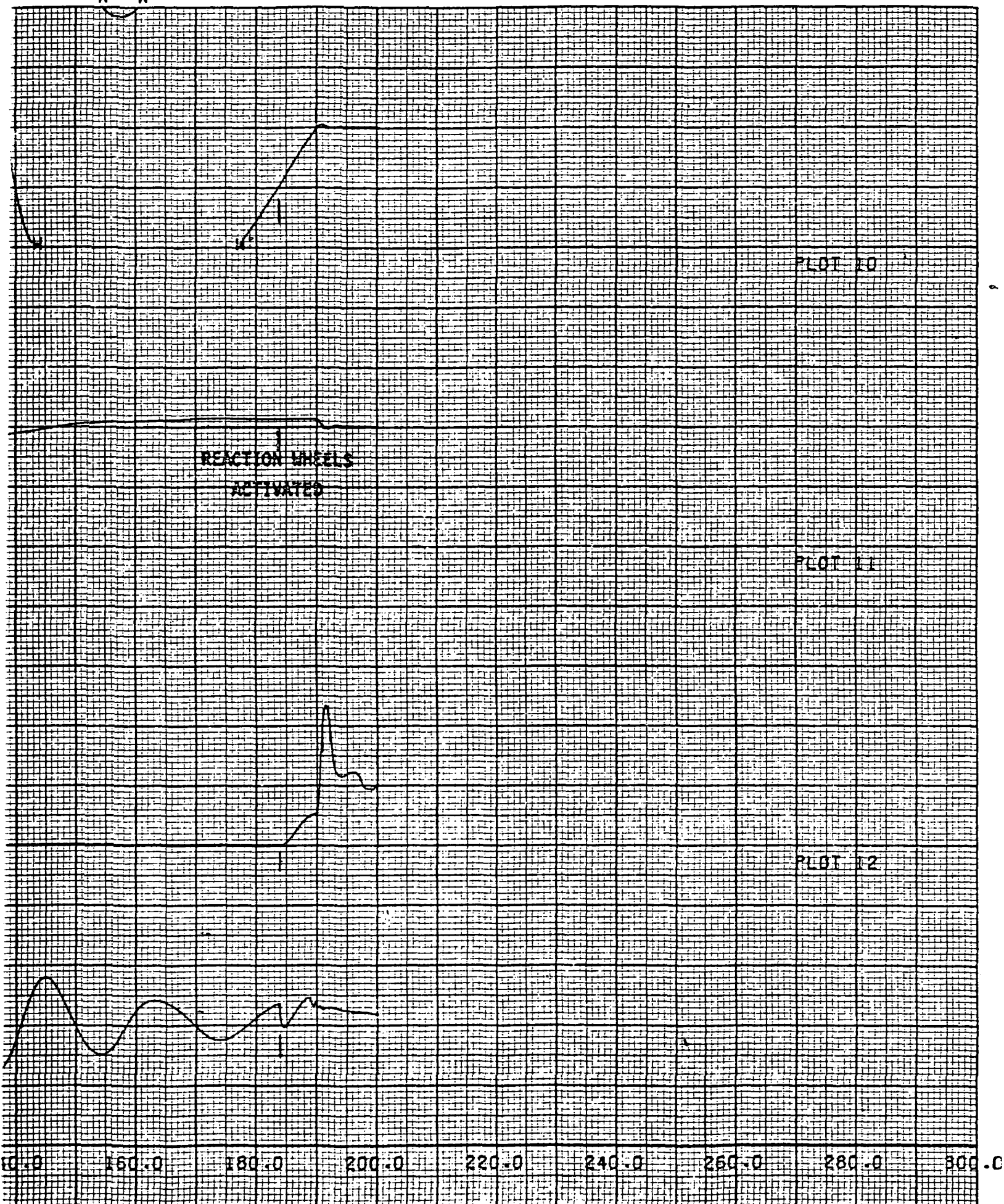


Figure 4-20. Roll Responses

POSITION<sub>W</sub> (HXB) K=.05 2K ATM2

TRW

63&lt;

10/31/73

HEAD-A

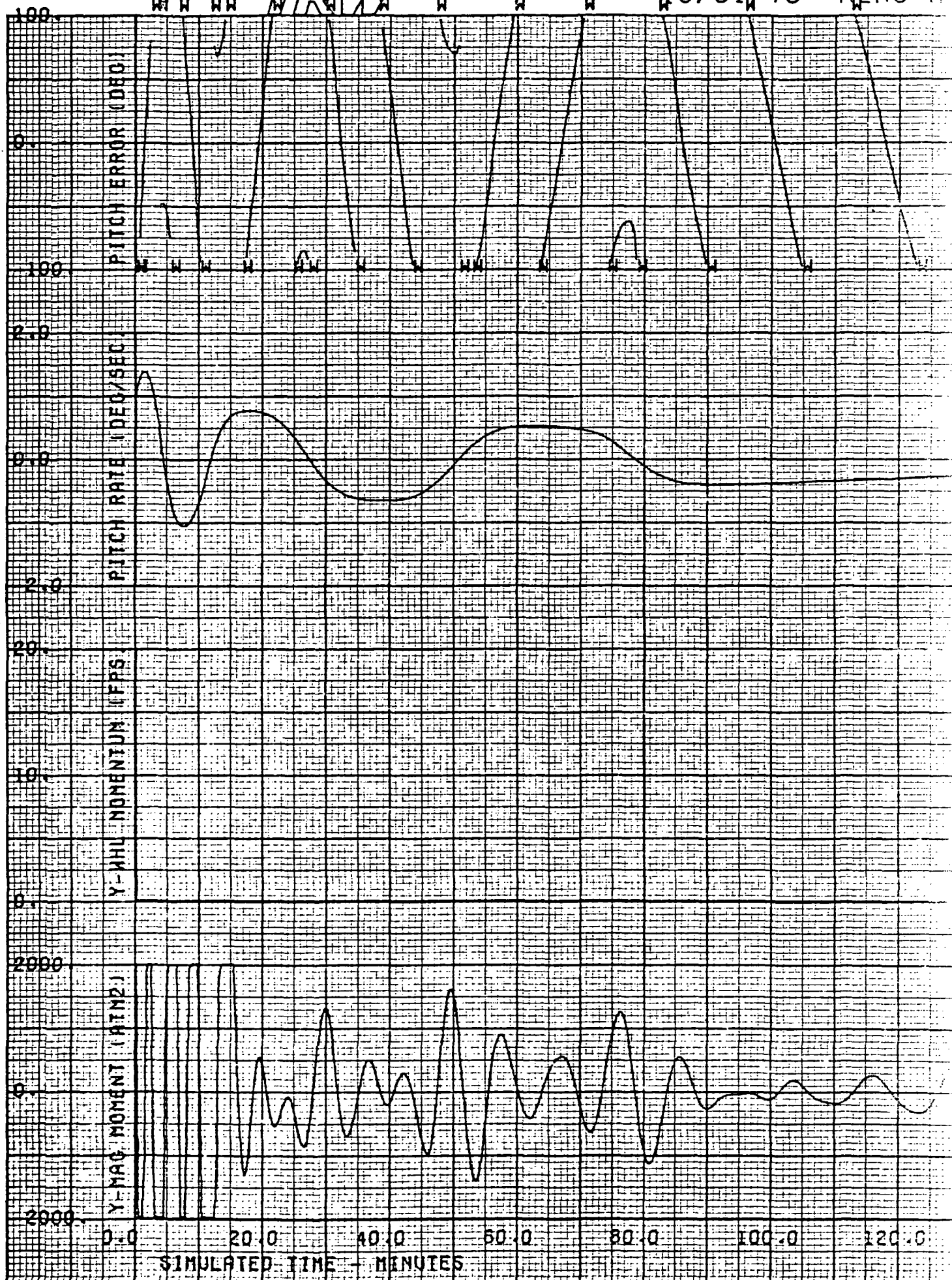


Figure 4-21. Pitch



POSITION (HXB) K=.05 2K ATM2

64&lt;

PLOT 13

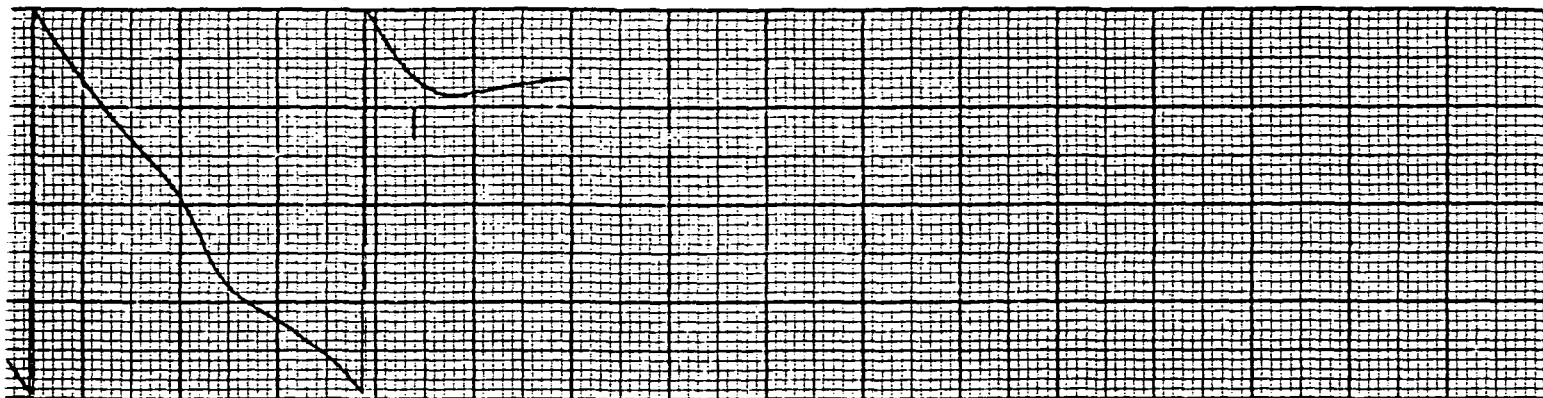
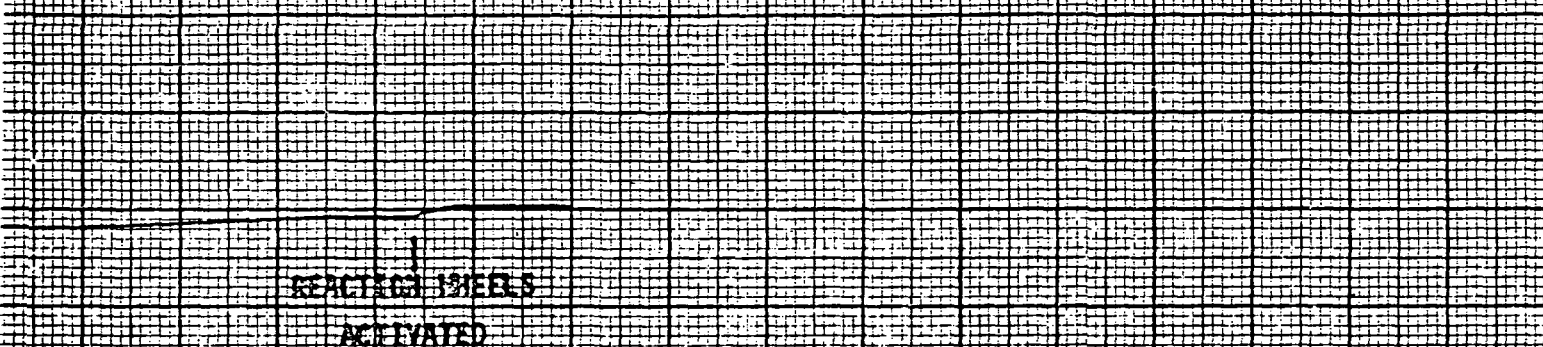
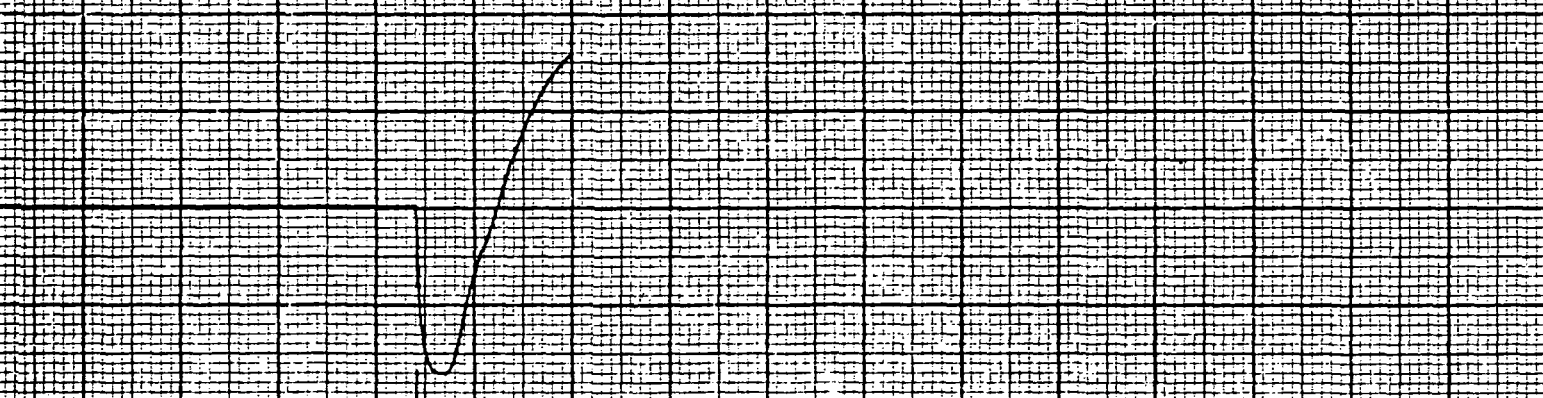


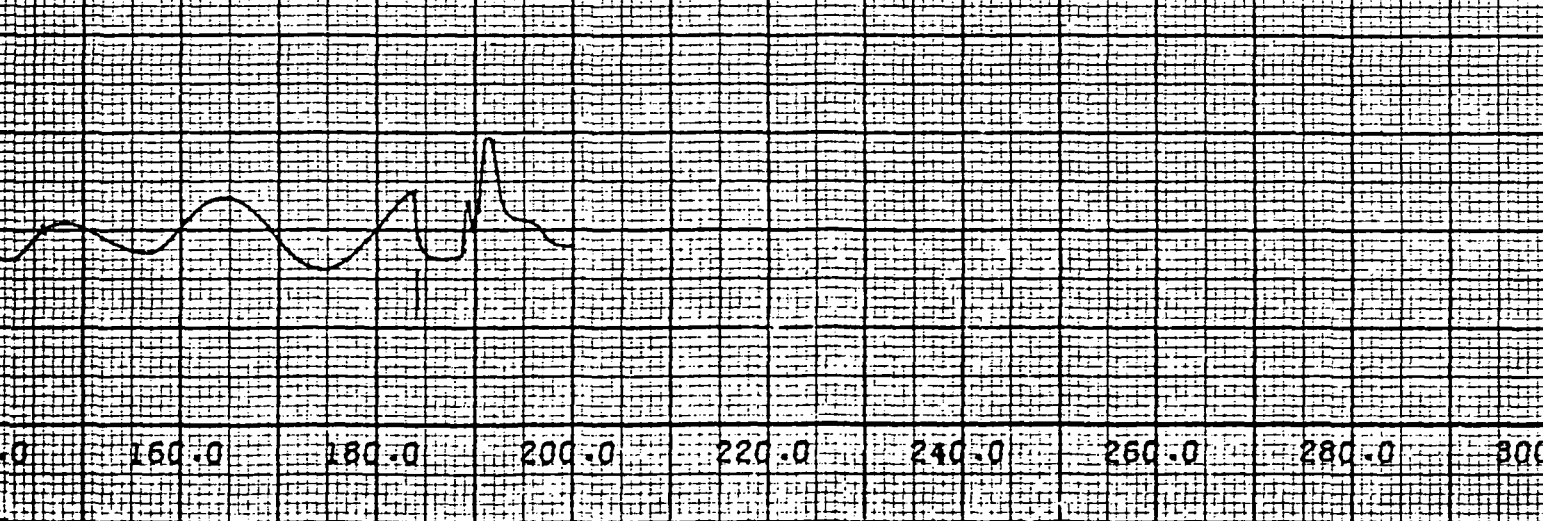
# PLATE 3



PLOT 15



PLOT # 6



## -- See HEAO 2 1974 HEAO A Transient Disturbances

1 2 3



TRW

65<

10/31/73 HEAD-A AC

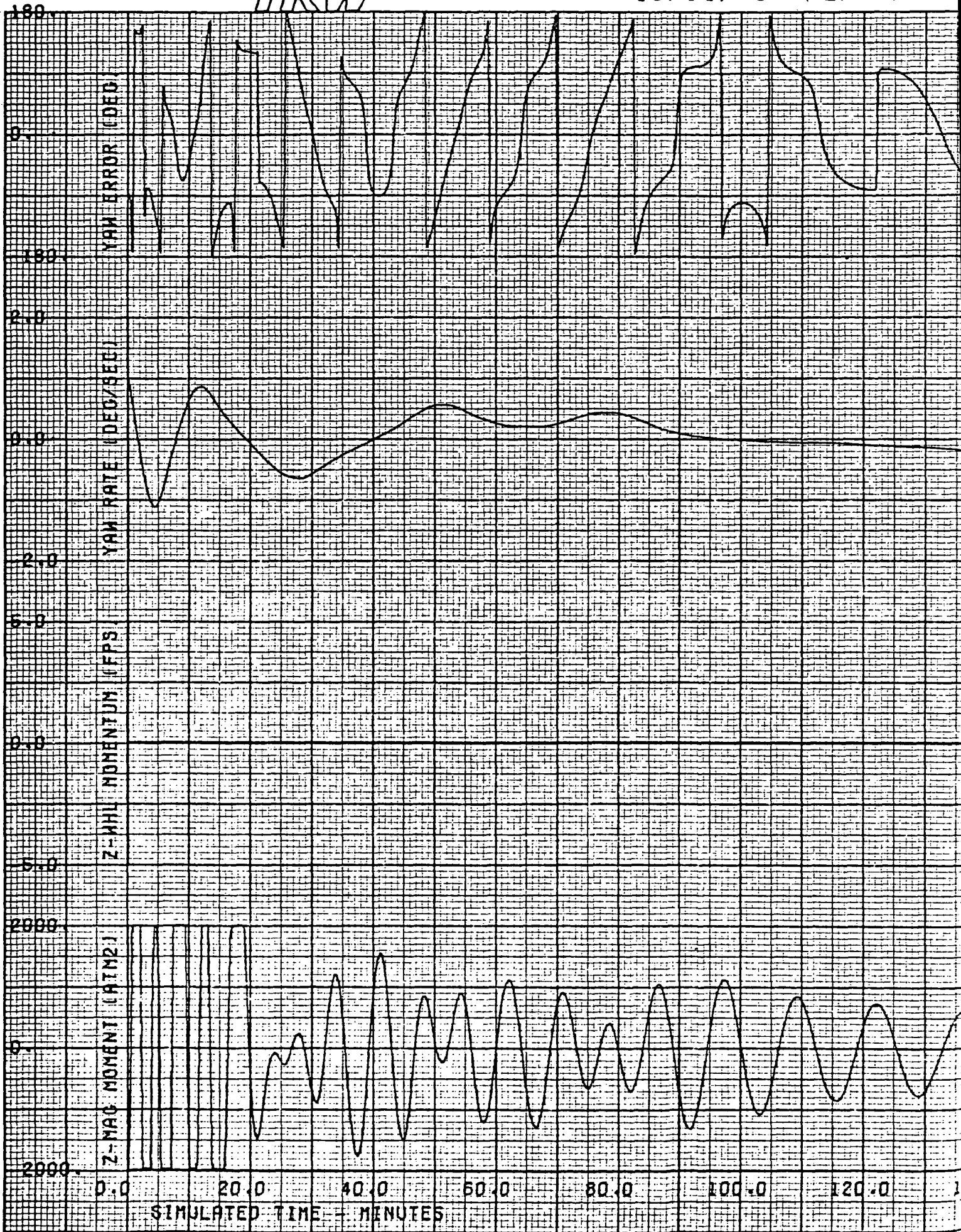
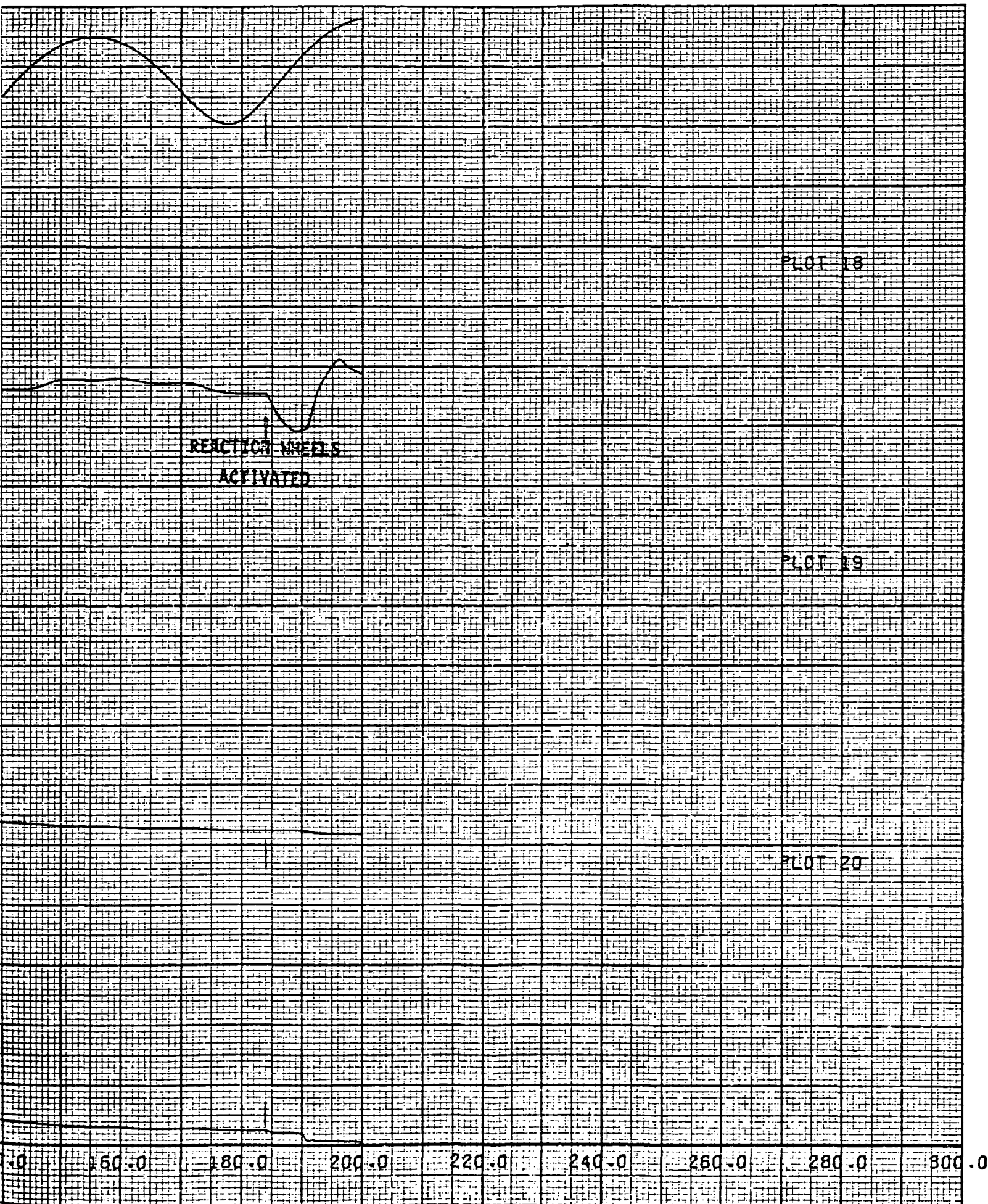


Figure 4-22 Yaw Response

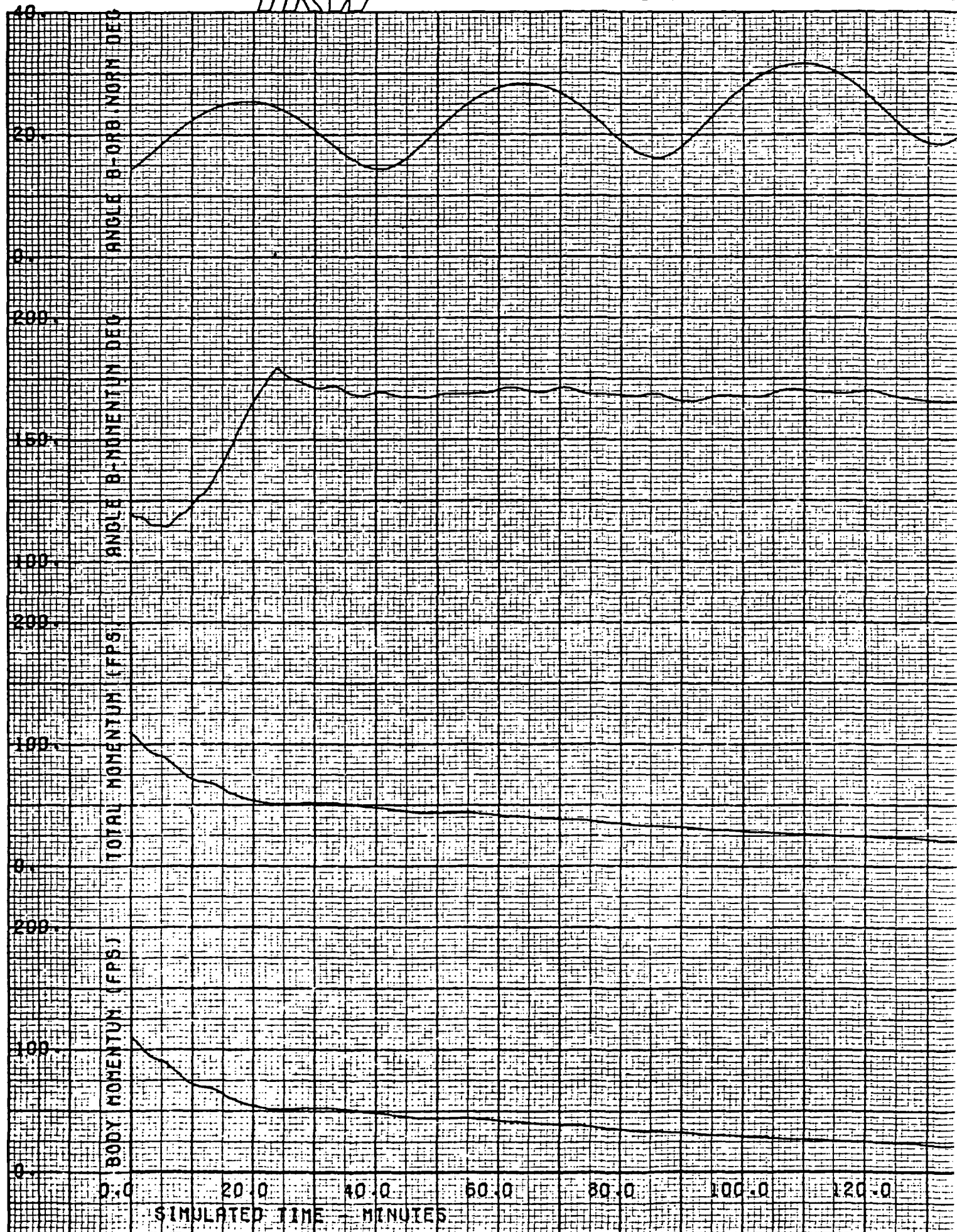


TRW

67&lt;

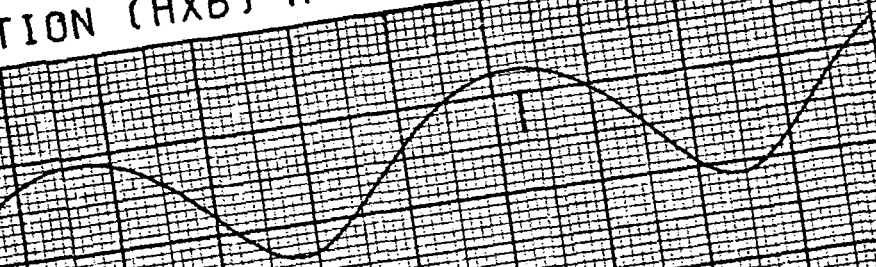
10/31/73

HEAD-A AC

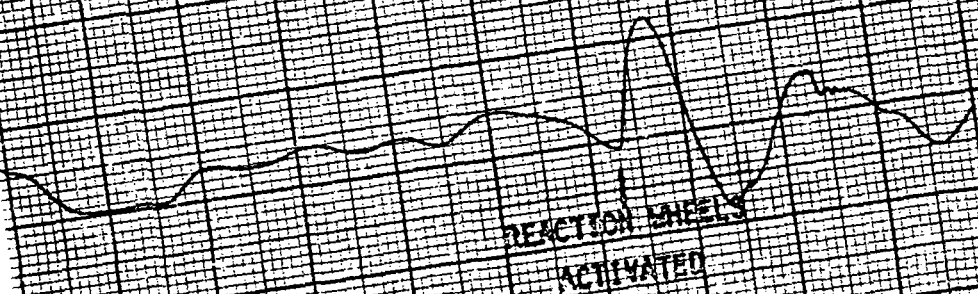




68<  
TION (HXB) K=.05 H//B

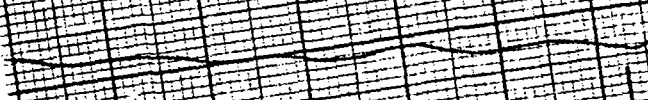


PLOT 18



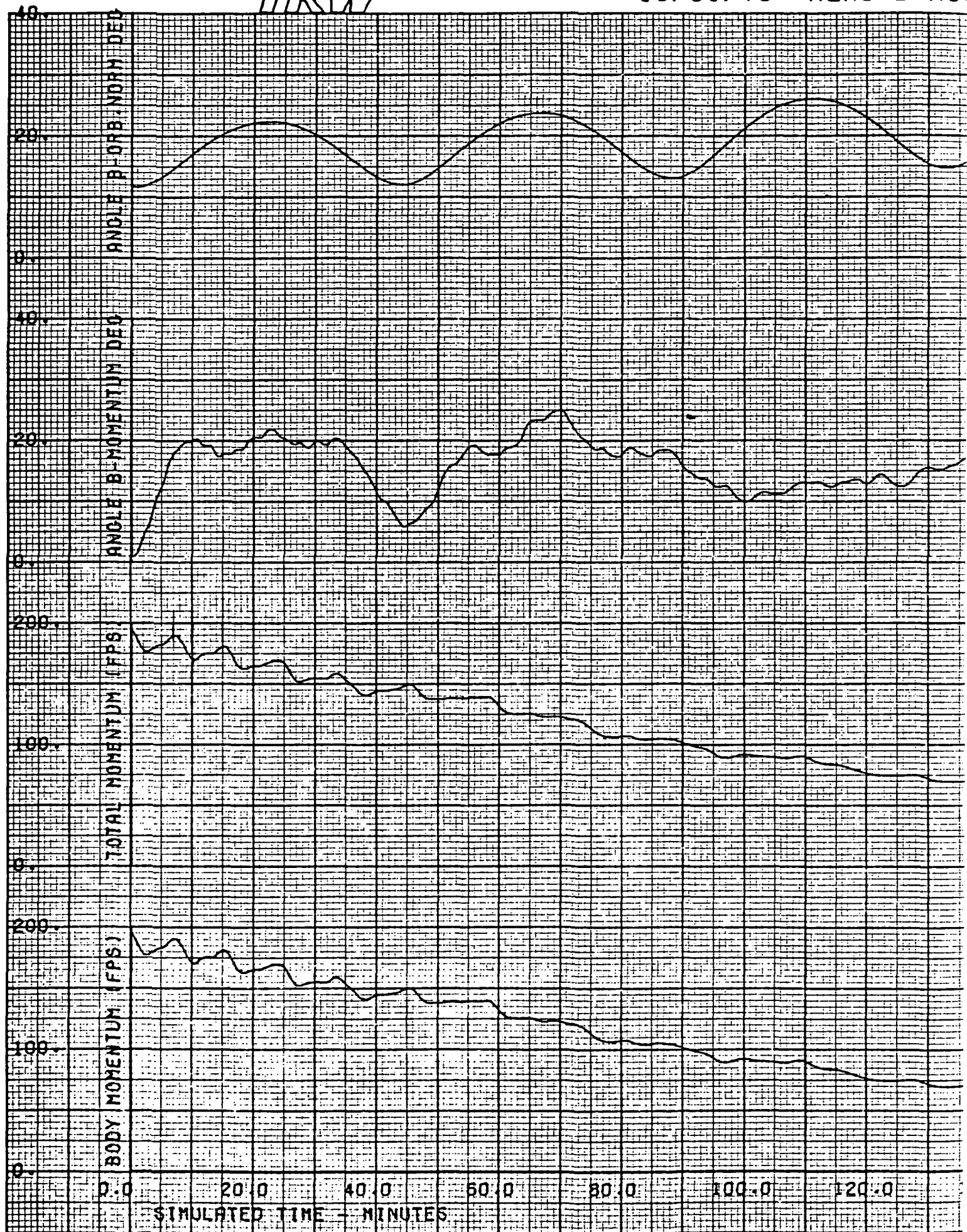
PLOT 19

REACTION LABELS  
ACTIVATED



PLOT 20

160.0 180.0 200.0 220.0 240.0 260.0 280.0



momentum to a level that transition to wheel control can be effected at about 200 minutes. Acquisition capture occurs at 240 minutes, compared to 200 minutes for the baseline, Case 1. The momentum/field relative orientation may be considered a random phenomenon with the case shown in Figure 4-24, representative of a worst case initial condition.

#### Wheel Activation Criteria Modification

The baseline criteria for transition from magnetics only to combined wheel and magnetic control was simultaneous satisfaction of the following angular rate conditions.

$$\omega_x \leq 0.573$$

$$\omega_y \leq 0.115$$

$$\omega_z \leq 0.115$$

as has been noted previously. These rates corresponded roughly to the allocation of 50% of the available wheel momenta for absorbing the spacecraft momentum from the tipoff rates. In actuality, considerably less than 50% was used in two of the control axes. Therefore, one simulation was run with the rate criteria increased such that 75-80% of the wheel momenta could be used for acquisition control. The rate criteria in Case 5 were:

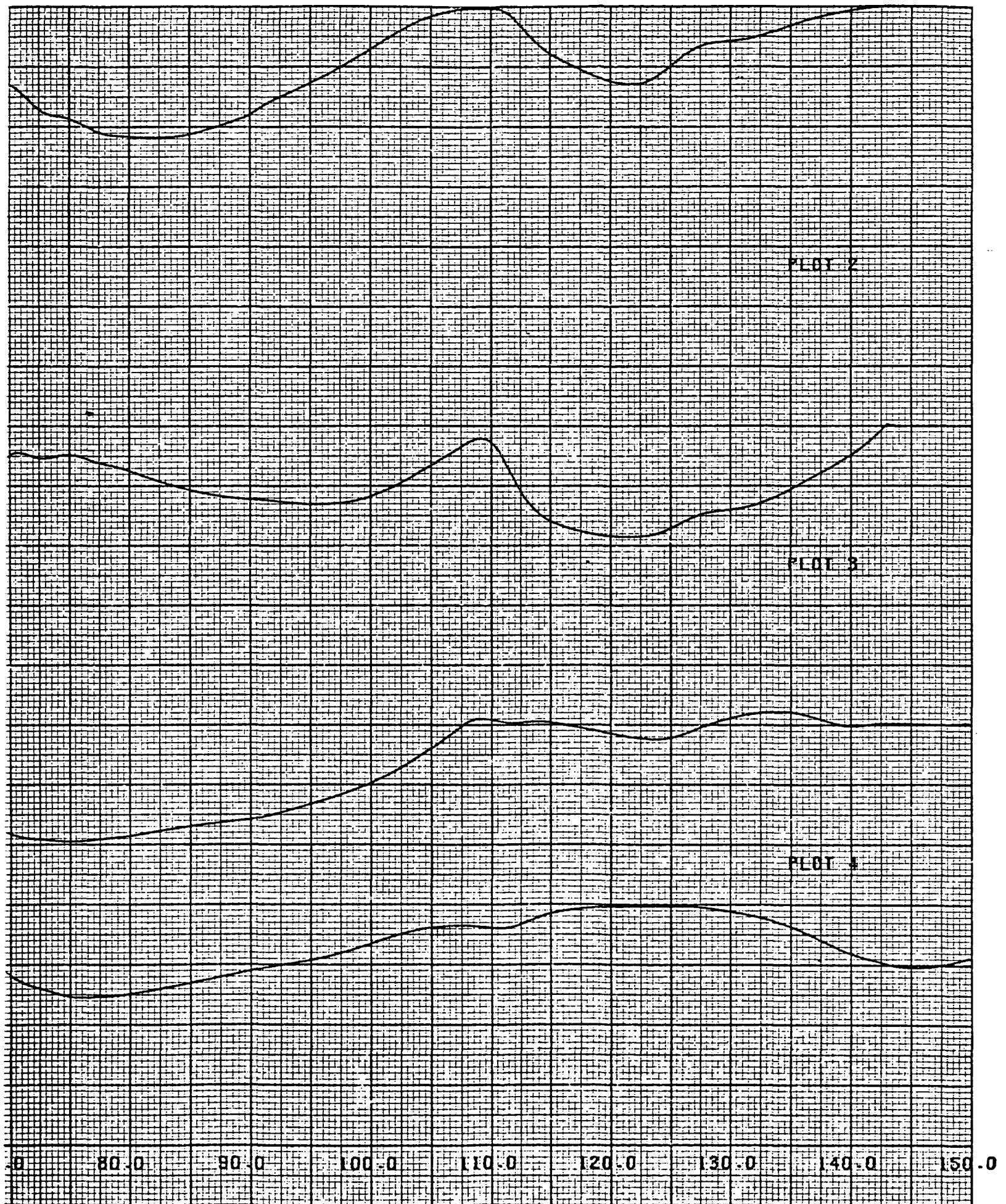
$$\omega_x \leq 1.3^\circ/\text{sec}$$

$$\omega_y \leq 0.35^\circ/\text{sec}$$

$$\omega_z \leq 0.36^\circ/\text{sec}$$

The results of this case are summarized in Table 4-7. The acquisition time is shortened to 150 minutes due to wheel activation at 92 minutes. As predicted, the wheels end up with about 50% more stored momentum than in the baseline case. The distribution of the momentum among the control axes is also more uniform.

The limiting case for wheel transition is to eliminate the initial phase altogether and activate wheel control immediately at mode entry. The results of this condition are shown in Figures 4-25 through 4-29, corresponding to Case 6. In this case, the wheels are used to remove





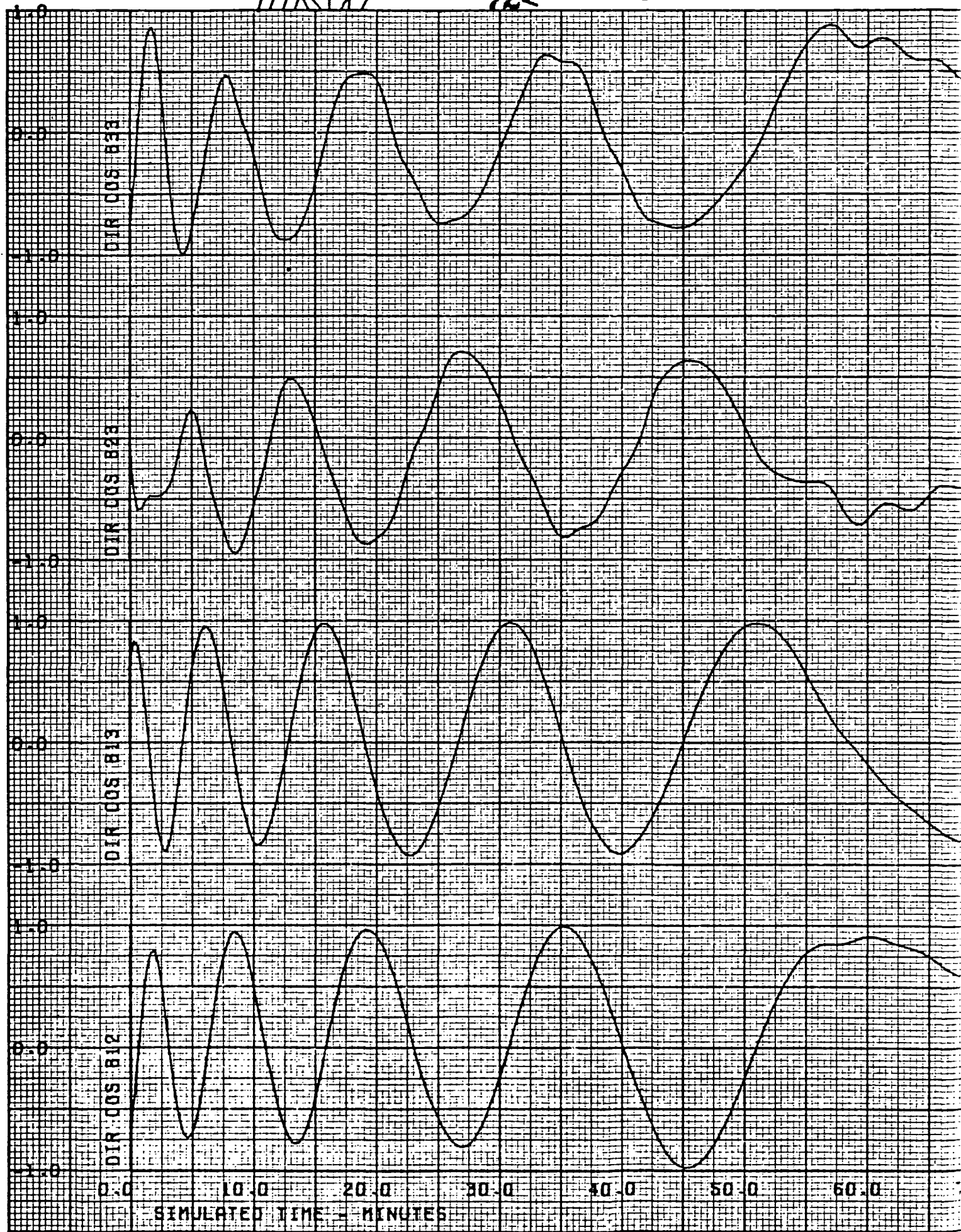
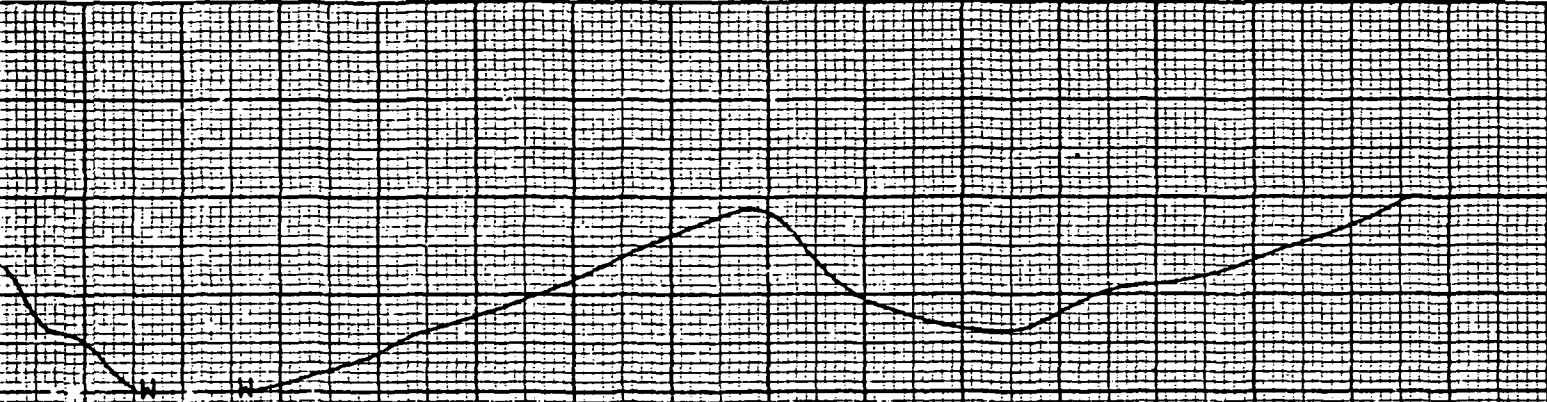
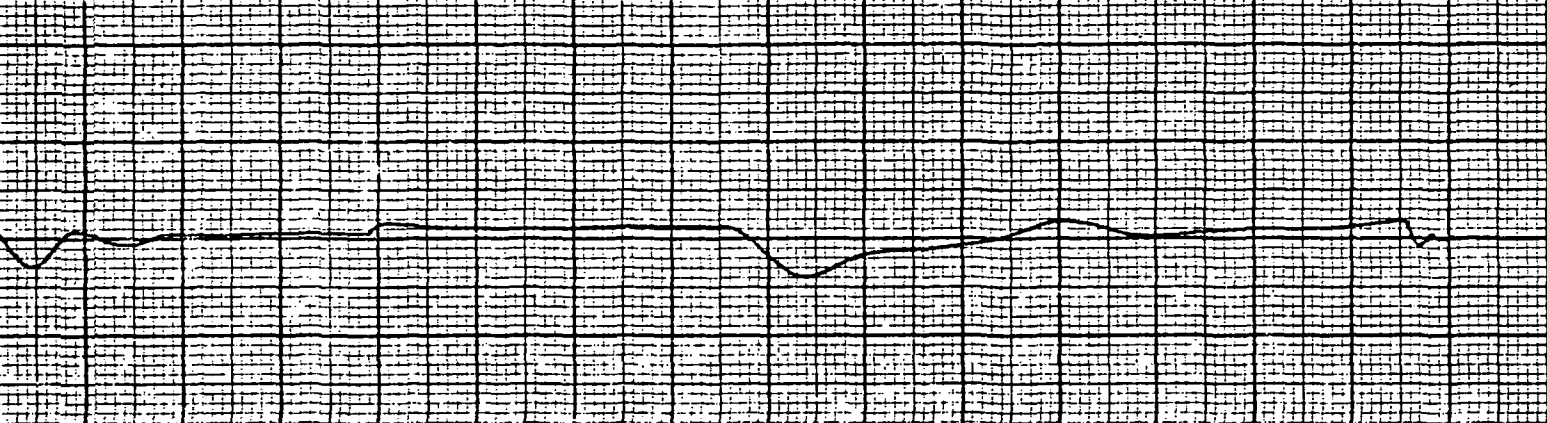


Figure 4-25. Attitude Response





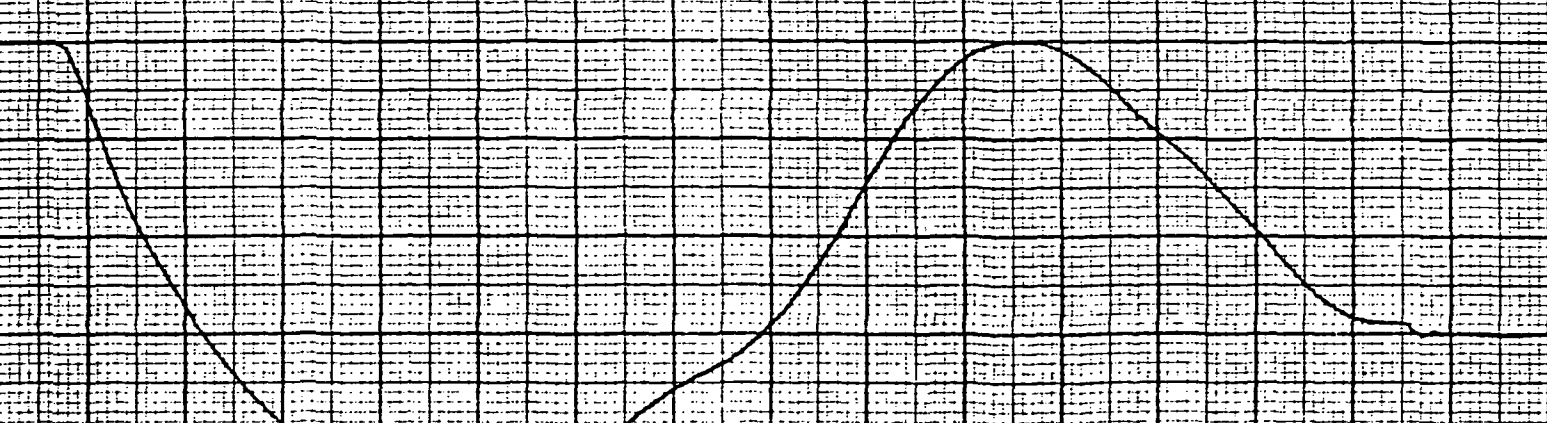
PLOT 6



PLOT 7



PLOT 8

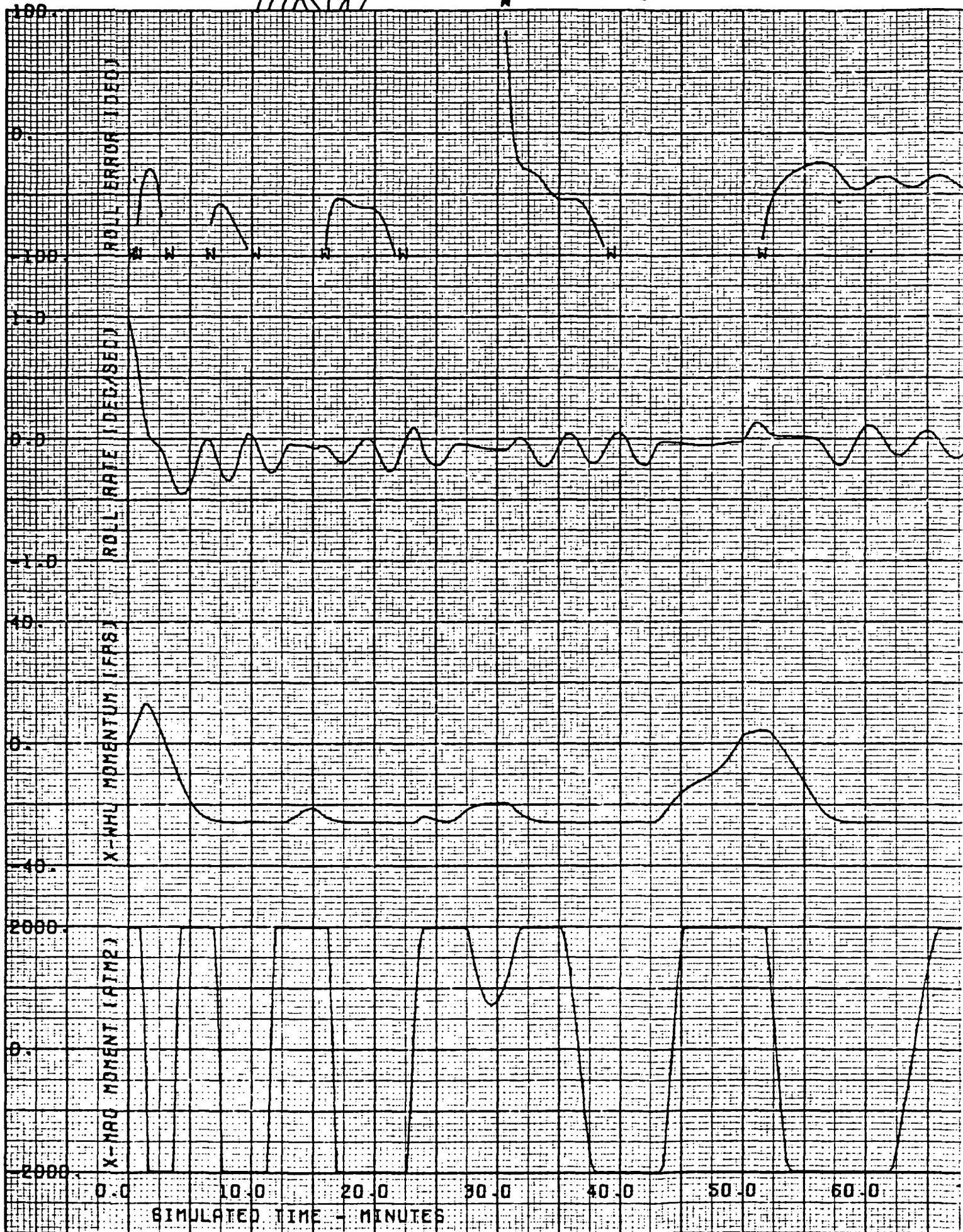


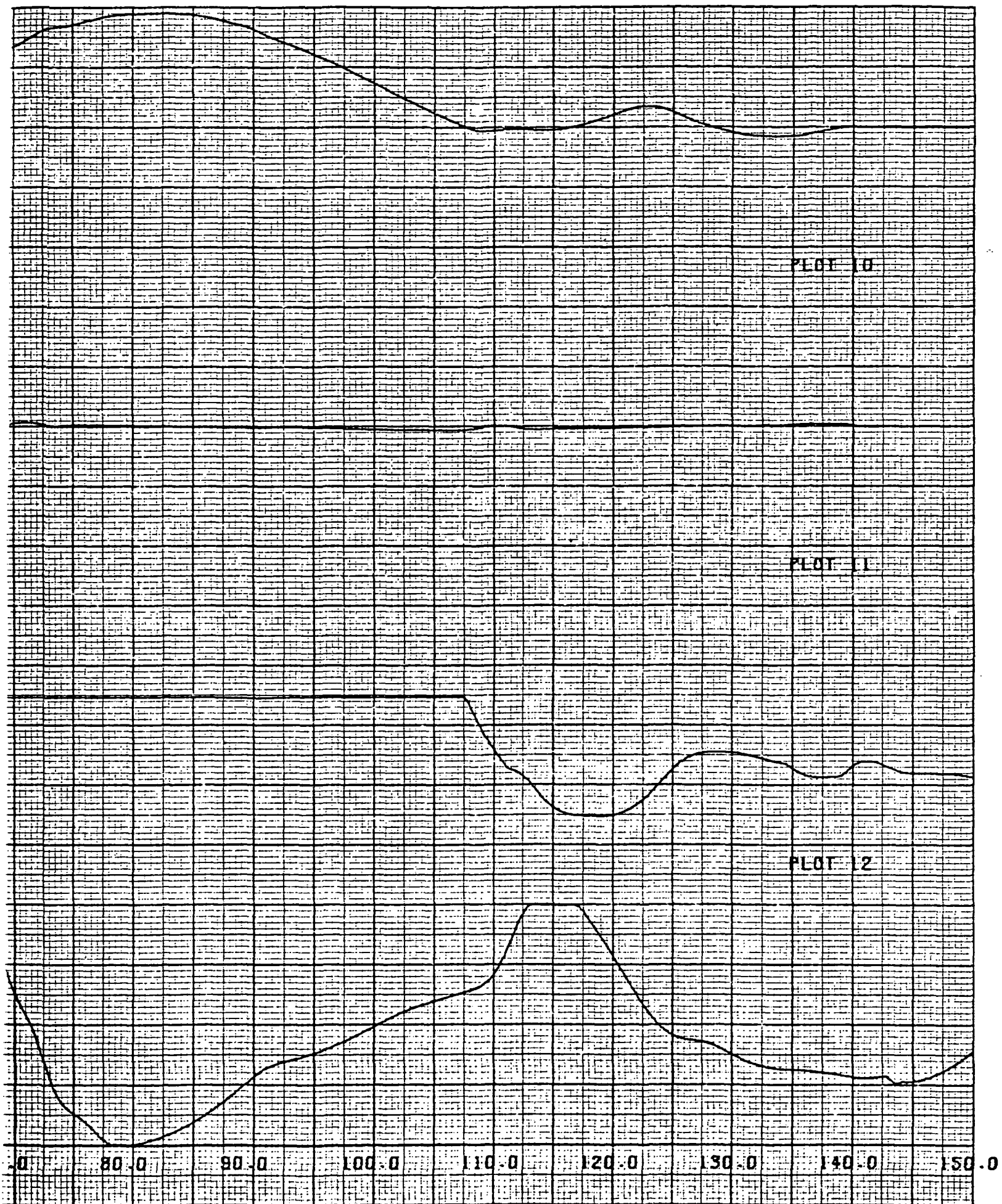
0 80.0 90.0 100.0 110.0 120.0 130.0 140.0 150.0

TRW

74<

11/06/73 HEAD-B AC





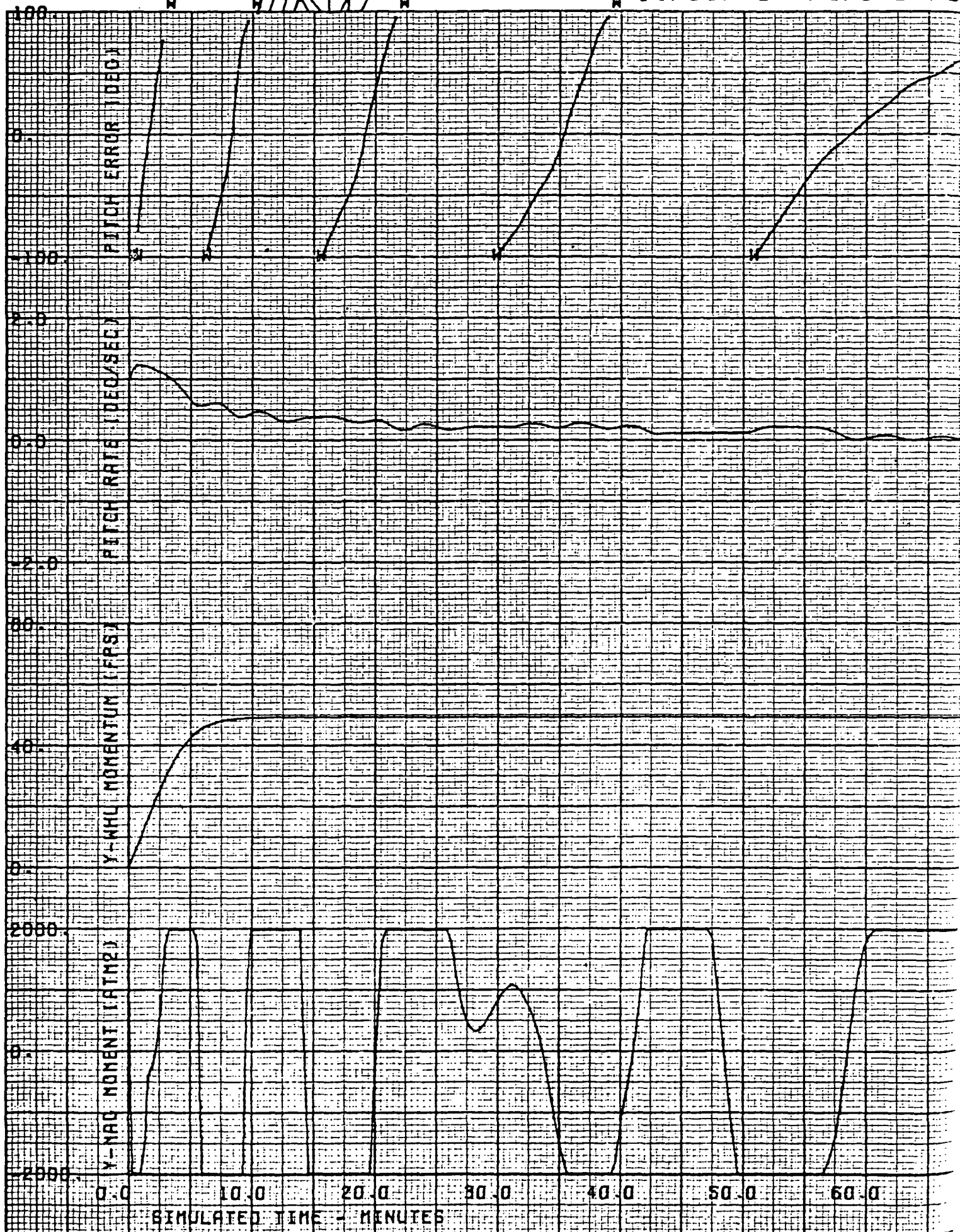


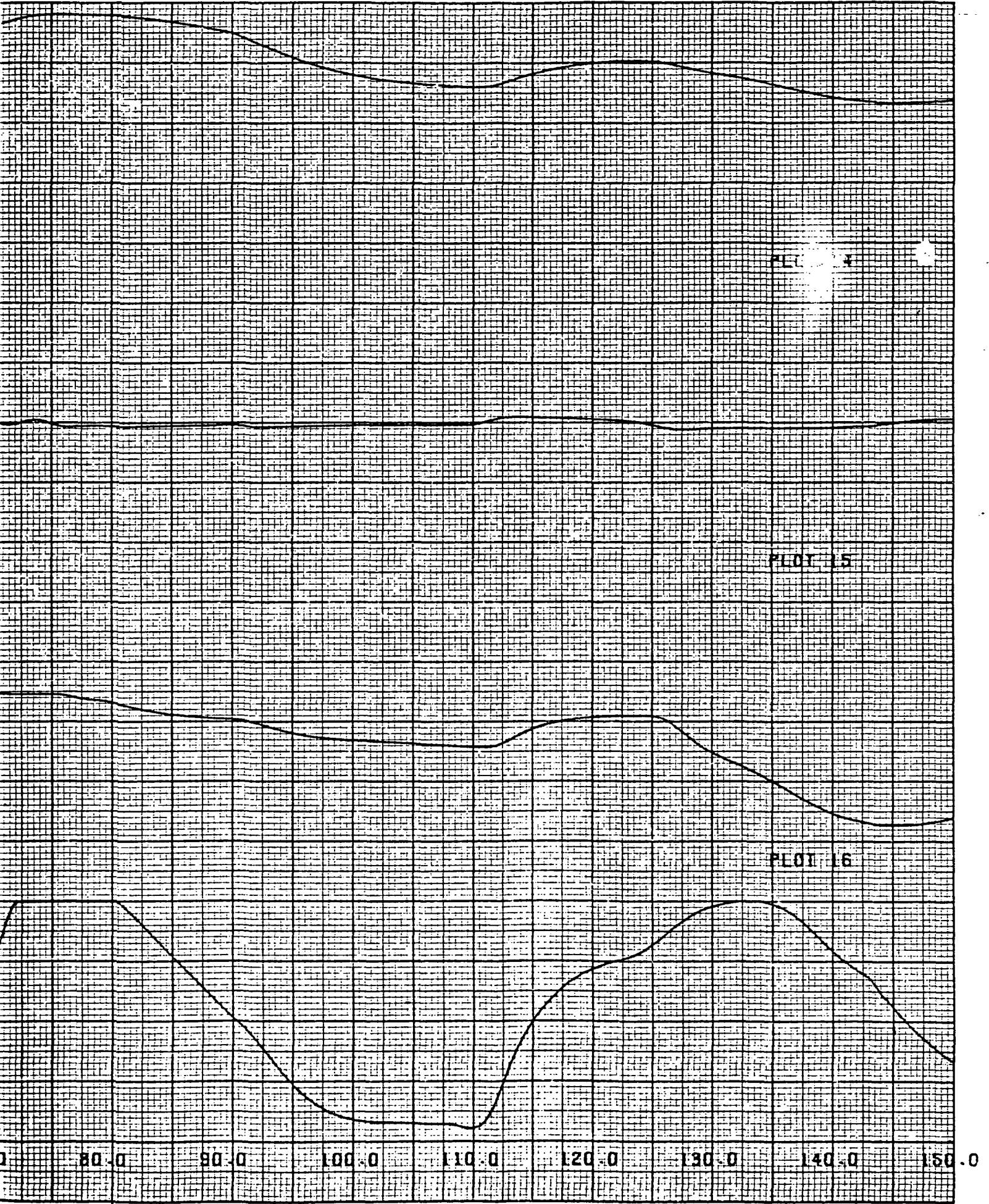
TRW

76<

11/06/73

HEAD-B AC





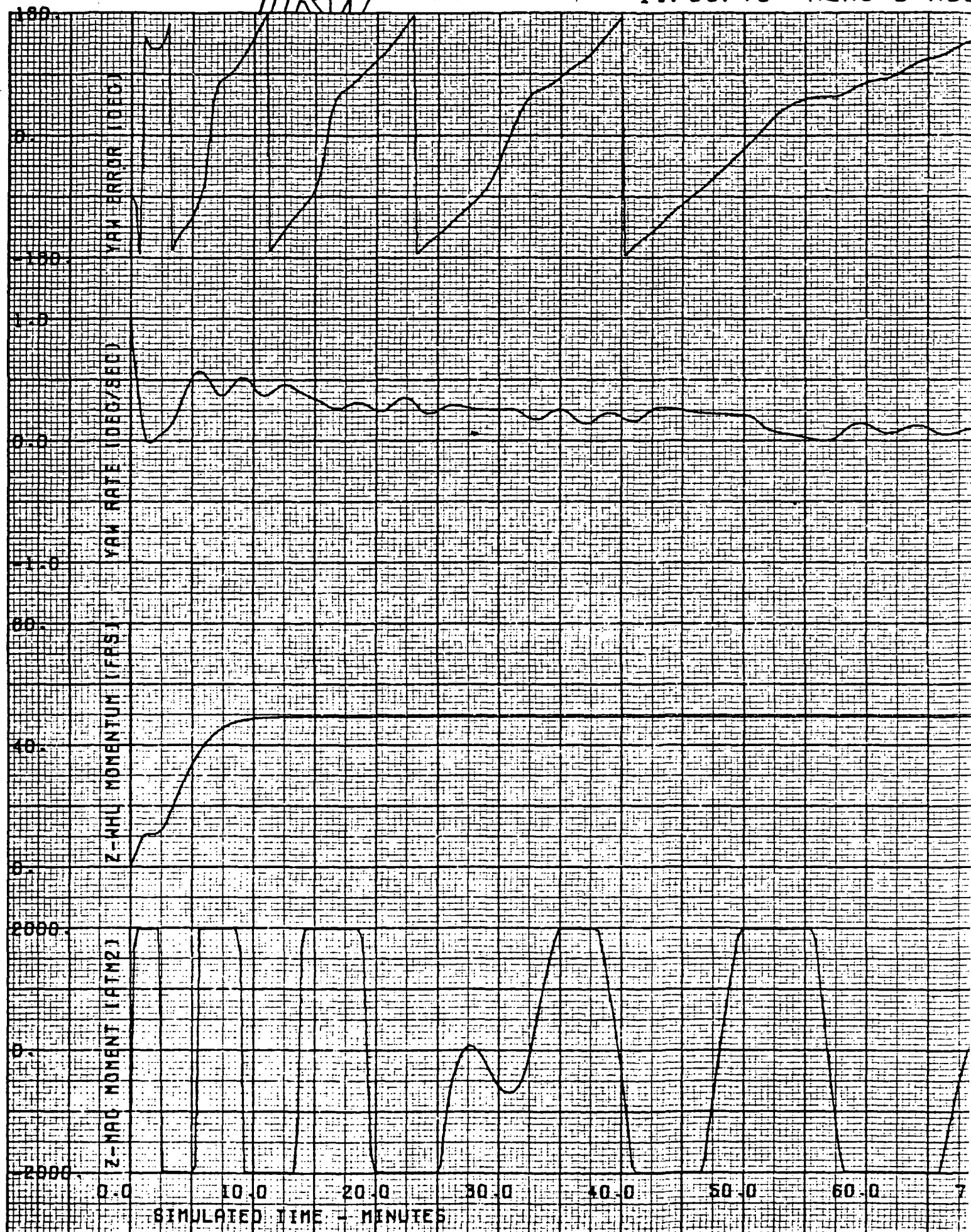
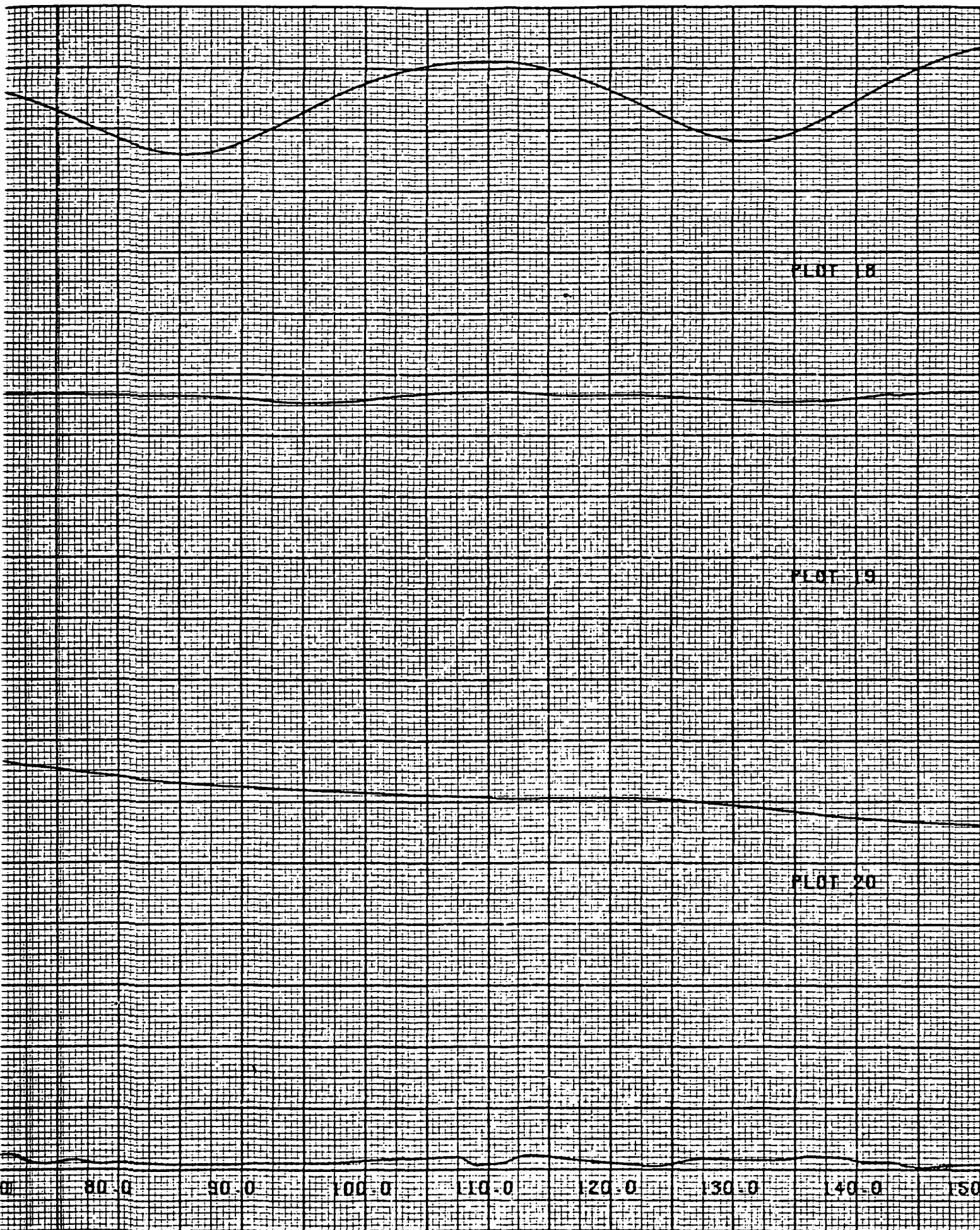


Figure 4-28. Yaw Respc

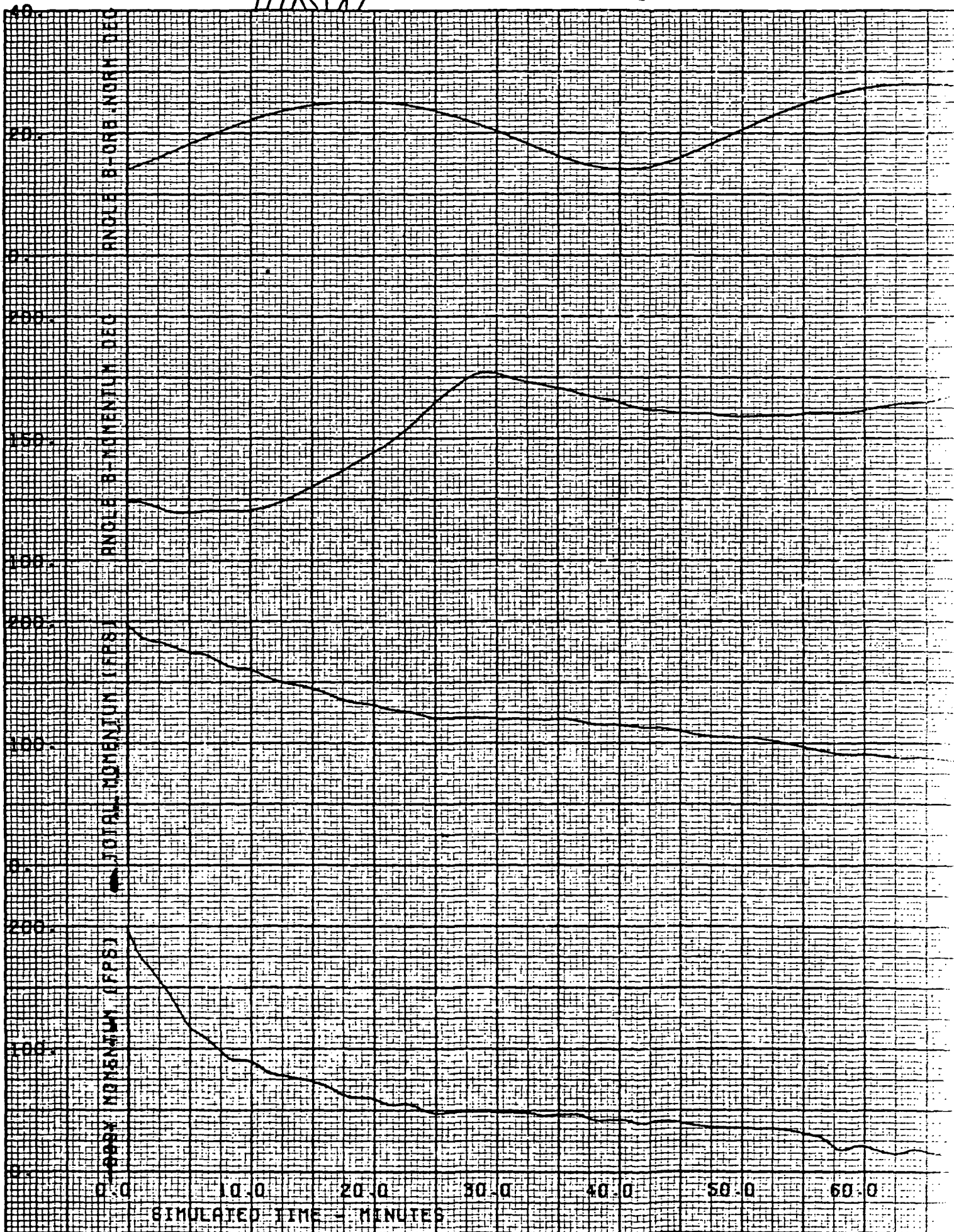




TRW

80<

11/06/73 HEAD-B AC





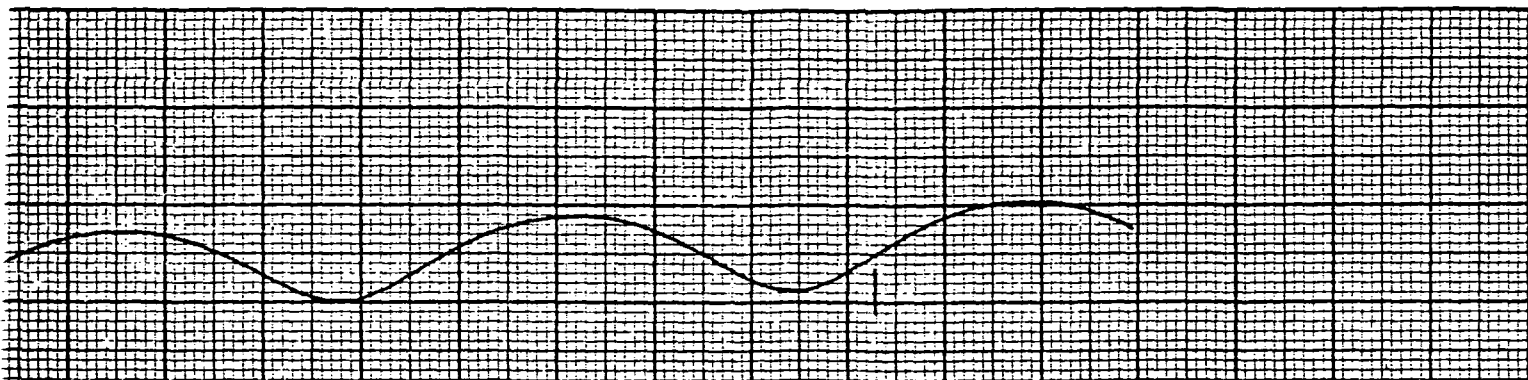
spacecraft rate and to initiate the maneuver toward the sun as quickly as possible. However, the wheels tend to saturate early and lose their control authority, although they are effective at nulling the spacecraft rates. Acquisition occurs after only 150 minutes, but results in significant levels of momentum left in the wheels. It would appear that unloading time on the order of 100 minutes would be required to unload the wheels from the terminal acquisition condition; however during this period, sun pointing could be maintained.

#### Magnetic Moment Sizing

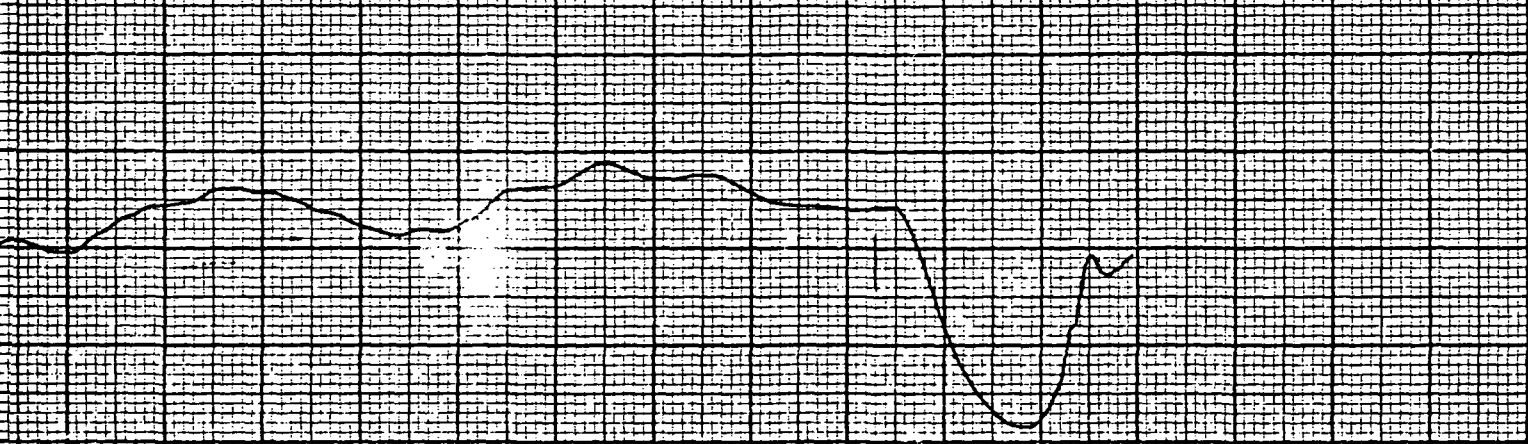
The magnetic moment capability of 2000 amp-turn-m<sup>2</sup> was established as the sizing baseline, based upon previous HEAO studies on the magnetic torquing concept. The digital simulation was used to provide an assessment of the validity of this design parameter. In this regard, runs with a maximum electromagnet moment of 1000 and 3000 amp-turn-m<sup>2</sup> were made, with results as shown in Figures 4-30 and 4-31, respectively. Reduction of the maximum magnetic moment available causes the time to wheel transition to increase approximately 55 minutes (30%) from that of the baseline, indicating significantly reduced average effectiveness of the magnetic controller. Increasing the maximum moment has essentially no effect upon the time to wheel transition. This was in part due to the fact that the selected control gain was that used for the baseline case and thus did not always result in commanded saturation. The relative increase in effectiveness of the 3000 amp-turn-m<sup>2</sup> case, compared to the 1000 case, is seen in the initial 20 minute segments of the momentum histories in Figures 4-30 and 4-31. The assessment of the payoff in increasing the maximum magnetic moment from the 2000 amp-turn-m<sup>2</sup> of the baseline was that no significant performance improvement could be identified at this time. In the same context, a reduction to 1000 amp-turn-m<sup>2</sup> caused significant decreases in performance capabilities during acquisition. Therefore, the 2000 amp-turn-m<sup>2</sup> design of the baseline was retained for the sizing analysis.

#### Residual Field Effects

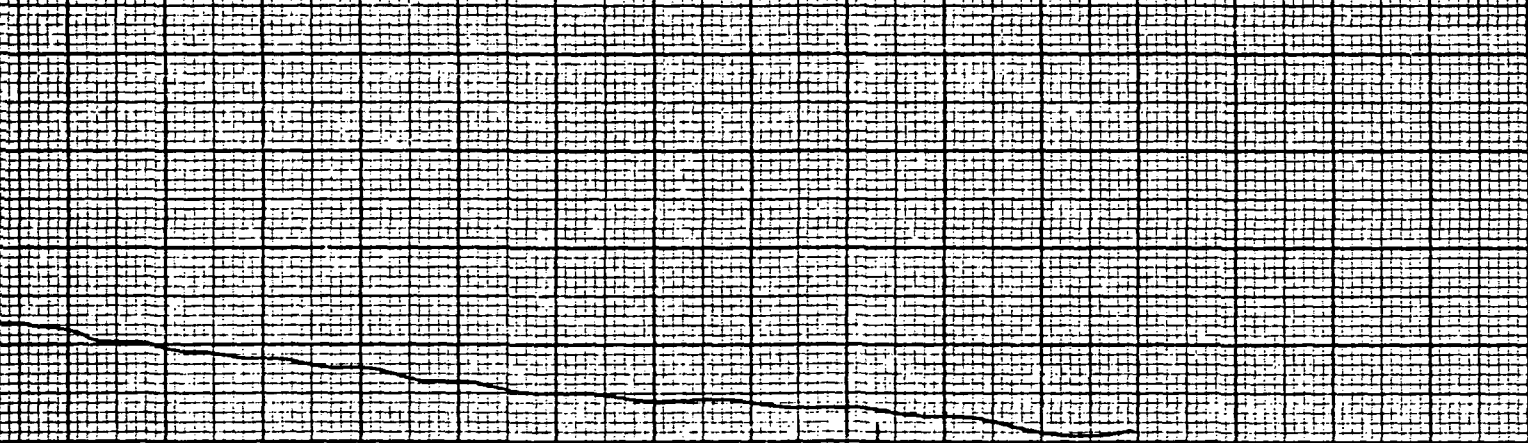
The magnetometer triad senses the overall magnetic field at the sensor location on the spacecraft. The sensed field may contain contributions in



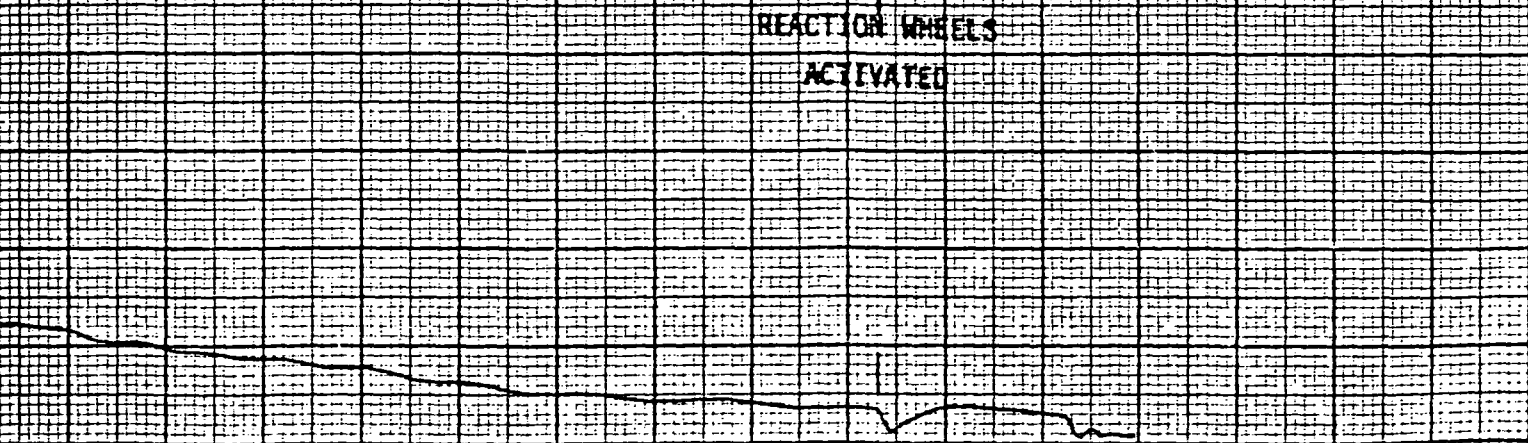
PLOT 18



PLOT 19



PLOT 20



REACTION WHEELS  
ACTIVATED

0 150.0 180.0 200.0 220.0 240.0 260.0 280.0 300.0

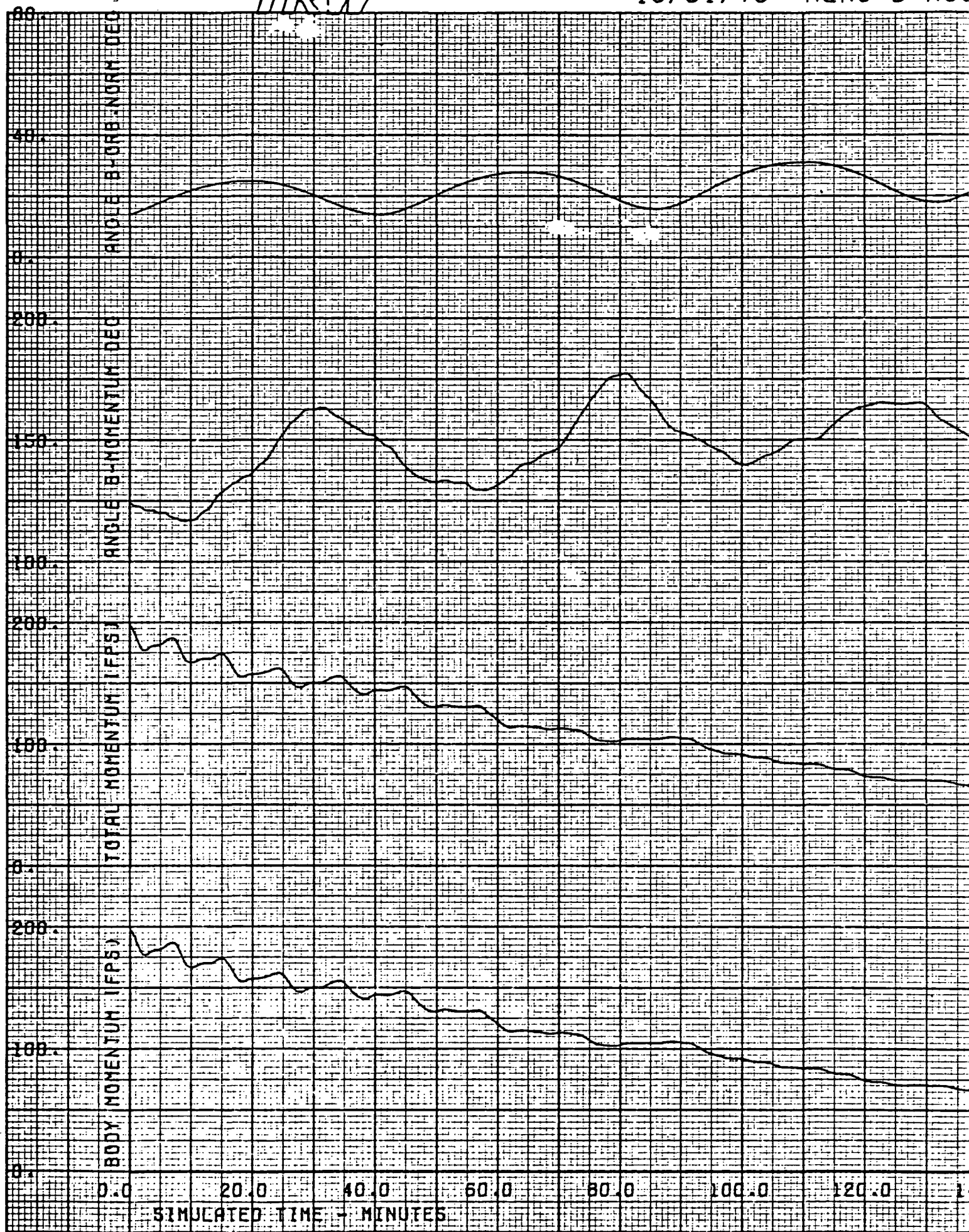
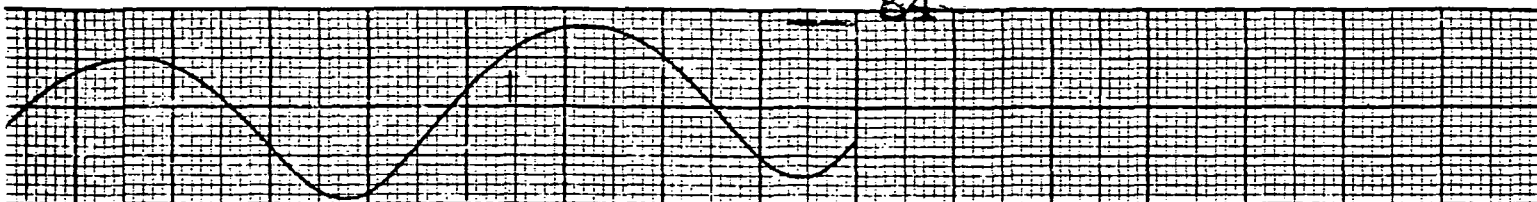
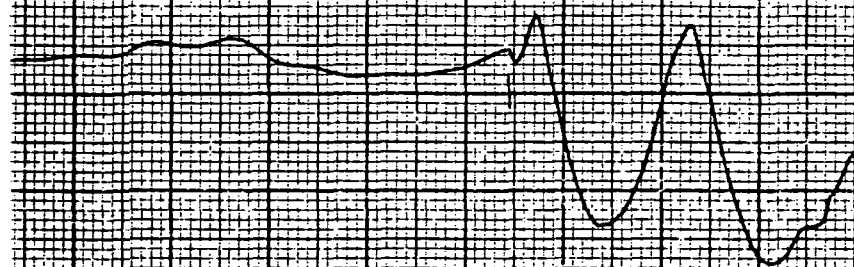


Figure 4-30. Magnetic Alignment and Mom

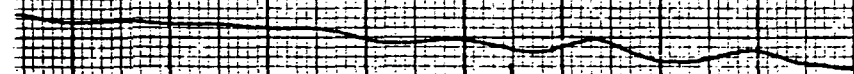
84



PLOT 18



PLOT 19



PLOT 20

REACTION WHEELS  
ACTIVATED



160.0 180.0 200.0 220.0 240.0 260.0 280.0 300.0



1112W

85<

10/31/73

HEAD-8 ACI

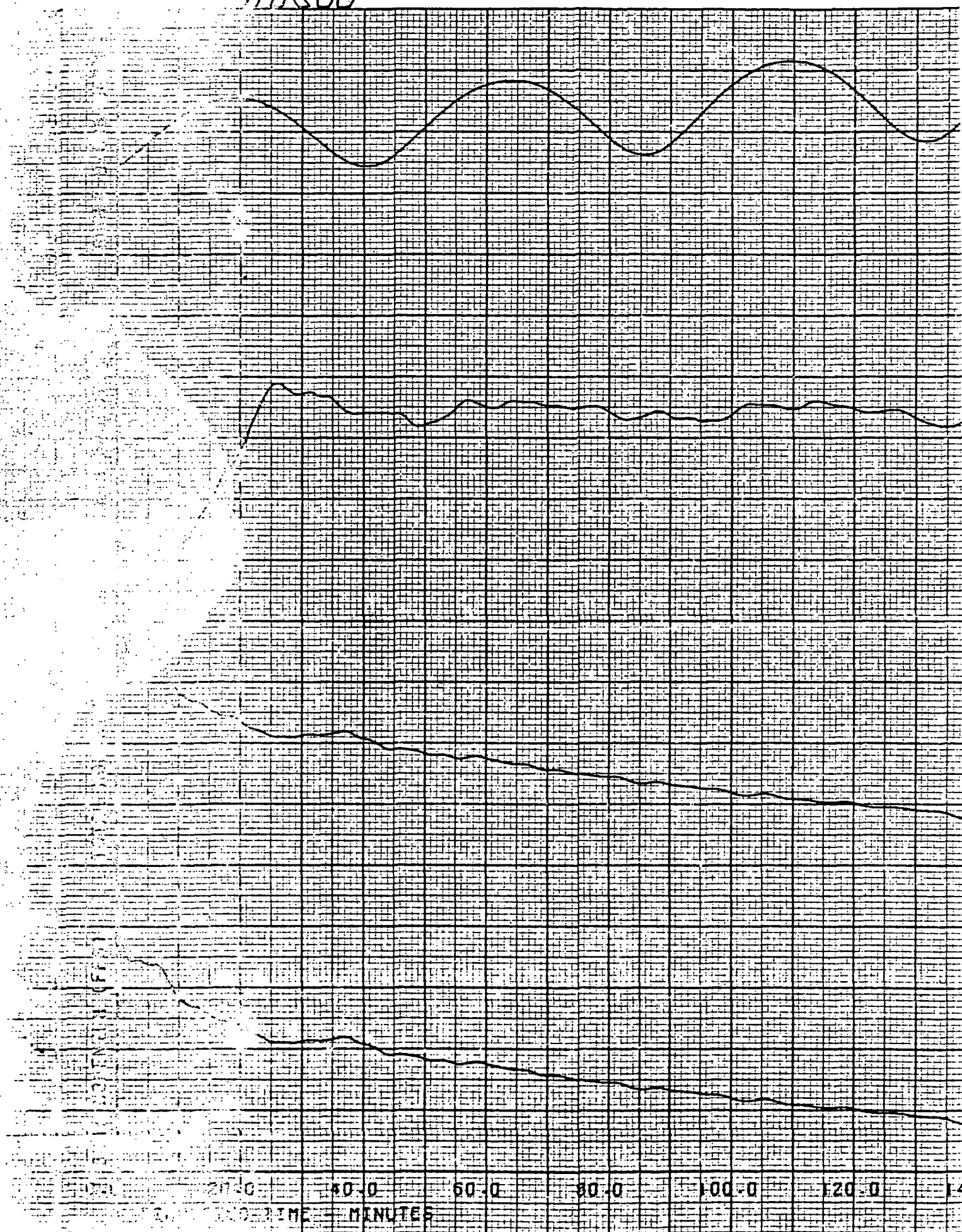


Figure 4-31. Magnetic Alignment and Mome

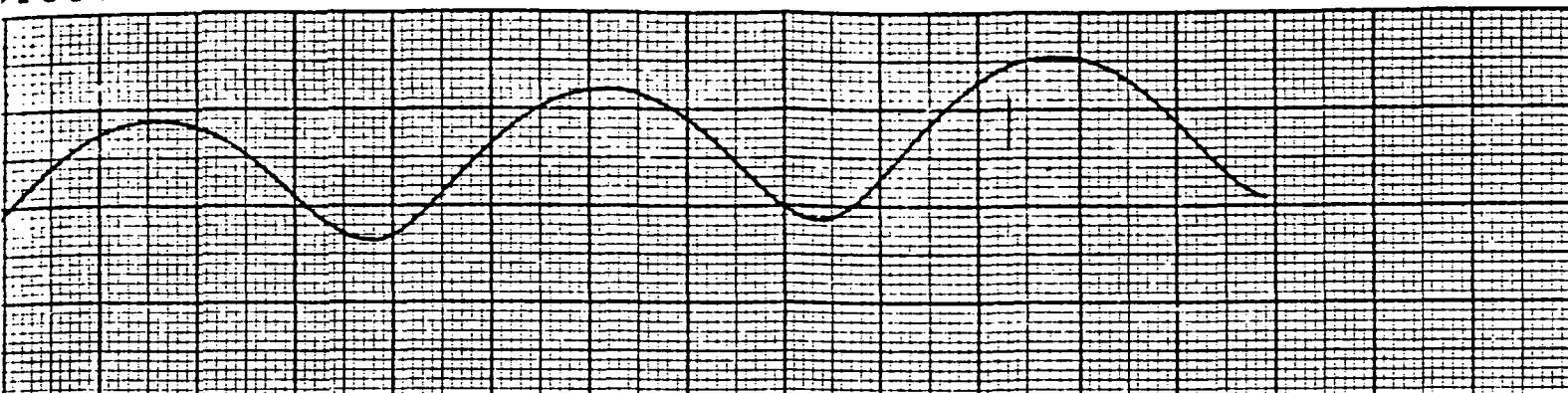
addition to the earth's magnetic field arising from sources on the spacecraft itself, such as experiments and electronic/electrical devices. These contributions will tend to create a body fixed field residual or bias to the desired magnetometer output. To the extent possible, this could be compensated by appropriate biases in the sensor processing. However, some residual is likely to exist. The effect of such a residual on the sun acquisition performance was studied. A magnitude of 1% of the maximum earth field in each axis was used for comparison. The results of this perturbation to the baseline case are shown in Figure 4-32, corresponding to Case 9. The net effect of the residual bias is to increase the time required to transition to the wheels. This is due to a decrease in the effective capability of the magnetic controller, resulting from activation of the electromagnets according to a sensed field, which was skewed relative to the real field which provided the control torques. This causes extraneous couplings and interactions which act to reduce the net controller effectiveness. Once transition to the wheels was accomplished, performance was not as significantly affected. The normal mode results of the next section illustrate this in more detail. The results of this perturbation indicate that attention must be paid to the residual field effect in terms of control performance during acquisition. This requires an assessment of the various field sources and their effects in the vicinity of the magnetometer and the electromagnets as the residual effect is a relative one in terms of these two units. Ideally, the magnetometer field should be the same as that present at the electromagnets.

#### Magnetic Control Coupling

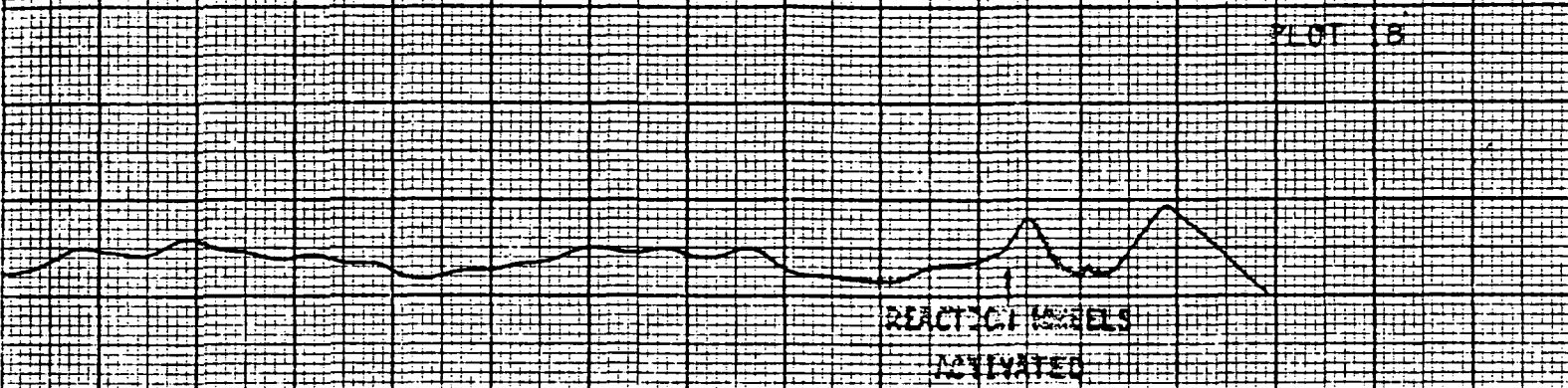
The magnetic control system implementation features a closed loop, using magnetometers for sensing and electromagnets for torquing. Both are magnetic devices; therefore a dynamic coupling path is present within the control loop. The electromagnets produce a magnetic field as consequence of the magnetic moment. The magnetometers are field sensing devices. Therefore, it is of interest to look at the effect of this feedback coupling mechanism. The degree of coupling is a function of the effective loop gain, which is dependent upon the controller gain and

87<  
POSITION (HXB) K=.05,.0035 RSD.FLD

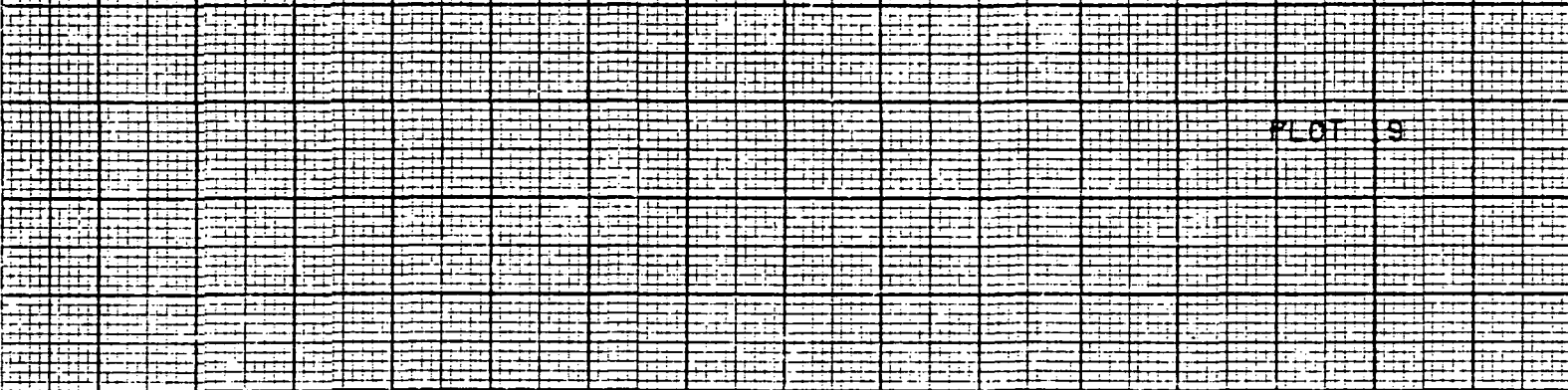
PLOT 17



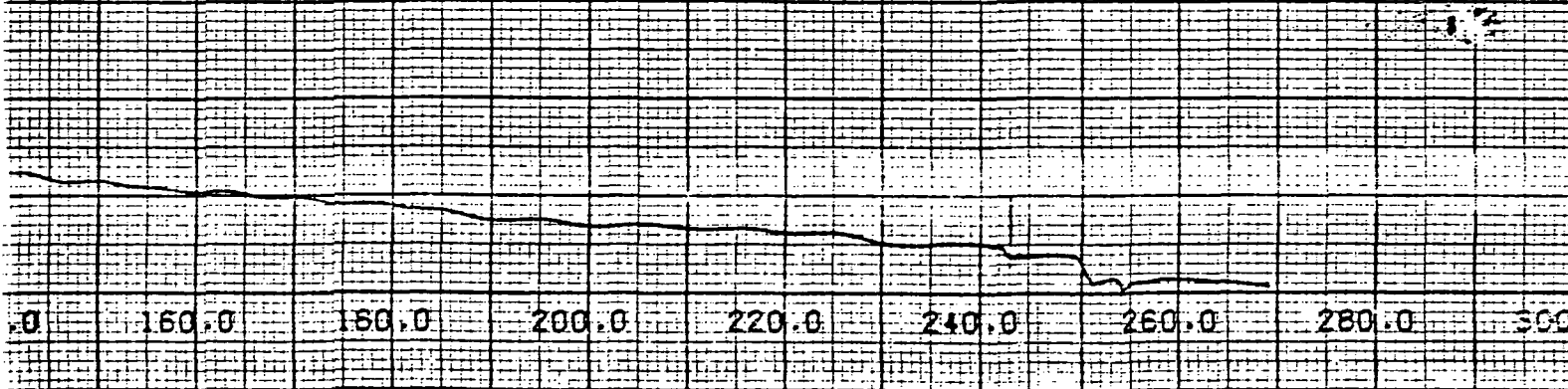
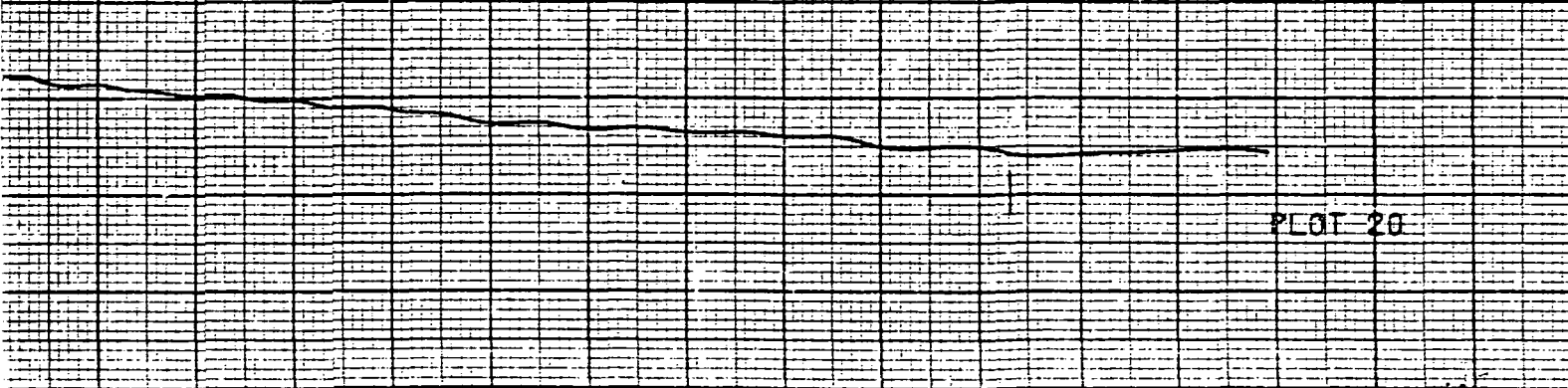
PLOT 18



PLOT 19



PLOT 20



0 160.0 180.0 200.0 220.0 240.0 260.0 280.0 300.0

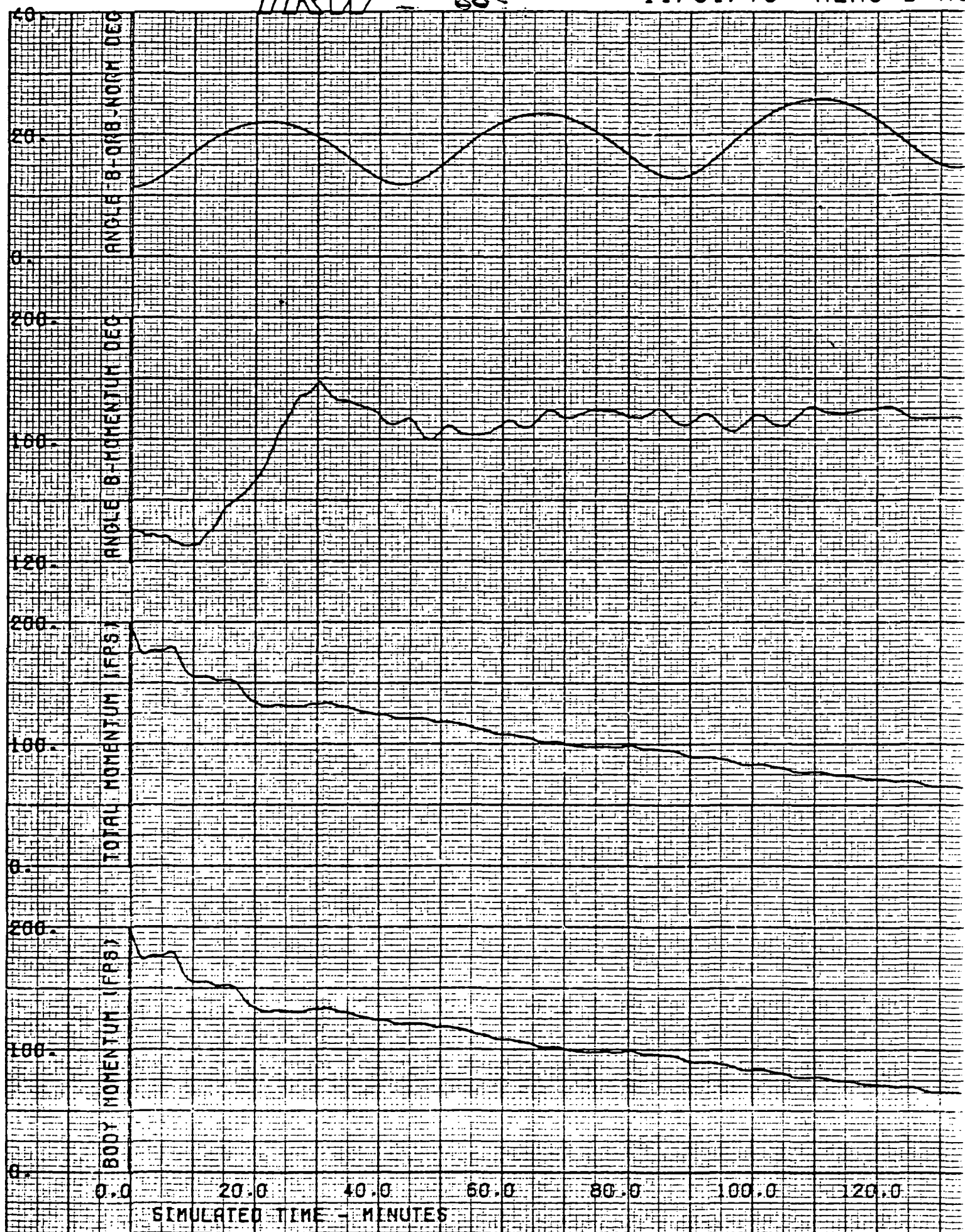


Figure 4-32. Magnetic Alignment and



the field potential characteristics of the electromagnets at the magnetometer location. Field strength generally follows the inverse cube decay characteristic as a function of separation distance. By proper relative placement electromagnets and the magnetometers, it is theoretically possible to make the effective coupling gain nearly zero. Location constraints exist, however, in the HEAO application due to limitations on the observatory size (see Figure 4-1). To avoid the necessity for employing extendable booms or other similar devices, the maximum electromagnet/magnetometer separation allowable is limited to the longitudinal dimensions of the observatory ( $\approx 25$  ft). As part of this study, an assessment of the field characteristics of the electromagnets was made. This encompassed both the near field (in equipment module) and far field (in vicinity of magnetometer) regions. Based upon these results, it was concluded that induced field levels at the magnetometers, from a saturated electromagnet, could be on the order of 5-10% of the maximum earth's field in magnitude. It was desired in the control performance analysis, to make this coupling worst case, if possible, by appropriate specification of the sign on the coupling magnitude. To aid in this specification, two analytical approaches were pursued. Consider the case when the x-magnetic control loop by itself is analyzed. The magnetic moment to be generated is given by the  $B \times H$  control law as:

$$M_x = K(H_y B_{zs} - H_z B_{ys}) \quad (4-29)$$

where:

$M_x$  = magnetic moment of x-magnet

$B_{ys}, B_{zs}$  = sensed magnetic field components

$H_y, H_z$  = y and z components of momentum

Assume that

$$B_{zs} = B_{zE} + \delta_{zx} M_x \quad (4-30)$$

and

$$B_{ys} = B_{yE} + \delta_{yx} M_x \quad (4-31)$$

where:

$\delta_{zx}$  = coupling gain of the z-magnetometer to the x-magnetic field

$\delta_{yx}$  = coupling gain of the y-magnetometer to the x-magnetic field

$B_{zE}, B_{yE}$  = earth's field components along z and y

By substitution in the moment expression then,

$$M_x = K(H_y B_z - H_z B_y + H_y \delta_{zx} M_x - H_y \delta_{yx} M_x) \quad (4-32)$$

or by arranging

$$M_x = \frac{K}{1 - K(H_y \delta_{zx} - H_z \delta_{yx})} (H_y B_z - H_z B_y) \quad (4-33)$$

Thus, for positive  $H_y, H_z$ , a destabilizing influence in the magnetic controller is generated when the coupling gains have the characteristics:

$$\delta_{zx} > 0, \delta_{yx} < 0$$

As an alternate approach, consider the case when the outer control loop is analyzed with the aid of Figure 4-33. This approach considers the effect of the coupling on spacecraft motion.

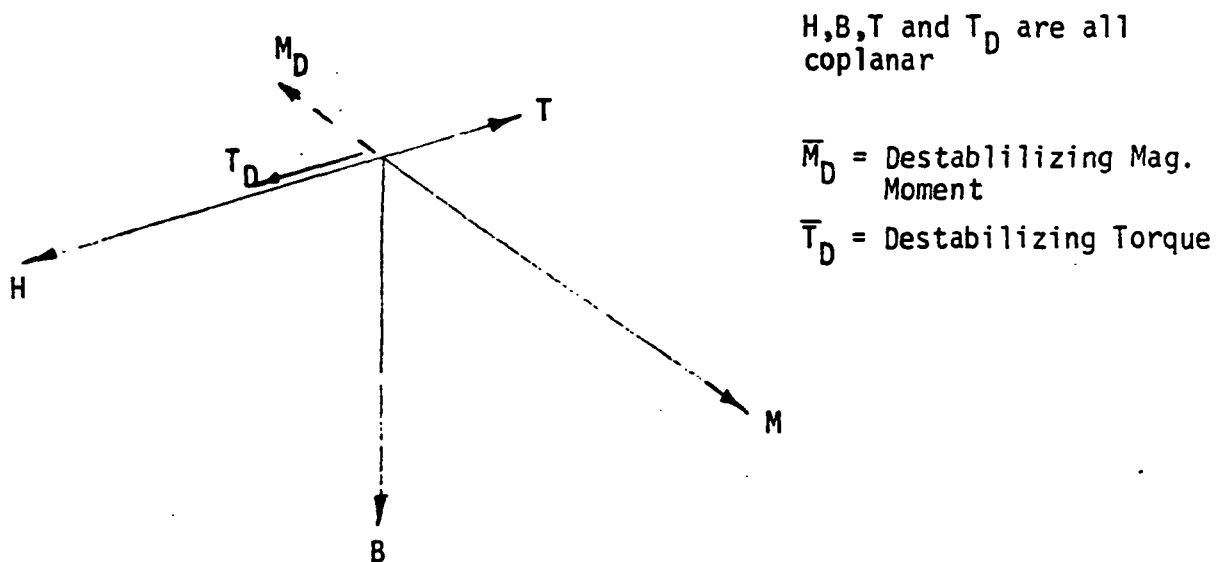


Figure 4-33. Vector Relationships for BxH Control Law

Again, the magnetic moment  $M$  is generated according to cross-product of the momentum vector and the sensed field so that:

$$M_x = K(H_y B_z - H_z B_y) \quad (4-34)$$

and the resulting torque is given by

$$T = \bar{M} \times \bar{B} \quad (4-35)$$

Rewriting Equation 4-34 in terms of the sensed field

$$M_x = K(H_y B_z - H_z B_y + H_y \delta_{zx} M_x - H_z \delta_{yx} M_x) \quad (4-36)$$

This is the same expression as before. However, here the argument is in terms of the torque produced by the coupling terms in the moment expression. If  $M_x$  were to be in the direction of  $M_D$ , the destabilizing moment of Figure 4-33, the torque produced would actually tend to increase the momentum vector ( $H$ ). This happens in a perturbation sense when  $\Delta M_x = K(H_y \delta_{zx} M_x - H_z \delta_{yx} M_x) < 0$ . Thus, a destabilizing influence exists when the coupling gains satisfy the following conditions:

$$\delta_{zx} < 0, \delta_{yx} > 0$$

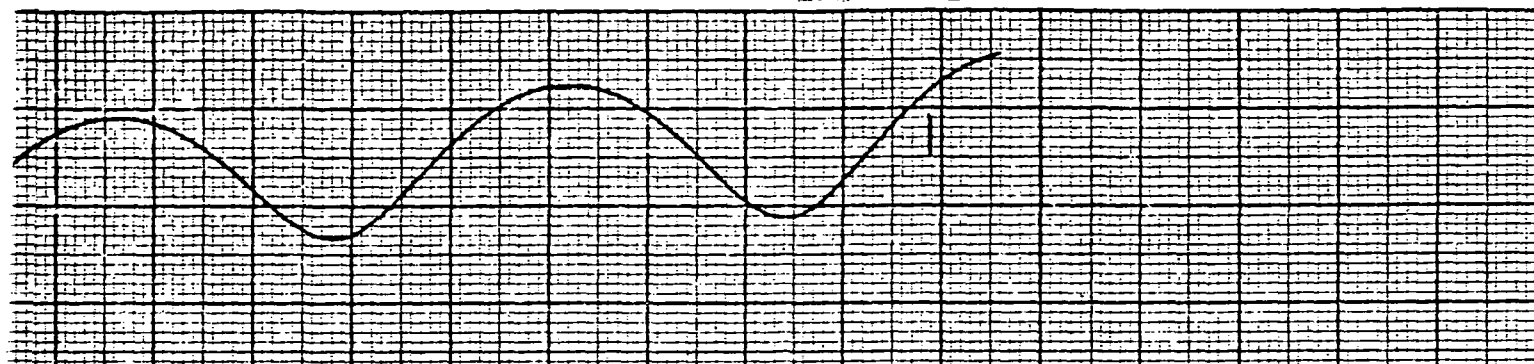
These signs are just opposite of those arrived at in the previous development.

This apparent ambiguity from the analytical approaches was pursued experimentally through use of the simulation. Various sign combinations were studied via simulations runs and it was observed that no true worst case set could be defined on a preliminary basis. Therefore, it was concluded that the effective feedback gain due to the coupling influence probably circulates through regions of stability and instability as a function of the acquisition dynamics and therefore, a worst case set of coupling signs does not exist in a general sense.

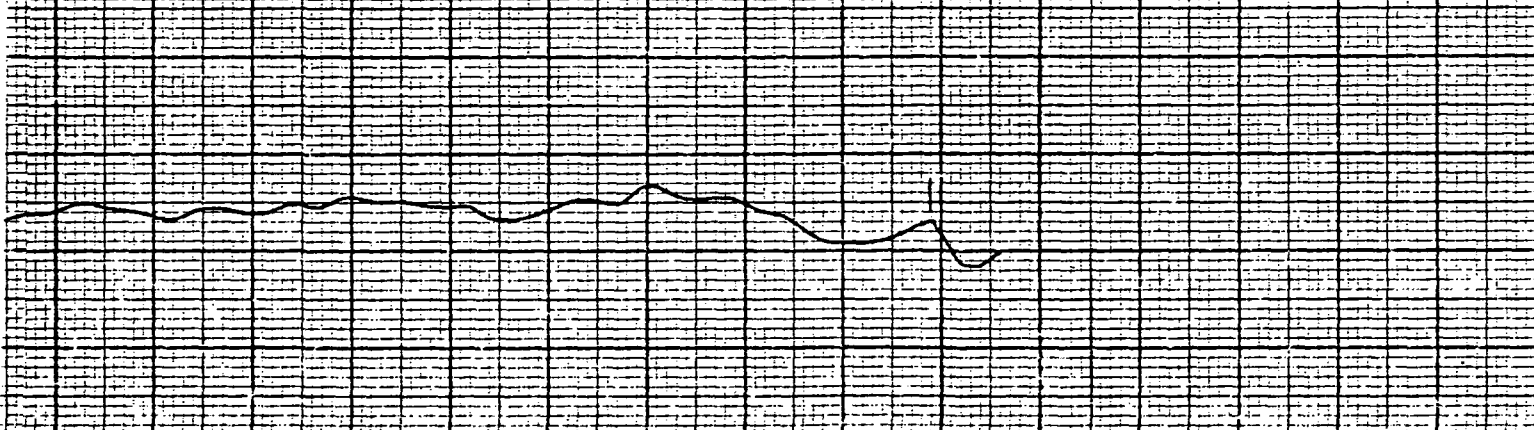
The acquisition performance for the baseline system with magnetic feedback to the magnetometers from each of the other two magnets is shown in Figure 4-34 for Case 10. The feedback gain was such that a saturated X magnet, for instance, cause the y and z magnetometers to sense fields

ITION (HXB) K=.05.MAG FDBK S2<

PLOT 17



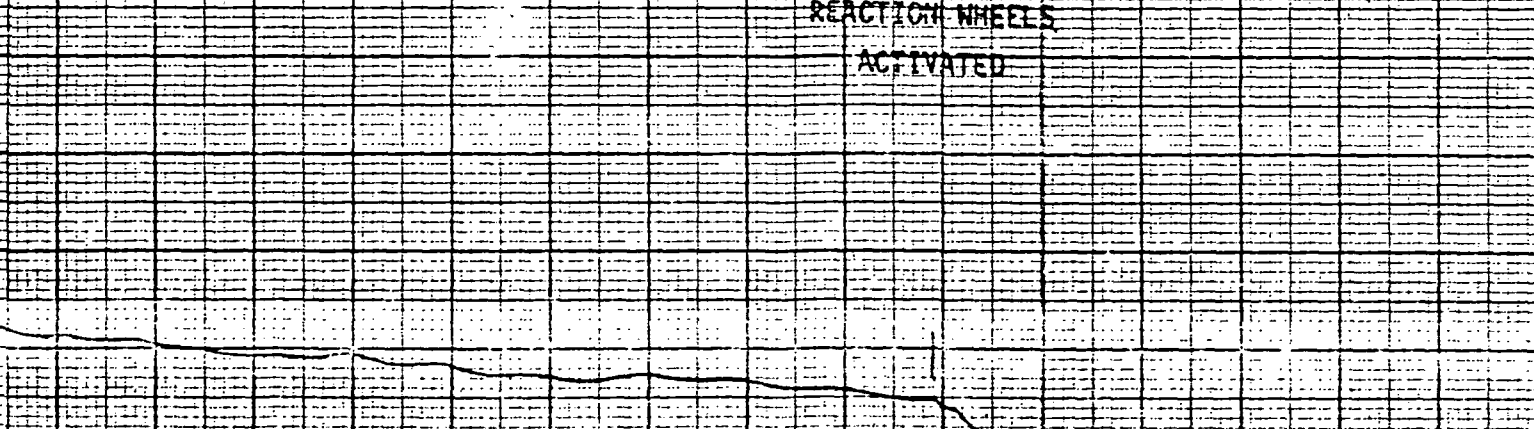
PLOT 18



PLOT 19



PLOT 20



REACTION WHEELS  
ACTIVATED

0 160.0 180.0 200.0 220.0 240.0 260.0 280.0 300.0

TRW

SLS

11/05/73

HEAD-B ACQ

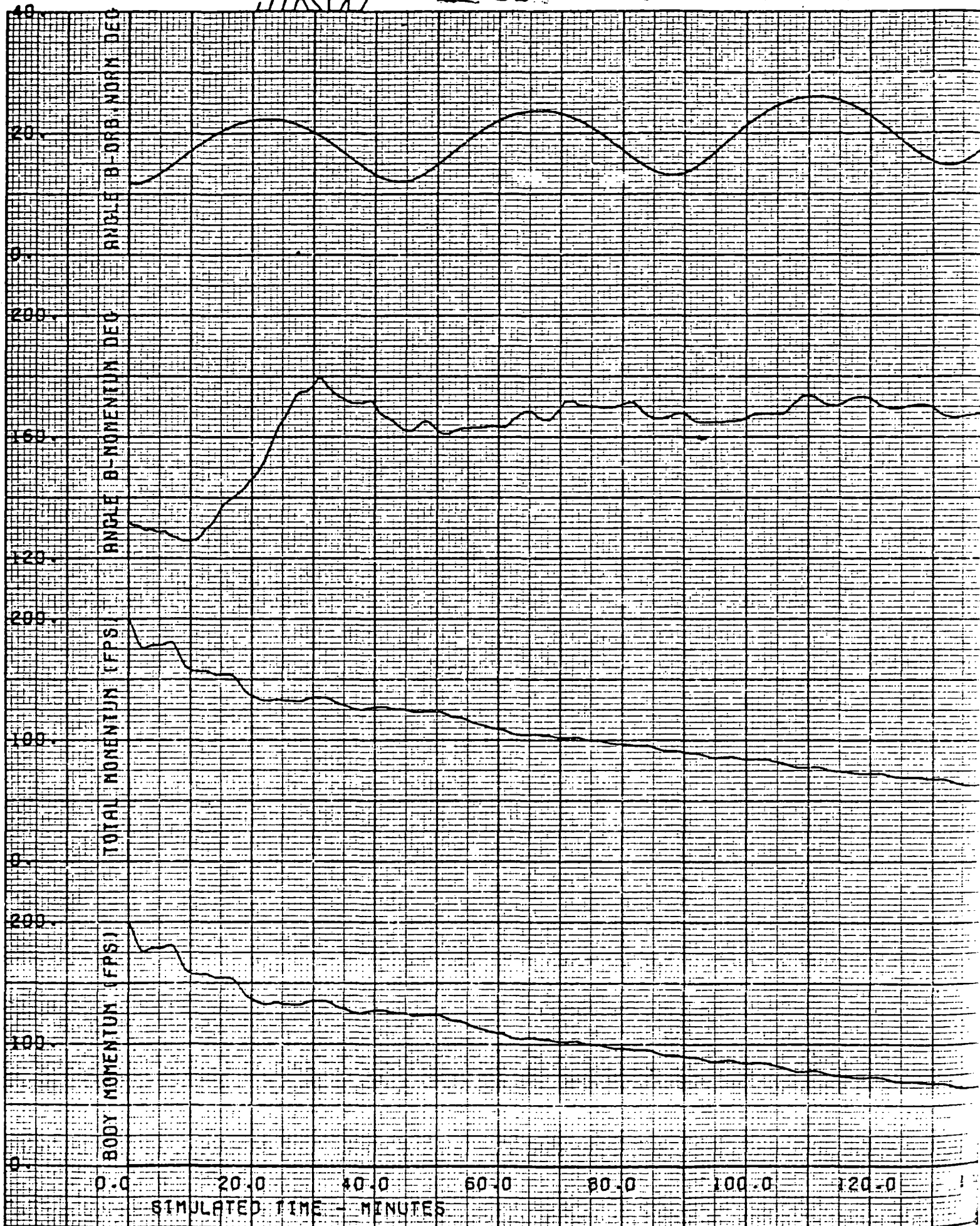


Figure 4-34. Magnetic Alignment and No

equal to five percent of the maximum earth's magnetic field in addition to the actual field at each instant. Although the simulation did not run to completion, it is deduced that sun acquisition would occur, since the wheels were activated at 239 minutes. On the basis of the other simulation results, once wheel activation is achieved, satisfactory acquisition capture follows.

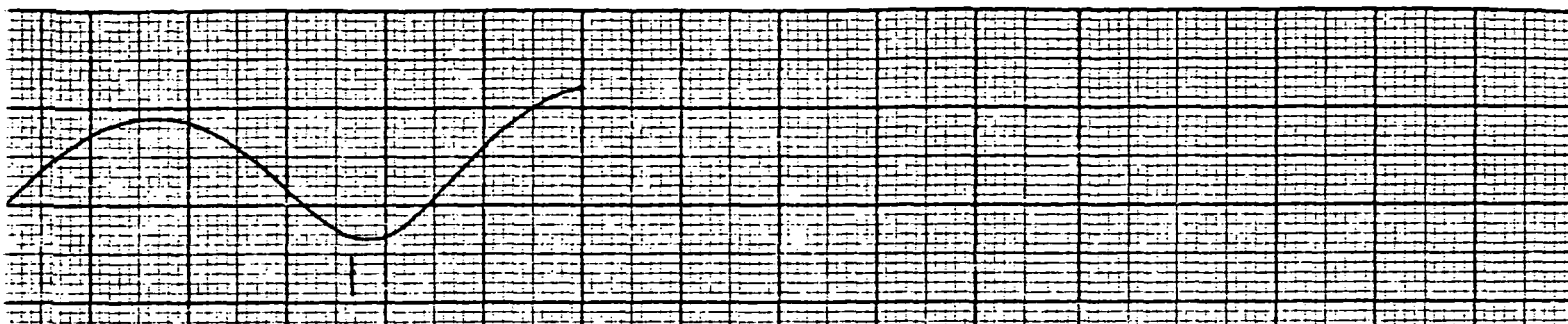
Once wheel transition is accomplished, acquisition performance is primarily determined by the wheel controller characteristics as the magnetics then act to unload the wheels in lieu of nulling spacecraft momentum. The estimated total time to acquisition capture is approximately 280 minutes, extrapolated from other wheel control performance results on combined wheel/magnetic control. The magnetic coupling is therefore a significant factor in acquisition performance. This consideration, like the residual field one, thus becomes an area for further analysis during the detailed design of a magnetic control system.

#### Tipoff Rate Effects

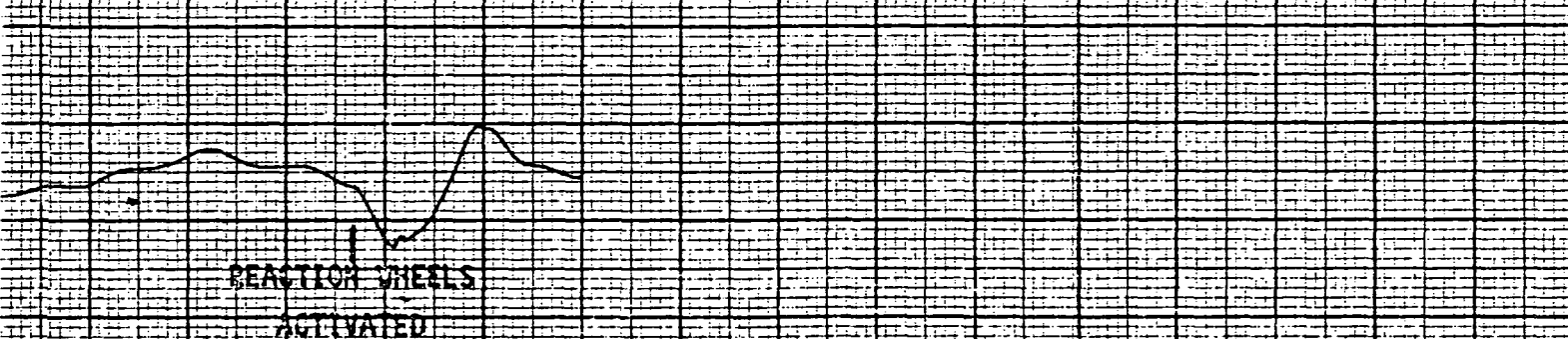
The initial angular rate conditions at initiation of the magnetic controller during Mode 1A translate into a spacecraft momentum which must be managed. The magnetic controller reduces the momentum to a level compatible with wheel transition. Since this is a fixed level, the smaller the initial momentum due to tipoff rates (as an example) the less will be the need for magnetic control action. This effect is shown quantitatively in Figure 4-35, which shows the results from a run with the baseline characteristics and magnetic coupling as in Case 10, but with initial rates of only  $0.5^\circ/\text{sec}$  in each axis in lieu of  $1^\circ/\text{sec}$ . The appropriate relative comparison is then with Figure 4-34, and the estimated extrapolation as shown in Table 4-7. Total acquisition time is reduced from  $\approx 280$  minutes to 200 minutes (30%) for a reduction of 50% in total initial momentum. The conditions of Figure 4-35 are considered representative of the worst case conditions for reacquisitions after extended periods of uncontrolled flight under the influence of large disturbance torques.

505

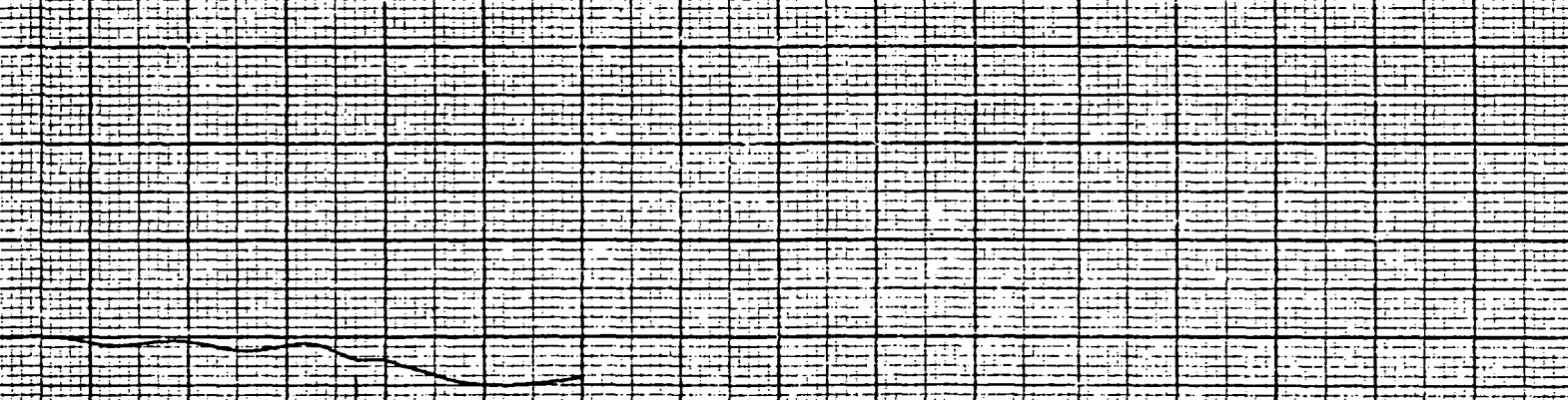
POSITION (HXB) K=.05,MAG FDBK



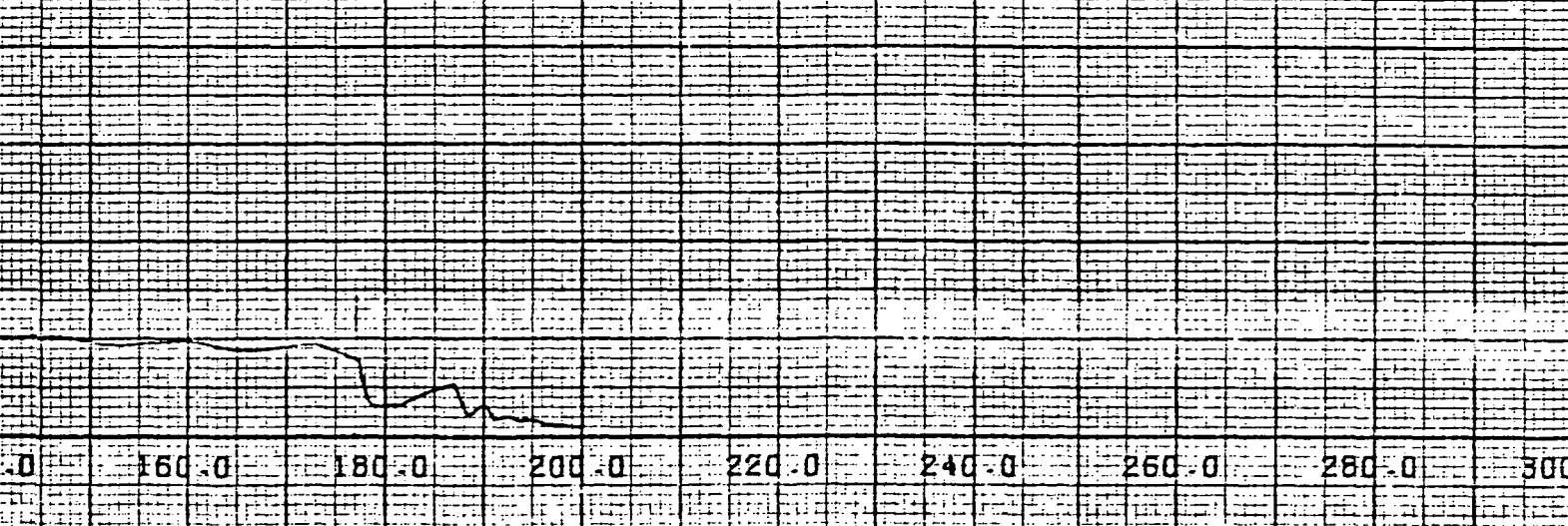
PLOT 18



PLOT 19



PLOT 20



0 160.0 180.0 200.0 220.0 240.0 260.0 280.0 300.0



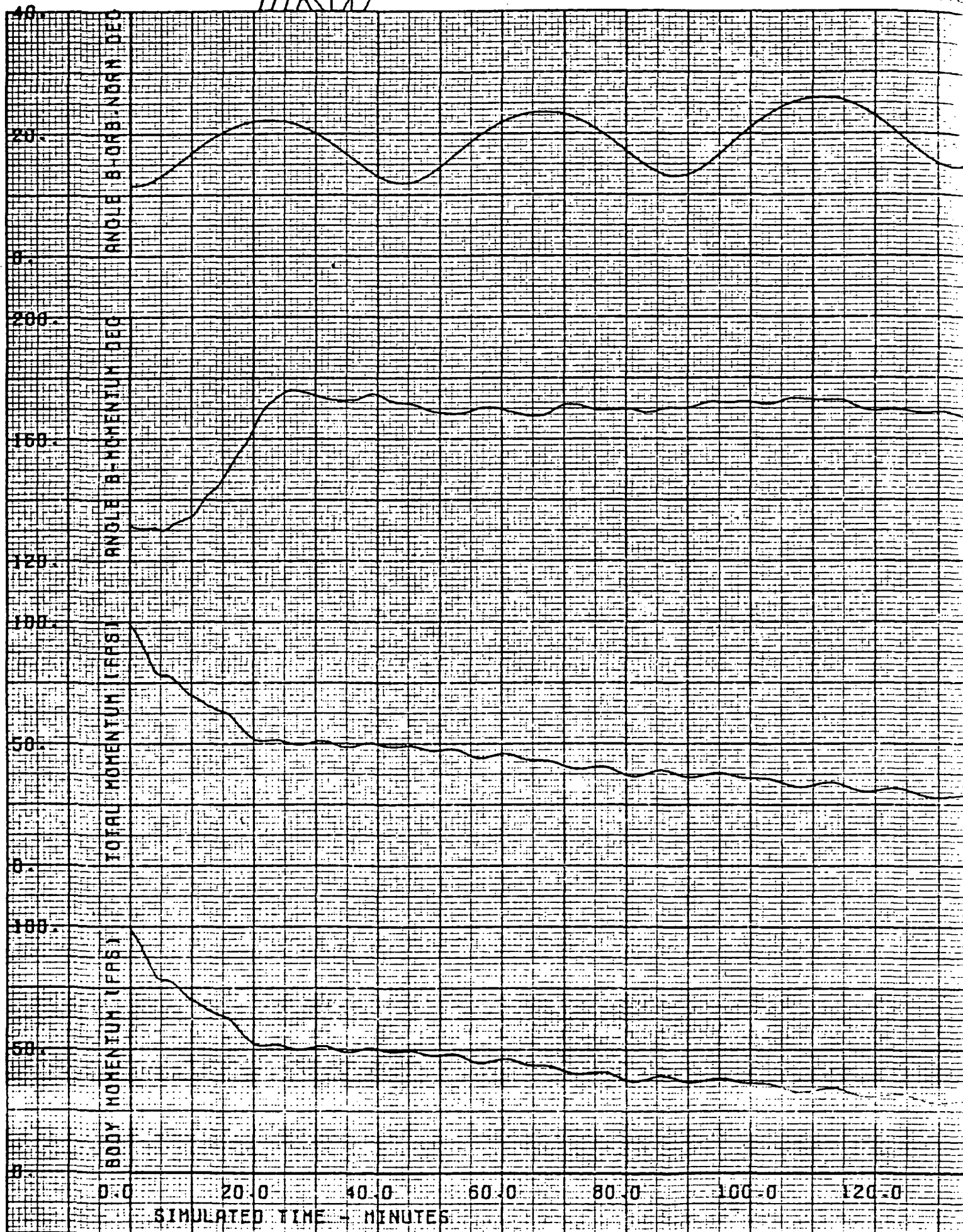


Figure 4-35. Magnetic Alignment and M



#### 4.3.2 System Performance During Normal Mode

The function of the magnetic controller during normal mode is to continuously unload the reaction wheels to counter the secular effects of environmental disturbances. Disturbances such as those due to gravity gradient torques will cause the reaction wheels to accumulate momentum as a result of control of the spacecraft attitude. The electromagnets are driven continuously by the BxH control law to provide spacecraft torques which will remove momentum from the wheels.

In the digital simulations of the spacecraft dynamics, it was assumed that the spacecraft was in the normal mode of operation with the wheels providing primary attitude control and the electromagnets unloading wheel momentum continuously. The specific areas of interest were the ability of the magnetic controller to keep stored wheel momentum down to a low level (several ft-lb-sec) and the definition of the magnetic moment authority required to achieve this characteristic. Performance results were obtained for the two primary cruise modes - celestial scan and celestial point.

##### 4.3.2.1 Performance During Celestial Scan

The HEAO-A configuration will normally operate in the celestial scan mode by rotating slowly about the z-body axis. The conditions selected in the study of operation in this mode were derived from previous disturbance analyses. These analyses developed the orbital conditions under which worst case secular disturbances occur. The following were the conditions used in the simulations and represented a worst case set:

Altitude	180 n. mi.
Inclination	22.5 deg
Right Ascension	180 deg
Sun Angle	-120 deg
Spin Rate	0.03 rpm
Orbit Position	0 deg

Figures 4-36 through 4-39 show the simulated performance at these conditions in the absence of magnetic control. The stored wheel momentum cycles back and forth between the x- and y-body axes as the spacecraft rotates about the z-axis. After 150 minutes, the wheel momentum has

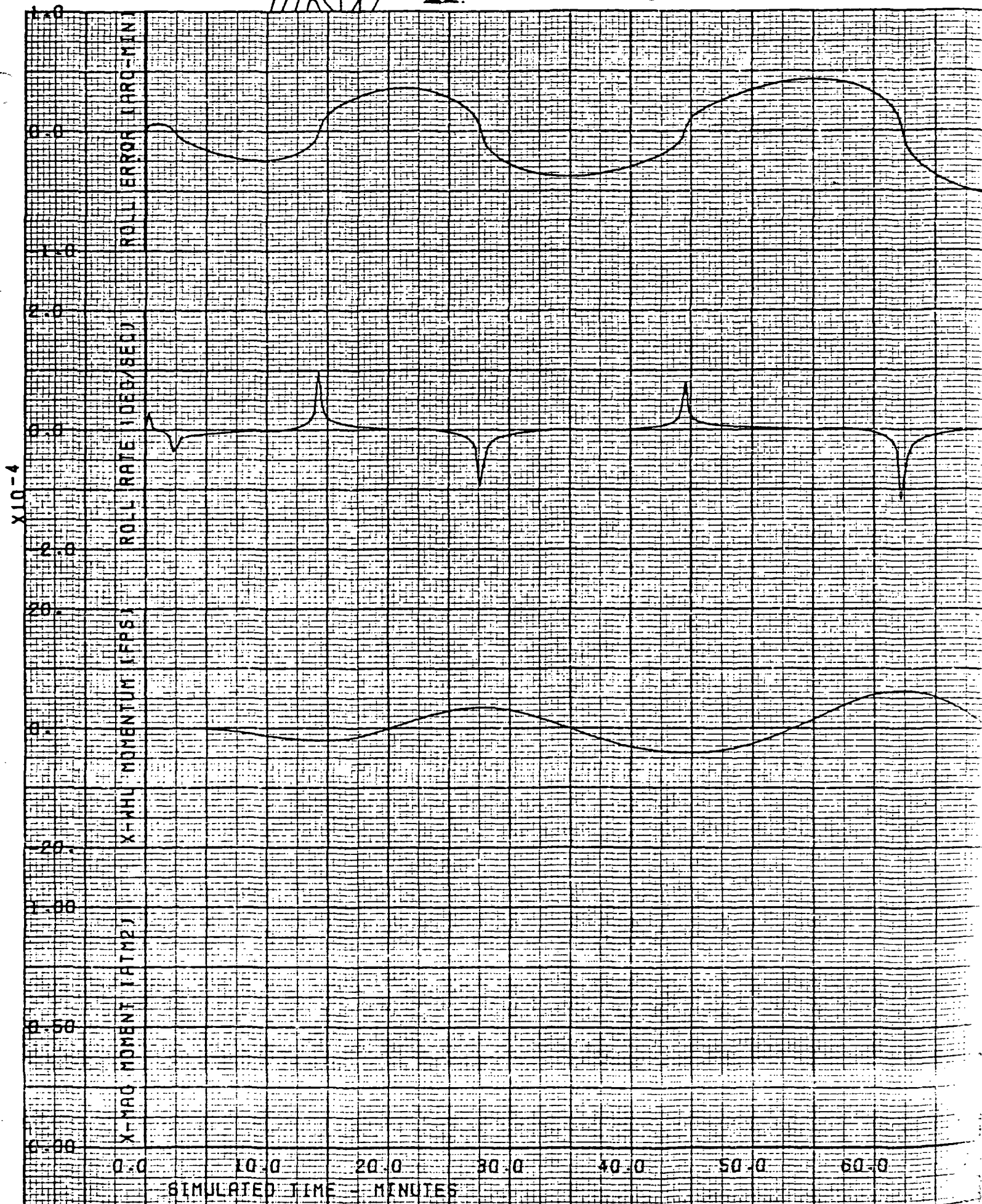
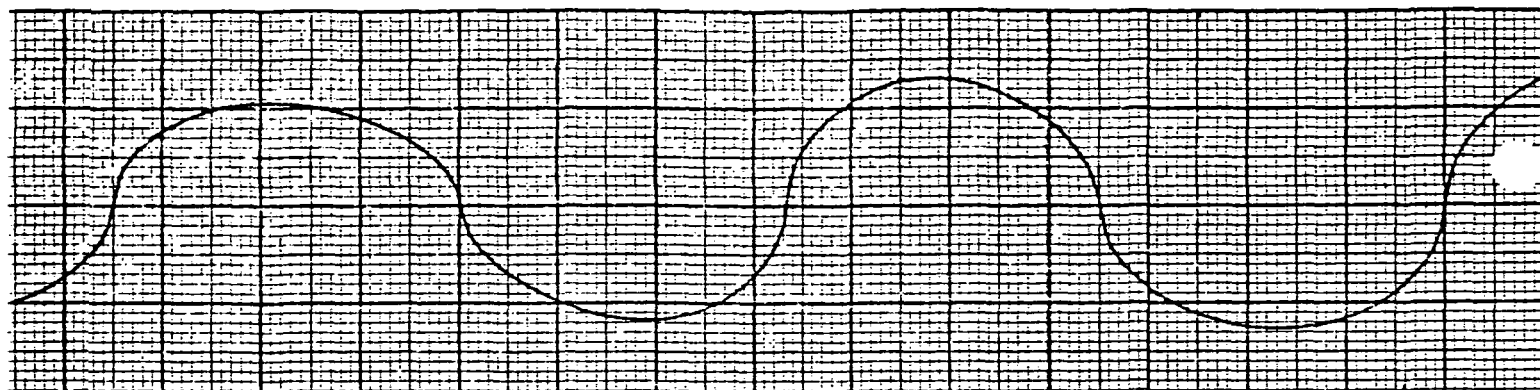
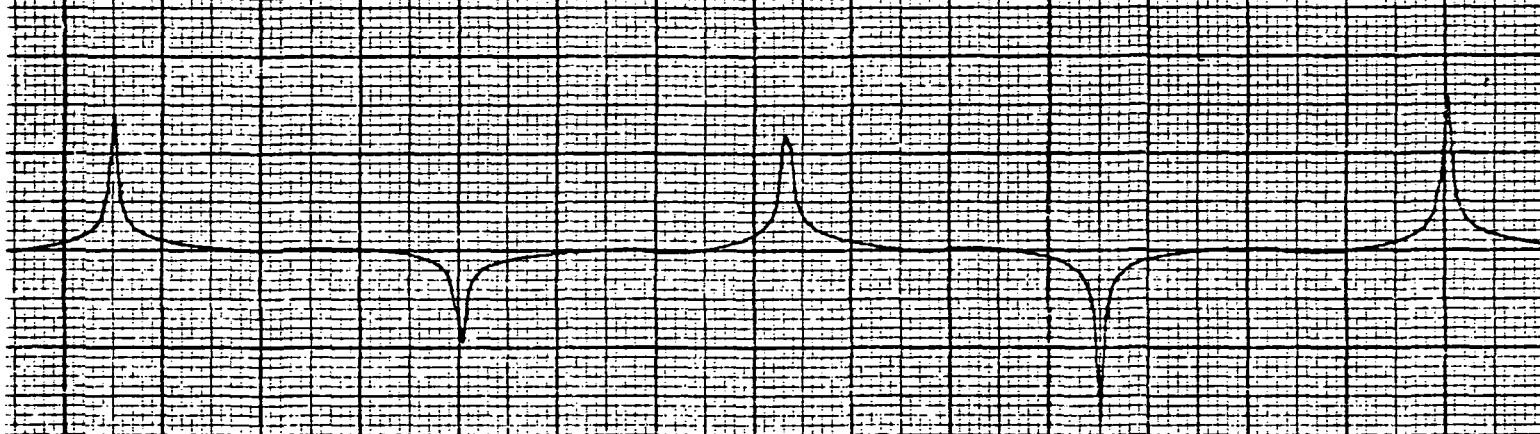


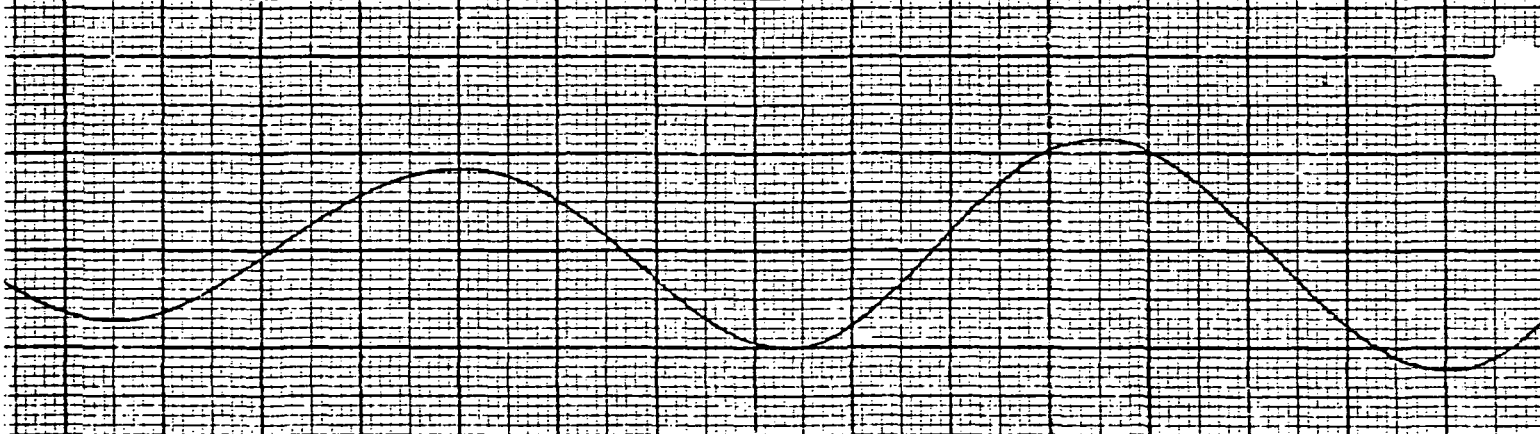
Figure 36. HEAO-A Normal



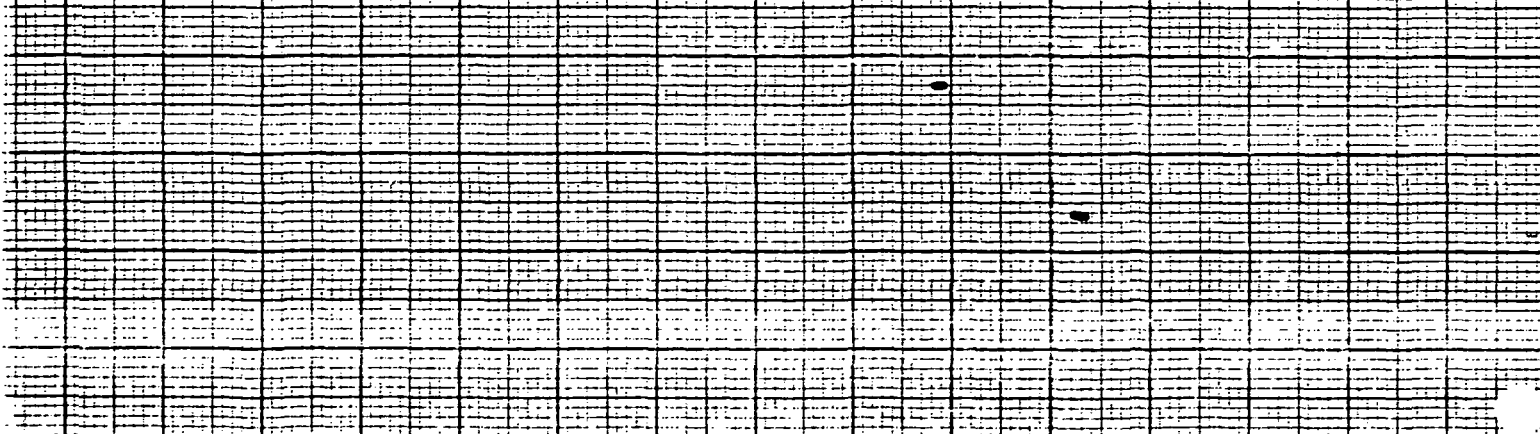
PLOT 6



PLOT 7



PLOT 8



80.0 90.0 100.0 110.0 120.0 130.0 140.0 150.0

TRW

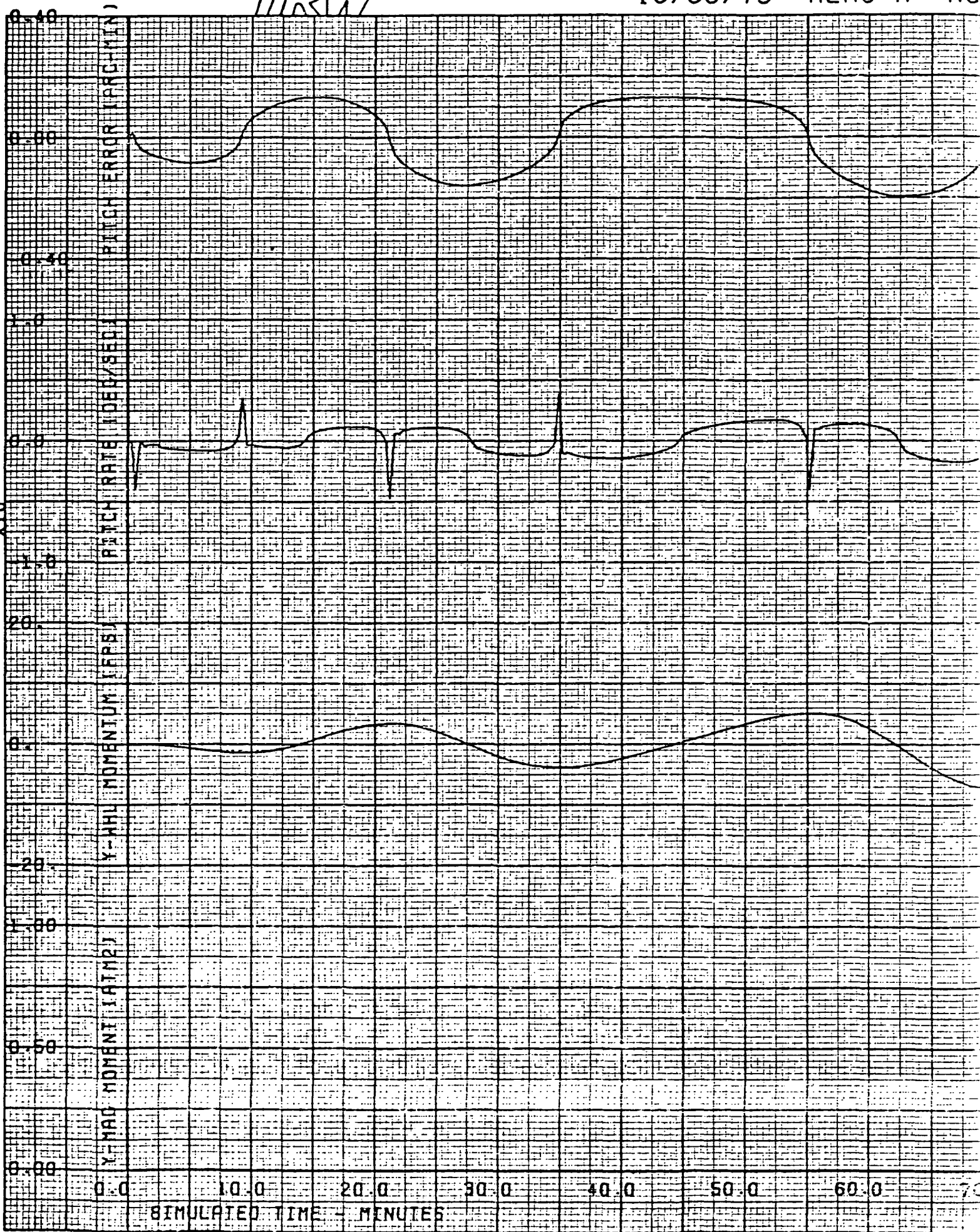
100<

10/30/73

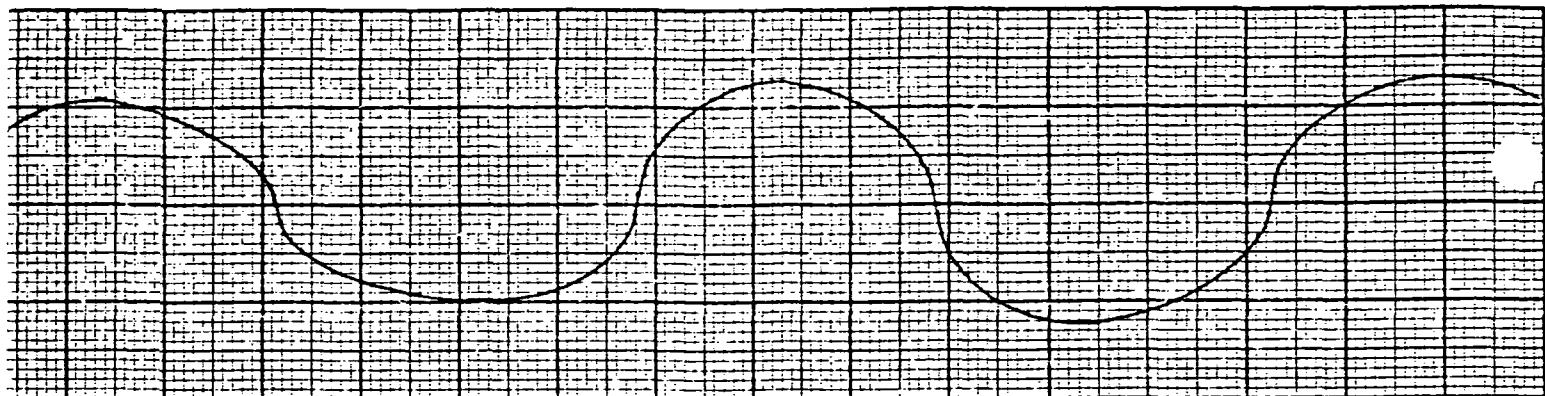
HEAD-A

NO

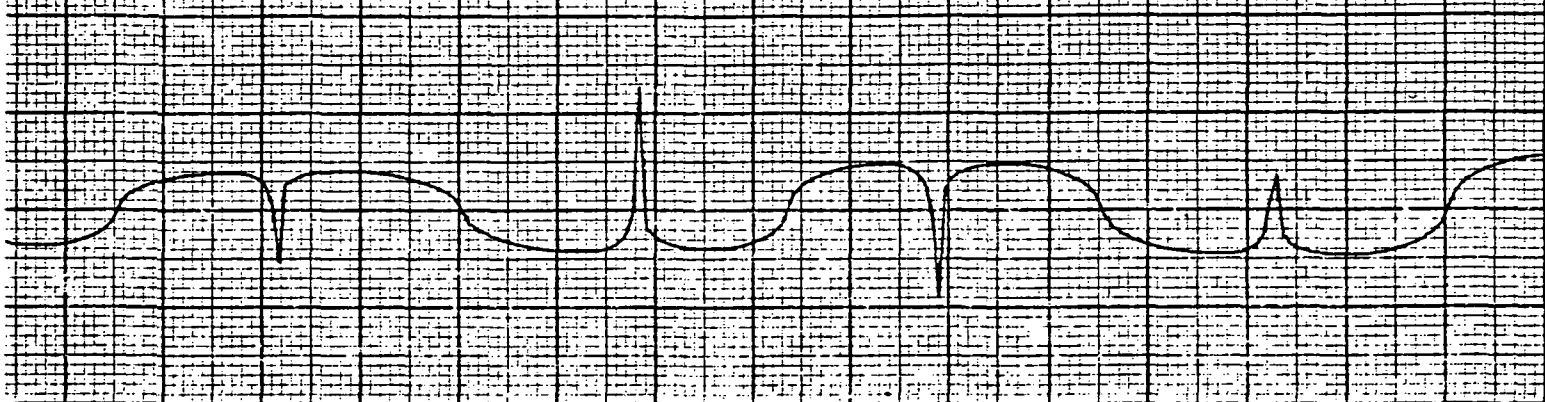
X10<sup>-4</sup>



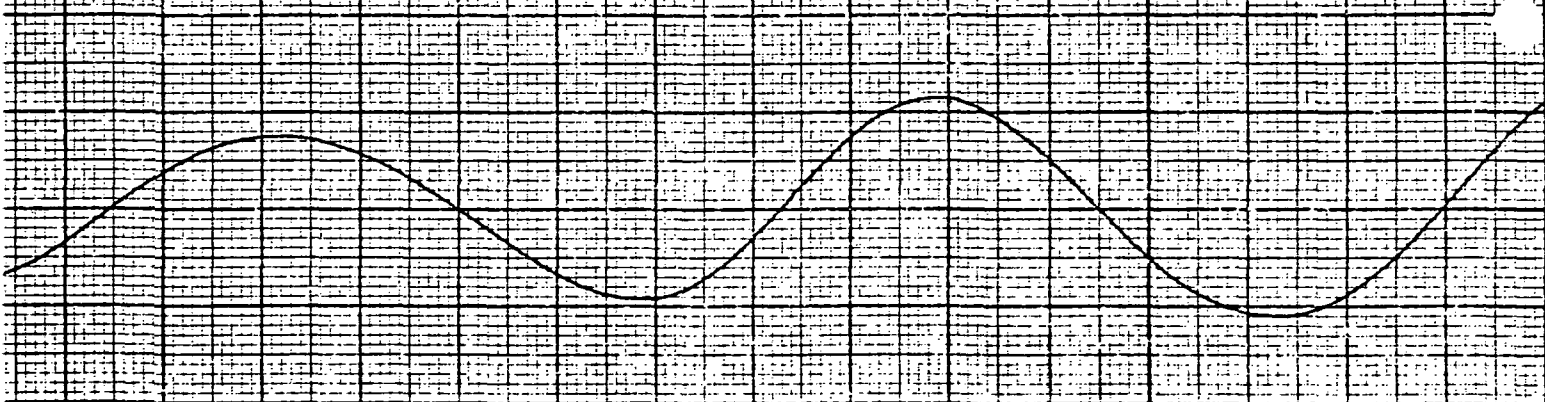




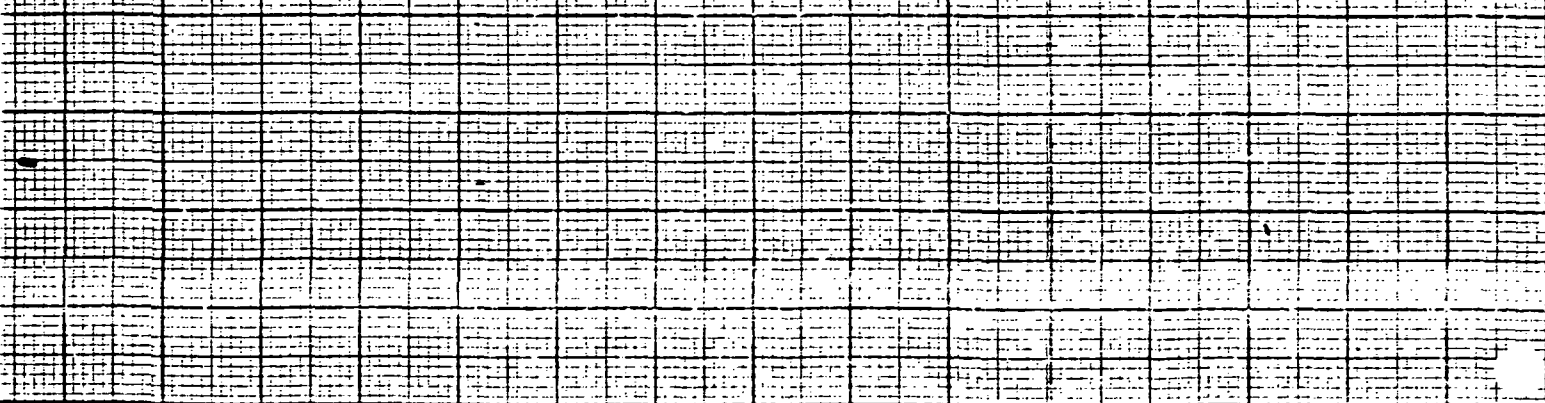
PLOT 10



PLOT 11



PLOT 12



80.0 90.0 100.0 110.0 120.0 130.0 140.0 150.0

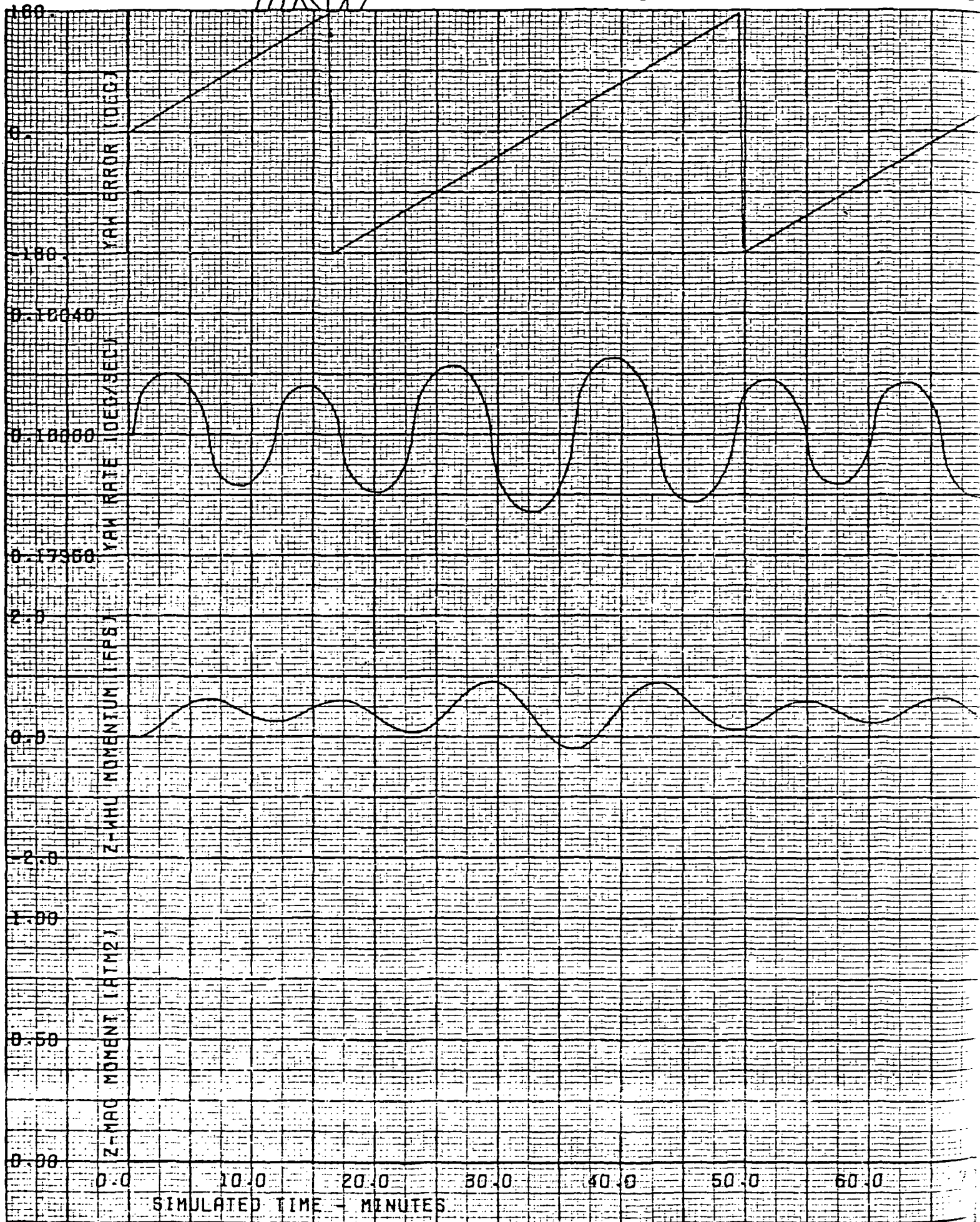
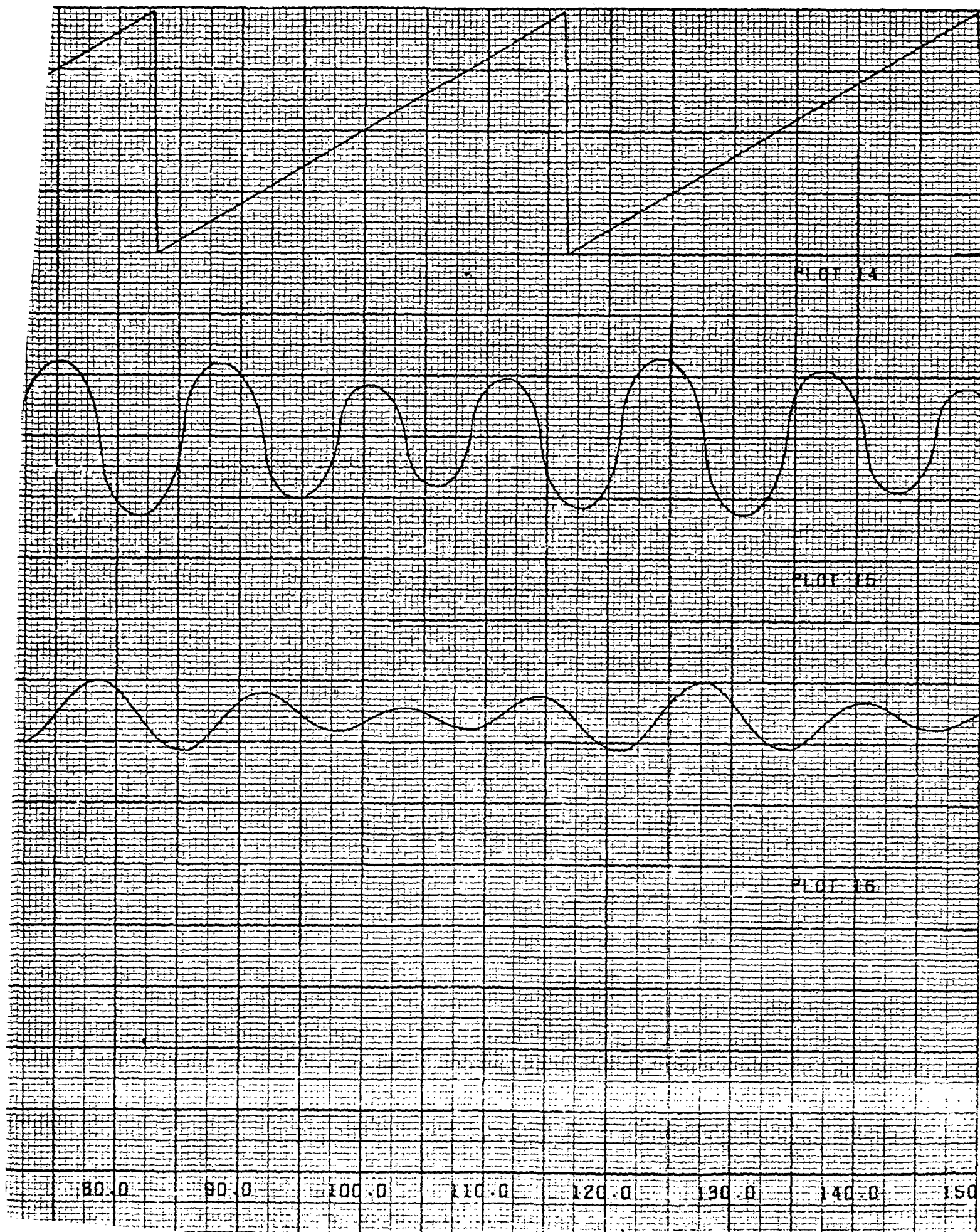


Figure 38. HEAO-A Nor

MODE NO UNLOADING

103<

PLOT 13

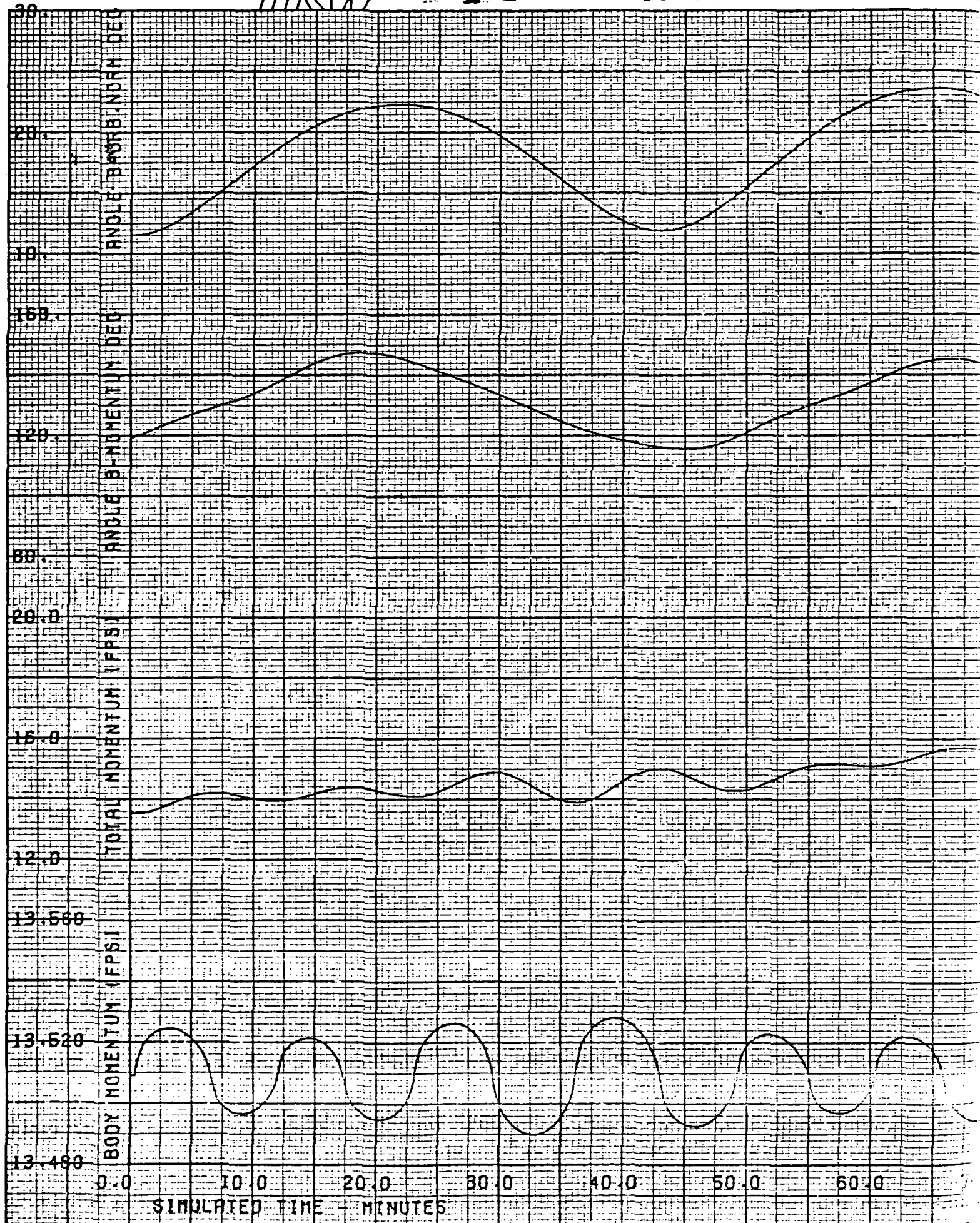




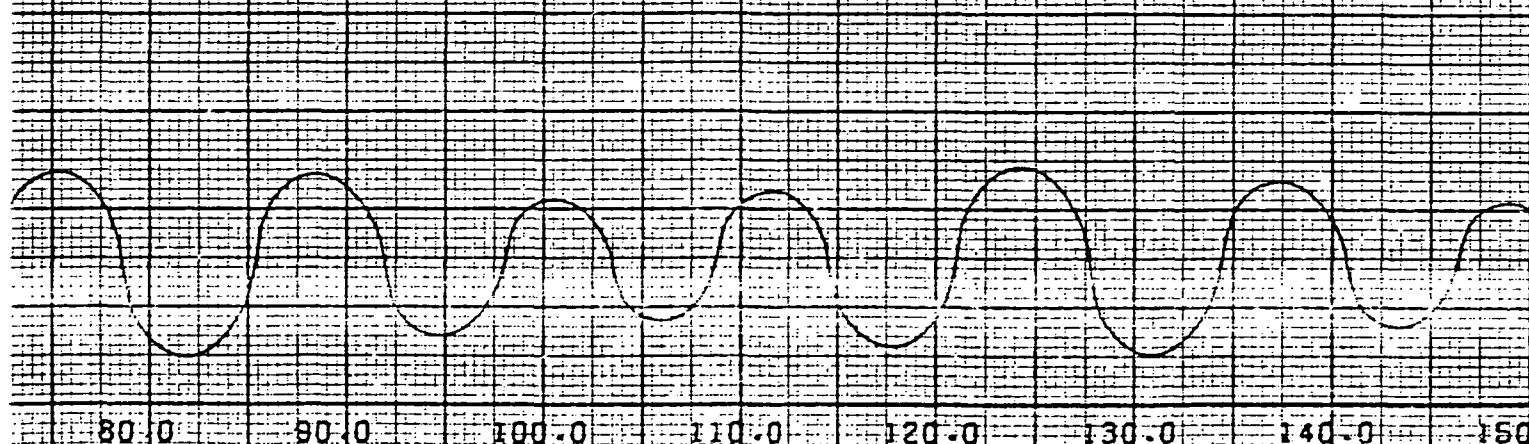
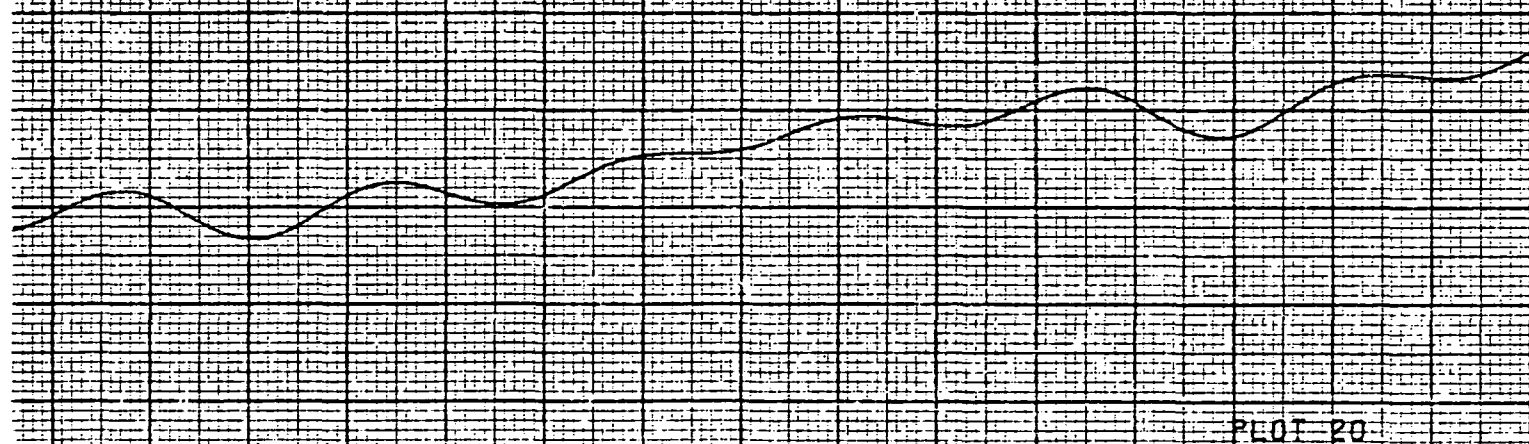
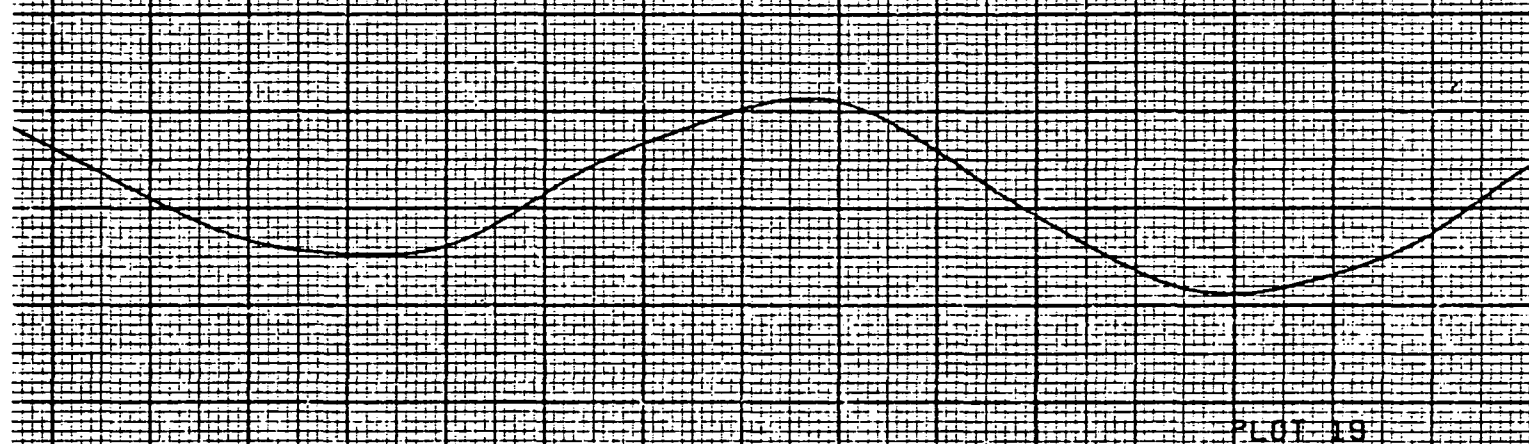
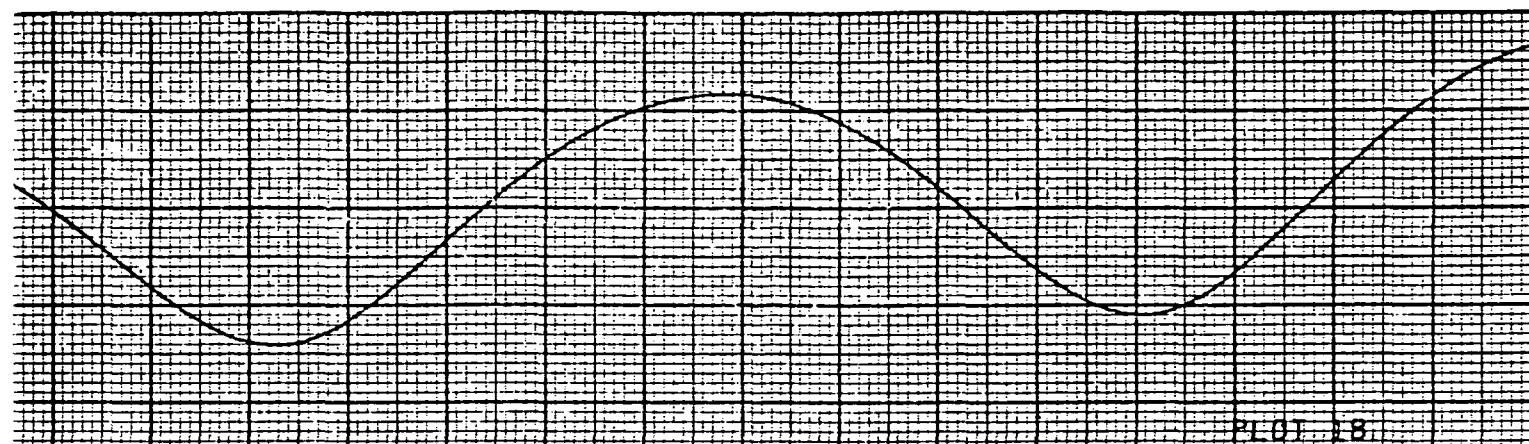
TRW

104<

10/30/73 HEAD-A NC







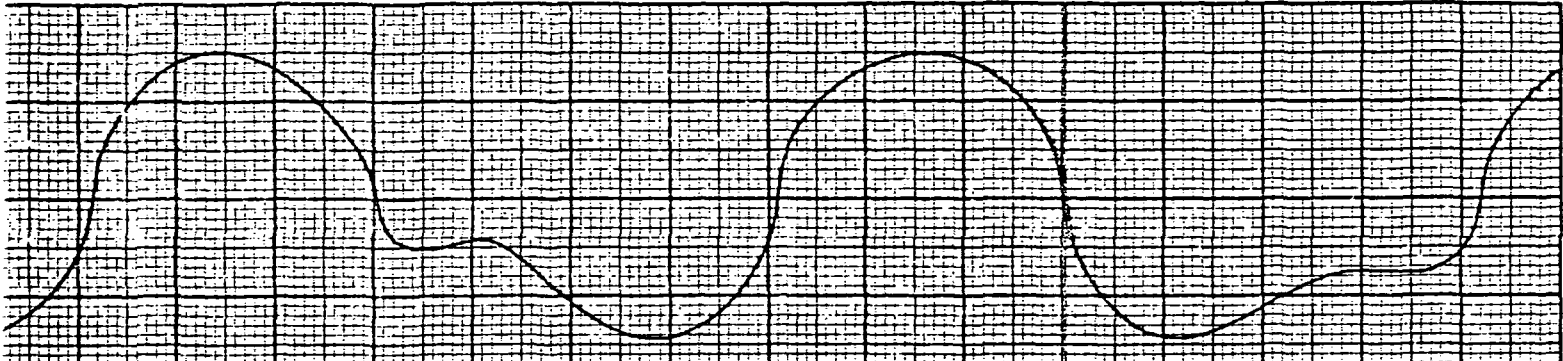
80.0 90.0 100.0 110.0 120.0 130.0 140.0 150.0

reached 12 ft-lb-sec due to the secular component of the gravity gradient torques in the xy plane. Note that the roll and pitch momenta functions appear as a growing sinusoid, whereas the corresponding error and rate functions are not sinusoidal. This behavior is characteristic of a control system where the wheels are torqued according to the square of the error signal, as was the case for this study.

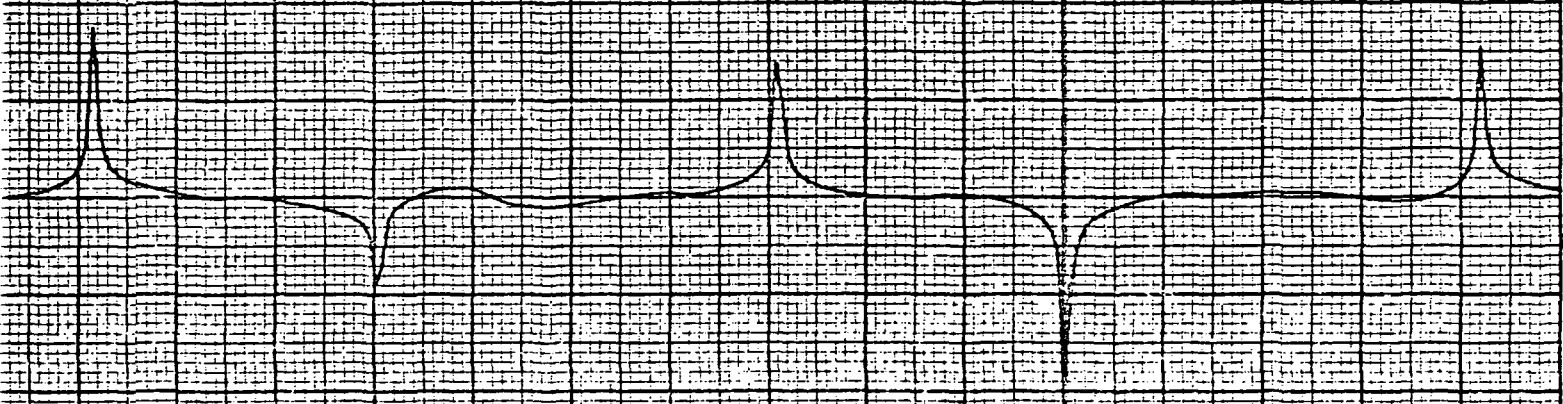
Figures 4-40 through 4-43 illustrate unloading performance with the magnetic controller. In addition to the conditions defined previously, the time of day for this run was chosen so that the Greenwich meridian was 50 deg from the Vernal Equinox to provide the least favorable initial orientation of the earth's magnetic field. The momentum stored in the x and y axes is bounded to about 2 ft-lb-sec through magnetic controller action. The magnetic moments required to perform this degree of unloading are less than 200 amp-turn-m<sup>2</sup> in each axis. The second time history from the top in Figure 4-43 shows that there are occasions during the orbit when the earth's field becomes closely aligned with the momentum error and the magnets cannot unload the wheels. This occurs when the angle between the field and momentum error approaches 180 deg. However, these periods are seen to be short (5 minutes or less) and their overall effect on unloading control performance is small.

The unloading run illustrated does not include the effects of electro-magnet inductance or electromagnet/magnetometer coupling. The low frequency nature of normal mode operation eliminates the first effect from consideration, as the coil time constant is on the order of one second or less. To assess the latter effect, a run which included a coupling effect was made. The results were essentially the same as the run without coupling. This would be expected due to the lower magnetic moments used during unloading. The effect of scan rate was also studied by a run with the scan rate increased to 0.1 rpm. System performance was not significantly changed.

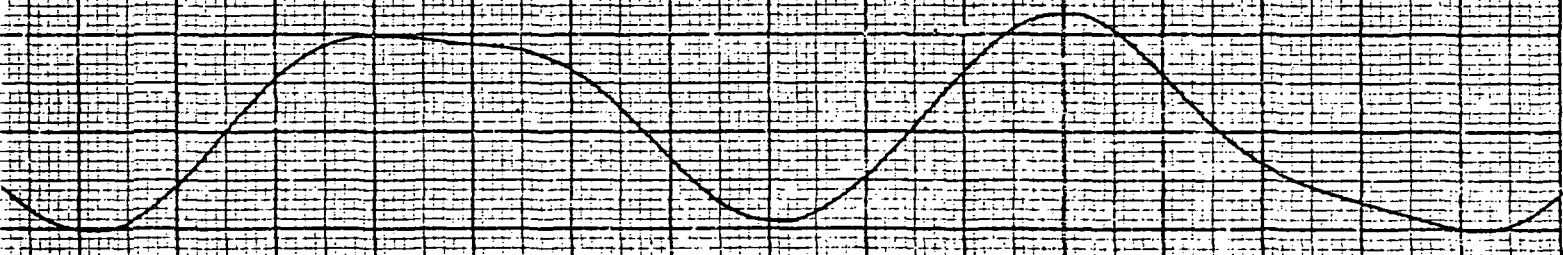
To summarize, the performance of the magnetic/wheel control combination during celestial scan operation was found to be satisfactory, and no significant problem areas were discovered. Wheel momentum could be maintained below 2-3 ft-lb-sec through use of a maximum magnetic moment of 200 amp-turn-m<sup>2</sup>. The roll and pitch attitude errors were also monitored



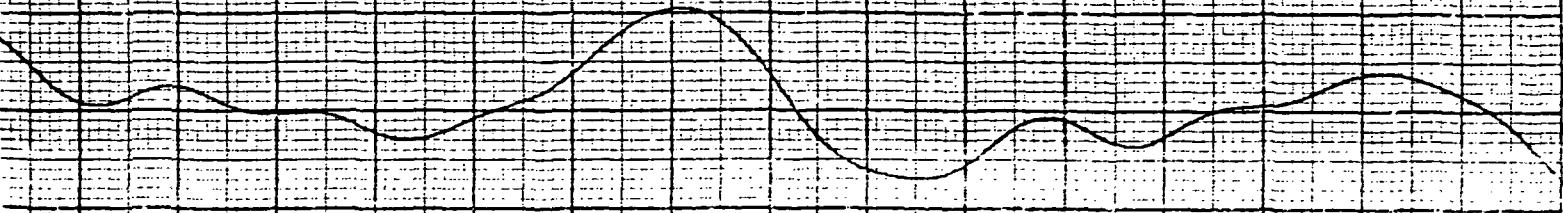
PLOT 5



PLOT 6



PLOT 8



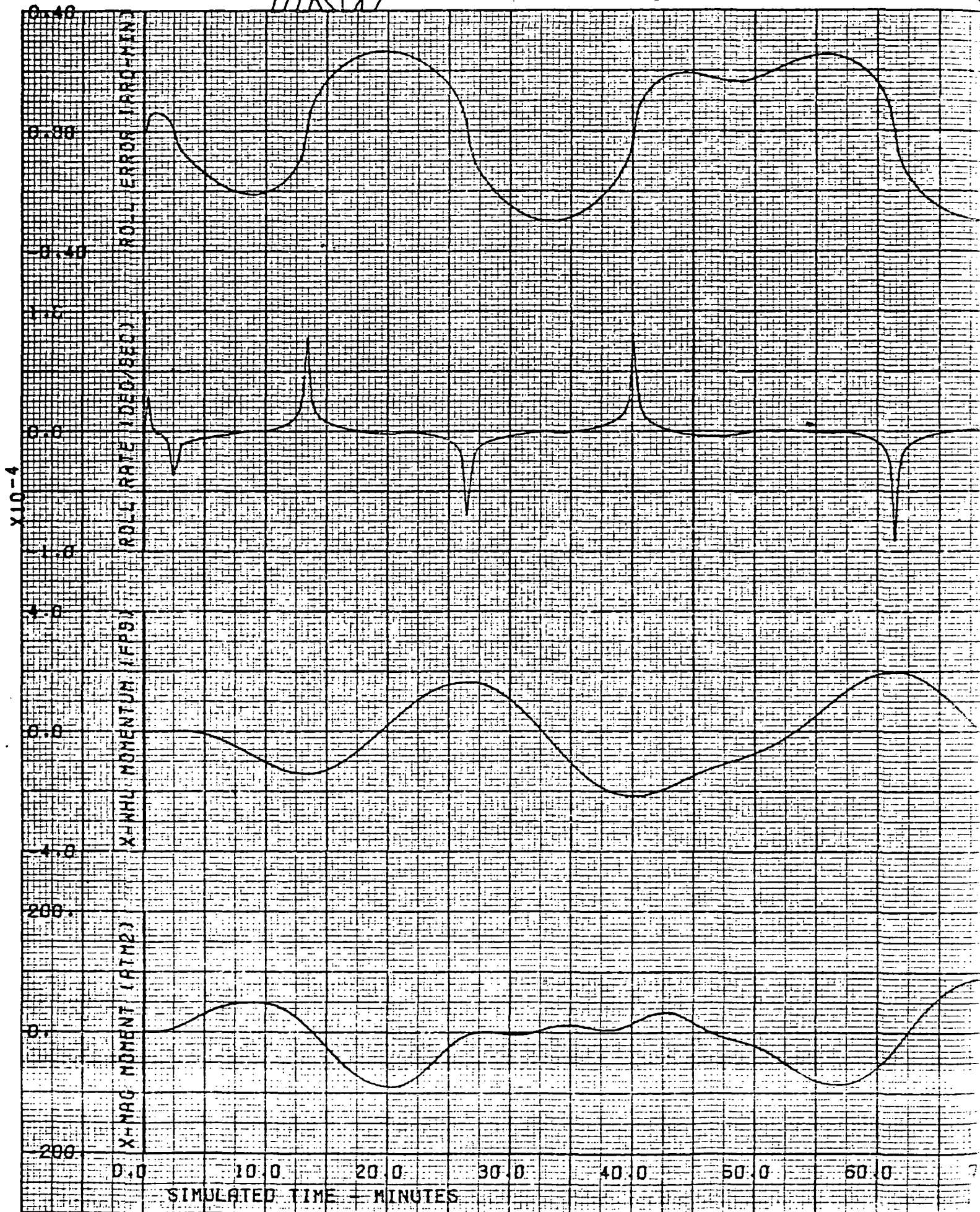


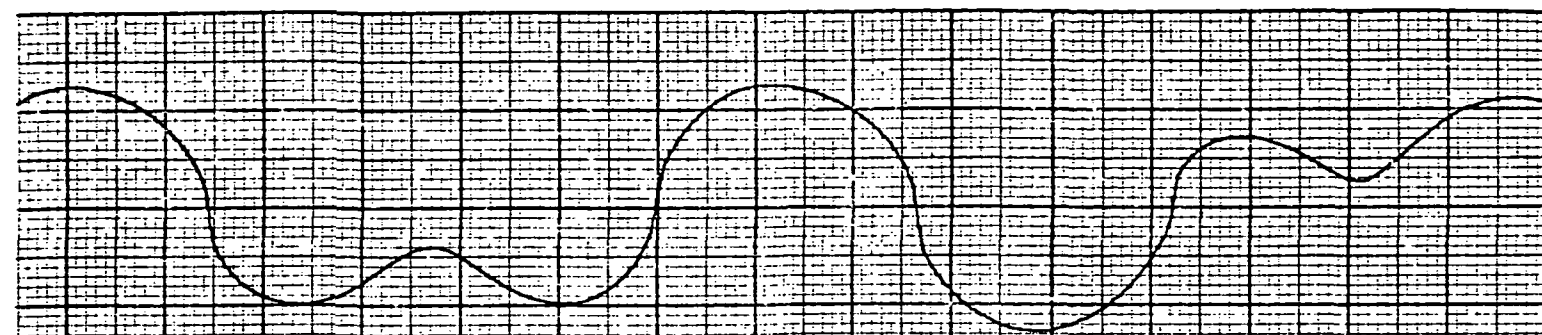
Figure 40. HEAO-A Normal



AL MODE WITH UNLOADING

109<

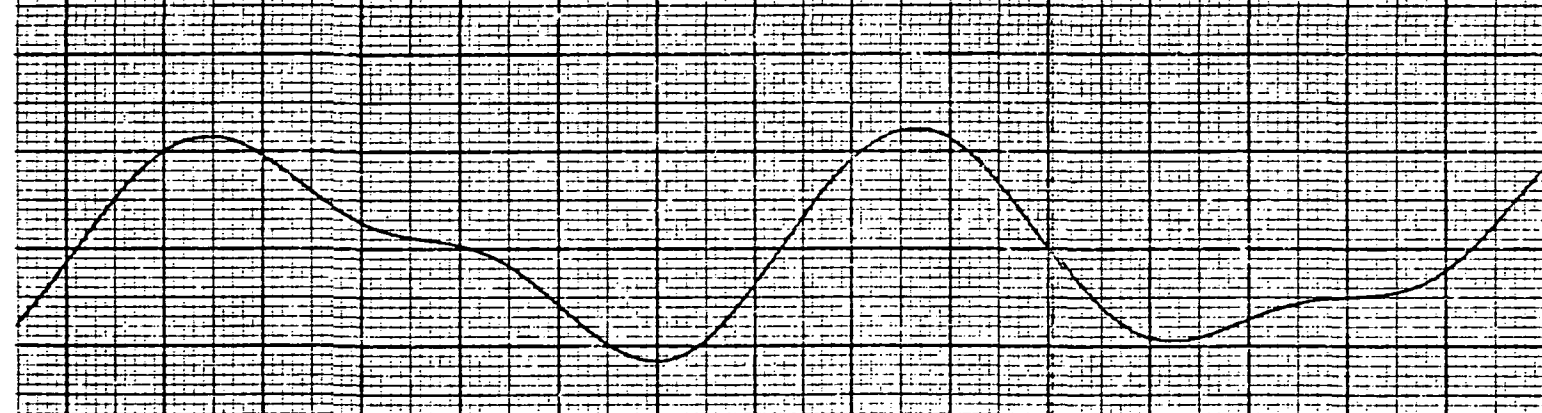
PLOT 9



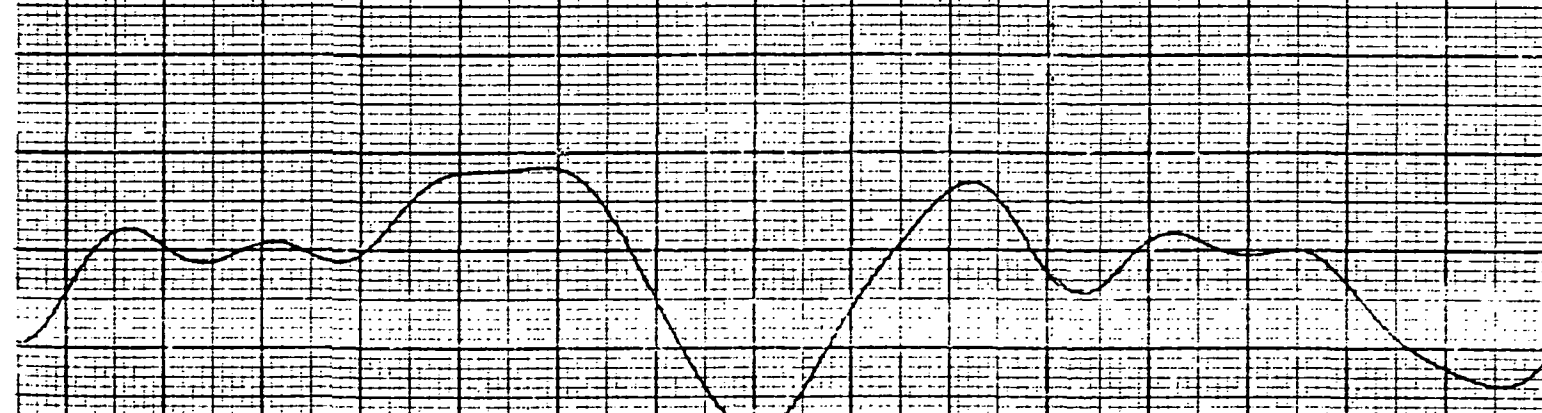
PLOT 10



PLOT 11



PLOT 12

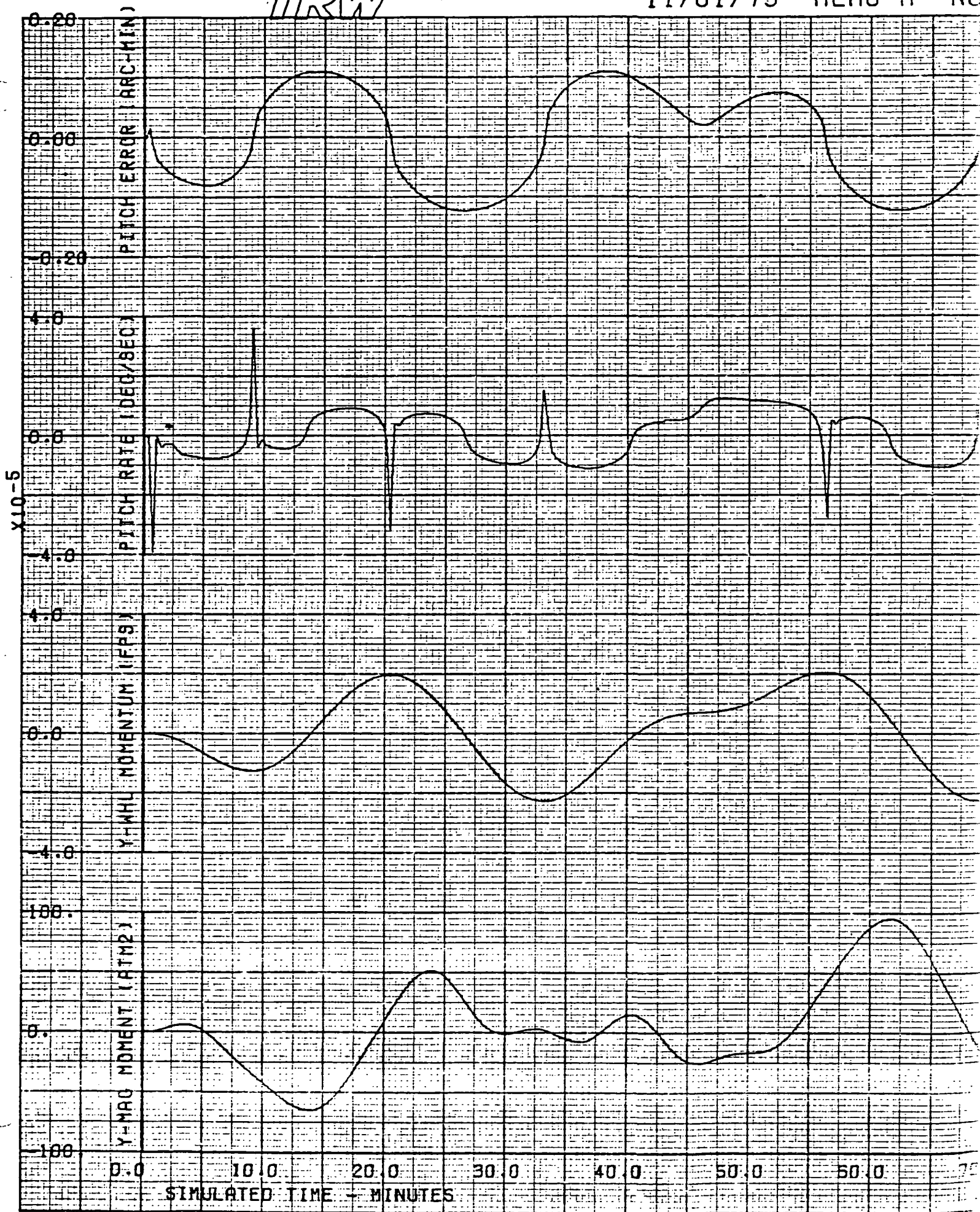


80.0 90.0 100.0 110.0 120.0 130.0 140.0 150.0

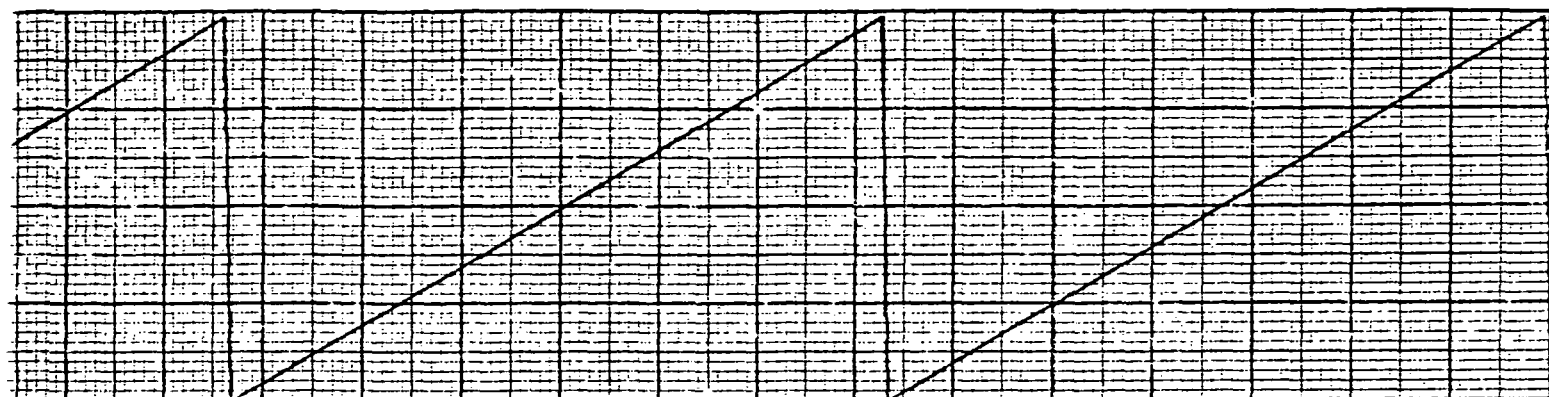
TRW

110<

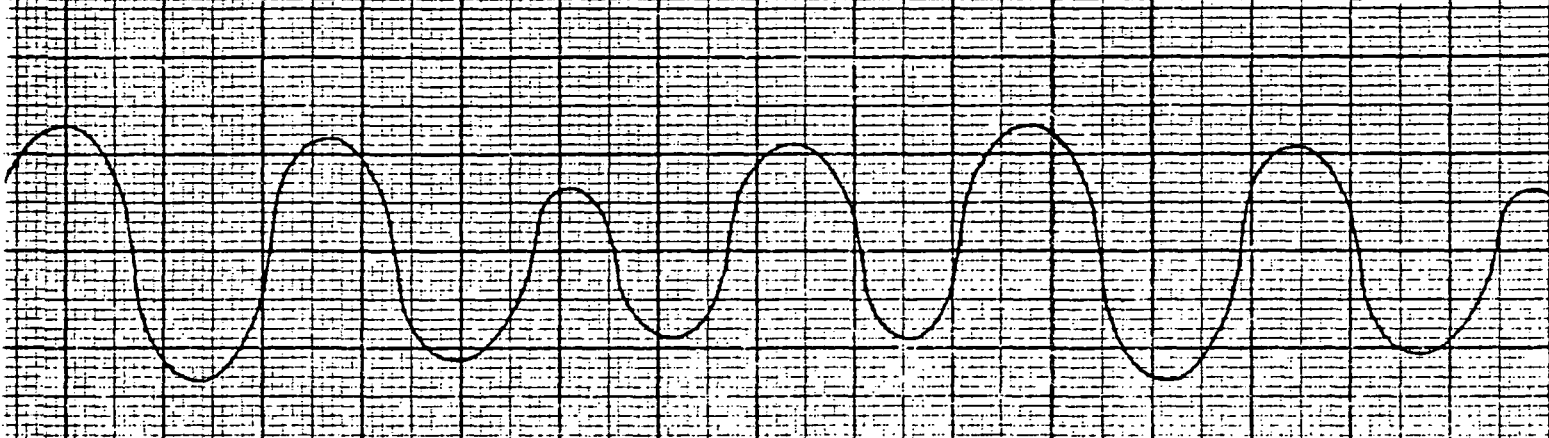
11/01/73 HEAD-A NO



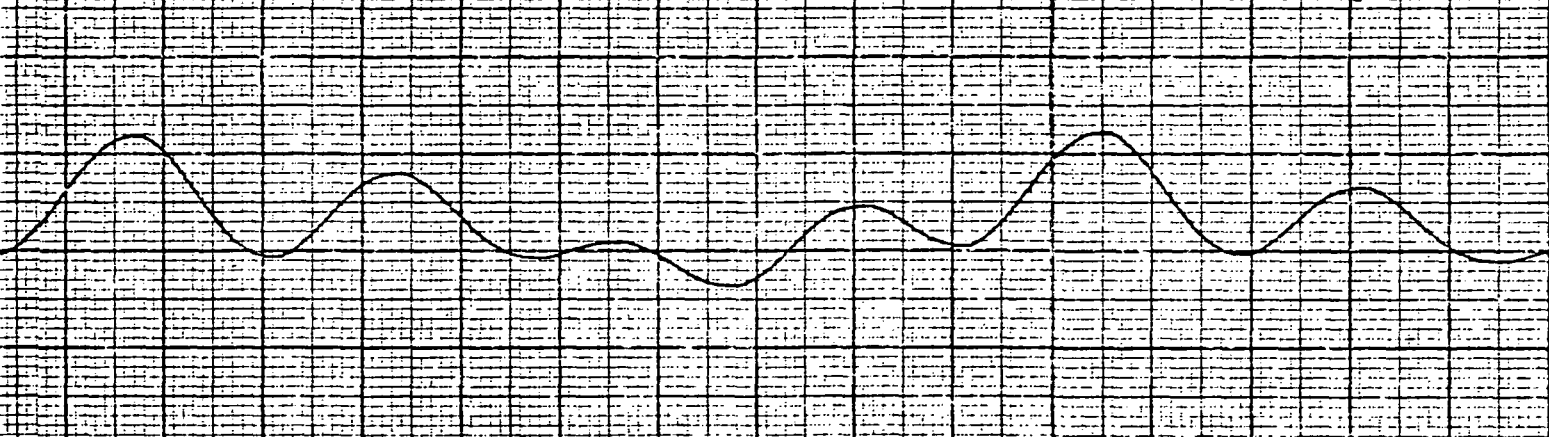




PLOT 14



PLOT 15



PLOT 16



80.0 90.0 100.0 110.0 120.0 130.0 140.0 150.0

TRW

112<

11/01/73 HEAO-A NO

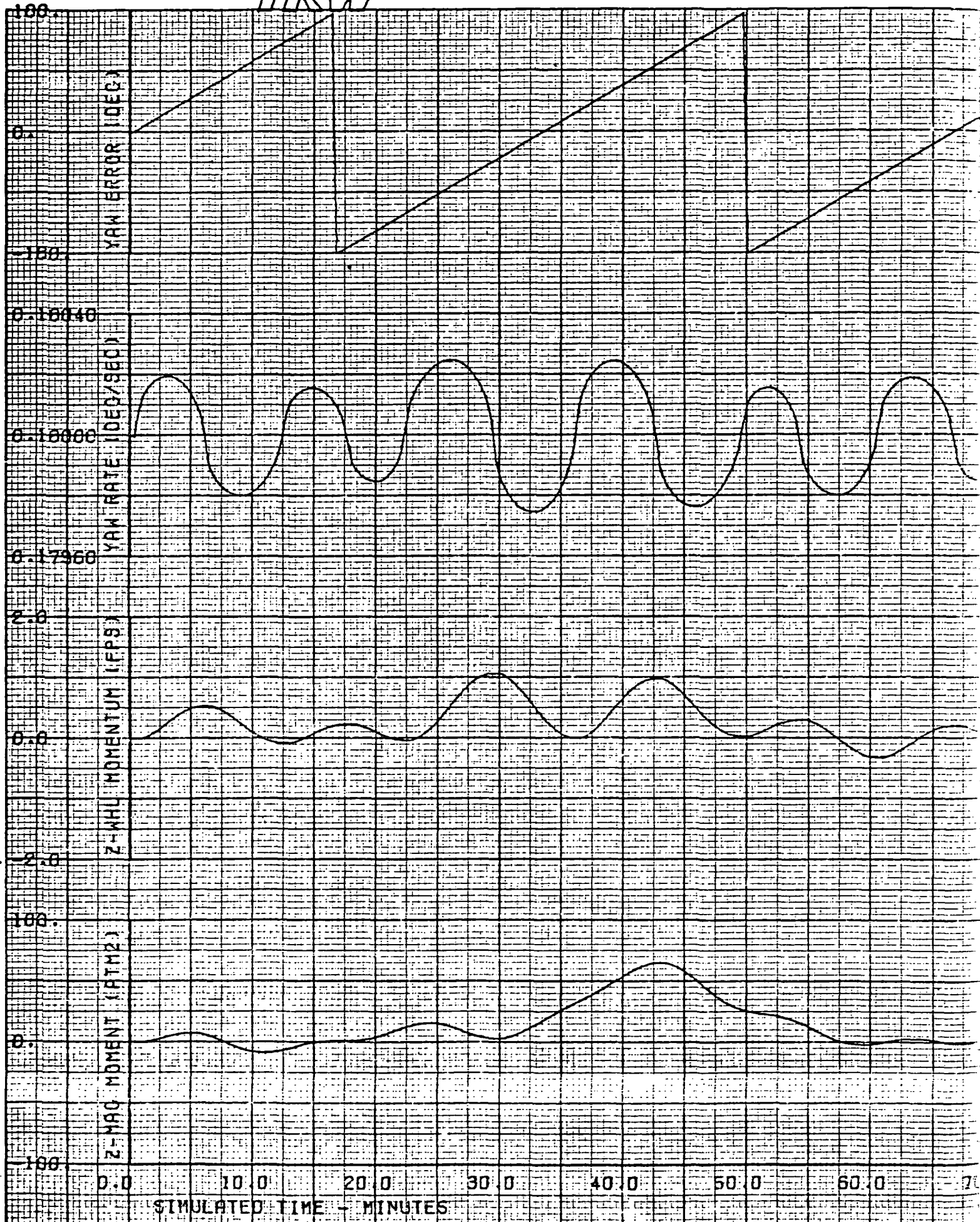
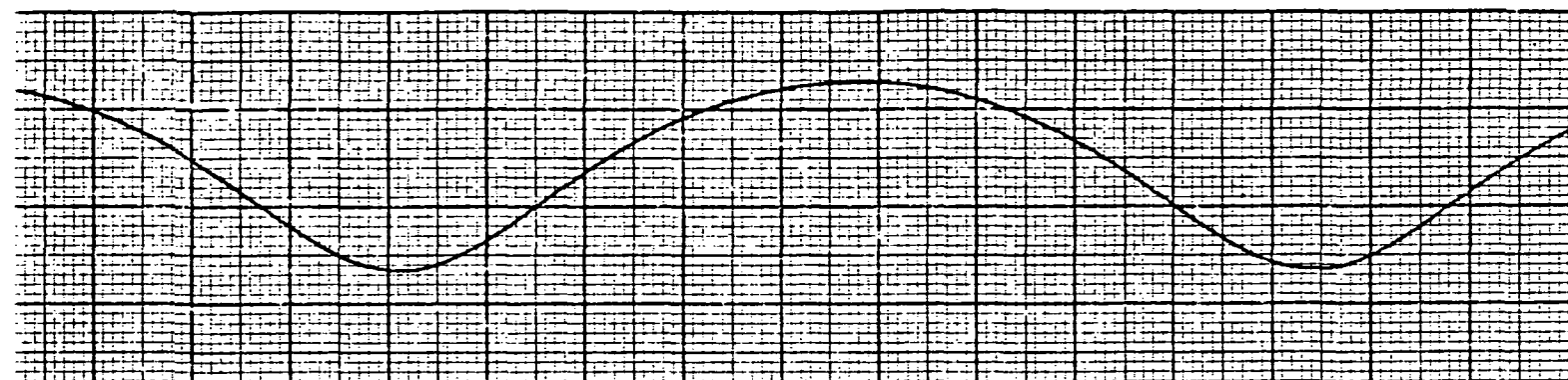
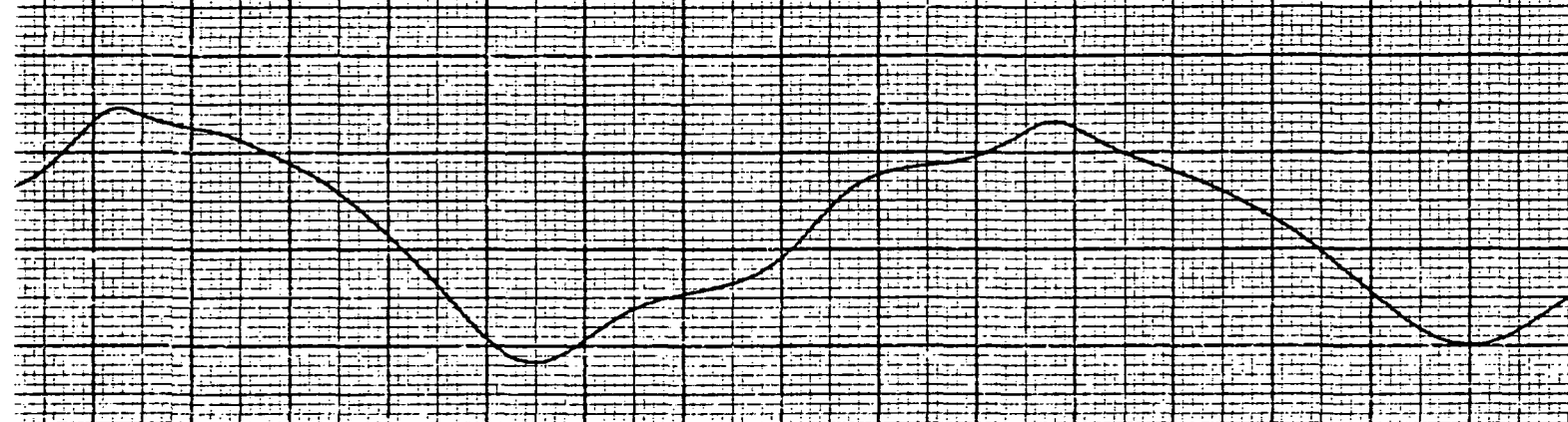


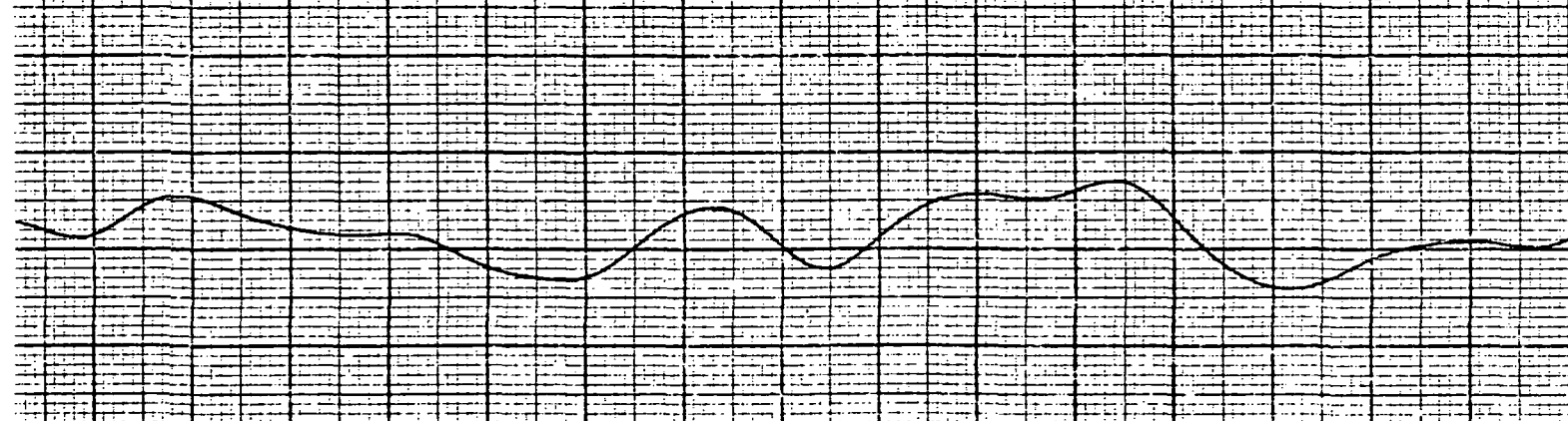
Figure 42 HEAO-A Normal Mo



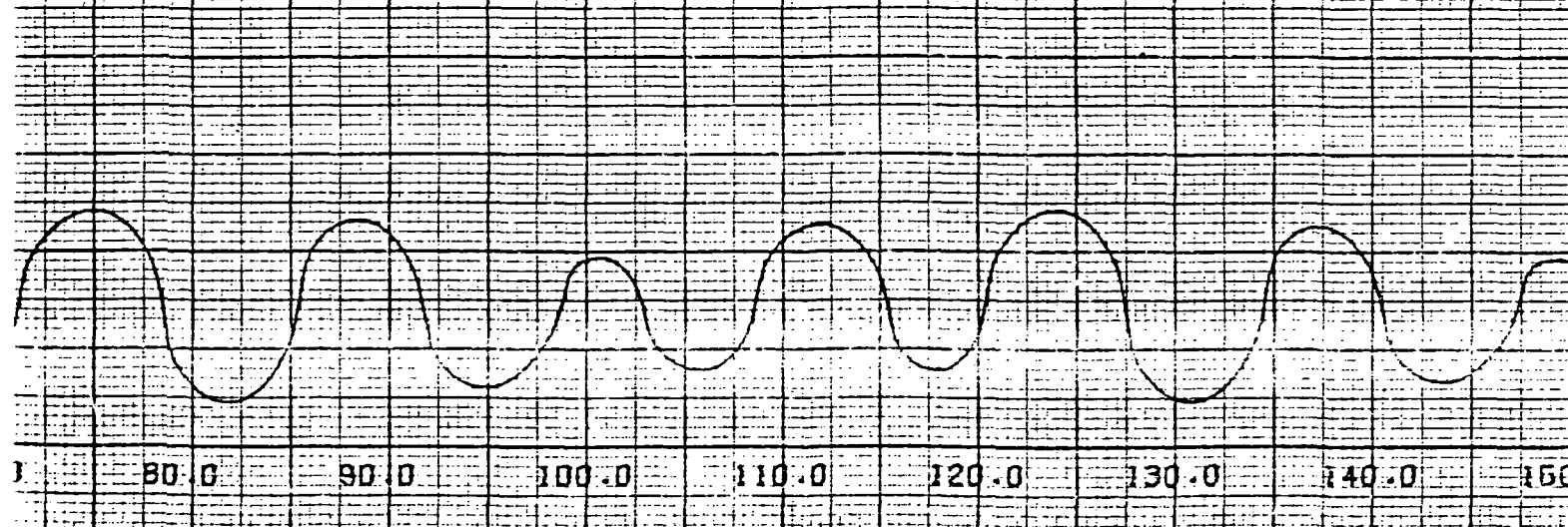
PLOT 18



PLOT 19



PLOT 20



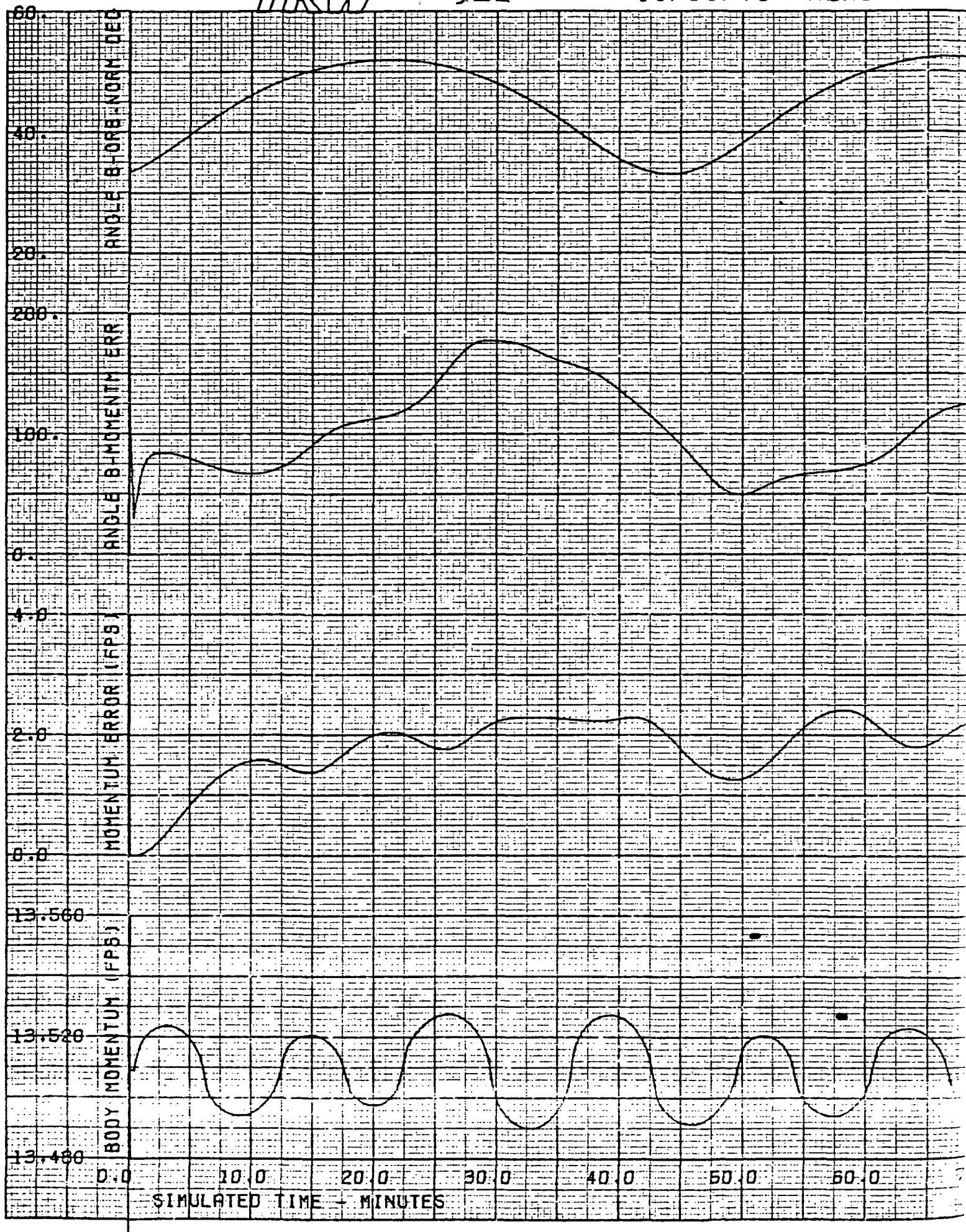


Figure 43. HEAO-A Normal Mode



at less than half an arc minute, satisfying the performance requirements for attitude control.

#### 4.3.2.2 Performance During Celestial Pointing

The HEAO-B observatory operates in a celestial pointing mode in which the inertial attitude is held fixed. As with the celestial scan cases, the conditions for these runs were selected to maximize the secular disturbance torque due to gravity gradient and thereby provide a worst case condition for study. The study conditions were:

Altitude	180 n. mi.
Inclination	22.75 deg
Right Ascension	0 deg
Z-axis argument	0 deg (from Vernal Equinox)
X-axis declination (above orbit plane)	45.0 deg

Figures 4-44 through 4-47 show simulated celestial point performance without magnetic control. The wheel momentum buildup due to secular disturbances is clearly shown. The yaw wheel saturates (39 ft-lb-sec) after only 105 minutes. Following this, the spacecraft quickly loses yaw control and begins to tumble, due to the continued disturbances.

The effectiveness of the magnetic control is illustrated in Figures 4-48 through 4-51. The electromagnets control the momentum buildup and keep the wheels safely away from the saturation point. The peak stored momenta are 3.5, 5.0 and 7.0 fps for the x, y and z axes, respectively, with a peak RSS value of 7.0 fps. The peak magnetic moment required is 380 amp-turn-m<sup>2</sup>, indicating that HEAO-B requires about twice the maximum magnetic moment of HEAO-A for normal mode control.

The unloading efficiency improves as the earth's field moves toward a favorable orientation (90 deg) with the excess momentum vector. This property is illustrated in Figure 4-51 by the plot of momentum error and the plot of angle between B-field and momentum error.

The unloading characteristics shown in Figures 4-48 to 4-51 include the effects of a spacecraft residual field of 1% of earth's field in all axes and electromagnet/magnetometer coupling of  $8.75 \times 10^{-6}$  gauss/amp-turn-m<sup>2</sup> in each axis. Other simulation runs also indicate there

TRW

116<

11/05/73

HEAO-8

N

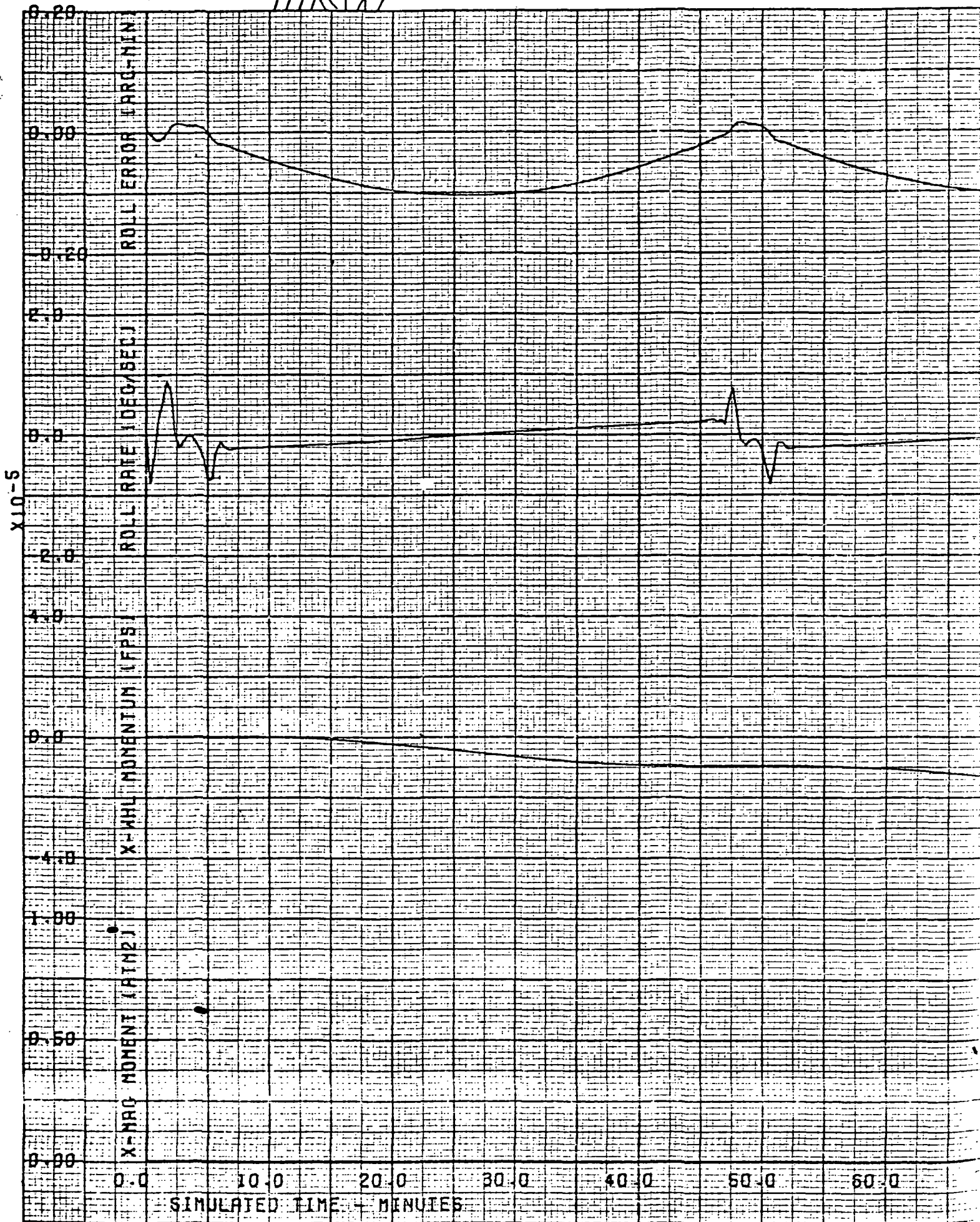
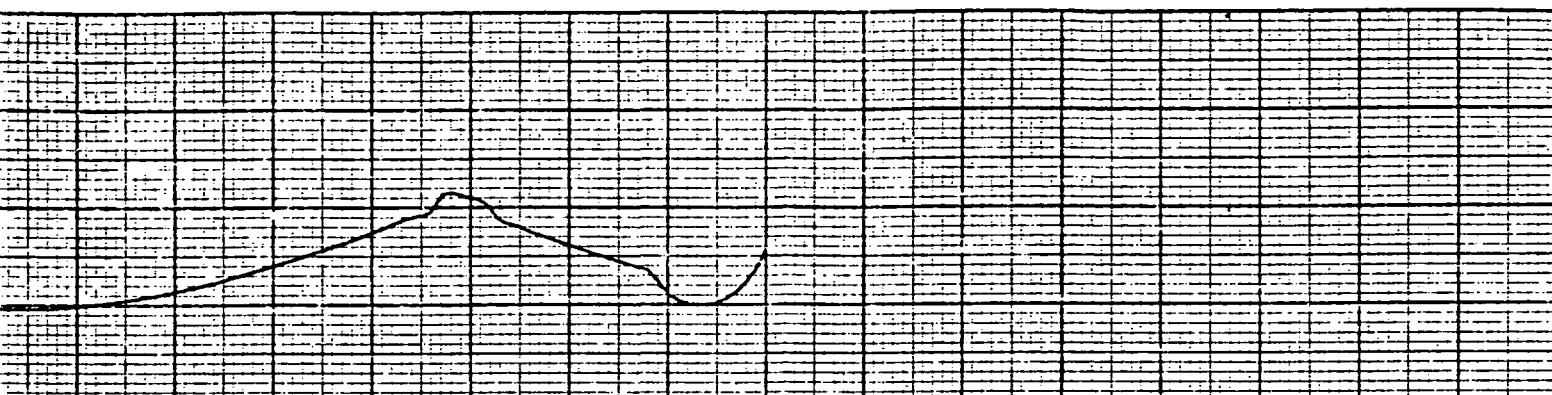
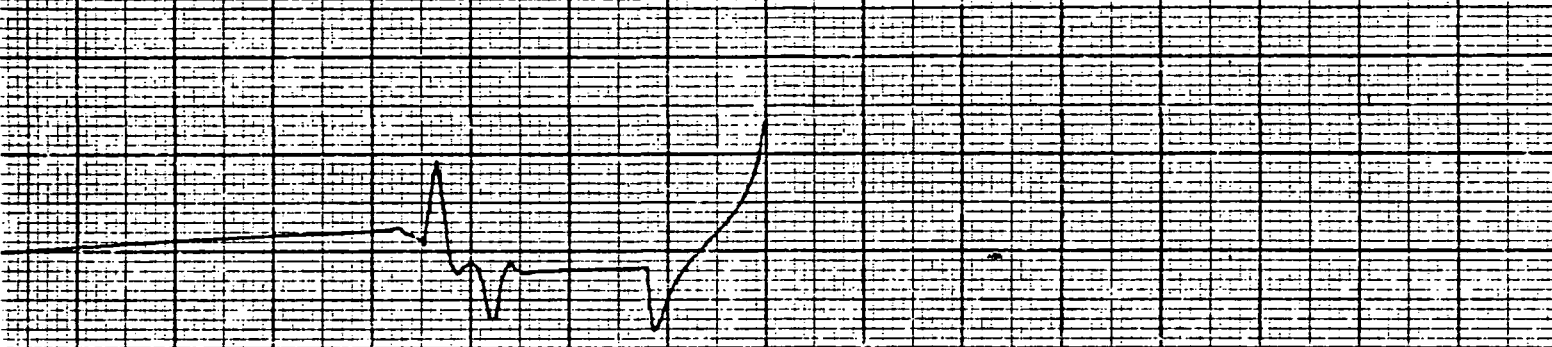


Figure 44. HEAO-8 Normal

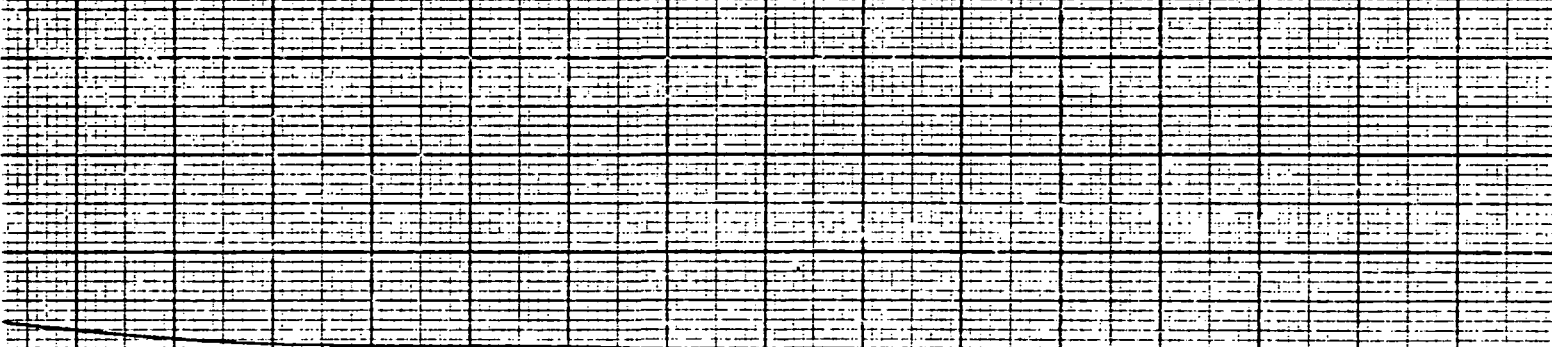




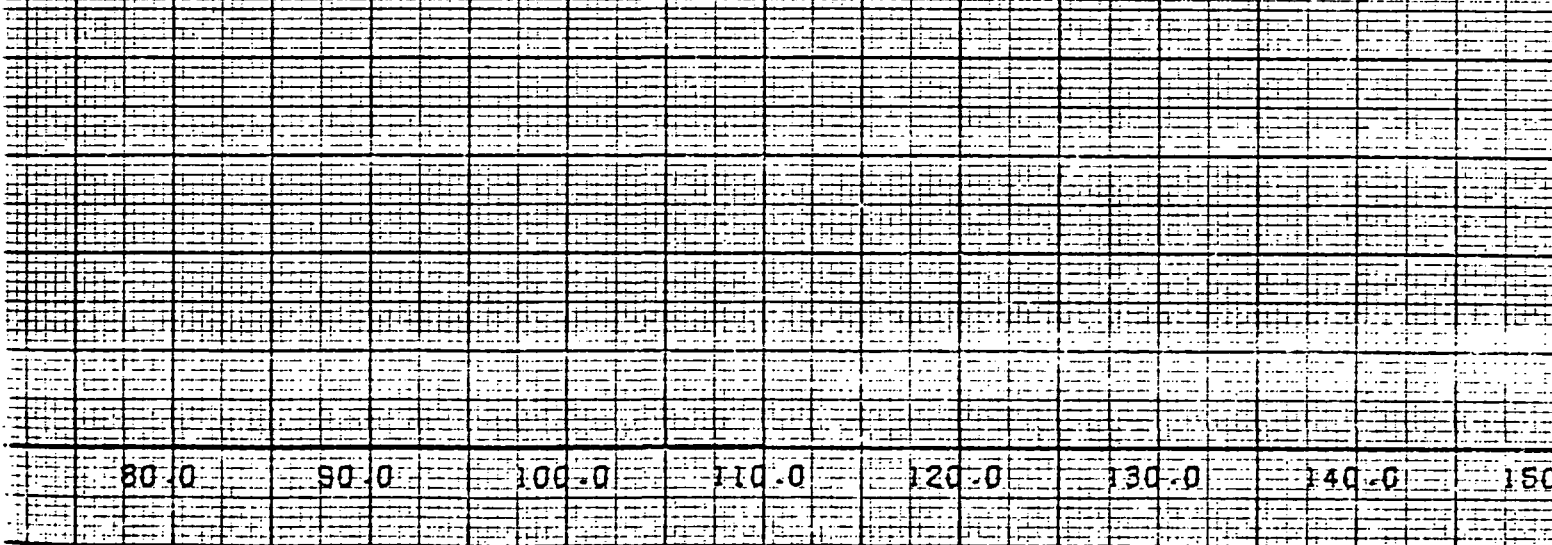
PLOT 6



PLOT 7



PLOT 8

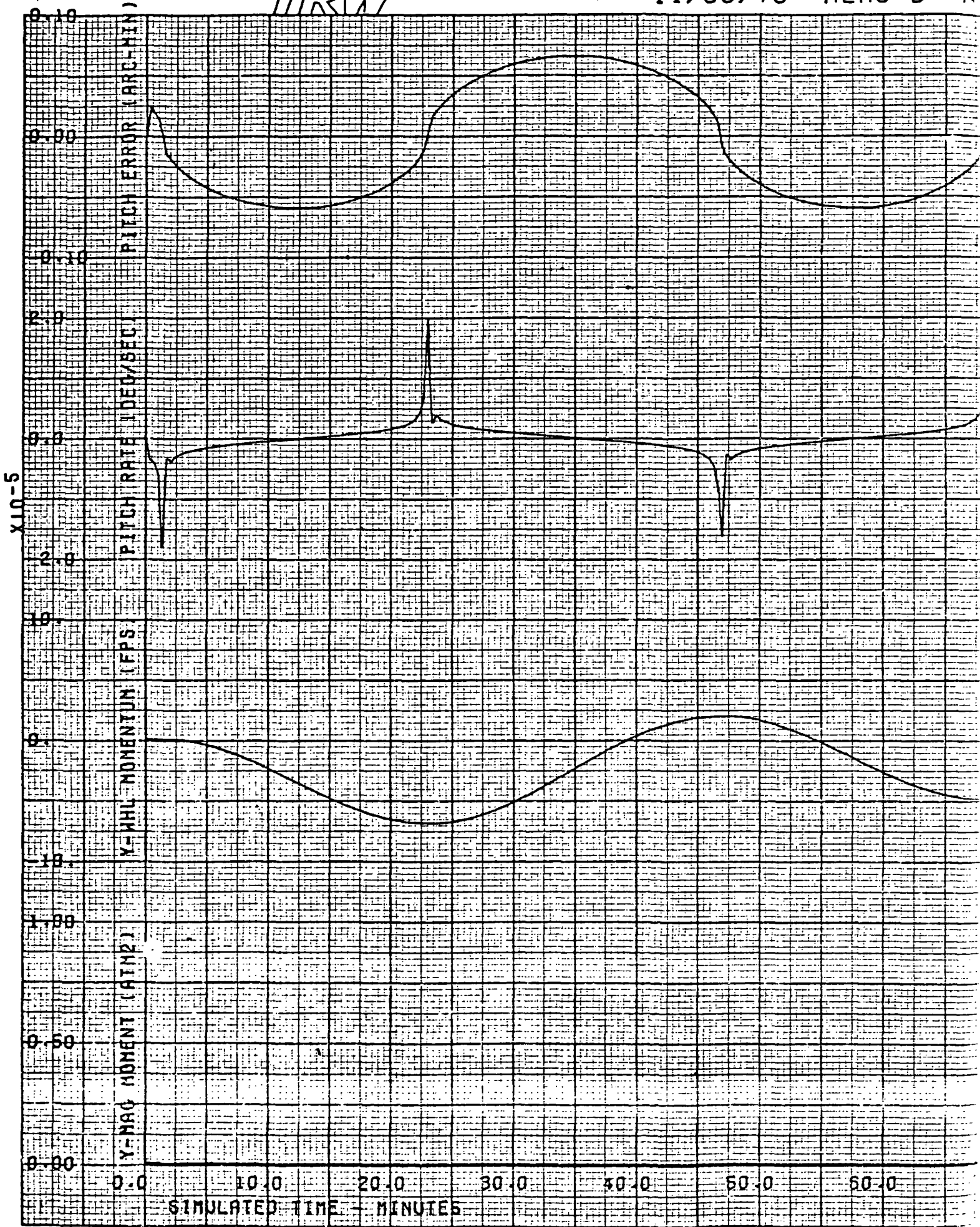


80.0 90.0 100.0 110.0 120.0 130.0 140.0 150.0

TRW

118<

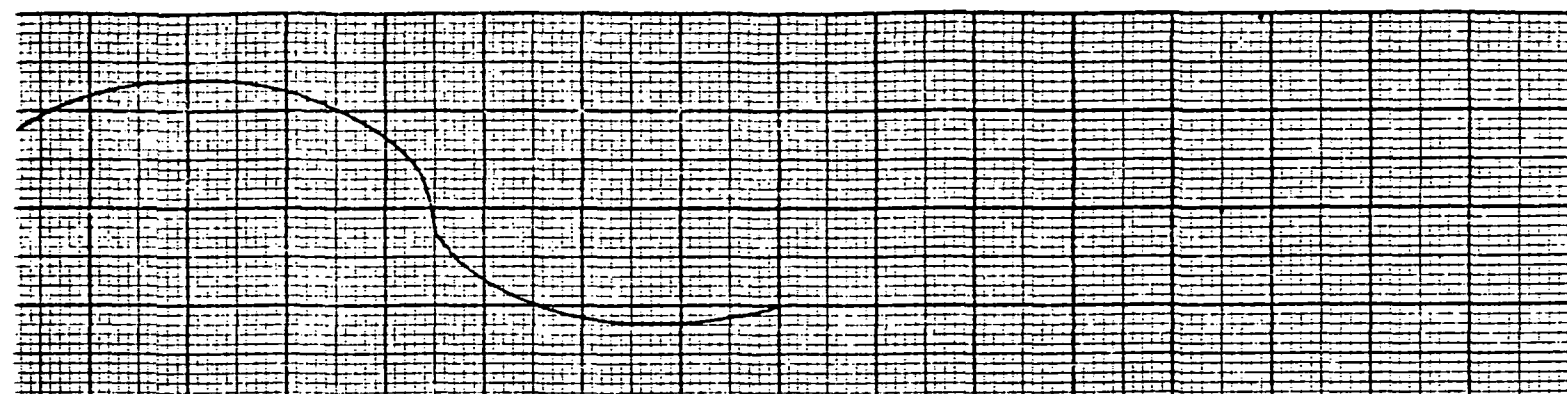
11/05/73 HEAD-B N



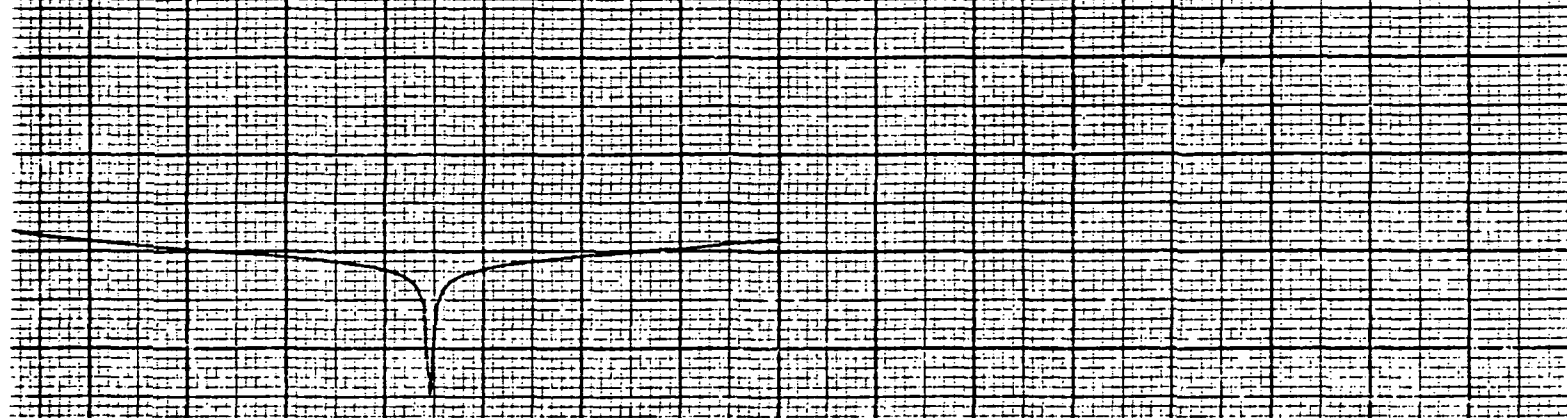
1AL MODE NO UNLOADING

119<

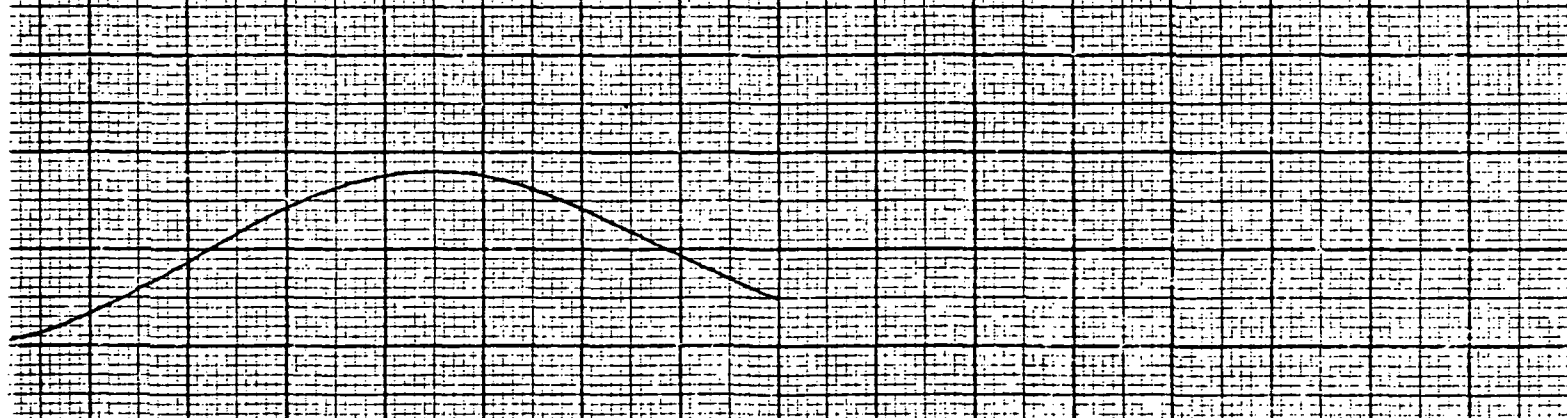
PLOT 9



PLOT 10



PLOT 11



PLOT 12



80.0 90.0 100.0 110.0 120.0 130.0 140.0 150.0

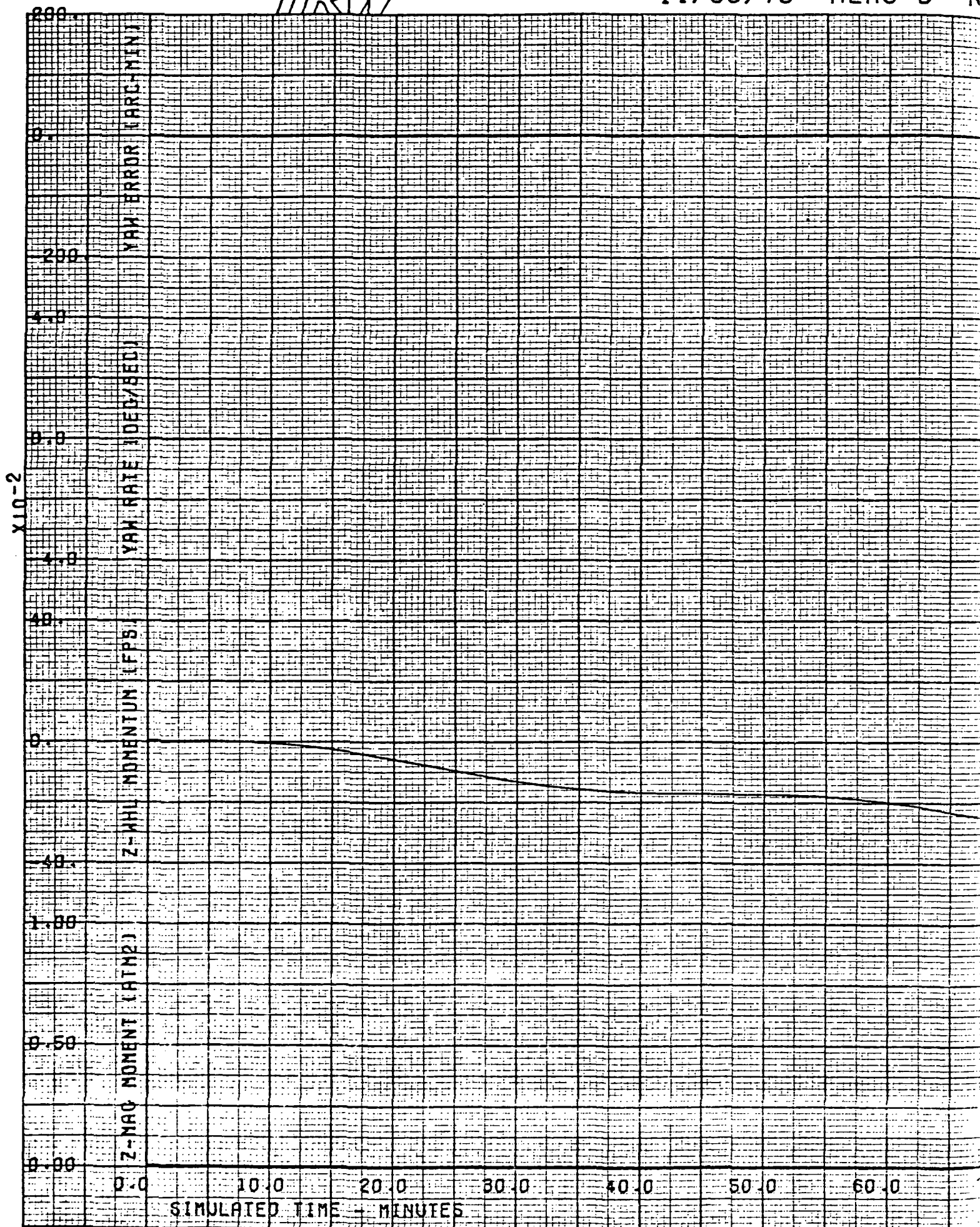
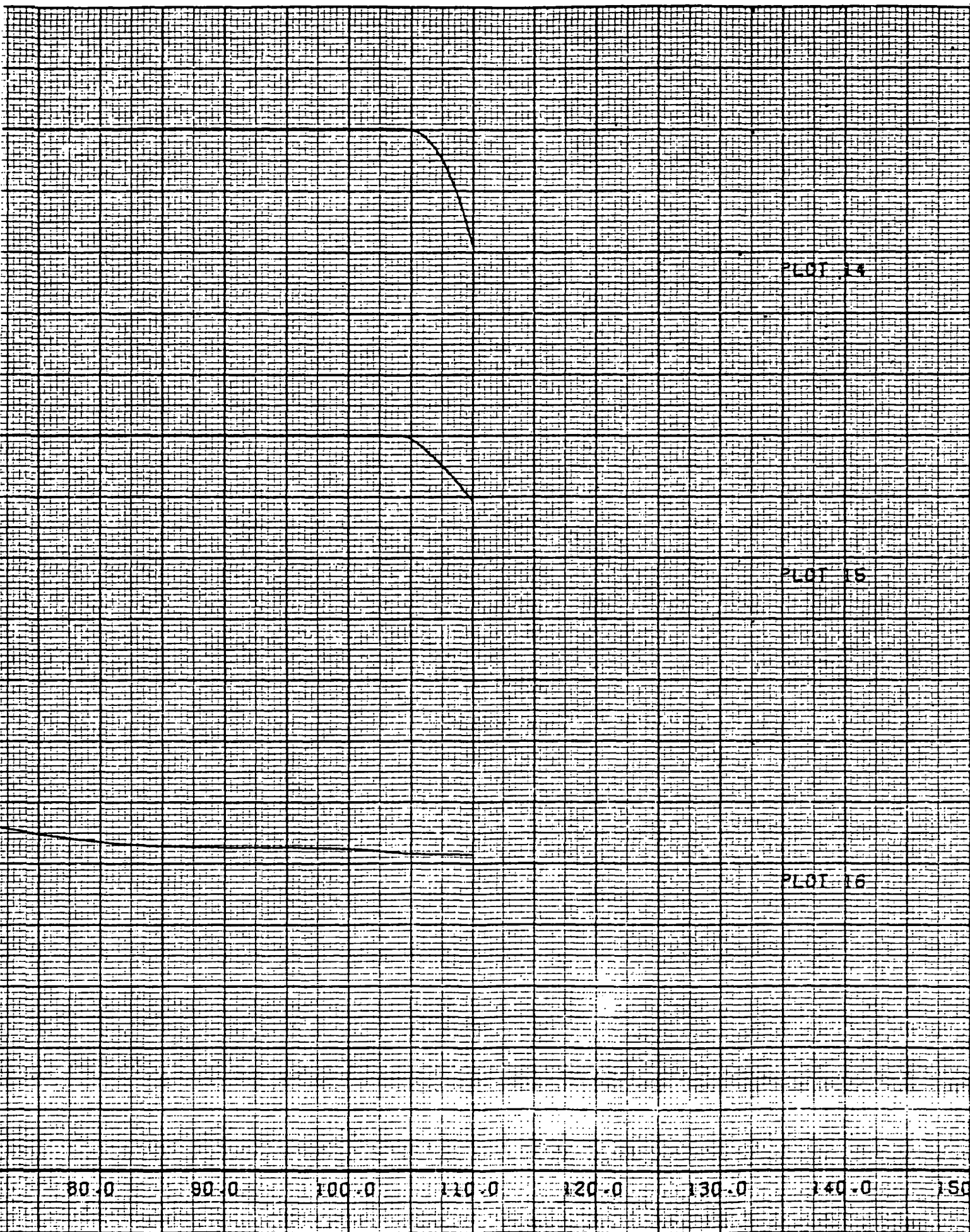


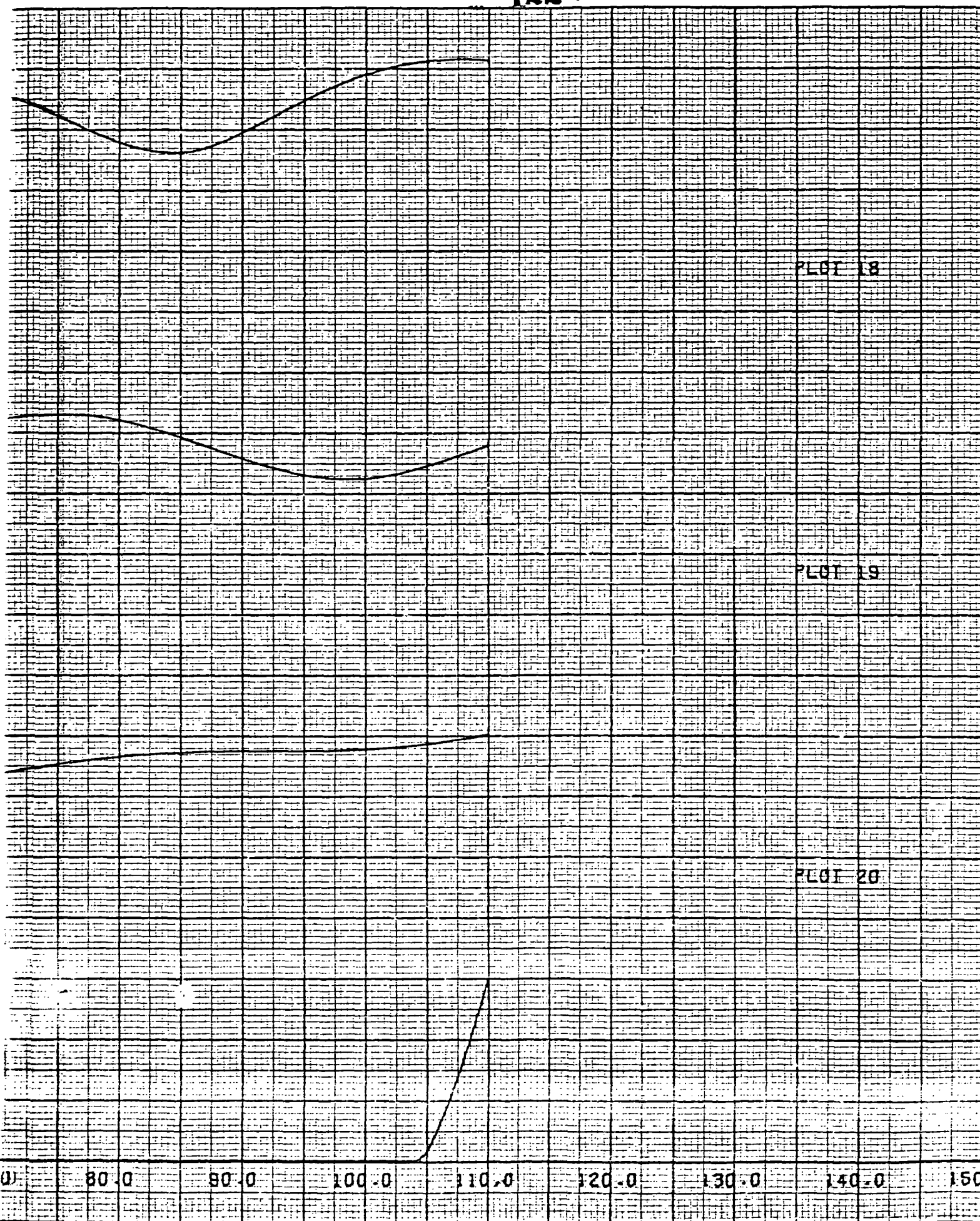
Figure 46. HEAO-B Normal





1AL MODE NO UNLOADING

122<





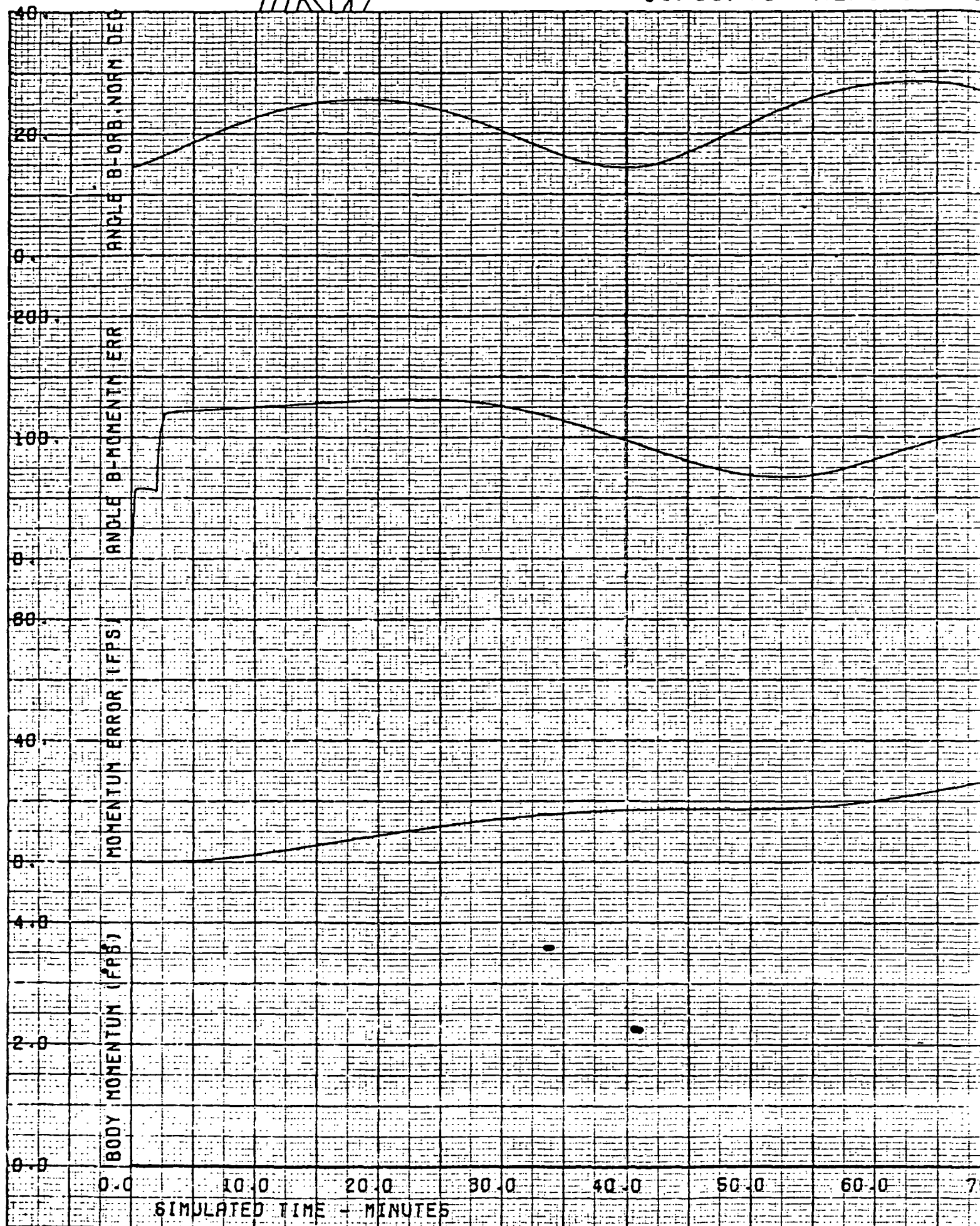


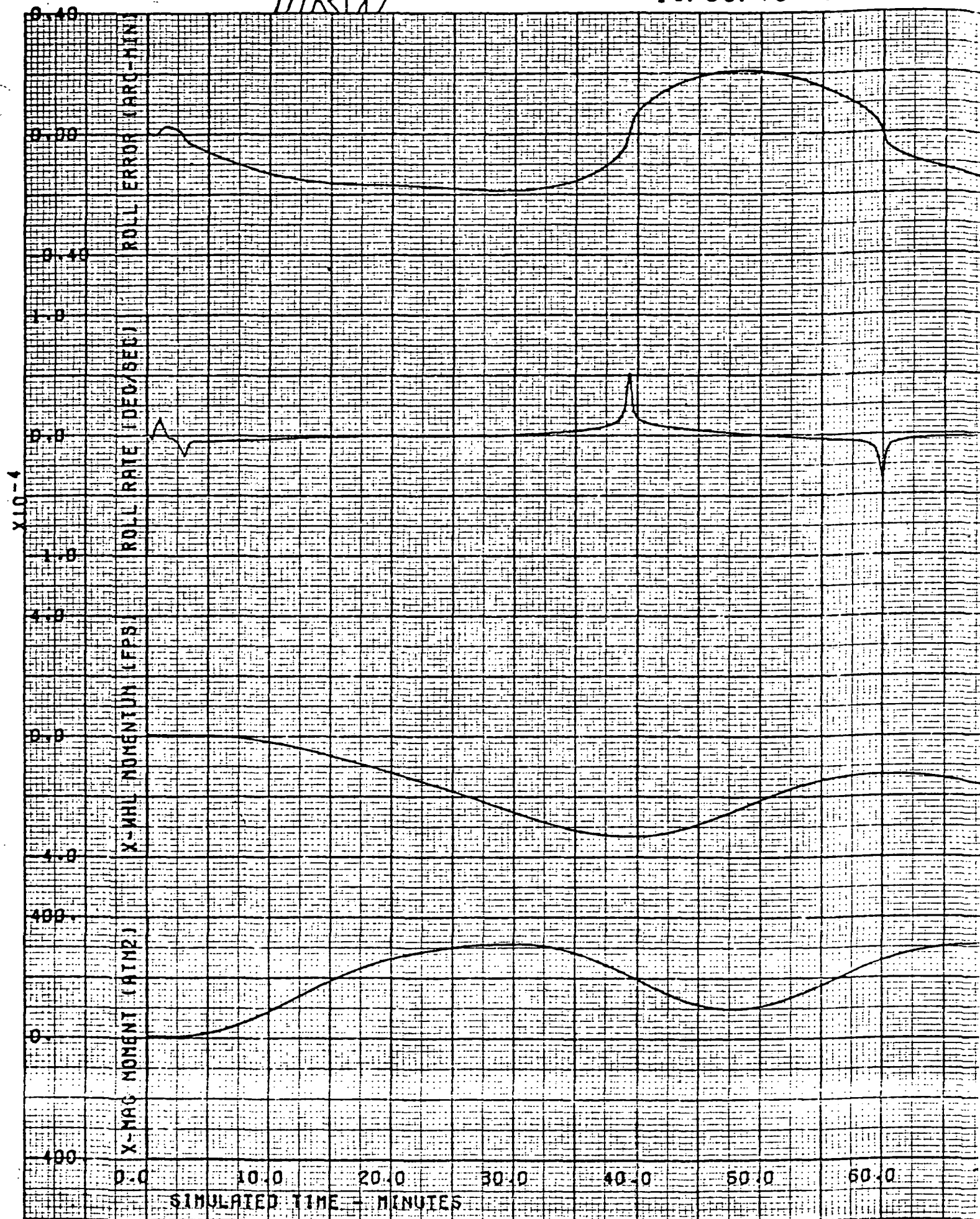
Figure 47. HEAO-B Normal Mode Magnetic

TRW

124&lt;

11/05/73 HEAO-B

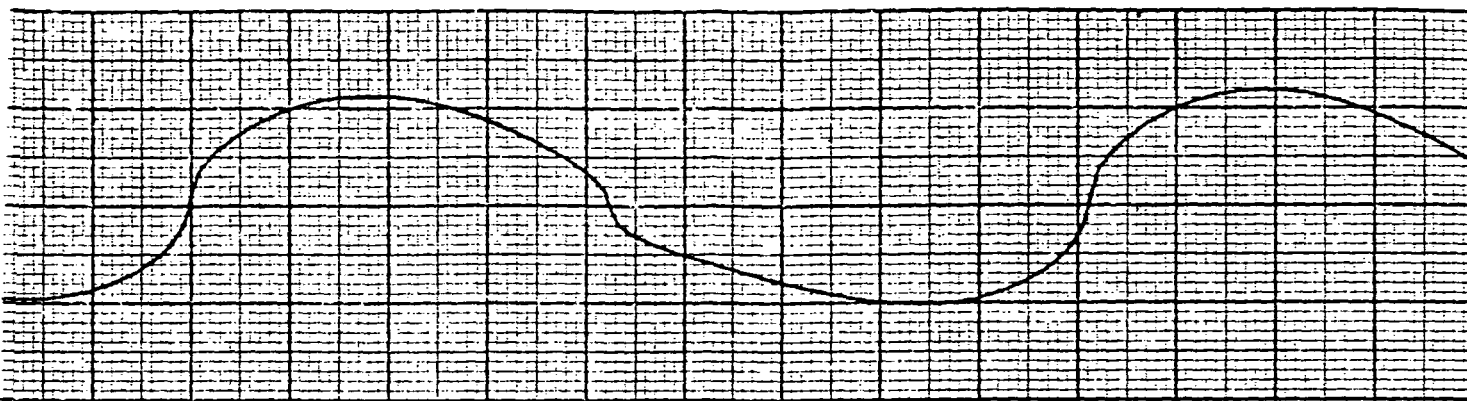
N



MODE 400 ATM WITH RESIDUAL FIELD

125<

PLOT 5



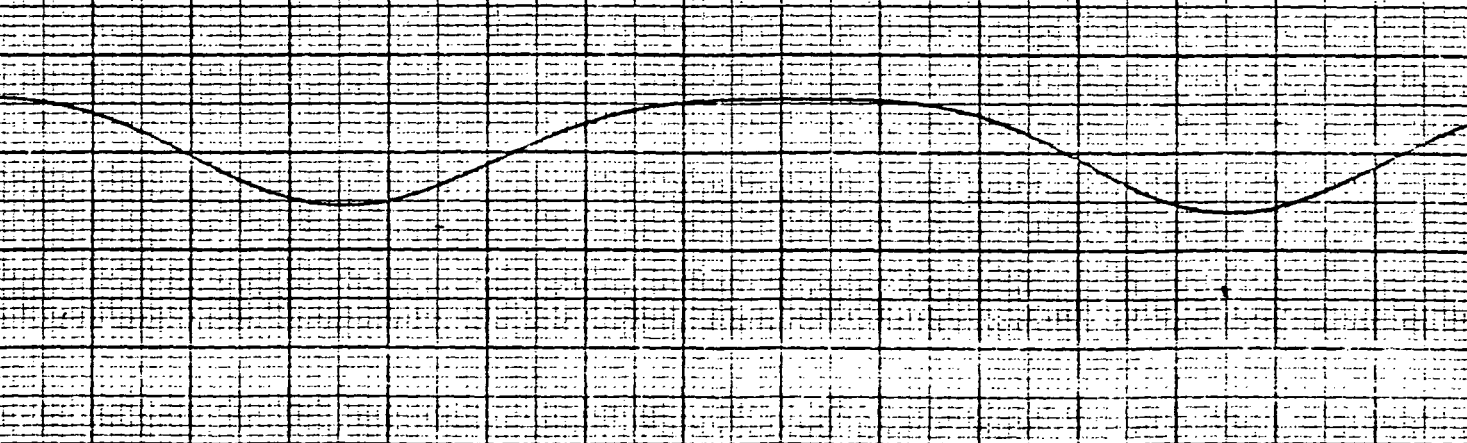
PLOT 6



PLOT 7



PLOT 8



80.0 90.0 100.0 110.0 120.0 130.0 140.0 150.0

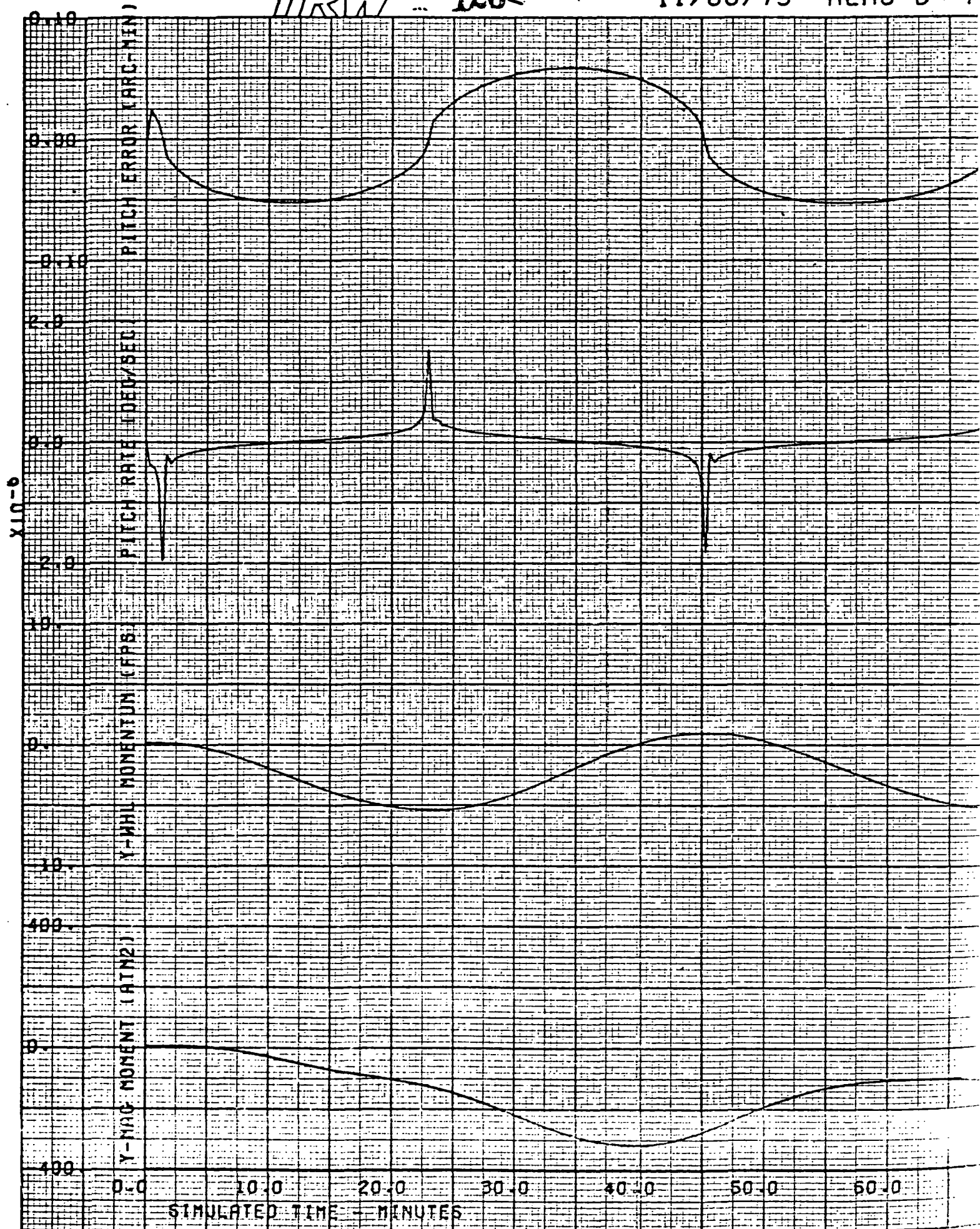
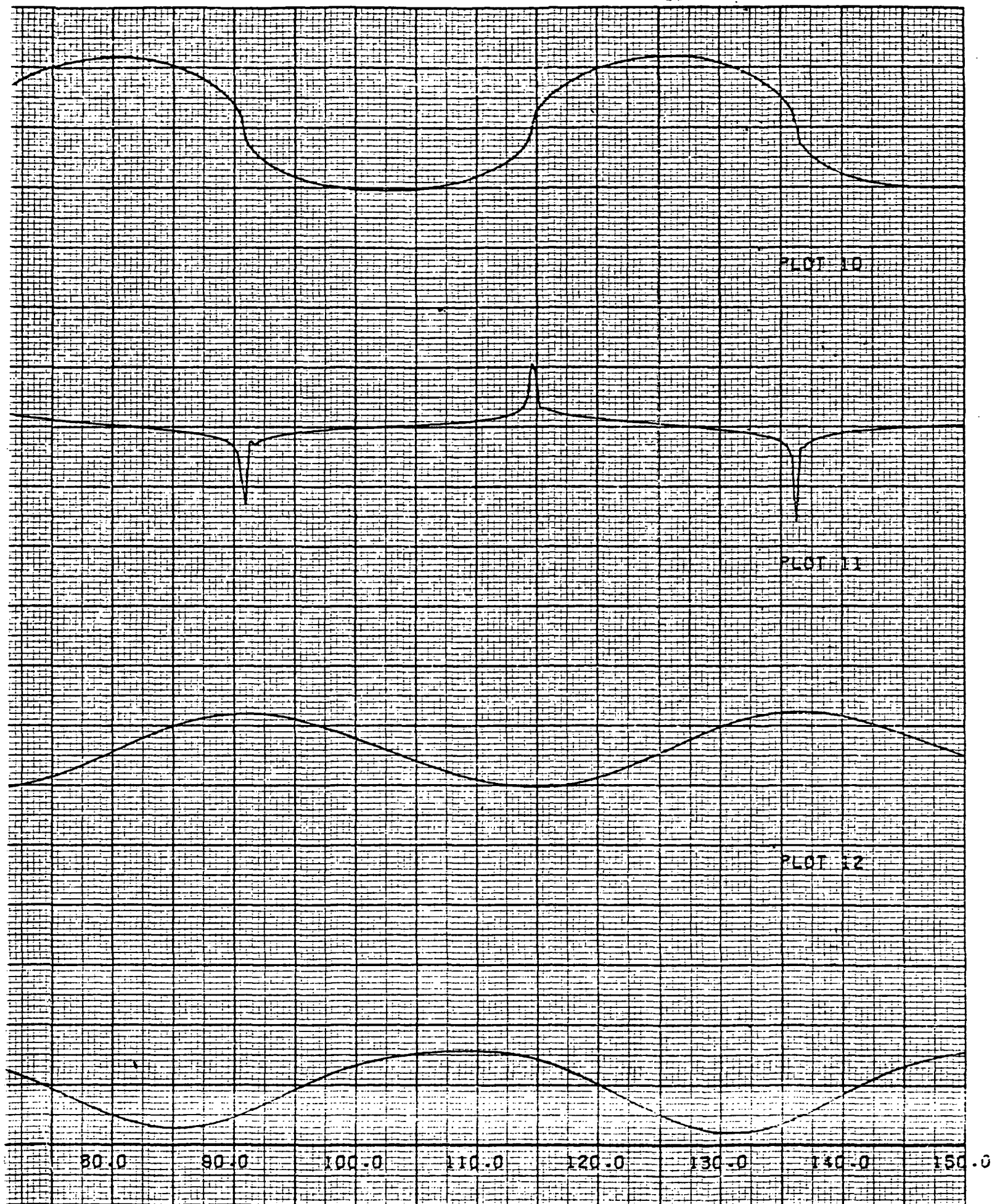


Figure 49. HEAO-B Normal Mode





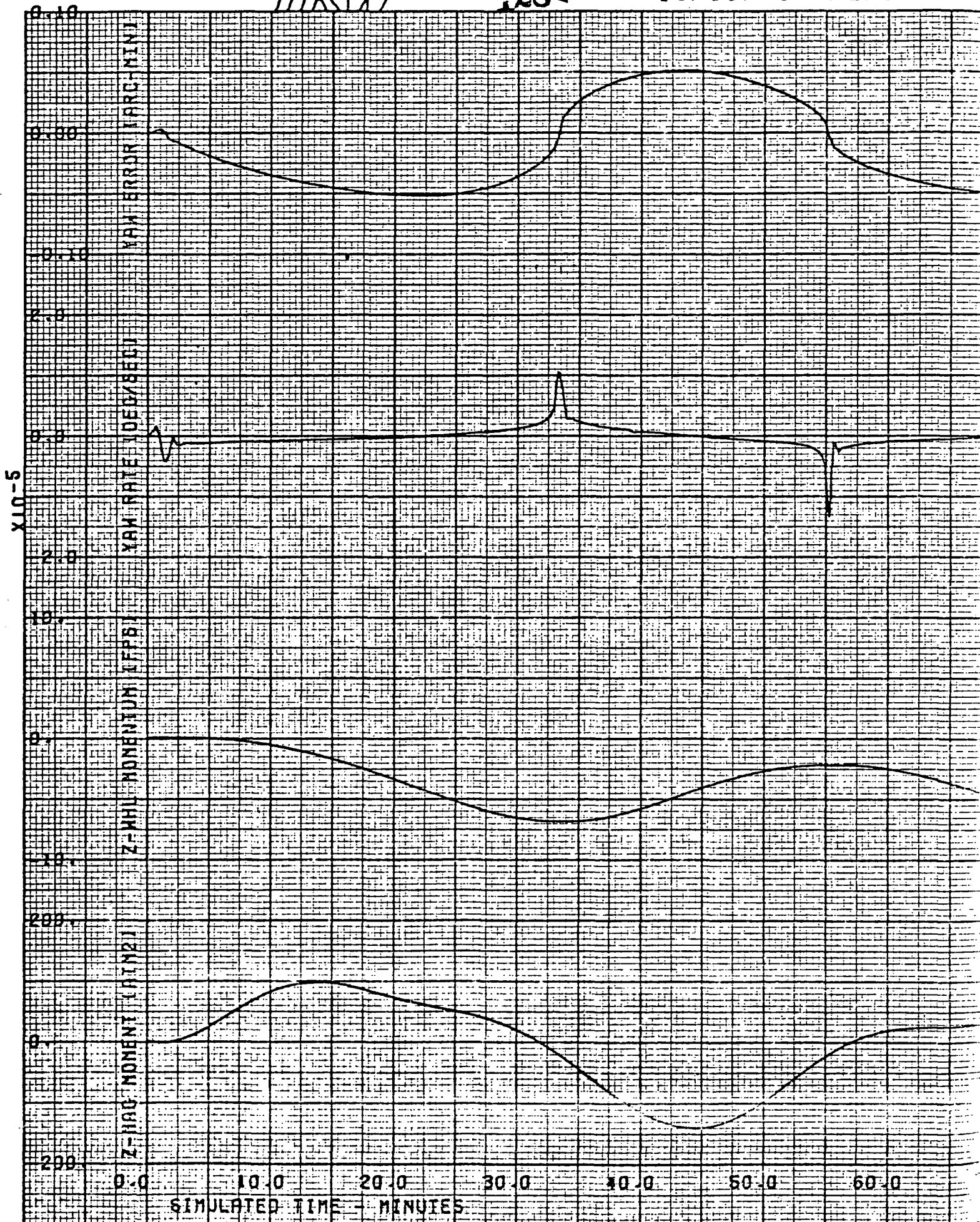
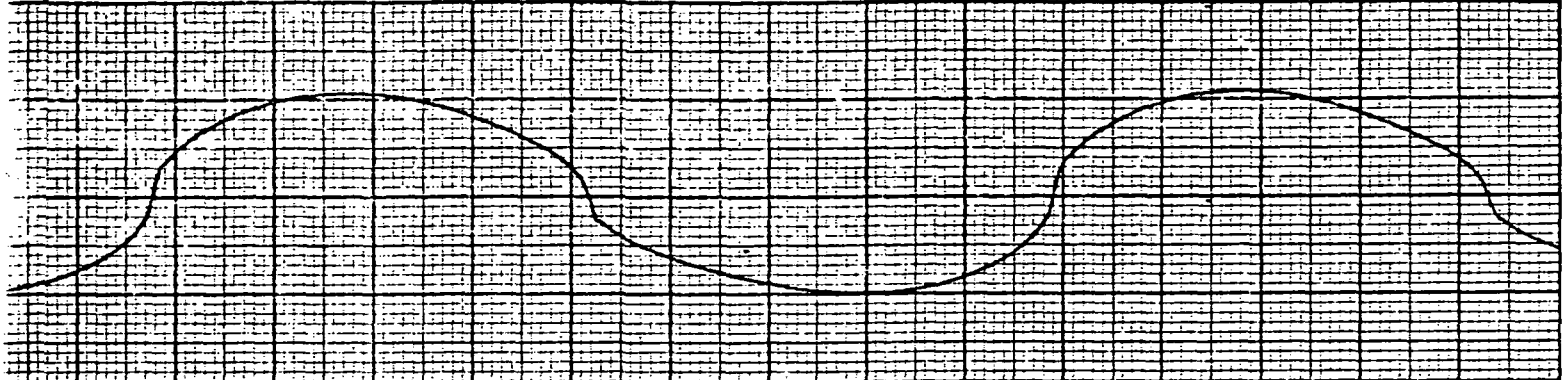


Figure 50. HEAO-B Normal Mode Yaw

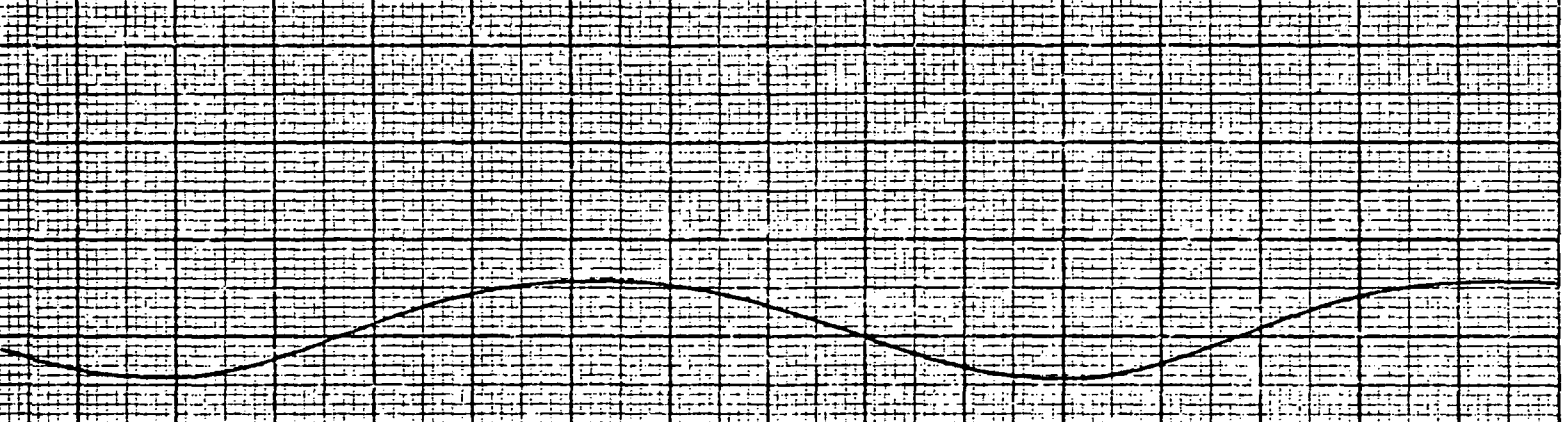




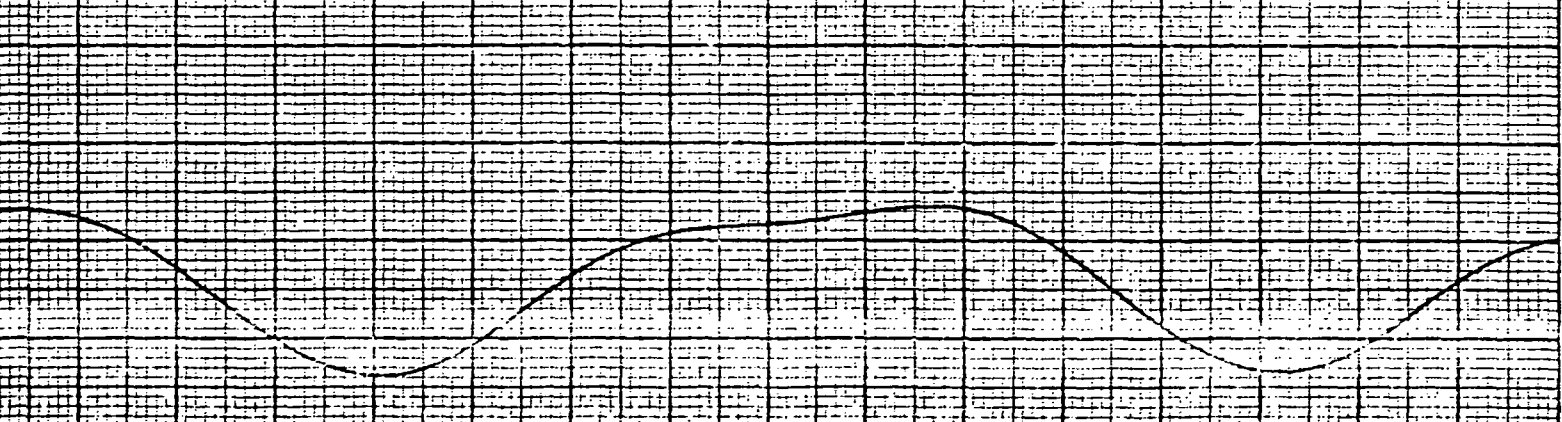
PLOT 14



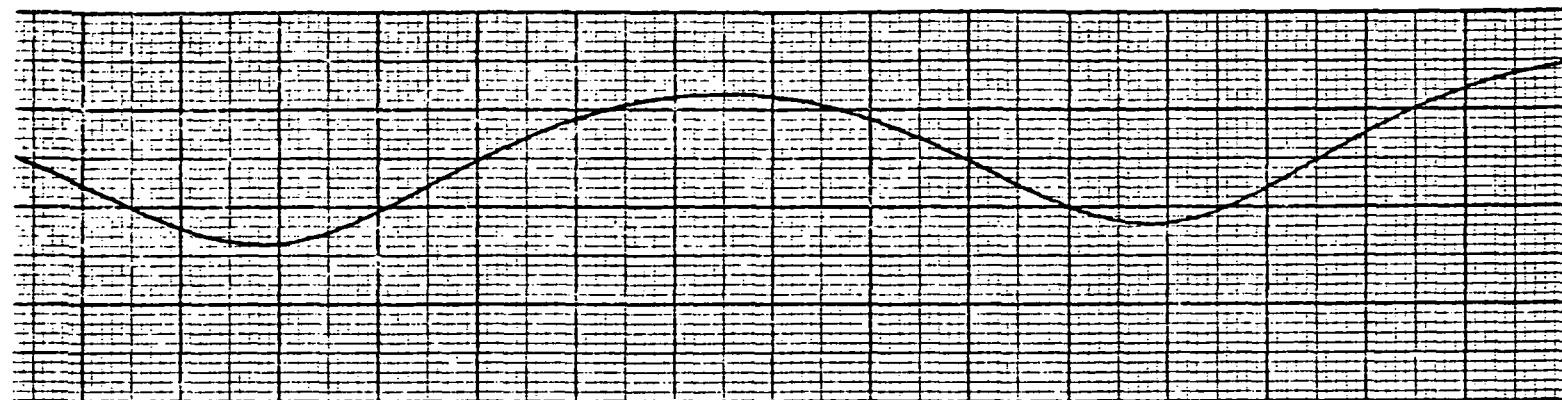
PLOT 15



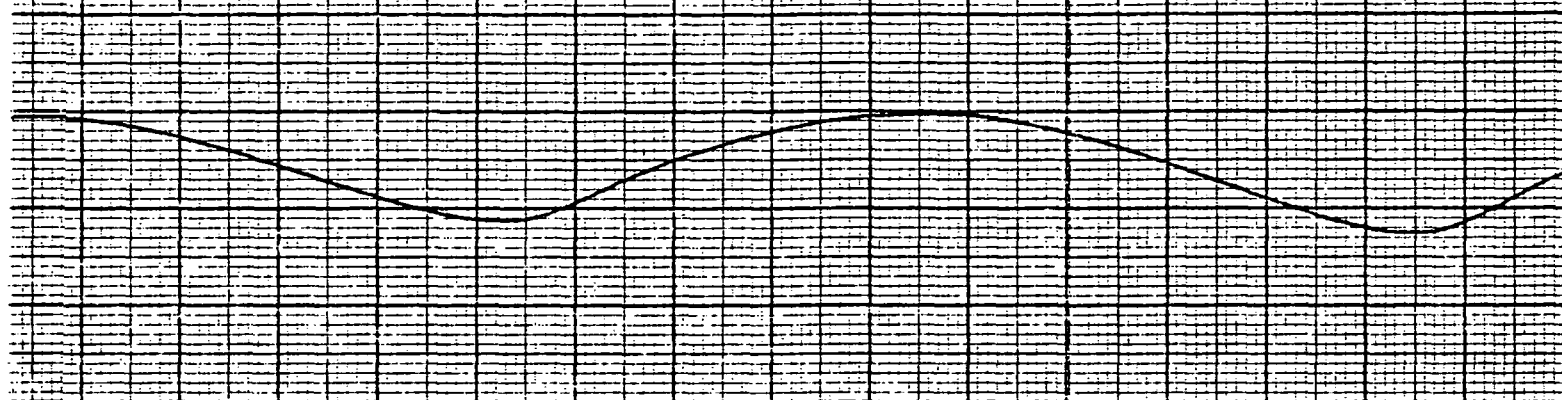
PLOT 16



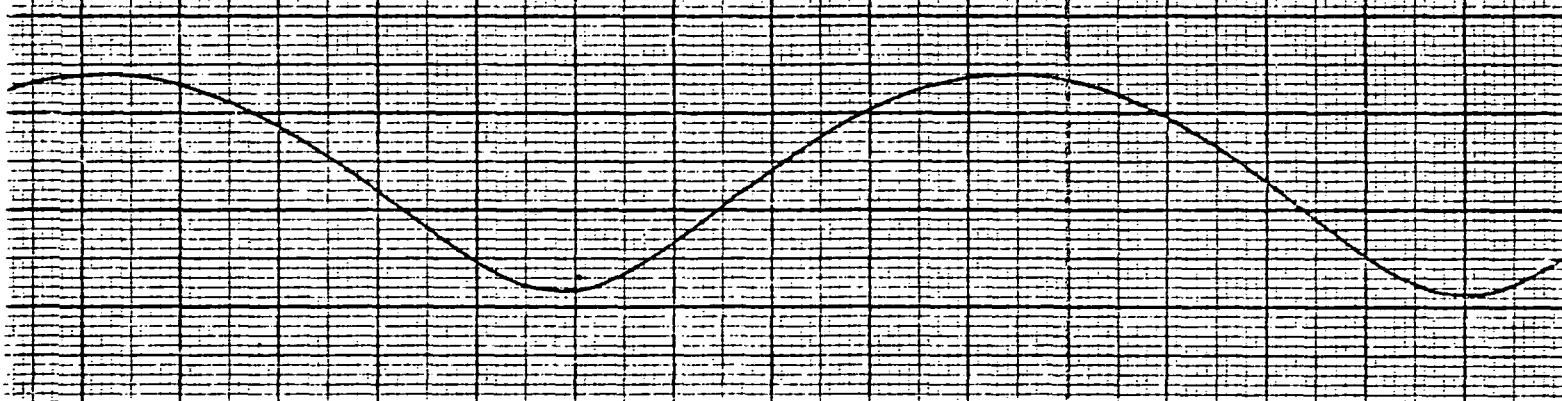
0 80.0 90.0 100.0 110.0 120.0 130.0 140.0 150.0



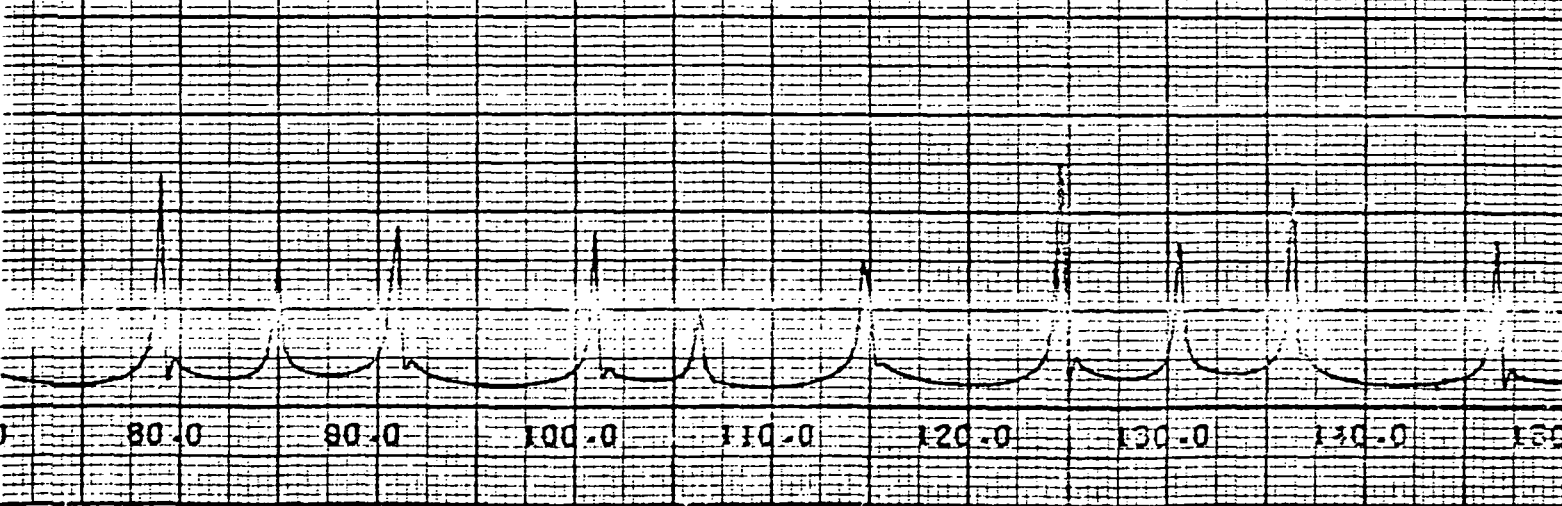
PLOT 18



PLOT 19



PLOT 20



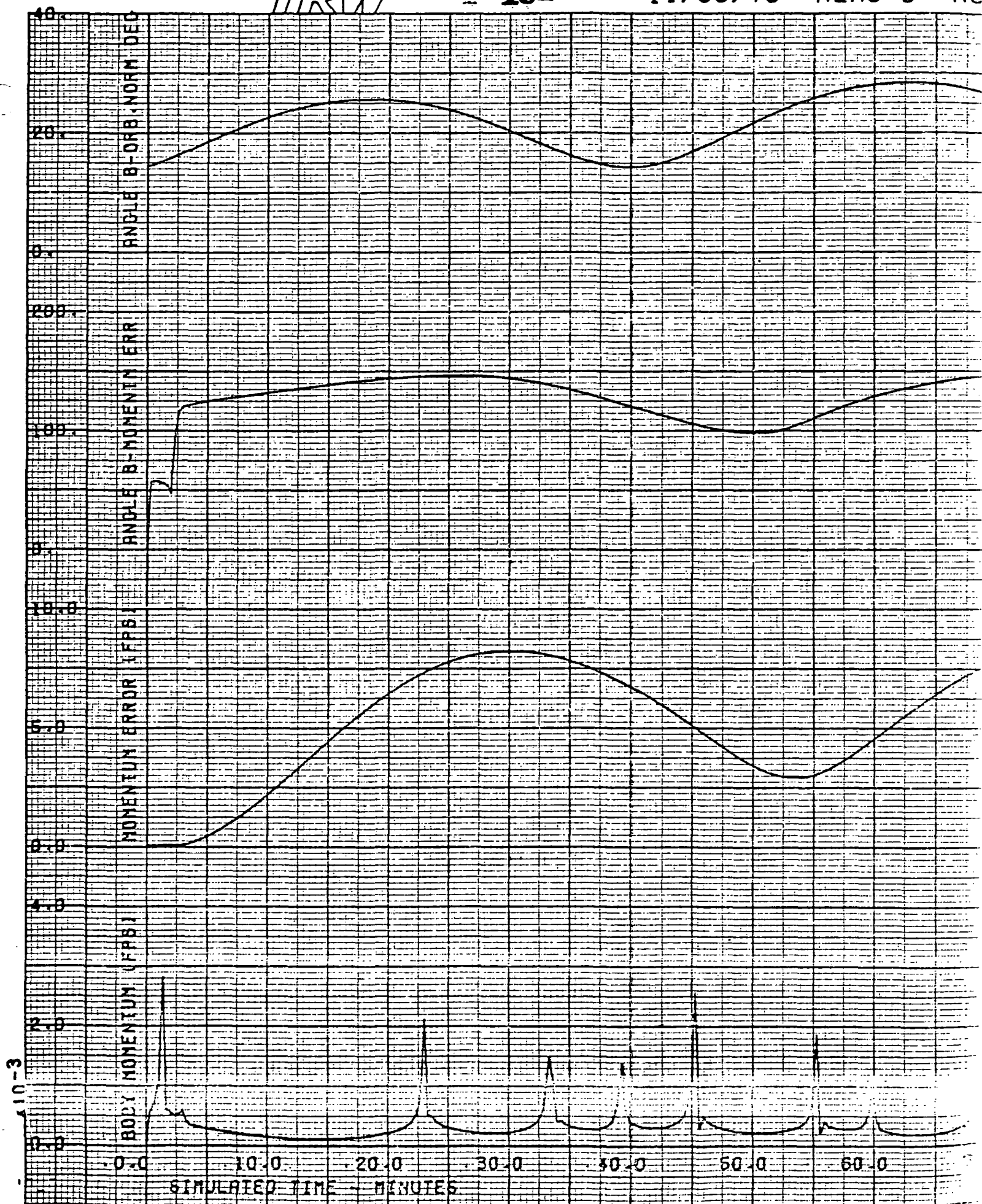


Figure 51. HEAO-B Normal Mode Magnetic and Coax

is no appreciable difference in unloading performance without these effects included.

For the unloading run described above, the unloading gain was set to

$$K_{\text{unld}} = 0.02 (\text{sec-gauss}^2)^{-1}$$

This amounts to twice the gain used in the HEAO-A runs. It was found that this upward adjustment in the gain lowers the magnitude of the stored momentum. However, a run at a higher unloading gain ( $0.04 \text{ sec}^{-1}\text{-gauss}^{-2}$ ) demonstrated the interactive property of the controller as the peak z-momentum was reduced (5.5 ft-lb-sec), but the momentum stored in the y-axis increased (6.5 ft-lb-sec). This characteristic is due to the fact the torque produced by the magnets will not be precisely aligned with the error momentum in the z-axis, thereby introducing undesired torques in the y axis. For this run, the y-axis was generally in the direction of the earth's magnetic field vector, and therefore the magnetic controller had difficulty unloading this momentum component. Hence the increase in y-stored momentum.

The nature of the BxH magnetic control law requires the stored momentum increase in the presence of larger disturbances, in order to produce increased offsetting magnetic torques. Thus some momentum must always be present in the wheels. To improve this situation, an alteration to the magnetic law is possible, which would allow the stored momentum to be reduced. The electromagnets could be driven from the combination of stored momentum and the attitude error signals used for wheel control in order to anticipate the buildup of wheel momentum. The control law form would be:

$$\vec{M} = K_{\text{unld}}(\vec{H} + \vec{\epsilon}) \times \vec{B} \quad (4-37)$$

where  $\vec{\epsilon}$  is the wheel command vector based upon attitude error and rate. The lead provided by the error component in this control law has the potential for allowing operation at a lower residual wheel momentum during normal mode. This control law form was not developed further in this study, but is an area for future study.

#### 4.3.3 Conclusions

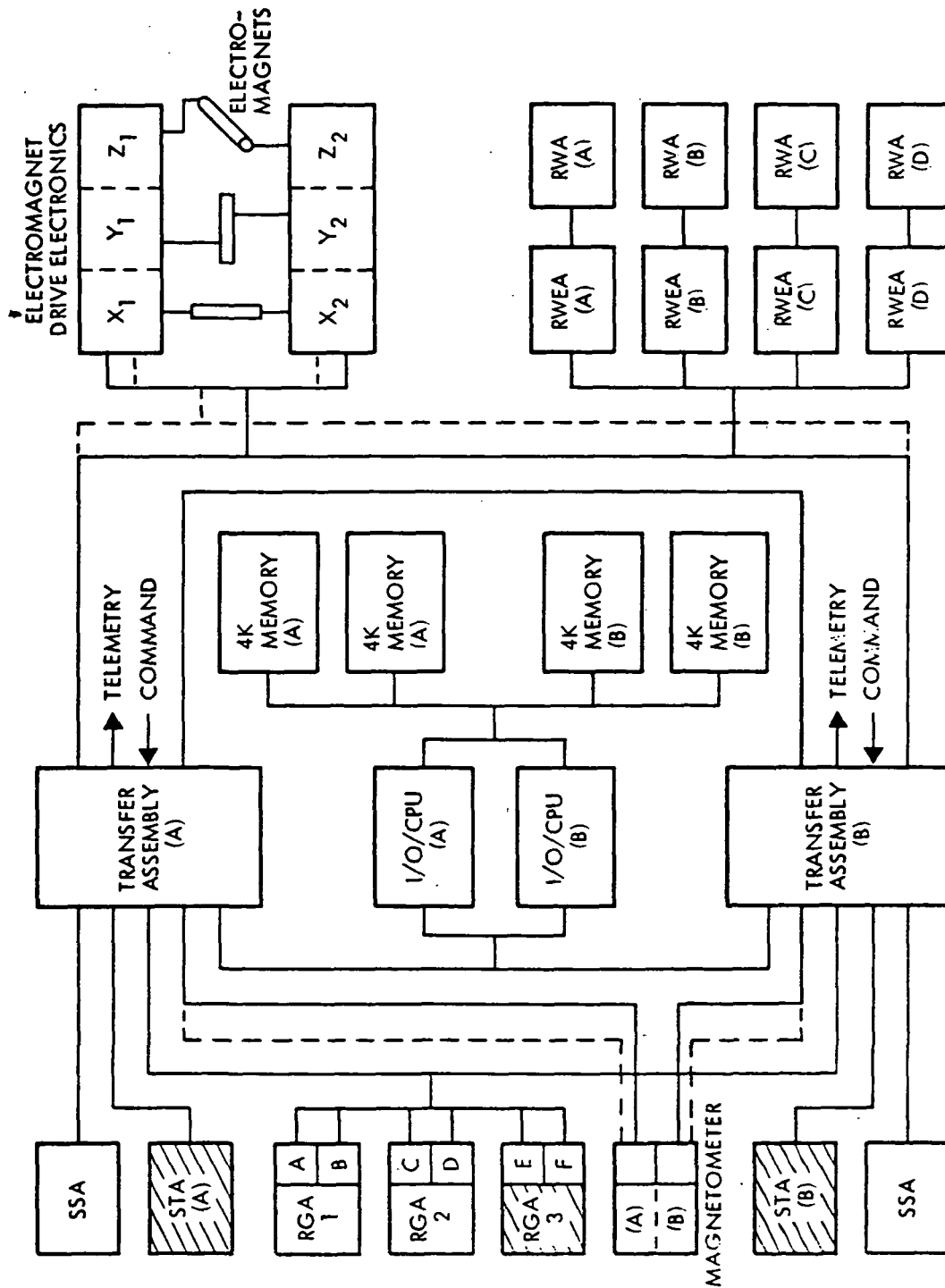
The performance analyses conducted through use of a digital computer simulation have indicated that the HEAO sun acquisition and normal mode control requirements can be satisfied with a combined magnetics and reaction wheel control system. Some constraints do result. However, at this time these are assessed as being satisfactory. The performance study results are summarized below:

- Sun acquisition mode requires a maximum magnetic moment capability of 2000 amp-turn-m<sup>2</sup> in each axis from the electromagnets
- Sun acquisition from worst case booster separation rates requires 2 to 3 orbits using combined magnetics/wheel control
- Reaction wheels can be maintained below 7-8 ft-lb-sec stored momentum in each axis in the celestial point mode and below 3-4 ft-lb-sec in the celestial scan mode with magnetic unloading
- Normal mode performance is generally insensitive to residual fields and magnetic coupling for expected magnitudes of these effects
- Sun acquisition mode duration is significantly influenced by residual field effects from body fixed magnetic sources and by electromagnet/magnetometer magnetic coupling effects. Current definitions of the potential magnitudes of these interactions indicates these effects are acceptable for the preliminary design. Design development studies should emphasize these design aspects
- The BxH magnetic control law provides satisfactory momentum management performance in both the acquisition and normal modes

#### 4.4 Subsystem Implementation

A baseline set of requirements and performance capabilities for the magnetic torquing design have been established in this study. The implementation of the design has been synthesized, which satisfies the operational and reliability requirements of the HEAO observatory. Figure 4-52 shows the ACDS implementation in block diagram form, including redundancy and functional interconnection. The basic topology of the subsystem is unchanged from that of the current baselines. The magnetic control equipment consists of magnetometers and electromagnets. The magnetometers have some associated electronics for sensor signal conditioning/processing and the electromagnets require driver electronics. The magnetometers

## SUBSYSTEM BLOCK DIAGRAM



----- INDICATES SECONDARY POWER INTERCONNECTION

Figure 4-52. ACDS Block Diagram



are connected one-to-one to the transfer assemblies with no cross-strapping. The electromagnet drivers are also connected one-to-one to the dual windings of the electromagnets. The transfer assemblies are cross-strapped to the electromagnet drivers. This low level of cross-strapping is readily implemented and provides an overall predicted spacecraft reliability which satisfies or exceeds the requirements.

The changes to the ACDS design from the current baselines are summarized in Table 4-8. The HEAO-A/C design is the one most significantly affected, due to the addition of the reaction wheel complement, as well as the magnetics. Additionally, the DPA memory sizing for HEAO-A/C has been expanded to the 8K active configuration (16K total) which was the baseline for HEAO-B previously. This increase is predicated upon the addition of the reaction wheel control and the magnetic control computations. The only deletion was that of the thruster control laws. This additional computing load necessitates the increase. The memory margin for A/C should be greater than that for B, however, since there are lesser requirements for the attitude reference in A/C. The weight, power and command and telemetry estimates for the magnetics design are summarized in Tables 4-9, 4-10 and 4-11, respectively.

Table 4-8. Summary Comparison of Required ACDS Modifications

HEAO-A/C:

- DELETIONS
  - PROCESSING OF THRUSTER CONTROL LAWS
  - TA INTERFACE WITH RCS/SIA
- ADDITIONS
  - 4 REACTION WHEELS + ELECT
  - 2 TRIAXIAL MAGNETOMETERS
  - 3 ELECTROMAGNETS
  - 2 4K MEMORY MODULES
  - TA INTERFACE WITH RWEA, EEA  
MAGNETOMETER ELECT
  - 49 TLM ADDRESSES IN S/C SUBCOM
  - 14 CMD ADDRESSES (BILEVELS & PULSE)

HEAO-B:

- DELETIONS
  - PROCESSING OF THRUSTER CONTROL LAWS
  - TA INTERFACE WITH RCS/SIA
  - 14 CMD ADDRESSES (BILEVELS & PULSE)
- ADDITIONS
  - 2 TRIAXIAL MAGNETOMETERS
  - 3 ELECTROMAGNETS
  - TA INTERFACE WITH EAA  
MAGNETOMETER  
ELECT
  - 19 TLM ADDRESSES IN S/C SUBCOM

Table 4-9. ACDS Weight Summary

<u>EQUIPMENT</u>	<u>HEAO-A/C</u>	<u>HEAO-B</u>
TRANSFER ASSEMBLY	16.0	16.0
DIGITAL PROCESSOR ASSEMBLY	14.5	14.5
REFERENCE GYRO ASSEMBLY	19.0	28.5
SUN SENSOR ASSEMBLY	1.0	1.0
REACTION WHEEL ASSEMBLY	114.0	114.0
REACTION WHEEL ELECTRONICS ASSY.	18.4	18.4
MAGNETOMETER ASSEMBLY	9.0	9.0
ELECTROMAGNET ELECT. ASSEMBLY	5.0	5.0
ELECTROMAGNET ASSEMBLY	153.0	153.0
STAR TRACKER ASSEMBLY	-	22.0
STAR TRACKER SHADE	-	7.0
TOTAL	349.9 LBS	388.4 LBS

TABLE 4-10. ACDS Power Requirements

<u>EQUIPMENT</u>	<u>HEAD-A/C</u>		<u>HEAD-B</u>	
	<u>ACQUISITION</u>	<u>NORMAL</u>	<u>ACQUISITION</u>	<u>NORMAL</u>
TRANSFER ASSEMBLY	16.5	16.5	16.5	16.5
DIGITAL PROCESSOR ASSEMBLY	16.0	16.0	16.0	16.0
REFERENCE GYRO ASSEMBLY	27.0	27.0	27.0	27.0
SUN SENSOR ASSEMBLY	-	-	-	-
REACTION WHEEL ASSEMBLY	15.0	10.0	30.0	23.0
RW ELECTRONICS ASSEMBLY	30.0	35.0	60.0	46.0
MAGNETOMETER ASSEMBLY	1.0	1.0	1.0	1.0
ELECTROMAGNET ELECT ASSEMBLY	6.0	3.3	6.0	3.3
ELECTROMAGNET ASSEMBLY	16.0	0.3	27.0	3.0
STAR TRACKER ASSEMBLY	-	-	5.0	5.0
STAR TRACKER SHADE ASSEMBLY	-	-	-	-
	<u>127.5 W</u>	<u>109.1 W</u>	<u>188.5 W</u>	<u>140.8 W</u>

TABLE 4-11. ACDS TLM/CMD Modifications

- HEAO-A/C REQUIREMENTS BECOME IDENTICAL TO THOSE PREVIOUSLY DEFINED FOR HEAO-B EXCEPT FOR RGA WHICH REMAINS 4 FOR A/C AND 6 FOR B.

- TLM ADDITIONS TO ALL SPACECRAFT ARE -

<u>FUNCTION</u>	<u>LOCATION</u>	<u>DATA TYPE</u>	<u>#OF ADDRESSES</u>
SENSED MAGNETIC FIELD	TA	ANALOG	6 S/C SUBCOM
TORQUER CURRENT CMD	TA	"	6 " "
MAGNETOMETER BIAS VOLTAGE	TA	"	2 " "
COIL CURRENT	TA	"	6 " "
EXCESS COIL CURRENT ALARM	TA	BI-LEVEL	6 " "

- CMD ADDITIONS TO ALL SPACECRAFT ARE -

<u>FUNCTION</u>	<u>LOCATION</u>	<u>SIGNAL TYPE</u>	<u># OF ADDRESSES</u>
EEA SELECT	TA	PULSE	2

- TLM DELETIONS ARE -  
EXCESS THRUSTER PULSE ALARM

- CMD DELETIONS ARE -  
NONE

## 5. REACTION CONTROL SUBSYSTEM (COLD GAS OPTION)

### 5.1 Introduction

The advantage of adding a cold gas system to the magnetics/wheels attitude control approach, is to decrease the time required for sun acquisition. With the larger control torques, initial sun acquisition can be effected in a matter of minutes versus the 2 or 3 orbits required with electromagnets. A secondary consideration is the capability of performing fast spacecraft maneuvers with the cold gas system (maneuver time can also be decreased by increasing the reaction wheel motor torque and the wheel momentum capacity). The number of maneuvers is, of course, limited by the available propellant.

The cold gas system was sized to perform 3 sun acquisitions assuming worst case spacecraft inertias (HEAO-B) and initial body rates of 1 degree/second about each axis. In addition, available propellant capacity was parameterized as a function of available storage vessels, with the upper bound on tank volume dictated by the volume currently allocated for the storage of hydrazine.

### 5.2 Cold Gas System Design

The cold gas RCS for performing acquisition maneuvers is shown schematically in Figure 5-1. The schematic arrangement is typical for this type of system except that redundant regulators and a regulator fail safe isolation capability have been incorporated to improve reliability. All components were selected from available qualified designs. The component equipment list showing mass properties and component derivations is summarized in Table 5-1. The system interface requirements for power, command and telemetry are summarized in Table 5-2. Detailed component descriptions are given in the following paragraphs.



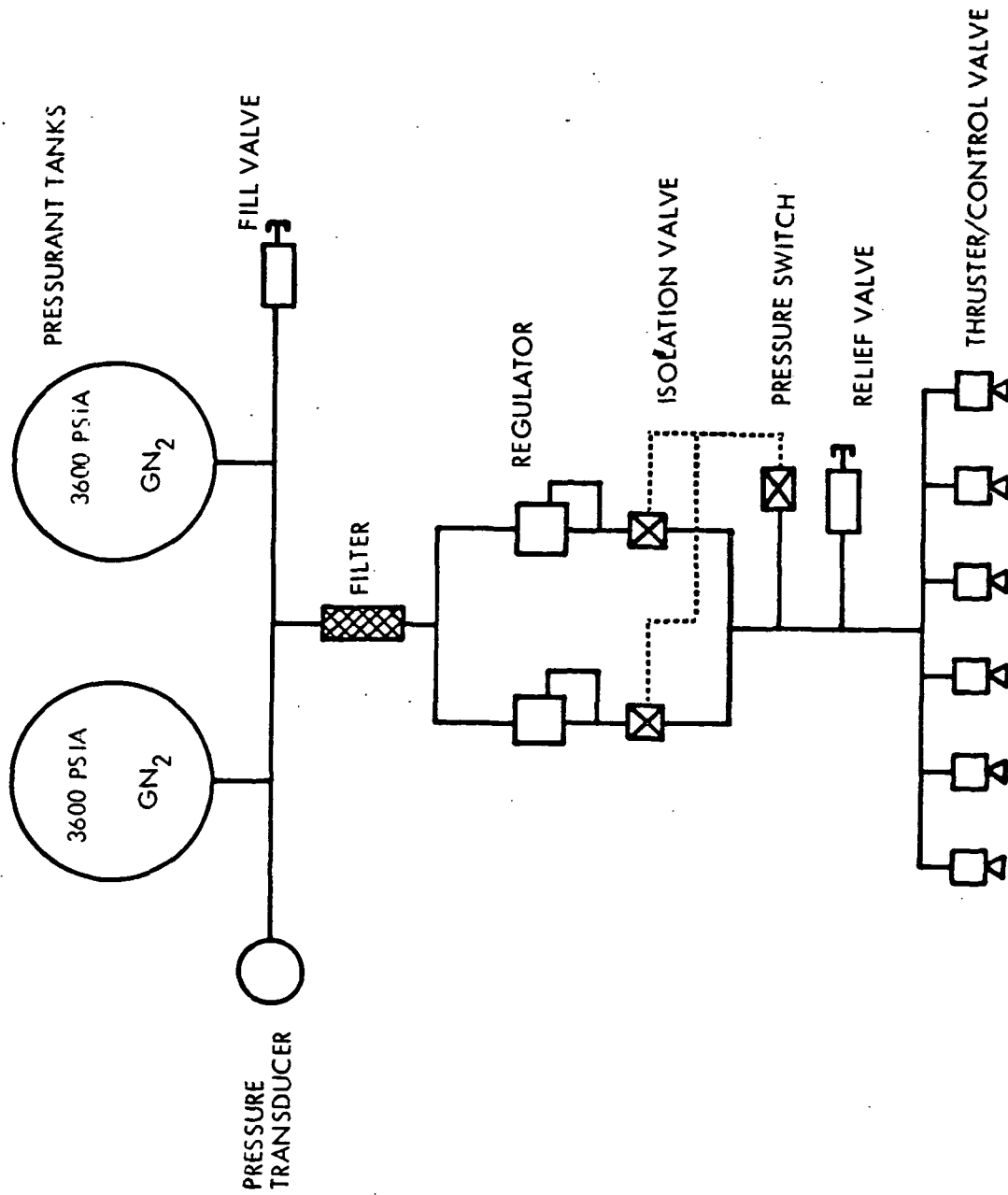


Figure 5-1. Cold Gas System

Table 5-1. Cold Gas System Weight

<u>Item</u>	<u>Source</u>	<u>Unit Weight</u>	<u>System Weight</u>
Thruster/Valve	Sterer	0.73	4.4
Regulator	Sterer/Fairchild	1.2	2.4
Pressure Transducer	Stratham	0.5	0.5
Filter	Wintec	0.5	0.5
Fill Valve	Pyronetics	0.1	0.1
Tanks	PSI	3.8	7.6
Isolation Valve	HRM	0.6	1.2
Pressure Switch	Hydro Electric	0.3	0.3
Relief Valve	Futurecraft	0.3	0.3
Lines/Brackets	TRW	3.0	<u>3.0</u>
	Dry Weight		20.3
	GN <sub>2</sub>		5.0
	Total		<u>25.3</u>

Table 5-2. Interface Requirements

Power

Average on orbit power will be negligible.

During operation the pressure transducer requires 0.5 watt from a 28 vdc source.

Propellant valves require 12 watts/valve; however, valves are operated in pulse mode for short duration, maximum of two valves operating at one time.

Telemetry

Gas pressure readout	Analog
Isolation valve No. 1 Position indication	Open/close
Isolation valve No. 2 Position indication	Open/close
Pressure switch Position indication	Open/close

Commands

Pressure transducer power	On/off
Isolation valve No. 1 actuation	Open/close
Isolation valve No. 2 actuation	Open/close
Thruster bank power	On/off

### 5.2.1 Component Descriptions

Thruster/Control Valve. A combination thruster/control valve is shown in Figure 5-2. The valve uses two ball poppets independently spring loaded in a closed position. The primary seat is made up of a tungsten-carbide ball (poppet) mating with a Stellite 6B seat, and the secondary or redundant seat is made up of a tungsten-carbide ball mating with a Kynar plastic seat. The secondary ball poppet is lifted off its seat by a rod pushed by the solenoid plunger whenever the coil is energized. The primary ball poppet, in turn, is raised off its seat by the secondary poppet through an inter-connecting (No. 2) stem.

The solenoid valve incorporates an integral expansion nozzle downstream of the series seats. Test ports are provided to measure independent seat leakage and nozzle chamber pressure. A 10-micron absolute filter prevents particular contaminants from entering the solenoid valve.

Pressure Regulator. Figure 5-3 shows a gas pressure regulator manufactured by the Sterer Engineering and Manufacturing Company. This unit has an integral relief valve incorporated into the low-pressure side. The function of the regulator is to control the pressure to the thruster control valves.

For the proposed system, which uses redundant regulators, the integral relief valve on each regulator would be replaced with a single relief valve in the common line.

As shown in the cutaway diagram the pressure regulator is a single-stage unbalanced ball-poppet, spring-loaded, diaphragm-type with an integral relief valve incorporated into the low-pressure side. The regulator is constructed with two seats in series. The primary seat is made up of a tungsten-carbide ball (poppet) mating on the titanium body, and the secondary or redundant seat is made up of a tungsten-carbide ball mating with a seat composed of a Kynar plastic insert. Concentricity of the balls with respect to the seats is maintained by close tolerance Stellite 6B guides.

Pressure regulation is not affected by the secondary seat during normal operation. The stem which forms a part of the diaphragm assembly acts directly on the secondary ball to push it off its seat. An inter-

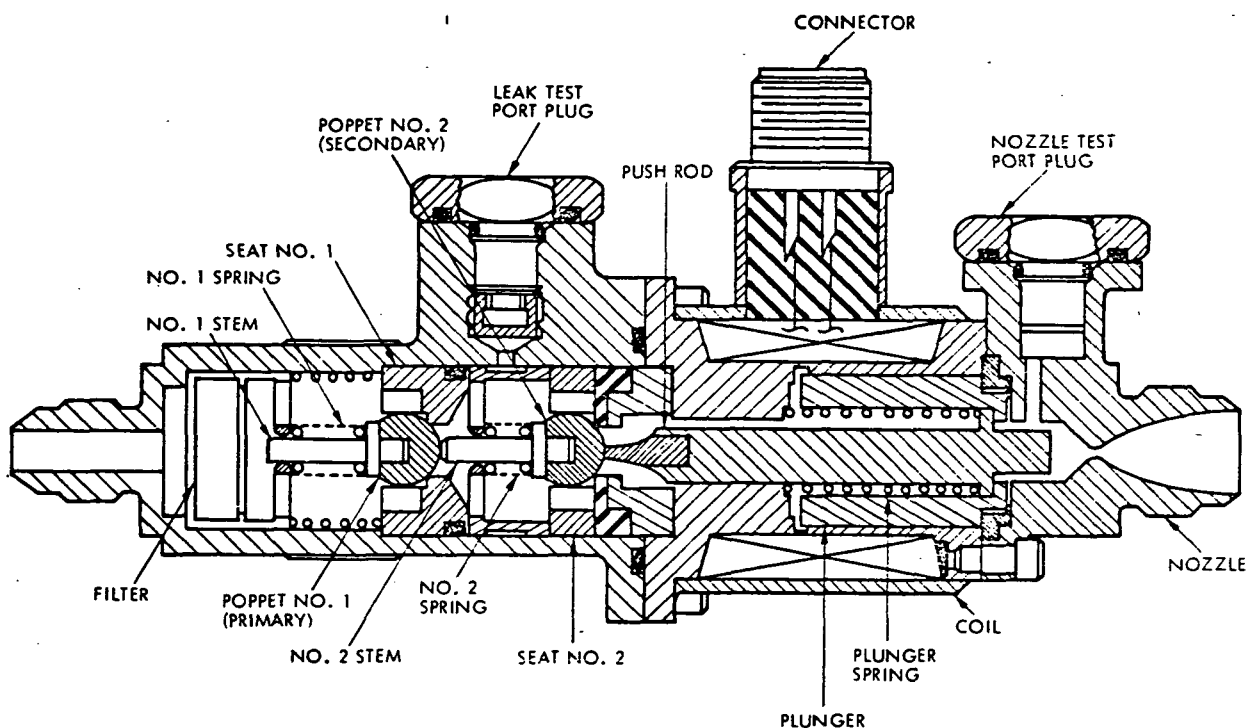


Figure 5-2. Thruster Control Valve - Cutaway View

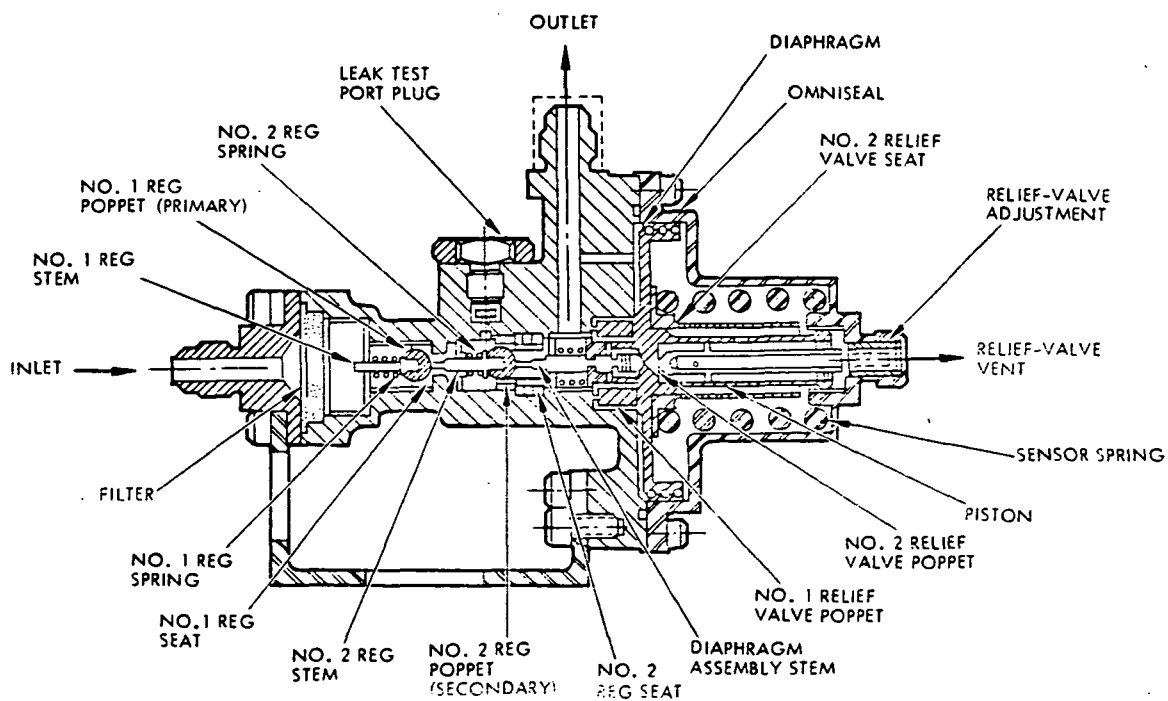


Figure 5-3. Pressure Regulator - Cutaway View

connecting pin between the secondary and primary balls is adjusted such that the pressure regulation is controlled by the primary seat during normal operation. However, in the event that the regulated pressure rises due to excessive leakage past the primary seat, the diaphragm is raised sufficiently by the higher pressure (2 to 4 psi) to permit the secondary seat to become operative.

The pressure regulator also incorporates an omniseal to backup the diaphragm, double seals on all body joints, a 10-micron absolute filter at the high-pressure inlet, and ports for the installation of the low-pressure transducer and for the measurement of secondary-seat leakage.

Pressure Switch. The pressure switch is incorporated into the thruster feed line to sense an over pressure condition in the event of a fail open or leaking regulator. The switch activates both isolation valves to the closed position to prevent gas from venting overboard through the relief valve. The isolation valves can subsequently be opened by ground command to diagnose the problem and to reactivate the system.

A representative pressure switch, manufactured by Hydra Electric, consists of a hermetically sealed, single-pole, double-throw microswitch with an RFI suppression circuit and an adjustable spring loaded diaphragm pressure sensing element installed in a cylindrical case. The RFI circuit suppresses the radio frequency interference generated by contact bounce and arcing to acceptable levels. The pressure switch is designed to actuate to either an increasing or decreasing pressure change. A schematic diagram of the pressure switch is shown in Figure 5-4.

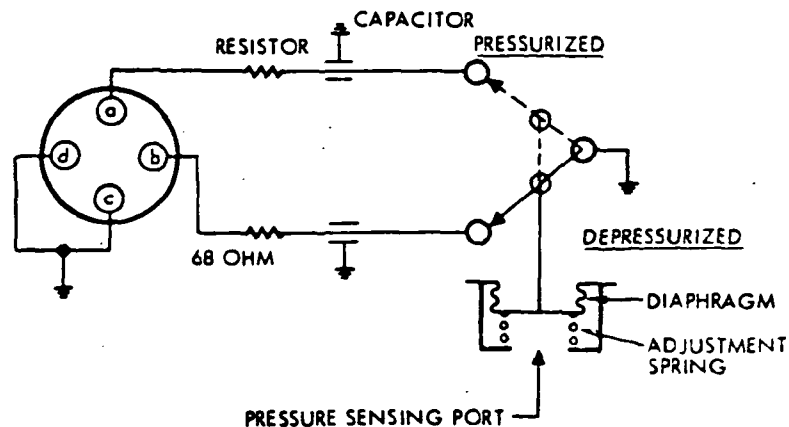


Figure 5-4. Pressure Switch Schematic

Filter. A filter typical of that used for cold gas systems is shown in Figure 5-5. The filter is an in-line screen-type filter made entirely of noncorrosive steel, manufactured by the Wintec Corporation. The element is normally nonremovable, and the filter forms an integral and permanent part of the system it protects. The screen area is sized to hold all particulate contaminants which would be expected throughout the life of the systems in testing, checkout, and flight.

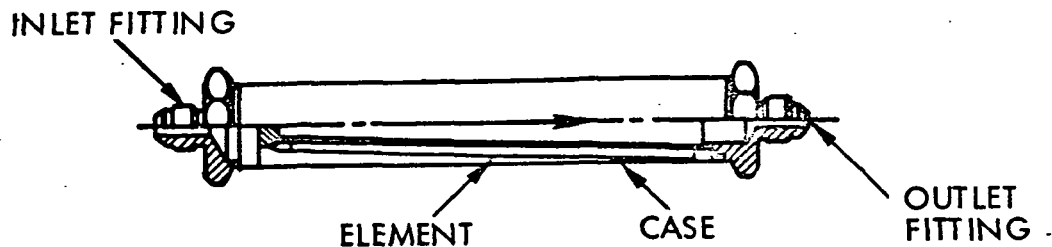


Figure 5-5. Filter-Cutaway View

The filter is rated at 15 microns absolute and is designed to hold at least 250 mg of particulate contamination at maximum flow. The clean pressure drop at rated flow is less than 1 psi. The maximum contamination will not increase the pressure drop by more than 2 psi.

The Filter element is constructed from single-layer type 340L twilled dutch double weave wire cloth, which is annealed and cleaned in the flat state. The wire cloth is resistance welded to end sheets and then corrugated to save space. The element and structural components are then heliarc welded. The effective screen area is 48 square inches minimum. Filters can be designed larger or smaller than this; however, the same basic fabrication and design techniques are used.

Pressure Transducer. The Statham Model PA 539-XX transducer (shown in Figure 5-6) is a typical high resolution, strain gauge transducer. It provides high accuracy through the entire pressure range with overpressure protection of 20 times the range without performance degradation. The vacuum deposited strain gauge sensors are mounted on a bending beam driven from a toroidal diaphragm through a pushrod. The strain gauges provide the input to a four-arm active wheatstone bridge in a Statham developed ampli-bridge electronic circuit.



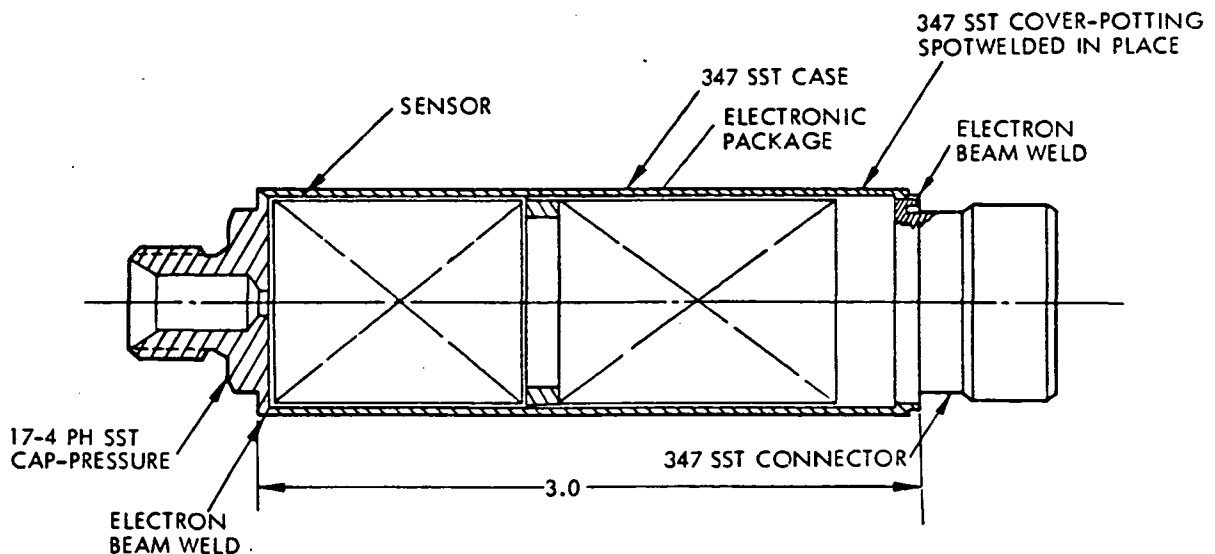


Figure 5-6. Statham Pressure Transducer

An integrated electronics package of all-welded construction provides a dc-to-dc converter for voltage and current regulation with coarsely regulated input voltage. A differential low gain amplifier increases the output signal to 5 volts. Output impedance is less than 100 ohms, and an internal single point calibration is included for functional checkout and data reduction.

Fill Valve. A typical fill valve is shown in Figure 5-7. It is manually operated with an ordinary open-end wrench. The poppet incorporates redundant seals and provides positive sealing against propellant or gas leakage. Current testing indicates leakage rates less than  $1 \times 10^{-5}$  scc/sec helium at 500 psi. When loading is completed, the fitting is capped for additional protection against leakage and contamination.

Isolation Valve. The isolation valve, shown in Figure 5-8, is a torque motor actuated design with latching forces in both the open and closed position supplied by a permanent magnet circuit. The torque motor is isolated from the fluid by a flexure tube which is also the primary valve spring.

The torque-motor contains two coils, wound in opposite directions. One coil is for opening the valve and the other for closing the valve.

With the valve in the closed position, the armature is held against the closed pole surfaces by permanent magnet attractive forces. The

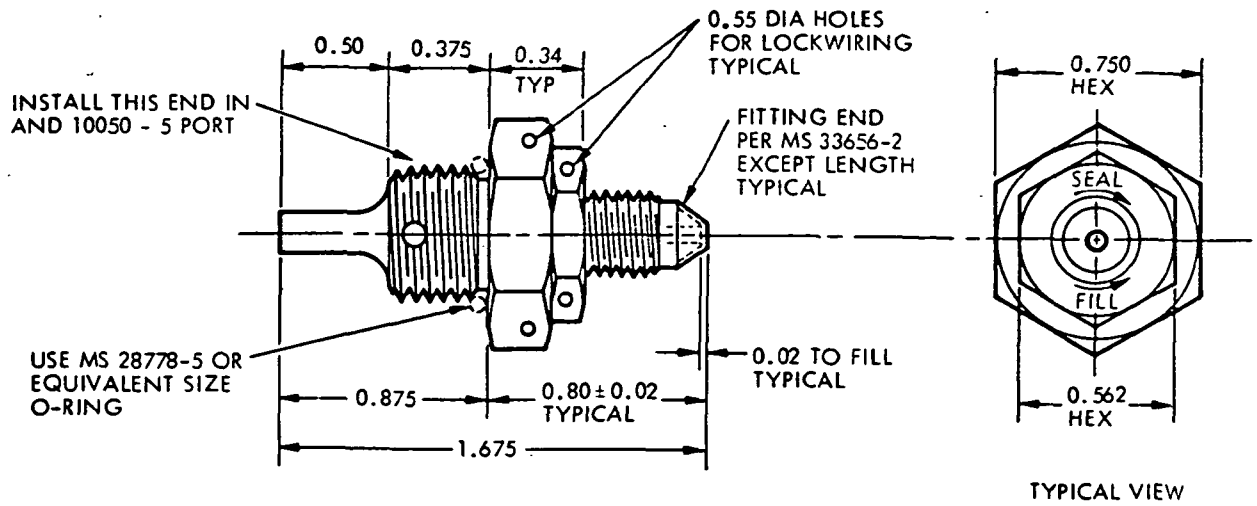


Figure 5-7. Fill Valve

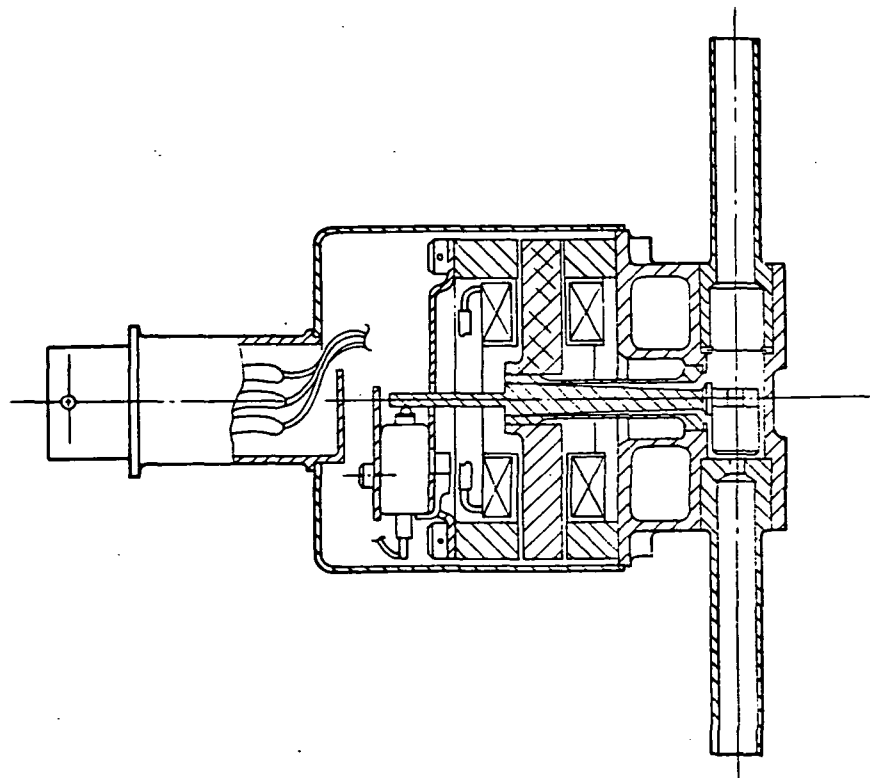


Figure 5-8. Latching Isolation Valve

magnetic force is significantly greater than the force required to deflect the flexure tube from a spring null position to the closed position.

To open the valve, a dc voltage is applied to the opening coil which establishes a magnetic field in opposition to that of the permanent magnet. This opposing field diminishes the attraction of the armature to the closed pole and increases its attraction to the open pole. When the total magnetic force is reduced to a level lower than the spring force, the armature moves off the closed poles and to the open poles where it is again retained by the permanent magnet forces.

### 5.3 Propellant Capacity

The system as currently configured has an impulse capability of 300 lb/sec. Increasing the system impulse can readily be achieved by increasing the gas storage capacity. Qualified tanks are available over a wide range of sizes in relatively close capacity increments. Table 5-3 lists a sampling of these tanks showing the system impulse capability, tankage size and weight, and propellant weight. Figure 5-9 plots the tank weights as a function of system impulse.

Table 5-3. Pressurant Tanks (Flight Qualified Designs)

<u>Tank Diameter (inches)</u>	<u>Tank Weight (pounds)</u>	<u>Gas Capacity (lb/GN<sub>2</sub>)</u>	<u>Impulse (lb/sec)</u>
7.6	3.8	2.3	150
9.6	6.0	4.0	260
11.5	13.3	7.7	500
12.7	11.9	9.5	620
13.0	16.9	11.5	750
15.0	23.3	17.5	1140
18.7	49.5	33.0	2150
20.5	63.4	43.8	2850

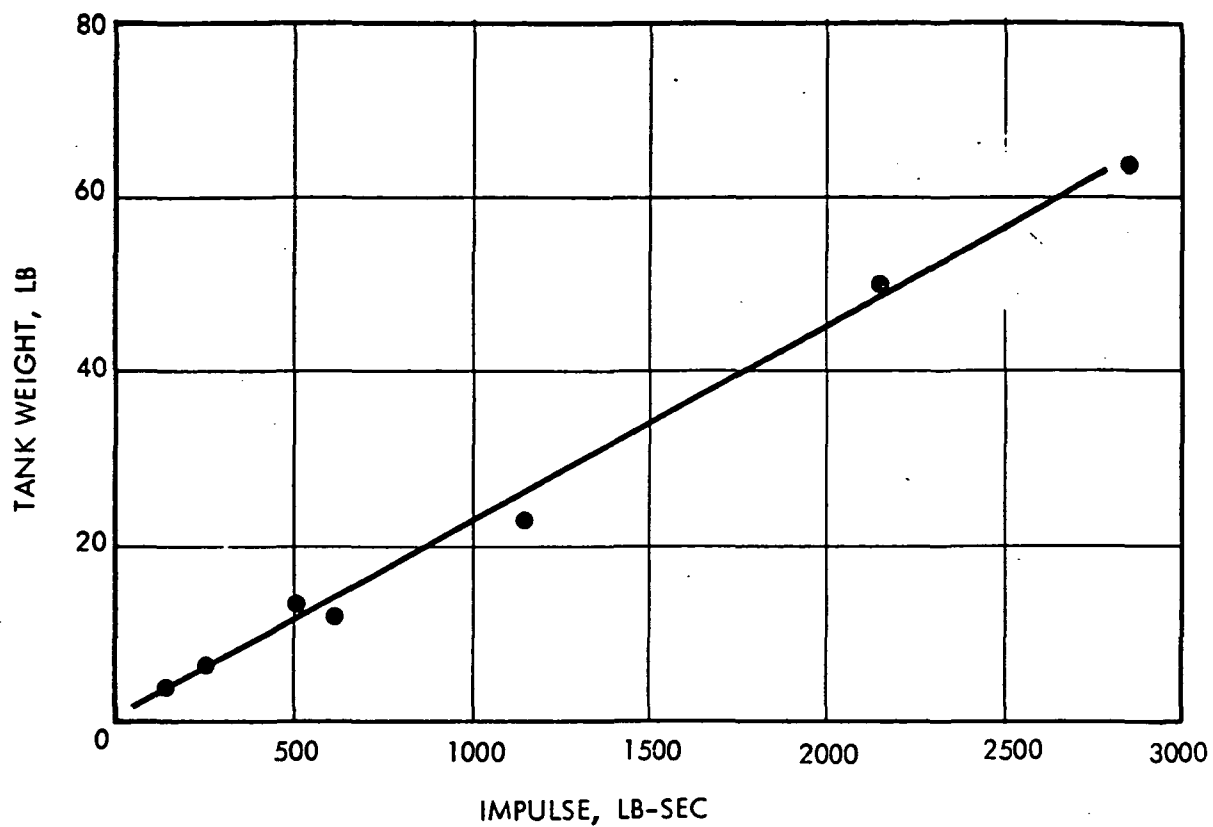


Figure 5-9. Tank Weight Versus Impulse

## 6. MECHANICAL DESIGN INTEGRATION

### 6.1 Introduction

The general design requirements used to configure the magnetics control components into the current spacecraft configurations were:

- The magnetometers shall be located atop the spacecraft structure to provide maximum separation distance between the magnetometers and the electromagnets.
- The electromagnets shall be located on the lower part of the spacecraft equipment module so that the magnetic field can be minimized at the experiments, key electronics equipment, and the magnetometers.
- Four reaction wheels are to be oriented within the spacecraft, such that the momentum axes are  $90^\circ$  to each other and placed symmetrically about the Y-Z plane and also canted  $\pm 20^\circ$ .
- Provisions shall be made for a cold gas system in lieu of the mono-propellant system currently configured. This system shall incorporate two 7-1/2 inch diameter spherical tanks in conjunction with thrusters which are similar in size to those used in the current RCS.
- Electronics assemblies for the magnetometers and electromagnet drivers shall be integrated into the spacecraft equipment module.

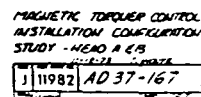
The proposed configuration for Magnetic Control is depicted on Figure 6-1.

### 6.2 Component Location and Support Structure

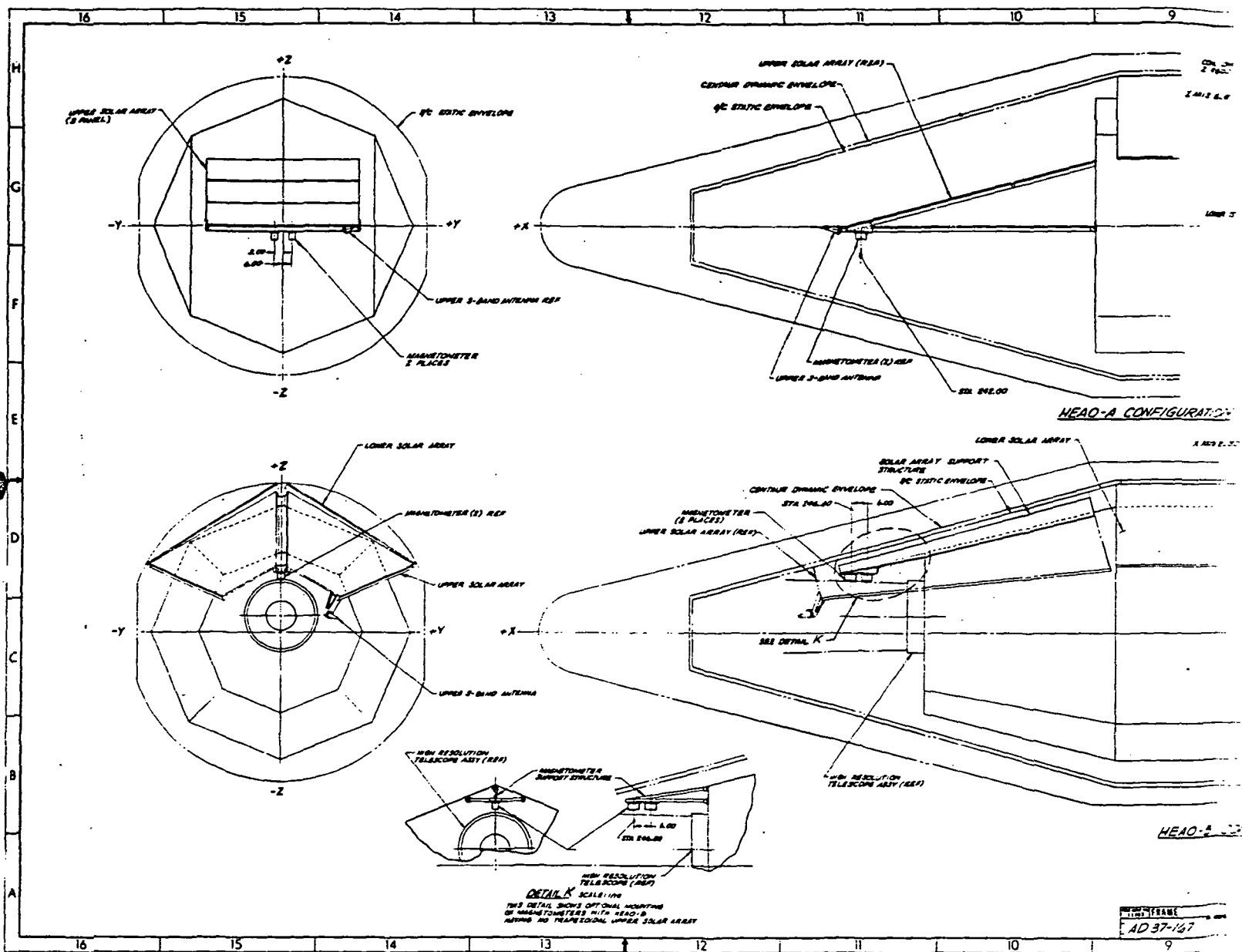
#### 6.2.1 Electromagnet

Three electromagnets are located on the spacecraft module. The design approach was to place these electromagnets at locations such that the magnetic fields generated are acceptable to the equipment in the spacecraft equipment module. However, this could not be accomplished without having to relocate some of the more magnetically sensitive components currently configured in the equipment arrangement.

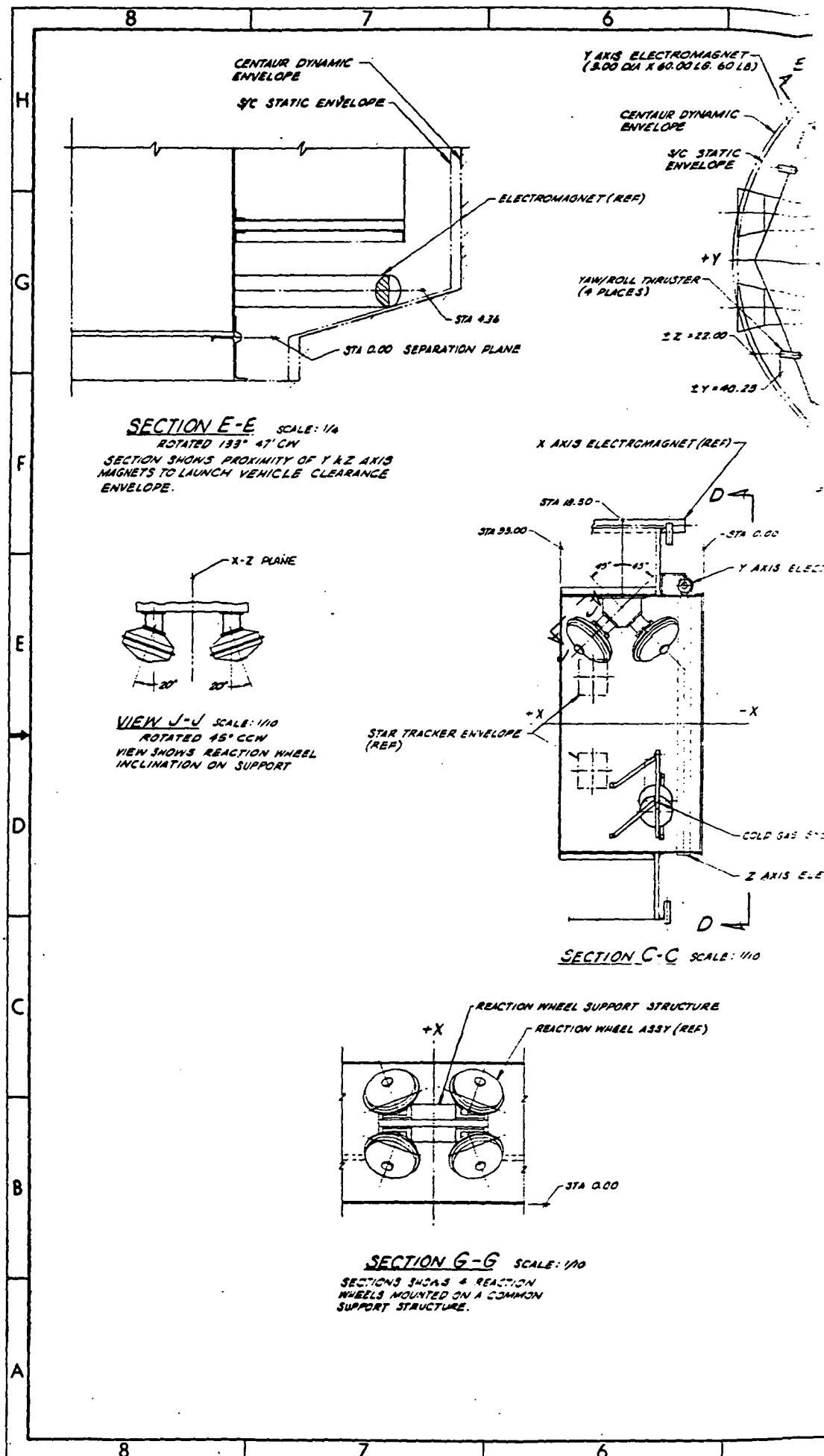
As depicted on Figure 6-1, one electromagnet is placed parallel to the spacecraft X axis and slightly offset from the solar array support structure on the +Z corner of the equipment compartment. This electromagnet is attached to the structure by two machined aluminum fittings with the lower end located no lower than station 4.50 to preclude interference with the aft omni antenna.











The other two electromagnets are located on the bottom surface of the equipment module platform and are attached to this surface in a similar manner. These electromagnets are oriented parallel to the Y and Z axes of the spacecraft and are located in optimum locations consistent with launch vehicle clearance and spacecraft equipment sensitivity constraints. In order to totally meet these constraints, the star trackers, rate gyros, digital processor assembly, tape recorders, and transponder had to be relocated to a more remote area away from the influence of the electromagnets' fields. This relocation, however, does not compromise the functional and access provisions previously provided for these components.

#### 6.2.2 Magnetometer

The magnetometers are remotely located on the forward end of the spacecraft away from the influence of the electromagnets and the experiments. As illustrated on Figure 6-1, two magnetometers are attached to the upper solar array structure of HEAO A with an aluminum bracket. This array support structure is required to accommodate the additional solar array module required to meet new electrical power requirements imposed by magnetic control. This proposed location isolates the magnetometers from any deleterious magnetic influences by providing adequate separation distance from the spacecraft.

On HEAO B, the magnetometers are mounted to the center support beam of the trapezoidal array with an aluminum sheet metal bracket. Figure 6-1 depicts the maximum height at which these magnetometers can be located and still not interfere with the experiment's field of view. When the experiment's sun shade configuration is defined, it may be necessary to lower the attachment of these magnetometers several inches to provide adequate clearance for the shade. In this case, the new location is expected to be acceptable because the magnetic field associated with HEAO B experiment is comparatively weak.

In the event that the trapezoidal array is deleted in favor of a solar array configuration with "flaps", then the magnetometers can simply be mounted on top of the experiment module or on a tripod should additional separation distance be necessary, as illustrated in Detail K, Figure 6-1.

### 6.2.3 Electromagnet Driver and Magnetometer Electronics

As illustrated on Figure 6-1, section A-A, the electromagnet driver electronics is integrated into the Data Handling Assembly as an additional standard slice. The magnetometer electronics, however, is packaged as a separate electronic assembly and is mounted to the central cylindrical of the equipment module. Both of these electronic assemblies are compact in size so that they can be accommodated within the equipment module without presenting any installation or access problems.

### 6.2.4 Reaction Wheel

Four reaction wheels identical to those used on the current ACDS installation are installed on the +Z side of the central cylinder of the spacecraft equipment module. The wheels are clustered on an integral bracket such that the momentum axes of these wheels are spaced  $90^\circ$  to each other and symmetrically oriented about the Y-Z plane. The momentum axes are then canted  $\pm 20^\circ$  from the Y-Z plane as depicted in section J-J of Figure 6-1. This arrangement is also illustrated in sections C-C and G-G and is consistent with the current HEAO modular approach philosophy.

### 6.2.5 Cold Gas Option

The optional cold gas system has been modularized into a configuration consisting of a small honeycomb platform to support the two cold gas tanks as well as other related equipment such as valves, filters and regulators which are generally and preferably pre-assembled in a clean room prior to its installation into the spacecraft. This module is attached to the central cylinder on the -Z side of the spacecraft equipment module and is stabilized by two struts. Feed lines from this module radiate out from this module to the six thrusters located on the lower surface of the equipment platform of the spacecraft equipment module. Fill and drain provisions will be provided in a similar manner as with the current RCS configuration.

The thruster orientation is similar to the current HEAO reaction control system. Furthermore, these thrusters will be similarly mounted to the spacecraft with machined fittings in a manner such that launch vehicle clearance constraints are not violated.

### 6.3 Mass Properties

#### 6.3.1 HEAO-A Mass Properties Impact

A weight increase of 55 pounds is necessary to use the Wheels/Magnetics Control system rather than the current Reaction Control system. An additional 30 pounds must be used to add the optional Cold Gas system to the Wheels/Magnetics Control system. It is assumed the upper solar array is increased from two to three panels for this study. Considering the current weight margin and contingency allocation, this increase would seem to present no significant problem. An obvious advantage in using the newly proposed control system is the relaxation of certain mass properties requirements such as allowable weight and center of gravity variations in spacecraft and experiment components. The requirement for limiting products and moments of inertia of the observatory would no longer be necessary. This would eliminate precise measurements of mass properties at the component level. Final measurements of observatory weight and center of gravity would suffice.

Table 6-1 is presented to compare the weights of the two system approaches for HEAO-A.

#### 6.3.2 HEAO-B Mass Properties Impact

A weight decrease of 147 pounds is possible for HEAO-B by using the Wheels/Magnetics Control system rather than the current Wheels/Reaction Control system. An additional 30 pounds must be used to add the optional Cold Gas system causing a net decrease of 117 pounds if the option is used. The significant reduction in weight is the elimination of 240 pounds of propellant required for the Reaction Control system.

Table 6-2 is presented to compare the weights of the two system approaches for HEAO-B.



Table 6-1. HEAO-A Attitude Control System Weight Comparison

<u>RCS Attitude Control</u>	<u>Weight (lb)</u>	<u>Wheels/Magnetics Attitude Control</u>	<u>Weight (lb)</u>
Plumbing	5	Electromagnet System	159
Isolation Valves (2)	1	Electromagnets (3)	153
Thrusters (6 duals)	18	Attach Fittings	5
Fill and Drain Valves (2)	2	Paint, Thermal Control	1
Tanks (4)	44	Electromagnet Electronics	5
Temperature Transducers (6)	1	Magnetometer System	10
Pressure Transducers (3)	1	Magnetometer Sensors (2)	1
In-line Filters (2)	1	Magnetometer Cable	4
Support Tank (4)	12	Magnetometer Electronics	4
Panels and Other Supports	5	Support Structure	1
Propellant	240	Reaction Wheels and Support	130
Pressurant	4	Reaction Wheels (4)	114
Contingency (15% dry wt)	13	Support Structure, Wheels	16
TOTAL	347	Reaction Wheel Electronics (4)	18
		Additional Solar Array	22
		Addition to Digital Processor	5
		Contingency, 15% dry wt.	53
		TOTAL	402
		Option	30
		Cold Gas System	20
		Gas, GN <sub>2</sub>	5
		Support Structure	2
		Contingency, 15% dry wt	3
		TOTAL INCLUDING OPTION	432

Weight penalty using Wheels/Magnetics Control = 55 lb  
 Weight penalty using Wheels/Magnetics/Cold Gas Control = 85 lb

NOTE: Common items for the comparative systems such as star trackers are not included.

Table 6-2. HEAO-B Attitude Control System Weight Comparison

<u>Wheels/RCS Attitude Control</u>	<u>Weight (lb)</u>	<u>Wheels/Magnetics Attitude Control</u>	<u>Weight (lb)</u>
RCS (see details, HEAO-A)	334	Electromagnet System (see details, HEAO-A)	159
Reaction Wheels and Support	130	Electromagnet Electronics (see details, HEAO-A)	5
Reaction Wheel Electronics	18	Magnetometer System (see details, HEAO-A)	10
Contingency, 15% dry wt	36	Reaction Wheels and Support (see details, HEAO-A)	130
TOTAL	518	Reaction Wheel Electronics	18
		Additional Solar Array	0
		Contingency, 15% dry wt.	49
		TOTAL	371
		Option	
		Cold Gas System (see details, HEAO-A)	27
		Contingency, 15% dry wt	3
		TOTAL INCLUDING OPTION	401

Weight saving using Wheels/Magnetic Control = 147 lb  
 Weight saving using Wheels/Magnetics/Cold Gas Control = 117 lb

NOTE: Common items for the comparative systems such as star trackers are not included.

#### 6.4 Separation Analysis

An analysis of the separation of the HEAO-A spacecraft from the Centaur has been accomplished to determine separation velocity and tipoff rates.

Separation can be achieved with a relative velocity of 2.1 ft/sec and tipoff rates of 0.52 deg/sec (pitch/yaw) and 1.02 deg/sec (roll) using four separation springs of the OGO design. The above rates are conditional on

- a. Preferential location of the four separation springs with respect to the spacecraft center of gravity
- b. Maximum Centaur induced rates ( $3\sigma$ ) at separation of 0.5 deg/sec (pitch/yaw) and 1.0 deg/sec (roll).

The most significant parameters contributing to total spacecraft rates are spacecraft C.G. offset and Centaur induced rates.

Because of the large C.G. offset,  $Y = +5.2$  in., for the HEAO-A spacecraft, minimum tipoff rates are attainable most efficiently by preferential location of the separation springs with respect to the spacecraft center of gravity.

This concept is practical since there are no constraints on location of the spring brackets on the circumference of the central cylinder or spacecraft adapter and locations can be specified late in the program schedule when mass property data is well defined.

Utilizing the mass properties and geometry shown on Table 6-3 and the spring locations and characteristics shown on Figures 6-2 and 6-3, the computed nominal tipoff rate "bias" is essentially zero. The effects of various tolerances which perturb the nominal rate are then individually evaluated and the predicted tipoff rate calculated from

$$\omega_S = \omega_N + \left\{ \omega_C^2 + \sum (\omega_K - \omega_N)^2 \right\}^{1/2}, \text{ where}$$

$\omega_S$  = predicted separation rate

$\omega_N$  = 0 Computed rate "bias" resulting from nominal spring characteristics and inertial properties, and preferential spring locations.

$\omega_C$  = Centaur induced rate at separation

$\omega_K$  = rate dispersions resulting from tolerances.

The effect of various spacecraft, Centaur, and spring tolerances on spacecraft rates are summarized in Table 6-3.

Table 6-4 summarizes the predicted spacecraft rates which include combined rate dispersion effects from tolerances and Centaur induced rates.

The requirement of preferential location of the HEAO-A separation springs to obtain a nominal tipoff rate "bias" of zero radians/sec precludes commonality with HEAO-B and C. If this technique is employed on HEAO-B and C a zero tipoff rate "bias" can be attained and therefore the predicted rates for HEAO-A should be applicable for the HEAO-B and C missions.

#### REFERENCES

1. GDCA-BKM71-005, SLV-3D Centaur AC-31-D-1A, "INTELSAT Mass Properties Report" Ref. A, October 10, 1972
2. TRW HEAO-S-73-709, "Mass Properties Status Report", 1 November 1973
3. NASA, HEAO-S-MSFC-253 "Launch Vehicle Induced Tip Off Rates for HEAO" dated 15 October 1973
4. TRW IOC 67.3522.1-111 "Basic Language Program for Spring Separation of Spacecraft" by R. Strom/L. T. Lee dated 28 August 1967

PREPARED T.J. OCKRY 10/30/73

REPORT NO.

PAGE

CHECKED

MODEL HEAD A

S/C SEPARATION ANALYSIS  
TIP OFF RATES

Table 6-3  
SPACECRAFT - SEPARATION RATE DISPERSION SUMMARY

CASE	VARIABLE	TOLERANCE	INFLUENCE COEFF.	TIP OFF DEG/SEC (1)	ROLL (2) DEG/SEC.	REMARKS
1	NOMINAL - S/C - CENTAUR & • SPRINGS SYM. ABT S/C C.G. • S/C C.G. Y = +5.2 IN. • CENTAUR C.G. Y = -1.26 IN.	—	—	-.41 x 10 <sup>-8</sup>	0	"Bias"
2	S/C C.G. OFFSET	± .5 IN.	± .1736 deg/sec/in.	.0868	—	
3	CENTAUR C.G. OFFSET	± 1.0 IN.	± .0252 deg/sec/in.	.0252	—	
4	S/C - CENTAUR & MISALIGNMENT	± .11 IN.	± .1736 deg/sec/in.	.0191	—	
5	CENTAUR INITIAL RATE - PITCH/YAW	± .1 deg/sec	± .988	.0988	—	
6	SPRING LOCATION - S/C & ADAPTER	± .10 IN.	± .0498 deg/sec/in.	.0050	—	LCB
6A	SPRING LOCATION - S/C SIDE	± .10 IN.	± .206 deg/sec/in.	.0206	—	
6B	SPRING LOCATION - ADAPTER SIDE	± .10 IN.	± .255 deg/sec/in.	.0255	—	
7	SPRING COMPRESSED HEIGHT	± .03 IN.	± .21 deg/sec/in.	.0063	—	
8	SPRING FREE LENGTH	± .03 IN.	± .212 deg/sec/in.	.0064	—	
9	AXIAL SPRING RATE	± 1.5 LB/IN	± .0204 deg/sec/in.	.0306	—	
10	LATERAL SPRING RATE	± 5.0 LB/IN	± .0042 deg/in/LB.sec	.0211	—	
11	LATERAL SPRING FORCE	± 2.5 LB	± .066 deg/LB.sec	.0264	—	
12	SPRING CUP - CIRCUMFERENCE	± .048 IN.	± 2.048 deg/sec/in.	—	.086	S/C ADAPTER
13	SPRING CUP - CIRCUMFERENCE	± .042 IN.	± 2.048 deg/sec/in.	—	.086	
14	S/C - ADAPTER MISALIGN	± .030 IN.	± 5.733 deg/sec/in.	—	.172	
15	LATERAL SPRG FORCE OF SK C.G.	± 1.50 IN.	± .0127 deg/sec/in.	—	.019	1.07 LBS

NOTE (1) REF. PG. 7.1.10  
(2) REF PG. 7.1.12

Reproduced from  
best available copy.

PREPARED T. J. OCKEY 11/3/73

REPORT NO.

PAGE

CHECKED \_\_\_\_\_

MODEL HEAD ASEPARATION ANALYSIS  
TRANSVERSE/ROLL RATESSUMMARY OF PREDICTED SPACECRAFT RATES  
AT SEPARATION.

Table 6-4

LAUNCH VEHICLE RATE - deg/sec		SPACECRAFT RATE - deg/sec		TOTAL S/C RATE deg/sec	
PITCH/YAW	ROLL	PITCH/YAW	ROLL	PITCH/YAW	ROLL
.1 (1)	—	.169 (3)	—	.195 (3)	—
.5 (2)	—	.169 (3)	—	.522 (3)	—
—	.5 (1)	—	.21 (4)	—	.523 (4)
—	1.0 (2)	—	.21 (4)	—	1.021 (4)

NOTES: (1) MINIMUM PER REF. 3  
(2) MAXIMUM PER REF. 3  
(3) REF. PG. 7.1.10  
(4) REF. PG. 7.1.12

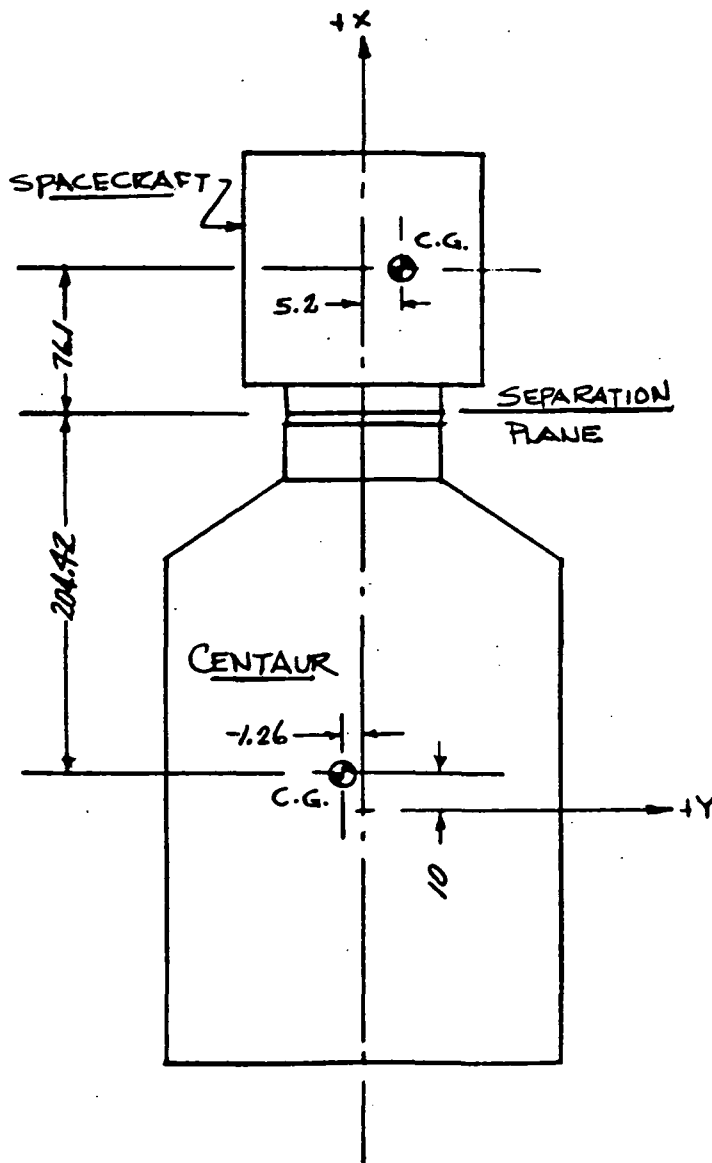


PREPARED T. J. OCKEY 11/1/73

REPORT NO.

PAGE

CHECKED \_\_\_\_\_

MODEL NEAO ASEPARATION ANALYSISSPACECRAFT - CENTAUR - GEOMETRY/MASS PROPERTIESMASS PROPERTIESSPACECRAFT - REF. 1

$$M_1 = 18.133 \text{ LB} \cdot \text{sec}^2/\text{IN.}$$

$$I_z = 52680 \text{ LB} \cdot \text{sec}^2/\text{IN.}$$

$$I_x = 21312 \text{ LB} \cdot \text{sec}^2/\text{IN.}$$

CENTAUR - REF. 2

$$M_2 = 12.914 \text{ LB} \cdot \text{sec}^2/\text{IN.}$$

$$I_z = 207000 \text{ LB} \cdot \text{sec}^2/\text{IN.}$$

$$I_x = 20400 \text{ LB} \cdot \text{sec}^2/\text{IN.}$$

S/C COORDINATE SYSTEM  
NO SCALE

PREPARED T. J. OCKEY 11/2/73

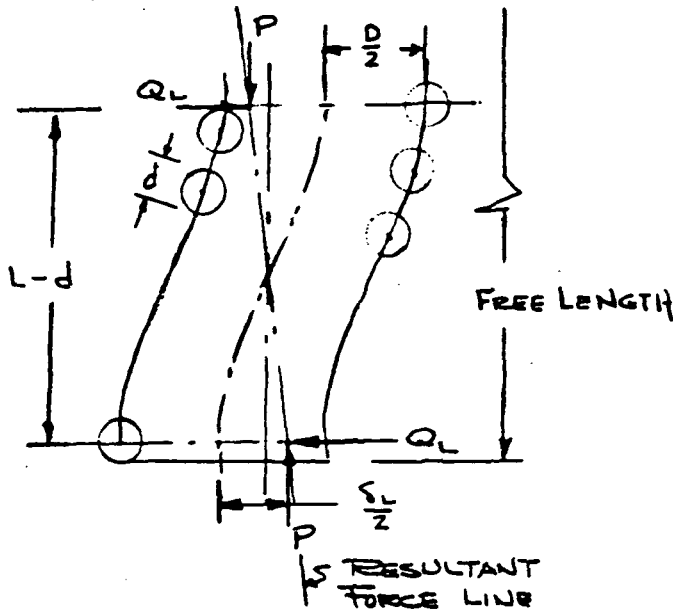
REPORT NO.

PAGE

CHECKED \_\_\_\_\_

MODEL NEAO A

# SEPARATION ANALYSIS



## SEPARATION SPRING DATA

MATL - 17-7PH CRES-DRNG 100702

$$G = 11 \times 10^6 \text{ PSI}$$

$$d = .263"$$

$$D = 3.253"$$

L = LOADED HEIGHT

Y = VERTICAL DEFL

H = 8" FREE LENGTH

N = 5.2 COILS

A = CORRECTION FACTOR

SL = LATERAL DEFL.

REF. "SPRING DESIGN & APPLICATIONS"  
BY N. P. CHIRONIS

LATERAL LOAD FOR STEEL SPRING FOR  $SL = 1.042"$

$$Q_L = \frac{10^6 d^4 S_L}{A D [ .204 (L-d)^2 + .265 D^2 ]} = \frac{200.94}{A (16.9156) [ .204 (L-d)^2 + 2.8042 ]}$$

$$Q_L = \frac{200.94}{A [ 3.451 (L-d)^2 + 47.435 ]}$$

A	Y	$\frac{Y}{H-d}$	$\frac{H-d}{D}$	$(L-d)^2$	$Q_L$
.15	.2	.02585	2.38	56.806	5.4
.53	.5	.0646		52.374	1.7
1.0	1.0	.129		45.387	.98
1.86	2.0	.258		32.913	.67
2.65	3.0	.388		22.439	.61
3.7	4.0	.517		13.965	.57
5.08	5.76	.744	2.38	3.9085	.65

## ADDITIONAL SPRING DATA

$$P = \frac{5.76 (11) 10^6 (.263)^4}{64 (1.625)^3 (5.2)} = 212 \text{ * (AXIAL)}$$

$$\frac{P}{S} = K_A = \frac{212}{5.76} = 36.8 \text{ */IN (AXIAL)}$$

Figure 6-3

PREPARED T. J. OCKEY 10/29/73

REPORT NO.

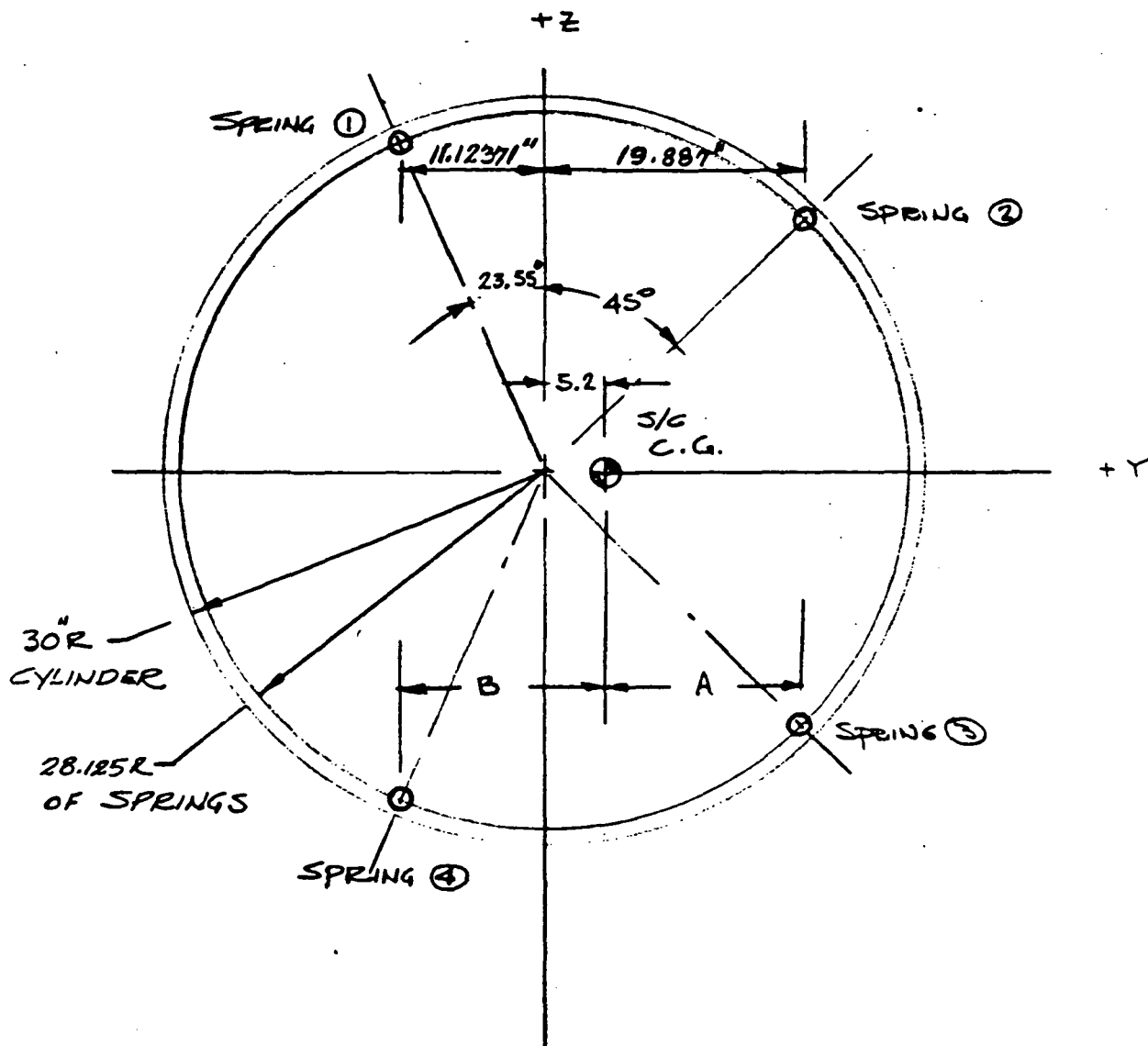
PAGE

CHECKED \_\_\_\_\_

MODEL HEAD A

# SEPARATION ANALYSIS

## SEPARATION SPRING GEOMETRY



NOTE: SPRING LOCATION ABOUT SPACECRAFT C.G., A = 14.687, B = 16.32371 FOR NOMINAL CONDITION.

Figure 6-2

PREPARED T. J. Ockey 11/2/73

REPORT NO.

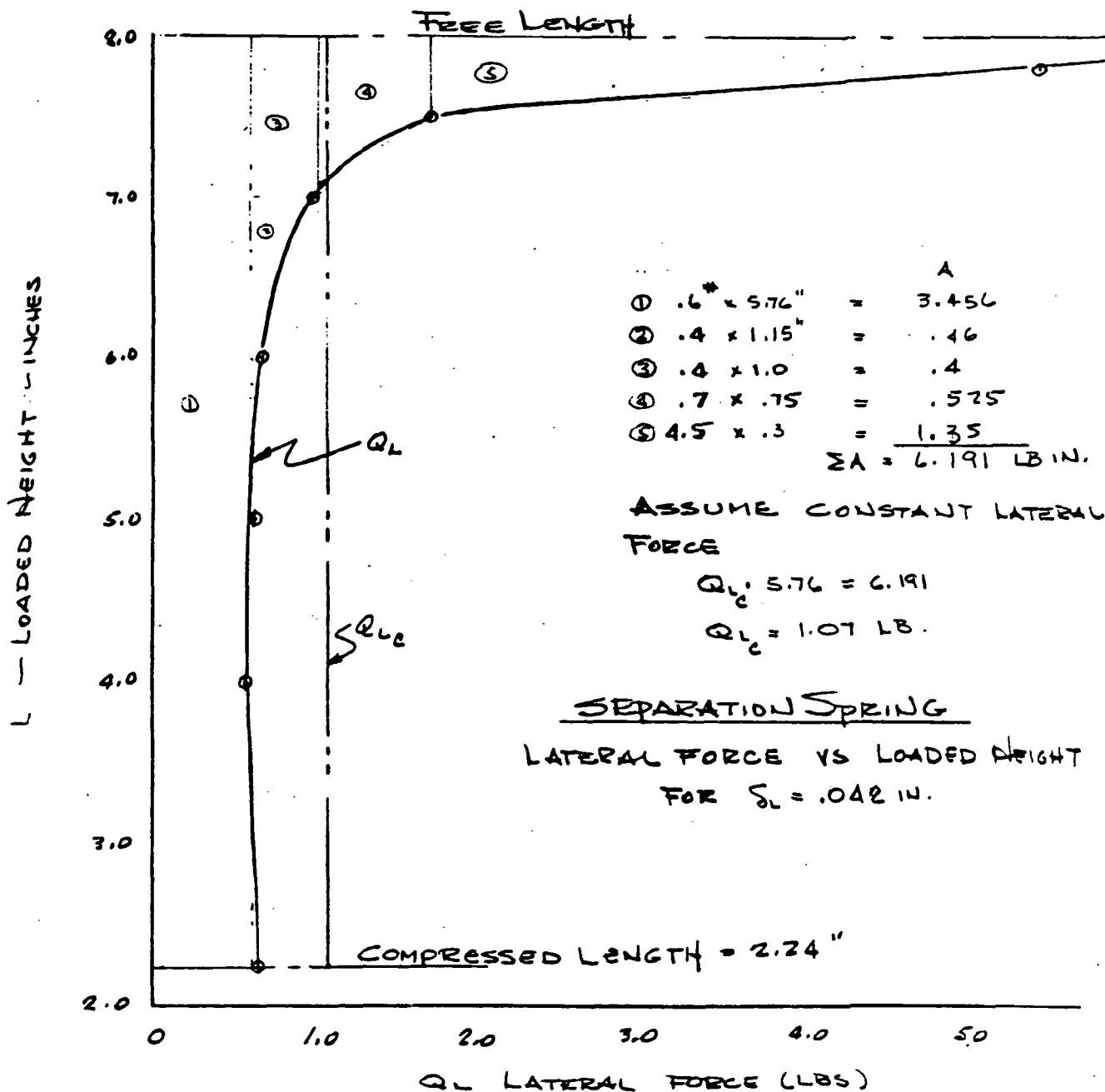
PAGE

CHECKED

MODEL

1040 A

# SEPARATION ANALYSIS



PREPARED T.J. Okey 10/30/73 REPORT NO.

PAGE

CHECKED \_\_\_\_\_

MODEL HEAD A

## S/C SEPARATION ANALYSIS

S/C TIPOFF RATE DISPERSIONS

THE EFFECTS OF VARIOUS SPACECRAFT AND CENTAUR TOLERANCES ON SPACECRAFT TIPOFF RATES PRODUCED BY THE SEPARATION EVENT ARE EVALUATED USING THE METHOD AND TSS COMPUTER PROGRAM OF REF. 4. THE PREDICTED TIPOFF RATE IS COMPUTED FROM:

$$(RSS) \quad W_S = W_N \pm \{W_C^2 + \Sigma(W_K - W_N)^2\}^{1/2}$$

Where  $W_N$  = TRANSVERSE RATE "BIAS"

$W_C$  = BOOSTER INITIAL TRANSVERSE RATE

$W_K$  = TRANSVERSE RATE DISPERSIONS

RESULTING FROM BOOSTER AND SPRING EFFECTS (REF TABLE 1)

TOLERANCES AND RESULTS FROM COMPUTER SOLUTIONS ARE SUMMARIZED IN TABLE 1.

$$\Sigma(W_K - W_N)^2 = [2(.0868^2 + .0252^2 + .091^2) + 4(.005^2 + .0235^2 + .0043^2 + .0064^2 + .0306^2 + .0211^2 + .0264^2)] = .028406$$

## PREDICTED S/C TRANSVERSE RATE

$$W_S = W_N \pm \{.028406\}^{1/2} = \underline{.169 \text{ deg/sec}}$$

REF. 3 FOR LAUNCH VEHICLE INDUCED TIPOFF RATE OF .1 deg/sec PITCH AND YAW THE S/C RATE IS .0988 deg/sec - REF. TABLE 1, CASE 5.

$$(RSS) \quad W_S = \{.0988^2 + .028406\}^{1/2} = \underline{.195 \text{ deg/sec.}}$$

FOR .5 deg/sec LAUNCH VEHICLE INDUCED TIPOFF RATE THE S/C RATE IS .0988(5) = .494 deg/sec

$$(RSS) \quad W_S = \{.494^2 + .028406\}^{1/2} = \underline{.522 \text{ deg/sec}}$$

PREPARED T. J. OCKEY 11/2/73 REPORT NO.

PAGE

CHECKED \_\_\_\_\_

MODEL

NEAO ASEPARATION ANALYSIS  
ROLL RATE DISPERSIONS/C ROLL RATE DISPERSIONS

THIS ANALYSIS CONSIDERS THE EFFECT OF TOLERANCE ON LOCATION OF THE SEPARATION SPRING ENDS (CUPS) AND THE LATERAL SPRING FORCE ASSOCIATED WITH A LATERAL DISPLACEMENT OF THE SPRING ENDS IN CALCULATING S/C ROLL RATES.

1. SPRING CUPS WILL BE LOCATED WITHIN  $\pm .03"$  FROM THE Z AND Y AXIS. RESULTING CIRCUMFERENTIAL DISPLACEMENT IS THE  
$$d_c = (.03^2 + .03^2)^{1/2} \approx \pm .042"$$
2. S/C SEPARATION FLANGE CAN BE INDEXED TO S/C ADAPTER FLANGE WITHIN  $\pm .03"$  ON CIRCUMFERENCE.

LATERAL FORCE OF SPRING IS ASSUMED CONSTANT OVER DEFLECTED LENGTH. REF. PREV. PG.

$$Q_{Lc} = 1.07 \text{ lbs.}$$

AT SEPARATION, THE TORQUE CAUSED BY  $Q_{Lc}$  ACTING PERPENDICULAR TO ROLL AXIS IS:

$$T \approx 1.07 (28.125) = 30.09 \text{ IN LBS}$$

THE SPRING ENERGY CAUSING S/C-CENTAUR ROLL IS

$$KE = 30.09 \times \beta \quad \text{where } \beta \approx \frac{.042}{28.125} \approx .0015 \text{ R}$$

$$KE = .045 \text{ IN LBS/SPRING}$$

TORQUE CAUSED BY LATERAL FORCE VECTOR OFFSET FROM C.G. OF S/C: OFFSET  $\approx 1.5 \text{ IN}$

$$T \approx 1.5 (1.07) = 1.605 \text{ IN LBS}$$

$$KE = 1.605 (.0015) = .00241 \text{ IN LBS/SPRING}$$

PREPARED T. J. O'KEY 11/2/73

REPORT NO.

PAGE

CHECKED

MODEL HEAD A

SEPARATION ANALYSIS  
ROLL RATE DISPERSION

THE FOLLOWING CASES ARE CONSIDERED IN CALCULATING S/C ROLL RATES FOR INDIVIDUAL VARIABLES. THE PREDICTED ROLL RATE IS THE ROOT-MEAN-SQUARE WEIGHTED AVERAGE OF THE INDIVIDUAL RATES. (PAGE

- CASE 12 : SPRING CUP ON S/C  $\pm .042''$   
 CASE 13 : SPRING CUP ON ADAPTER  $\pm .042''$   
 CASE 14 : S/C - ADAPTED MISALIGN  $\pm .030''$   
 CASE 15 : LATERAL SPRING FORCE VECTOR MISALIGN  
 $\pm 1.07 \text{ LBS}, 1.5 \text{ IN. OFF S/C C.G.}$

ASSUME THE S/C AND BOOSTER  $\phi$  COLLINEAR AND COINCIDING WITH S/C AND BOOSTER C.G.'S. THEN CONSERVING ENERGY AND ANGULAR MOMENTUM ABOUT SYSTEM MASS CENTER:

$$\frac{1}{2} I_B \omega_B^2 + \frac{1}{2} I_S \omega_S^2 = K.E.$$

$$I_B \omega_B - I_S \omega_S = 0$$

COMBINING:

$$\omega_S^2 = 2 K.E. \div \left\{ \frac{I_S^2}{I_B} + I_S \right\}$$

$$\omega_S = \left\{ 5.009(10^{-5}) K.E. \right\}^{\frac{1}{2}} \text{ R/sec}$$

$$I_{B_{\text{Roll}}} = 21312 \text{ LB. IN SEC}^2$$

$$I_{S_{\text{Roll}}} = 20400 \text{ LB IN SEC}^2$$

$$\frac{I_S^2}{I_B} + I_S = 39927$$

- CASE 12 :  $K.E. = .045$   $\omega_S = .0015 \text{ R/sec} = .086 \text{ deg/sec}$   
 CASE 13 :  $K.E. = .045$   $\omega_S = .0015 \text{ R/sec} = .086 \text{ deg/sec}$   
 CASE 14 :  $K.E. = .045(4)$   $\omega_S = .003 \text{ R/sec} = .172 \text{ deg/sec}$   
 CASE 15 :  $K.E. = .00241$   $\omega_S = .00034 \text{ R/sec} = .019 \text{ deg/sec}$

$$\text{RSS } \omega_{S_{\text{Avg}}} = \left\{ .086^2 + .086^2 + .172^2 + .019^2 \right\}^{\frac{1}{2}} = .21 \text{ deg/sec.}$$

$$\text{FOR L/V ROLL RATE} = .5 \text{ deg/sec} \quad \text{RSS } \omega_S = \left\{ .5^2 + .21^2 \right\}^{\frac{1}{2}} = .523 \text{ deg/sec}$$

$$\text{FOR L/V ROLL RATE} = 1.0 \text{ deg/sec} \quad \text{RSS } \omega_S = \left\{ 1.0^2 + .21^2 \right\}^{\frac{1}{2}} = 1.021 \text{ deg/sec}$$



## 7. ELECTRICAL DESIGN INTEGRATION

### 7.1 Power Budgets for HEAO-A/C and -B

If a magnetic controller was used for sun acquisition, a long period would be added between the launch phase and the orbital average conditions. The corresponding power requirements are:

	<u>HEAO-A/C (watts)</u>	<u>HEAO-B (watts)</u>
Launch (before liftoff to observatory separation)	191.9	186.4
Sun Acquisition (4 hours)	245.7	299.2
Orbital Average (less experiments)	247.8	274.5
Orbital Average (with experiments)	427.8	488.5

The requirements during the sun acquisition phase include the operation of the wheels for final stabilization. On HEAO-B (the worst case) this power can amount to near 900 watts. This peak power is included in the table above.

### 7.2 Command and Telemetry Requirements

The electromagnet electronics unit will interface with the ACDS transfer assembly for its command telemetry interface requirements. Presently the only commands required are for the selection between the redundant electromagnet electronics assemblies. These commands are easily supplied with the present system hardware. Telemetry signals from the electromagnet electronics are all analog and can be accommodated in the present spacecraft telemetry allocations.

One telemetry function is deleted by the addition of the magnetic controller for a net increase of five telemetry functions for ACS hardware. Approximately 11 telemetry measurements will be deleted and 12 command functions will be deleted from the system for the RCS hardware.

### 7.3 Power Distribution Requirements

The magnetic controller requires both primary power (28V) and secondary voltages for command, telemetry and logic functions. It is assumed for this study that the ACDS TA's will control all power switching to the electromagnet electronics and the magnetometer electronics. It is intended that the magnetometer be channelized with the TA's in terms of power distribution and that the electromagnet electronics will be cross-strapped with the TA's. This includes the command and telemetry functions as well as for the electromagnet electronics.

A separate fused distribution line will be supplied to each electromagnet electronics assembly for supplying 28 volts power to the electromagnets. The generation and susceptibility requirements for the primary power bus is described in Section 7.4, EMI Implications.

The baseline system provides secondary power to the TA's from the SIA converters. The power for the electromagnet electronics and the magnetometer electronics would also come from the SIA converter. Separate windings would be required in order to prevent platform currents from existing between the TA's and the electromagnet electronics. This power would be routed to the TA's for power switching.

### 7.4 EMI Implications

The magnetic controller must be considered relative to electromagnetic interference. The electromagnets and electromagnet electronics will be contributors to the primary power electrical transient environment. Current transients will be relatively mild because of the long time constant inherent in the electromagnet design. Voltage transients will be of moderate severity and must be contained in the subsystem by filtering and shielding. The magnitude of these transients is limited by suppression of the coil back-emf at discharge, which is inherent in the bridge switch configuration chosen, to a voltage step from approximately +28 VDC to approximately -28 VDC of back-emf. These voltage transients will contain considerable high frequency energy due to the use of fast transistor switches.

Large amounts of energy are drawn and delivered by the electromagnets only if used during acquisition when the electromagnet fields would be reversed during control cycling. In cruise mode, the energy stored in the electromagnet fields will be relatively constant on the average, except at initiation and termination of operation. Rigorous filtering of the primary power input, including radio frequency filter elements, will be required to contain these transients.

Both inductive and capacitive coupling from the electromagnets to adjacent interconnect cabling are potential EMC problems. Control of EMI coupling from the electromagnets will require careful routing of interconnect cabling relative to the electromagnets. In addition, interconnect circuits may require twisting and/or shielding.

Potentially the most severe EMC problem due to the electromagnets will be the direct effects of the quasi-static magnetic fields propagated throughout the spacecraft volume on devices employing magnetic fields or materials. Potential magnetic susceptors among the HEAO component complement include:

- Photomultiplier tubes
- Image dissector tubes
- Ferrite core inductors
- Ferrite microwave isolators
- Magnetic tachometer sensors
- Relays
- Solenoid valves
- Plated wire memories
- Tape recorders
- Reference gyros

This problem must be attacked by geometric isolation (placement and orientation) of susceptible components to achieve tolerable magnetic environments for each. Magnetic shielding of susceptible elements can

also be implemented but should be limited to avoid degrading the stability of the spacecraft magnetic field as viewed by the control magnetometer. Magnetic shielding materials are by nature magnetically soft and may maintain some residual fields.

The control magnetometer will be susceptible to degradation primarily from spacecraft power currents and unpredictable changes in the spacecraft magnetic field. The single point ground scheme for spacecraft power will protect the magnetometer from uncontrolled power currents. Limiting the use of magnetically soft materials contributes to stabilizing the spacecraft field. The control magnetometer is being placed to reduce spacecraft EMI effects on the instrument.

In conclusion, the EMC impact of the magnetic controller will be real but not insurmountable. Rigorous filtering and shielding of the electromagnet electronics will be required. Interconnect cabling protection, including twisting and shielding, may be necessary on specific additional circuits. Placement and orientation of some components will be constrained.

## 8. ELECTRICAL SUBSYSTEM

Because of increased ACDS power, the Electrical Subsystem is required to supply additional orbital power (HEAO-A, and -C). If magnetics were used for acquisition, then additional launch-acquisition power (for approximately four hours) would be necessary. These requirements are tabulated below:

<u>S/C</u>	<u>Power Requirement (Watts)</u>			
	<u>Launch</u>	<u>Acquisition</u>		<u>Orbital <math>\Delta</math>*</u>
		<u>Power</u>	<u><math>\Delta</math></u>	
HEAO-A	192.4	245.7	+42.7	+44.5
HEAO-B	186.4	299.2	+19.2	- 5.8
HEAO-C	192.4	225.7	+68.4	+44.5

In order to satisfy the orbital requirements, additional solar array is required for HEAO-A and -C and all three S/C will need the capability to operate at large battery depths of discharge during launch, if magnetics are used for acquisition.

Assuming that the baseline HEAO-A array is the two upper module configuration shown in Figure 8-1, the requirements for additional power could be met by the three module configuration of Figure 8-2. Characteristics of the two configurations at 6 months life are tabulated below:

	<u>Configuration</u>	
	<u>2 Upper Modules</u>	<u>3 Upper Modules</u>
Load Capability	459 watts	505 watts
$\Delta$ Load	--	+46 watts
$\Delta$ Weight	--	+25 pounds

HEAO-C with a 40 watt lower load requirement could possibly be powered by a two module configuration with related savings in weight and cost. HEAO-B average orbital power requirements decrease slightly and require no array increase.

If magnetics are used for acquisition then supplying the launch and acquisition loads of 245.7 watts for HEAO-A and 229.2 watts for HEAO-B would result in battery depth of discharge (DOD) of 50% and 60% respectively.

\* Does not include contingency

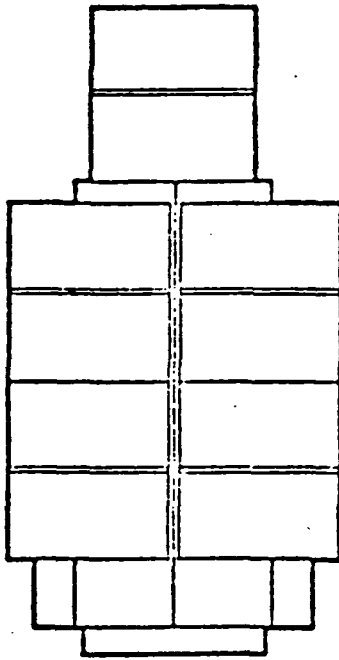


Figure 8-1. HEAO-A with Two Upper Modules

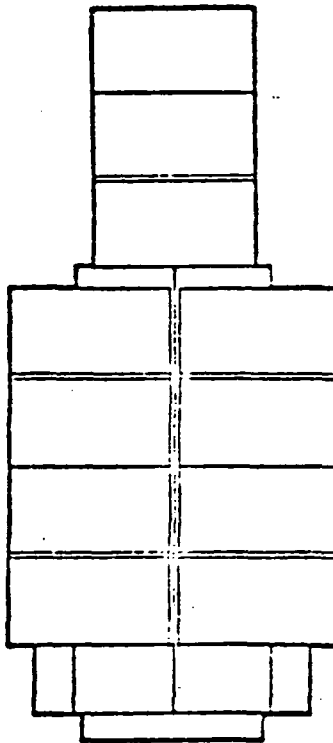


Figure 8-2. HEAO-A with Three Upper Modules

This is based upon a worst case assumption of no sunlight for the four hour period. Should the S/C spin so that the Z-- axis points near the sun periodically, then DOD will be reduced dependent upon time and sun angle. With the S/C spinning in either the Y-Z or X-Z planes and array shadowing occurring in eclipse, DOD's could be reduced to 20% and 25% respectively. In either case, DOD's approaching 50% or 60% are considered to be within the battery capability for onetime operation, at beginning of life.



## 9. EXPERIMENT INTEGRATION

Experiment Integration support to the magnetic torque control study was concerned with the following tasks.

- a) Calculation of magnetic field due to single solenoid of given length, radius, number of turns, current, and core permeability.
- b) Calculation of the magnetic field due to a rectangular current loop as an approximation to the field due to current flowing in the solar array.
- c) Calculation of the field at the magnetometer due to the solar array current.
- d) Assessment of the field at the magnetometer due to the permanent magnets in experiments A-1 and A-2 on HEAO-A.

Each of these will be discussed in turn.

- a) We start with the expression for the vector potential of a single current loop of radius  $a$ , current  $I$ , and permeability  $\mu$  in cylindrical coordinates  $(\rho, z)$  with the coil axis along the  $z$ -axis and the turn in the  $x$ - $y$  plane with center at the origin.  $\phi$  is the angle in the  $x$ - $y$  plane measured from the  $x$ -axis. From the axial symmetry of the problem, the only non-zero component of the vector potential  $\vec{A}$  is  $A_\phi$ .

$$A_\phi = \frac{\mu I}{10} \oint \frac{ds}{R} = \frac{\mu I}{5} \int_0^\pi \frac{a \cos \phi d\phi}{[a^2 + \rho^2 + z^2 - 2a\rho \cos \phi]^{1/2}}$$

where  $I$  is in amperes,  $\mu$  is in gauss/oersted and all lengths are measured in centimeters. If we now consider a solenoid of  $n$  turns per unit length and of total length  $2\ell$ , then

$$A_\phi = \frac{\mu I a n}{5} \int_{z-\ell}^{z+\ell} d\alpha \int_0^\pi \frac{\cos \phi d\phi}{[\alpha^2 + a^2 + \rho^2 - 2a\rho \cos \phi]^{1/2}}$$

The field components are obtained from  $\vec{A}$   
according to  $\vec{B} = \text{curl } \vec{A}$

$$\text{In our case } B_\rho = -\frac{\partial A_\phi}{\partial z} \text{ and } B_z = \frac{1}{\rho} \frac{\partial}{\partial \rho} (\rho A_\phi)$$

after carrying out the integration and partial differentiation,  
we obtain for the field components:

$$B_\rho = -\frac{\mu I n a}{5} \int_0^\pi \frac{\cos \phi \, d\phi}{[\alpha^2 + a^2 + \rho^2 - 2a\rho \cos \phi]^{1/2}} \quad \left| \begin{array}{l} \alpha = z+l \\ \alpha = z-l \end{array} \right.$$

and

$$B_z = \frac{\mu I n a}{5} \int_0^\pi \frac{\alpha (a - \rho \cos \phi) \, d\phi}{[\alpha^2 + a^2 + \rho^2 - 2a\rho \cos \phi]^{1/2} [a^2 + \rho^2 - 2a\rho \cos \phi]} \quad \left| \begin{array}{l} \alpha = z+l \\ \alpha = z-l \end{array} \right.$$

where evaluation at the  $\alpha$  limits may be carried out after evaluation of the  $\phi$  integrals.

The  $\phi$  integrals can be evaluated in closed form in terms of known tabulated functions. The results are given below:

$$B_z = \frac{\pi \mu I n}{10} \left[ \frac{\alpha k}{\pi \sqrt{a\rho}} K(k) - \left| \frac{(\rho - a)\alpha}{(\rho + a)\alpha} \right| \lambda_0(\beta, k) \right] \quad \left| \begin{array}{l} \alpha = z+l \\ \alpha = z-l \end{array} \right.$$

$$B_\rho = -\frac{\mu n I}{5} \left( \frac{a}{\rho} \right)^{1/2} \left[ \frac{(2 - k^2)K(k) - 2E(k)}{k} \right] \quad \left| \begin{array}{l} \alpha = z+l \\ \alpha = z-l \end{array} \right.$$

where  $K(k)$  and  $E(k)$  are complete elliptic integrals of the first and second kind respectively and  $\lambda_0(\beta, k)$  is the Heuman Lambda Function\*, and where

---

\*All these functions are tabulated in "Handbook of Elliptic Integrals for Engineers and Physicists" P. F. Byrd and M. D. Friedman; Springer-Verlag 1954.

$$k^2 = \frac{4ap}{a^2 + (a+p)^2} \quad \text{and} \quad \beta = \tan^{-1} \left| \frac{a}{p-a} \right|$$

Unfortunately, the above expressions, while correct, were not practical to use for numerical calculations of interest in the present study. This is because one is dealing with the difference between two numbers which are very nearly equal. Thus, the errors are relatively large.

A satisfactory program was written, however, to numerically integrate the previous algebraic expressions for  $B_p$  and  $B_z$ . This led to consistent accurate results.

To take into account the iron core, an effective permeability  $\mu'$  was used where

$$\mu' = \frac{\mu}{1 + (\mu - 1)L} \quad \text{where } L \text{ is a "demagnetizing factor."}$$

We approximate the long iron core by a prolate spheroid. (The case of a cylindrical rod cannot be solved analytically.) In this approximation

$$L = \frac{1}{2} \left( \frac{1-e^2}{e^3} \right) \left[ \ln \frac{1+e}{1-e} - 2e \right]$$

$$\text{where } e \text{ is the eccentricity} = \left( 1 - \frac{c^2}{a^2} \right)^{1/2}$$

and the length of the major axis is  $2a$  and the minor axes lengths are equal to  $2c$ .

The solenoid parameters used in the calculations were as follows:

$$\mu' I = 406 \text{ ampere-gauss-oersted}^{-1}$$

$$a = 2.095 \text{ cm}$$

$$2\ell = 148 \text{ cm}$$

$$N = 6545 \text{ turns}$$

$$n = 4.2 \text{ turns/cm}$$

Tables 9-1 and 9-2 show the results of the calculations for a single coil. These tables represent the maximum field that the coil can produce if magnetics were used for acquisition.

Table 9.1 Electromagnet Near Field (Gauss)\*

		$\rho(\text{in})$									
		10	20	30	40	50	60	70	80	90	100
$\rho(\text{in})$	10	10.1	5.91	3.30	1.92	1.18	.764	.517	.365	.265	.199
	20	21.8	8.13	3.79	2.05	1.22	.777	.523	.367	.266	.199
	30	38.0	9.28	3.93	2.06	1.21	.773	.520	.365	.265	.199
	40	17.0	6.92	3.35	1.86	1.13	.735	.501	.355	.260	.196
	50	6.60	4.11	2.45	1.52	.983	.664	.465	.336	.249	.189
	60	3.18	2.41	1.69	1.17	.811	.575	.417	.309	.233	.180
	70	1.79	1.50	1.16	.874	.649	.484	.364	.277	.214	.168
	80	1.11	.981	.816	.653	.513	.399	.312	.244	.193	.154
	90	.742	.677	.588	.493	.404	.327	.264	.212	.172	.139
	100	.522	.486	.435	.377	.320	.268	.222	.183	.151	.125

Table 9.2. Electromagnet Intermediate Field (Gauss)

		$\rho(\text{in})$			
		150	200	250	300
$z(\text{in})$	150	.0371	.0205	.0120	.00745
	200	.0247	.0157	.0100	.00660
	250	.0163	.0115	.00801	.00560
	300	.0110	.00842	.00627	.00464

\*The variables  $\rho$  and  $z$  represent the radial and axial distance (respectively) from the electromagnet center.

- b) In order to calculate the magnetic field due to the solar array, the field due to a rectangular current loop was derived in the following manner.

We use rectangular coordinates and place the loop in the x-y plane with center at the origin. The loop is of length  $2\ell$  in the x-direction and length  $2m$  in the y-direction. Then the z component of the vector potential vanishes and we have

$$A_x = \frac{\mu I}{10} \int_{-\ell}^{\ell} dx \left( \frac{1}{r_1} - \frac{1}{r_2} \right)$$

$$A_y = \frac{-\mu I}{10} \int_{-m}^m dy \left( \frac{1}{r_3} - \frac{1}{r_4} \right)$$

where  $r_1^2 = x^2 + (y-m)^2 + z^2$

$$r_2^2 = x^2 + (y+m)^2 + z^2$$

$$r_3^2 = (x-\ell)^2 + y^2 + z^2$$

$$r_4^2 = (x+\ell)^2 + y^2 + z^2$$

Current is in amperes, lengths in centimeters and  $\mu$  in gauss/oersted.

Since  $\vec{B} = \text{curl } \vec{A}$

$$B_x = \frac{\partial A_y}{\partial z}, B_y = -\frac{\partial A_x}{\partial z}, B_z = \frac{\partial A_x}{\partial y} - \frac{\partial A_y}{\partial x}$$

Carrying out the integrations and partial differentiations, we get

$$B_x = \frac{\mu I z}{5cd(d+m)(c+m)} \left[ m(c-d) - 4x\ell \right] + \frac{\mu I z}{5} \left( \frac{1}{b_1^2} - \frac{1}{b_2^2} \right)$$

$$B_y = \frac{\mu I z}{5fg(f+\ell)(g+\ell)} \left[ \ell(f-g) - 4ym \right] + \frac{\mu I z}{5} \left( \frac{1}{a_1^2} - \frac{1}{a_2^2} \right)$$

$$B_z = \frac{\mu I \ell}{5} \left( \frac{y+m}{a_2^2 g} - \frac{y-m}{a_1^2 f} \right) + \frac{\mu I m}{5} \left( \frac{x+\ell}{b_2^2 d} - \frac{x-\ell}{b_1^2 c} \right)$$

$$\text{where } a_1^2 = (y-m)^2 + z^2 \quad a_2^2 = (y+m)^2 + z^2$$

$$b_1^2 = (x-\ell)^2 + z^2 \quad b_2^2 = (x+\ell)^2 + z^2$$

$$c^2 = b_1^2 + m^2 \quad d^2 = b_2^2 + m^2$$

$$f^2 = a_1^2 + \ell^2 \quad g^2 = a_2^2 + \ell^2$$

- c) The solar array current loop which was closest to the magnetometer was used to calculate the field at the magnetometer. It was shown that the effect of superimposing the fields due to the other loops in the solar array panel made a negligible contribution compared to the nearest loop.

The parameters for this closest loop were:

$$x = 0, y = 1.725, z = 4.94, m = 2.5, \ell = 27$$

$$I = 0.75 \text{ ampere and } \mu = 1 \text{ gauss/oersted}$$

where all dimensions are in inches.

The results are:

$$B_x = 0$$

$$B_y = 4.76 \times 10^{-3} \text{ gauss}$$

$$B_z = 7.91 \times 10^{-3} \text{ gauss}$$

$$|B| = 9.23 \times 10^{-3} \text{ gauss}$$

This is less than 2% of the earth's field and therefore should not interfere with the magnetometer.

- d) For experiment A-1, we start with their proposed broom made up of 150 Gecor magnet chips per module, each with a magnetic moment  $M$  of 1.59 ampere  $\text{-cm}^2$  or  $1.59 \times 10^3$  abampere  $\text{-cm}^2$ . We

assume the worst case - namely that there is no attempt to compensate the dipole moment by aligning the magnets in adjacent modules in the opposite sense. We further assume that the magnetometer to nearest module distance is large enough (103 inches) to permit using the dipole approximation. We also ignore the field direction and just take the magnitude to be  $\frac{M}{R^3}$  gauss where R is the distance in cm. We measure all distances along the x-axis from the module center lines in the y-z plane. Thus we have one module at the closest distance, three at the next closest and two at the furthest distance. The total magnetic moment of each module then is  $2.385 \times 10^5$  abampere-cm<sup>2</sup>. The three distances involved are 261 cm, 373 cm, and 475 cm.

Therefore, in this conservative, worst case approximation

$$B = 2.385 \times 10^5 \left[ \frac{1}{(261)^3} + \frac{3}{(373)^3} + \frac{2}{(475)^3} \right] \text{ gauss.}$$

$B = 0.03$  gauss.

Although this is only about 10% of the earth's field, we feel we have overestimated the calculated field by at least an order of magnitude. We conclude, therefore, that the magnetic brooms in Experiment A-1 will not interfere with the intended operation of the magnetometers.

At the time of this report, we have not yet been able to get the necessary information from Experiment A-2 in order to assess the magnitude of the magnetic field at the magnetometers due to their magnets. The distance, however, from the center of their low energy modules to the magnetometers is 104 inches. Furthermore, their field component in that direction is near the minimum. Therefore, we anticipate that the A-2 magnetic brooms will not present a problem for the magnetometers in their proposed location.



## 10. COMMUNICATIONS AND TAPE RECORDER

10.1 Design Implications of Magnetic Fields.10.1.1 Transponder

The transponder is sensitive to magnetic fields as a result of a ferrite isolator used in the output of the transmitters. This isolator is necessary to protect the transmitter from open circuits or short circuits that may cause large amounts of reflected power impinging upon the transmitters. When an external magnetic field is applied to the transponder the isolator losses increase above the nominal value. At a magnetic field level of 25 gauss the increased loss reaches 0.2 to 0.3db which is considered the maximum tolerable for undegraded subsystem performance. Results of the magnetic tests performed on the transponder are summarized in paragraph 10.4.

A design modification to delete the isolator would violate the MSFC specification and would not be recommended due to the susceptibility of the transmitter to reflected power.

Shielding the isolator does not appear practical due to the limitations of space within the transponder. There are two possible solutions that are acceptable to the communication hardware. These are shielding the entire transponder to reduce the field of 25 gauss or locating the unit where the ambient level is below the sensitive level of 25 gauss.

10.1.2 Tape Recorder

The tape recorder is a major concern with regards to the ambient magnetic fields. Since the unit is a magnetic tape recorder, any field levels near the record level will degrade the performance of the unit. Tests were performed on a A-E tape recorder to establish the levels of sensitivity. The results of these tests and detailed analysis of the mechanics of the interference are included in a report provided in paragraph 10.3. The tests indicated that the tape itself is sensitive to an external field once the field is above 5 to 10 gauss and is

completely degraded at 30 gauss. Also the tape appears to take on a "bias" once it has been exposed to an external field making it more sensitive to the next exposure. This increases the sensitivity by approximately 5 gauss. In the record and playback mode the read and record heads are affected by the external field. The read bit errors go from zero (0) with no external field applied to all errors and levels above 25 gauss. Again the threshold of sensitivity appear to be near 5 gauss. From this it can be seen that the recorder is somewhat more sensitive to (by approximately 5 gauss) external magnetic fields when in the record and playback mode then when it is in the standby or off mode. Additionally, tests were made on the unit's inherent magnetic field before and after exposure and as can be seen from the test report the unit takes on an increased self magnetism as a result of the externally applied field. This increased magnetization however did not appear to degrade the units performance once the external field was removed.

Shielding the entire tape recorder or keeping it in fields below 5 gauss appears to be the only practical way of protecting the unit. Shielding of individual sensitive components (tape, recording playback heads) is not practical within the present configuration.

#### 10.2 Magnetic Field Limitations

The maximum magnetic field in which both the transponder and the tape recorder can be operated without degradation has been determined by testing each unit in a magnetic field. As stated in the preceeding paragraphs the transponder can operate in a field up to 25 gauss with acceptable performance degradation. The tape recorder must be operated in a field of 5 gauss or less to eliminate data errors. It is expected that the units can tolerate fields up to 100 gauss without permanent damage.

### 10.3 Tape Recorder Test Results and Analysis

#### 10.3.1 Susceptible Elements in a Magnetic Recorder

The A-E tape recorder is shown in Figure 10-1 and the susceptible magnetic components illustrated in Figure 10-2. The effect of a field on the motor, tachometer and relays (if any) are discussed later.

The magnetic heads are fabricated from high permeable ( $\mu \approx 10^4$ ) materials and will therefore attract flux lines through them. The magnetic tape has a .2 mil thick coating consisting of roughly 30% minute permanent magnet particles. The effective permeability is very low, (1-3) and the tape packs on the reels will have negligible effect on the external field.

Figures 10-3, 10-4 and 10-5 show how three different field orientations are deflected by passage through the recorder. From these we can deduct the following information:

##### 10.3.1.1 Concentration of Fields by Magnetic Heads

The perpendicular field causes no contribution to the useful longitudinal field in the gap, i.e., it should not effect erasure, recording or playback. The side-to-side field does concentrate the field in the head gap where it could off-set an otherwise symmetrical recording field and cause partial erasure at the playback gap. It would further dc magnetize the tape at the erase gap.

The front-to-back field gives the largest field concentration in the gaps and the effects mentioned in the preceding paragraph are accentuated. The fields in the gaps are moreover longitudinal and will hence interfere directly with the intended field in the magnetic erase, record and playback design.

An order-of-magnitude estimate is in order. Assume the external field has a strength of  $H_0$  Oersted and roughly approximating the core structure with a sphere, the internal flux is

$$B = \mu H_0$$

where  $\mu$  is the permeability of the core. The bulk permeability, after

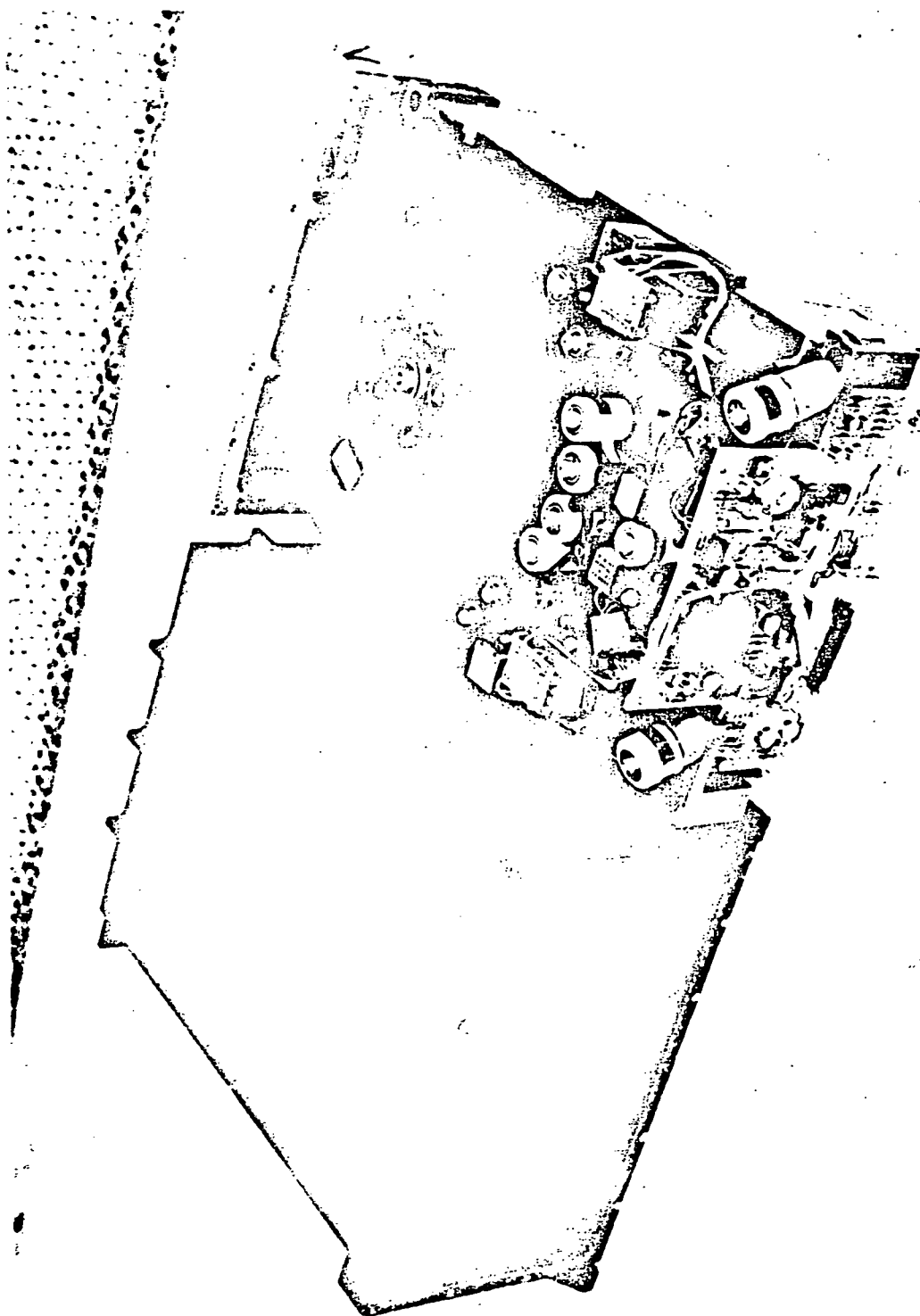


Figure 10-1. OSO Tape Recorder out of Enclosure

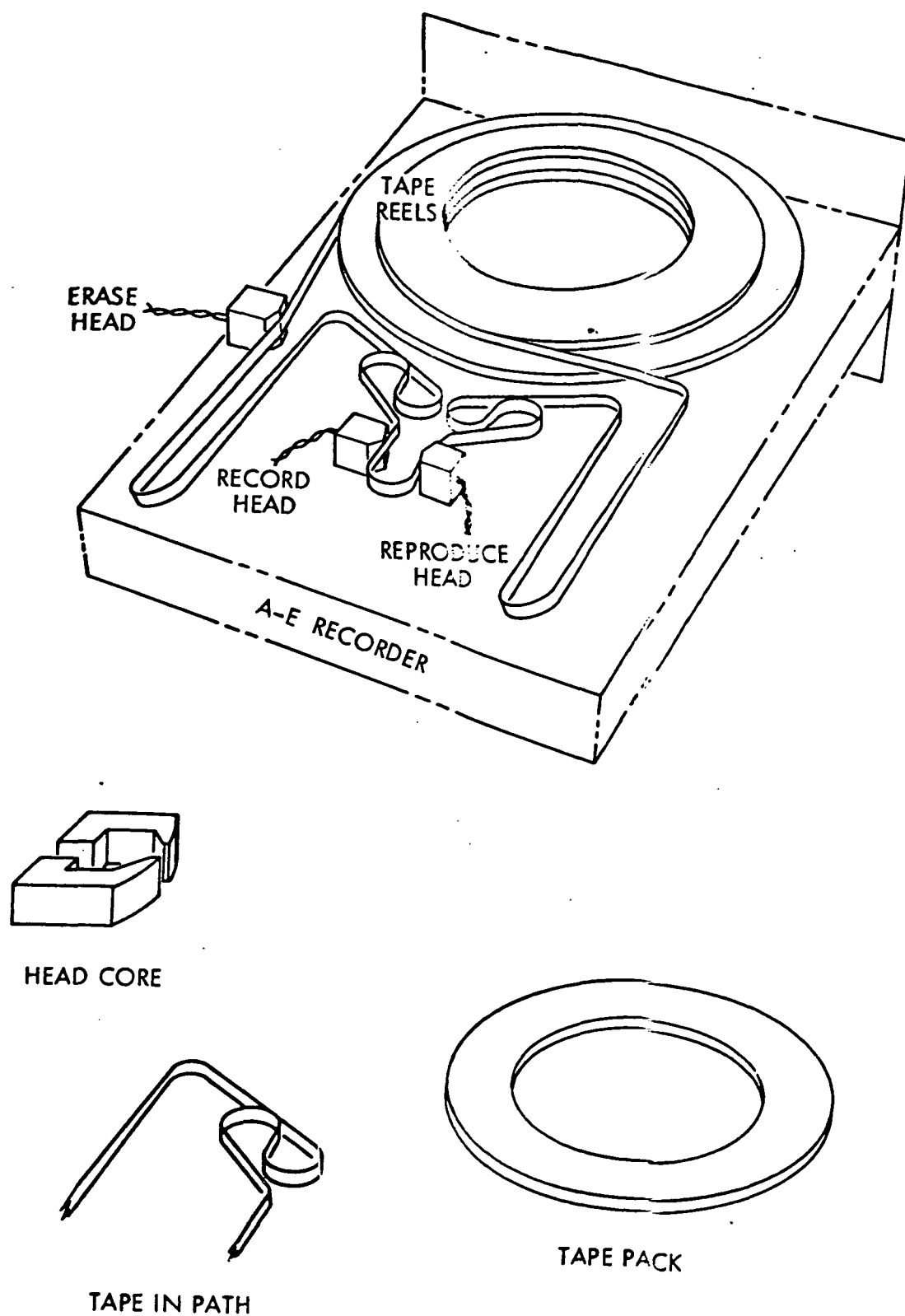


Figure 10-2. Magnetic Components in A-E Tape Recorder  
(Except Motor, Tachometer and Relays)

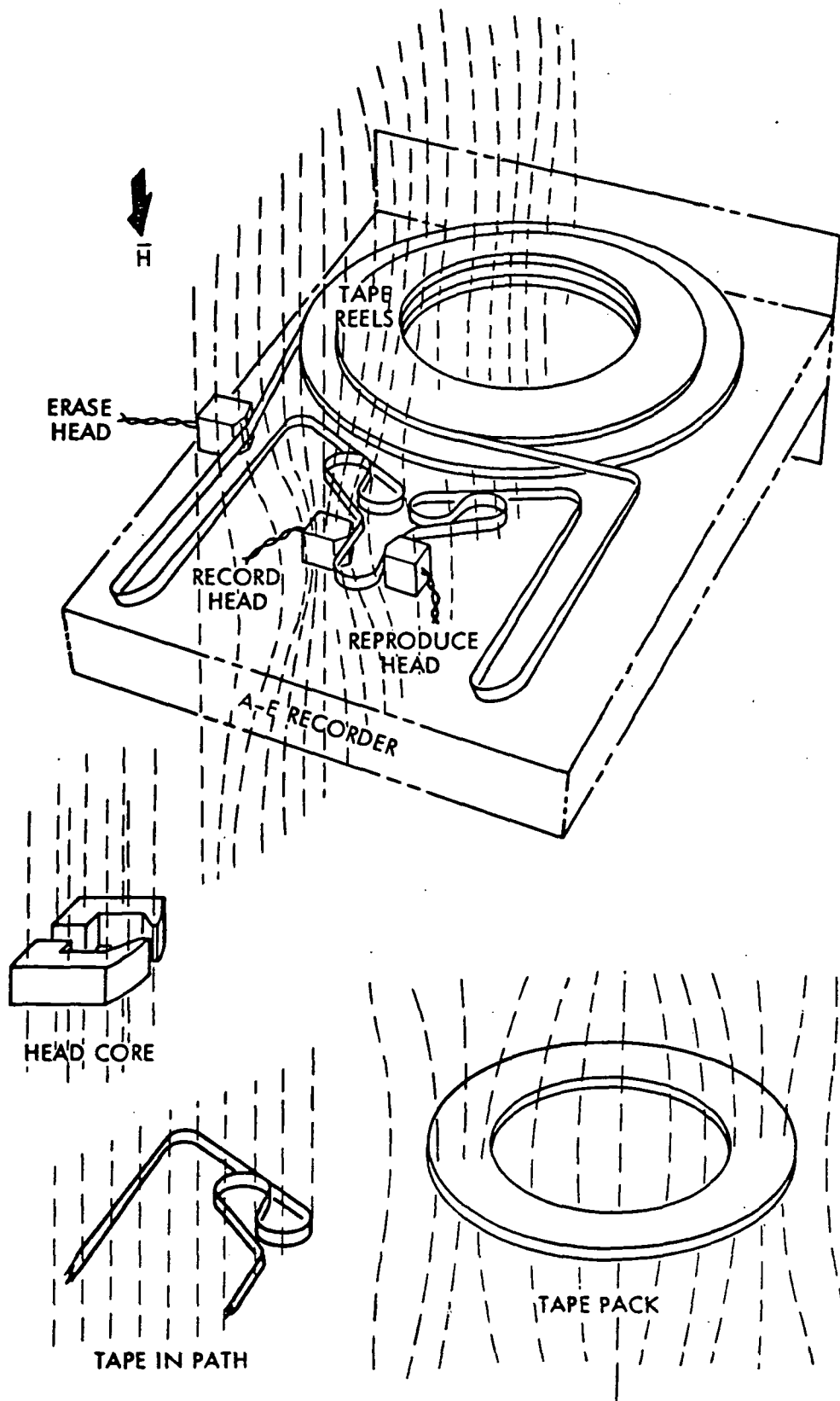
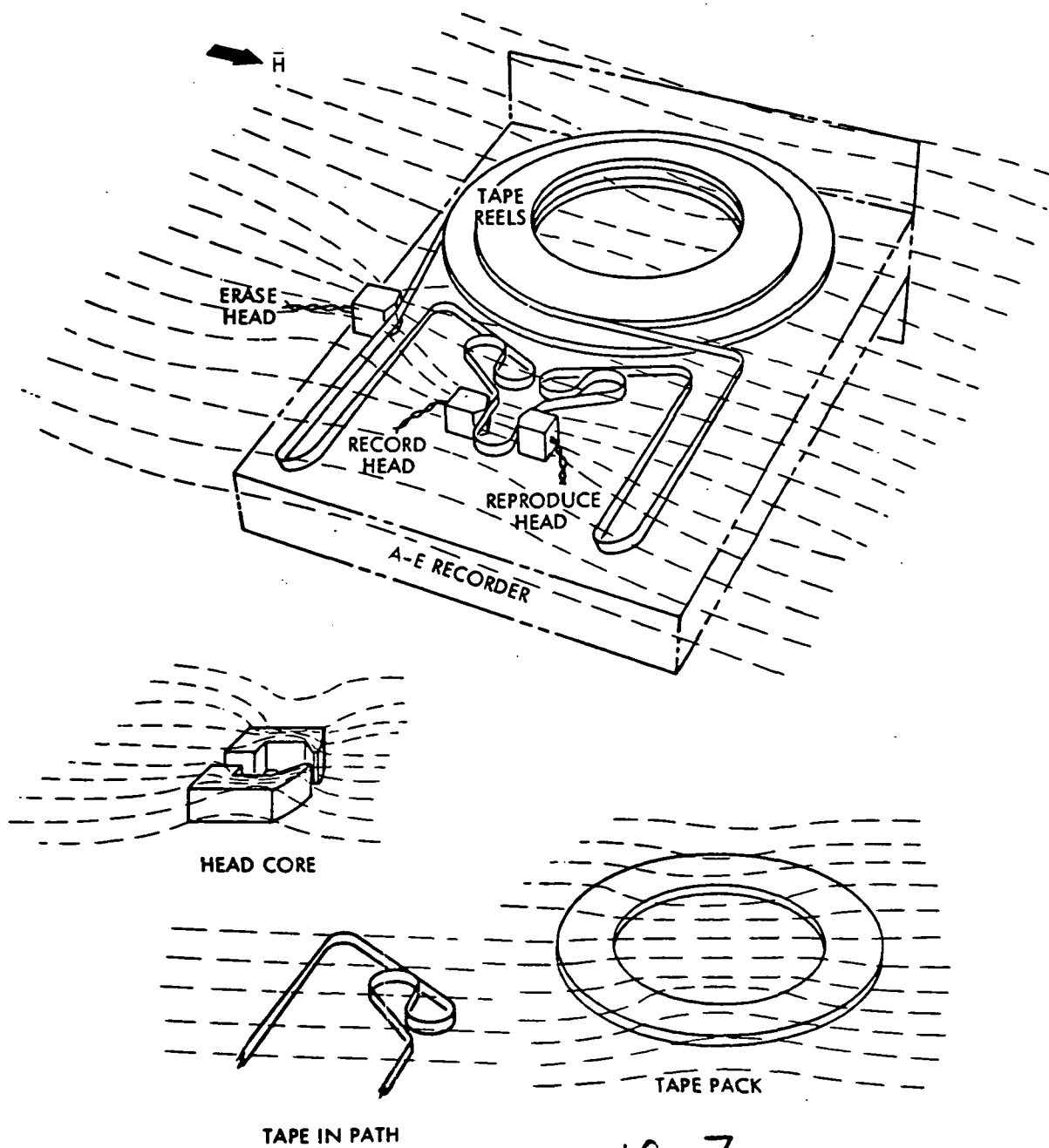


Figure 10-3. Deflection of a Perpendicular Magnetic Field



10-7

Figure 10-4. Deflection of a Side-to-Side Magnetic Field



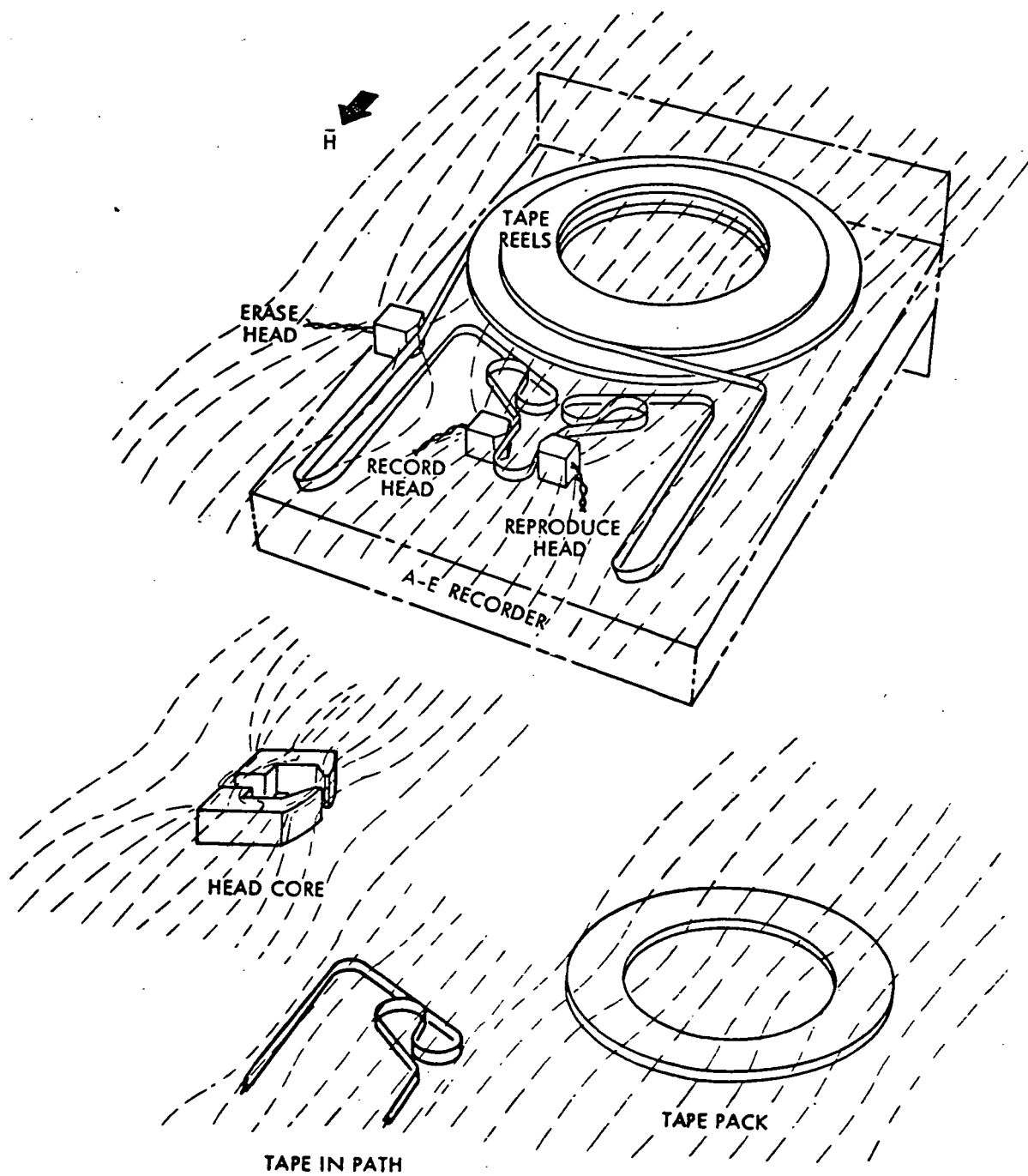


Figure 10-5. Deflection of a Front-to-Back Magnetic Field

head fabrication is in the order of  $10^3$ . The presence of gaps in the core reduces this to an effective value of 30 (for a typical record head). The internal flux is further reduced by demagnetization of the assumed sphere, which is a factor of  $1/3$ .

An external field of magnitude  $H_0$  will therefore produce a core flux of roughly  $10 \times H_0$ , a fact we shall use later.

#### 10.3.1.2 Deflection of Field by Magnetic Tape Pack

The effective permeability of the tape pack is so close to one (1) that field deflections can be disregarded. The field direction will however have influence on the magnitude of erasure.

The perpendicular field will be reduced inside the tape pack due to demagnetization:

$$H = H_0 - N \times J$$

where  $H$  is the inside field,  $N$  the demagnetization factor and  $J$  the magnetic intensity formed on the outside layer of the pack. The magnitude of  $N$  is approximately (1) for a field perpendicular to a plate, and we can therefore predict reduced erasure of inside recorded tracks as compared to edge tracks, i.e., the tape pack serves as a shield for its own tracks (although with low efficiency).

The side-to-side or front-to-back fields do penetrate the tape packs since the demagnetization factor is less than  $10^{-1}$  for a disc in these field orientations.

#### 10.3.1.3 Deflection of Field by Magnetic Tape

The free tape in the tape path through the recorder has negligible effect on the magnetic field lines.

The perpendicular field will cause a dc magnetization bias of the magnetic coating, which will affect any recording. This effect will be less than found for the side-to-side or front-to-back fields, where the tape loops back and forth and therefore is subjected to fields of alternating orientation.

### 10.3.2 Erasure of Magnetic Tape

Accidental erasure of magnetic recordings have been reported in the past, and MMM Co. experimented to find the amount of erasure for a given AC-field strength. Their data are plotted in Figure 10-6.

A qualitative analysis of erasure in a dc field is illustrated in Figures 10-7 and 10-8. (Erasure is really a misleading term, distortion of recorded data is more appropriate.)

The tape has, in Figure 10-7, been NRZ-saturation recorded, with polarities  $-B_s$  and  $+B_s$ . Exposure to an external positive field has no effect on the  $+B_s$  polarities, while increasing field strength cause the  $-B_s$  polarity to shift toward and into positive values  $-B'_s$ ,  $-B''_s$ , and  $-B'''_s$  by following the minor and major hysteresis loops. The corresponding remanence values (after removal of the external field) are  $-B'_r$ ,  $-B''_r$ , and  $-B'''_r$ , by following minor loops. The net result is shown in Figure 9, that shows signal degradation and erasure for increasing fields. Erasure is not complete except for very large fields ( $H > 100$  gauss), but the drastic increase in erasure above 200 gauss is evident, corresponding to Figure 10-6.

A recording at a level of 6db below saturation suffers a similar degradation, (refer to Figures 10-8 and 10-10). Both positive  $+B_r$  and negative  $-B_r$  magnetizations are affected and complete erasure occurs above 500 gauss.

If the recording is subject to an alternating field, as is the case where the tape loops through the recorder (see Figures 10-4 and 10-5, bottom), the degradation is even worse. The result is shown in Figure 10-14, constructed from the hysteresis loops in Figures 10-11, 10-12 and 10-13.

Here the transition between minimal and maximum erasure is even more pronounced, occurring around 270 gauss, which is a typical value for the coercivity  $H_c$  of a magnetic tape.

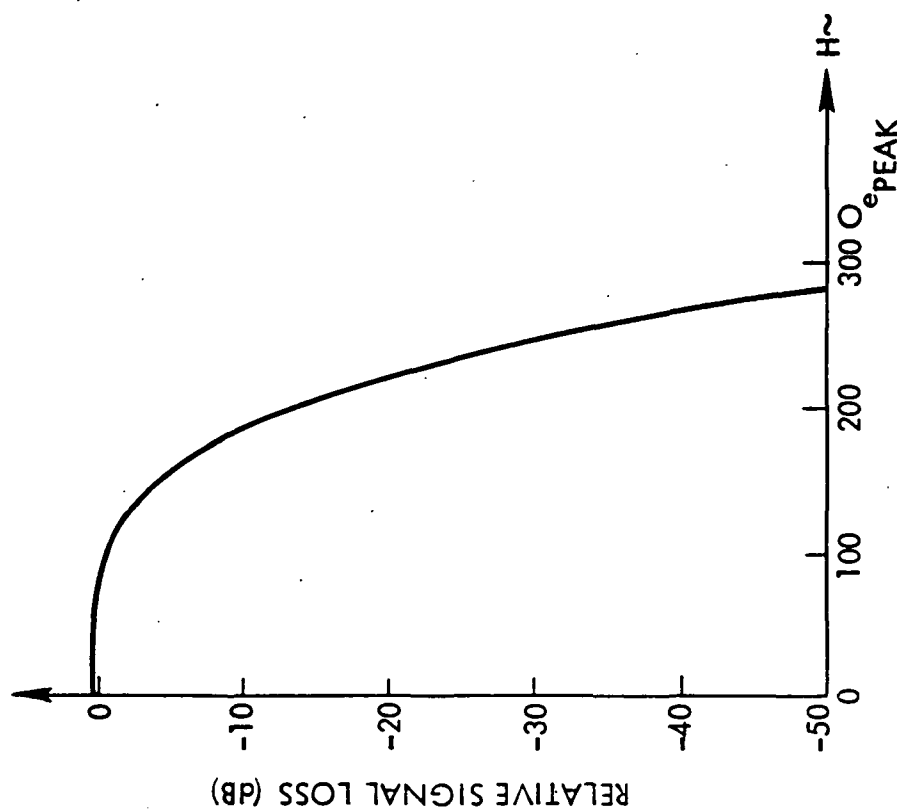


Figure 10-6. Erasure of Magnetic Tape in an A.C. Magnetic Field (after  $3MC_0$ )

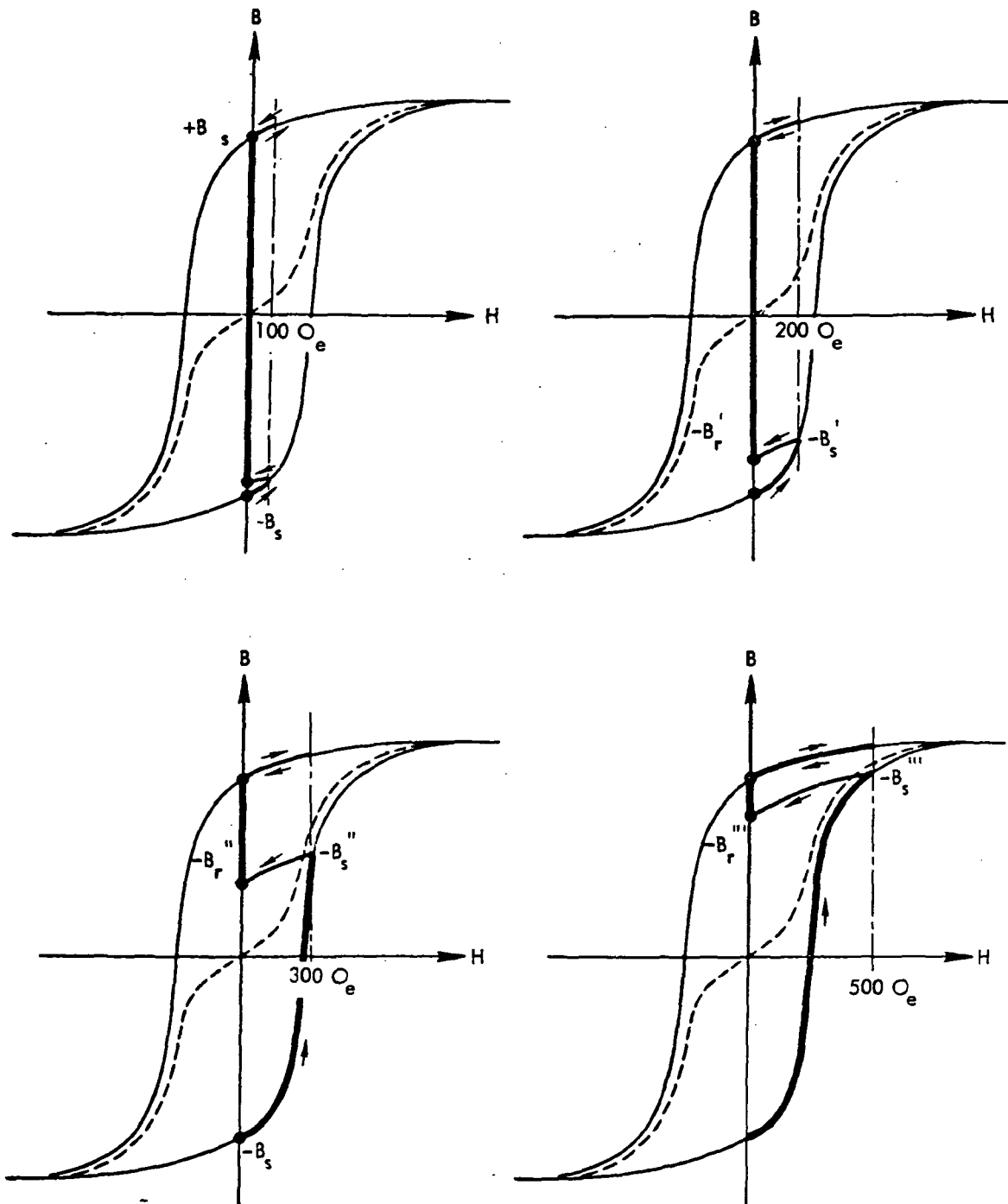


Figure 10-7. Distortion of Recorded Data in a DC Magnetic Field of Strengths 100, 200, 300 and 500 Oersted. Original Recording Saturation

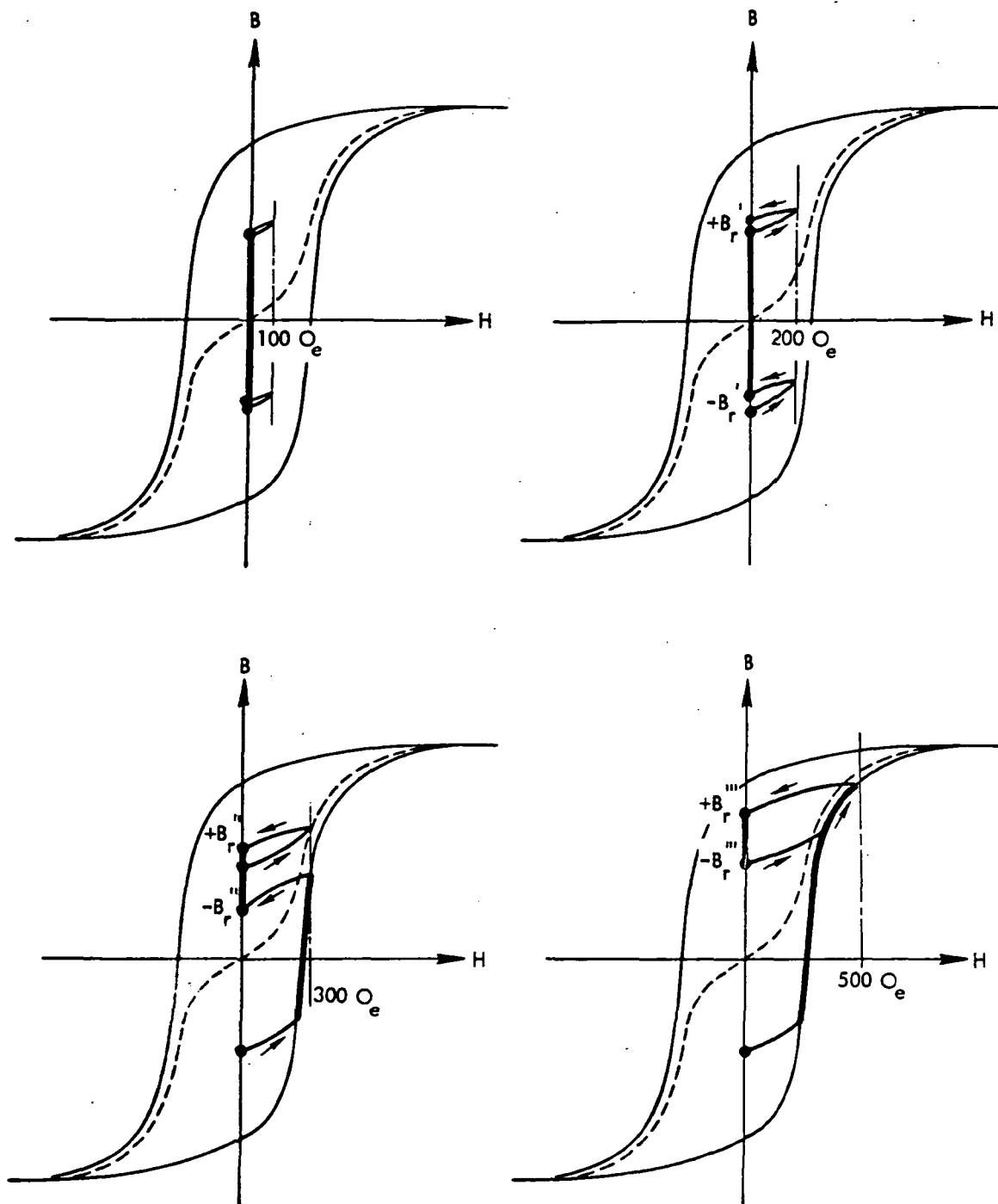


Figure 10-8. Distortion of Recorded Data in a DC Magnetic Field of Strengths 100, 200, 300 and 500 Oersted. Original Recording 6 DB-Below-Saturation

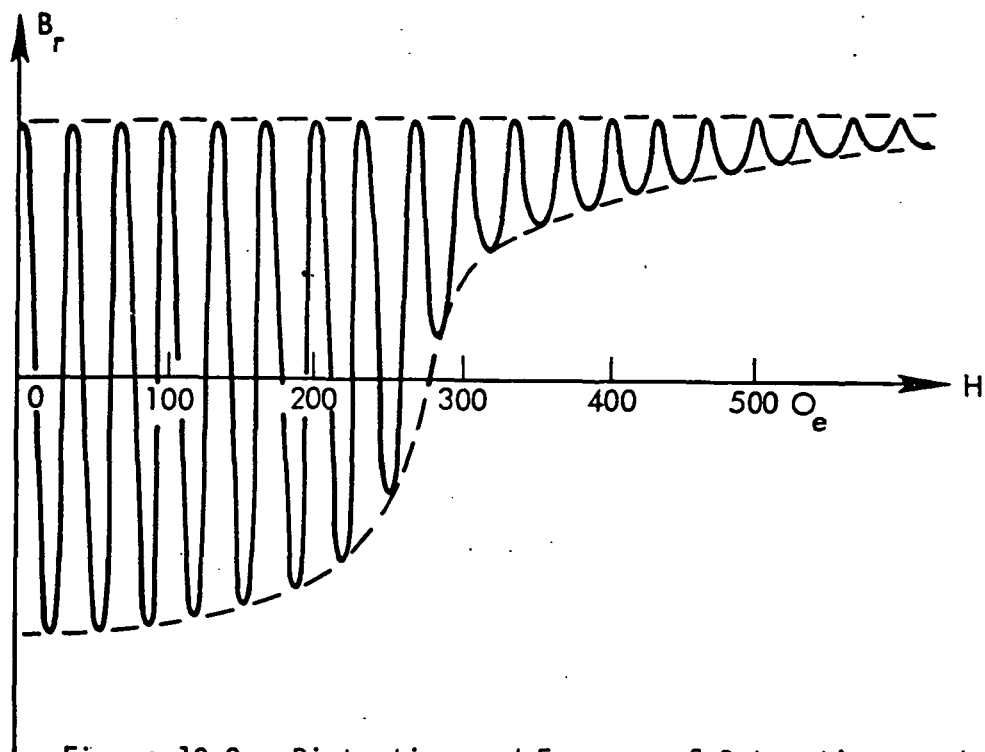


Figure 10-9. Distortion and Erasure of Saturation Recording by an External Field H

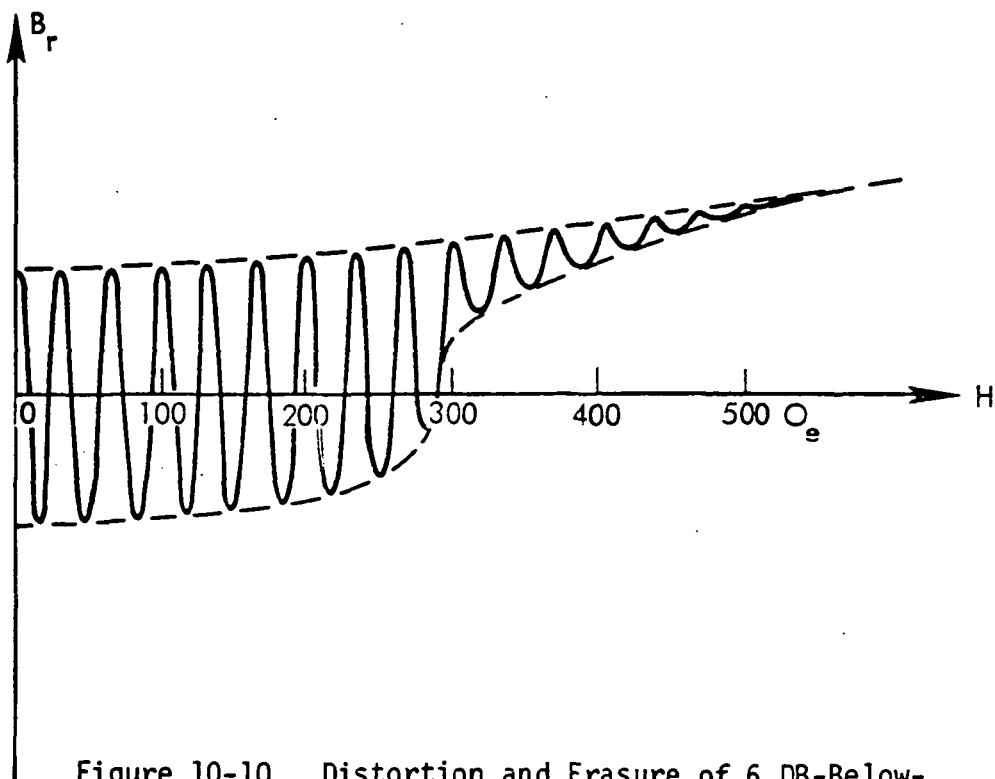


Figure 10-10. Distortion and Erasure of 6 DB-Below-Saturation Recording by an External Field H



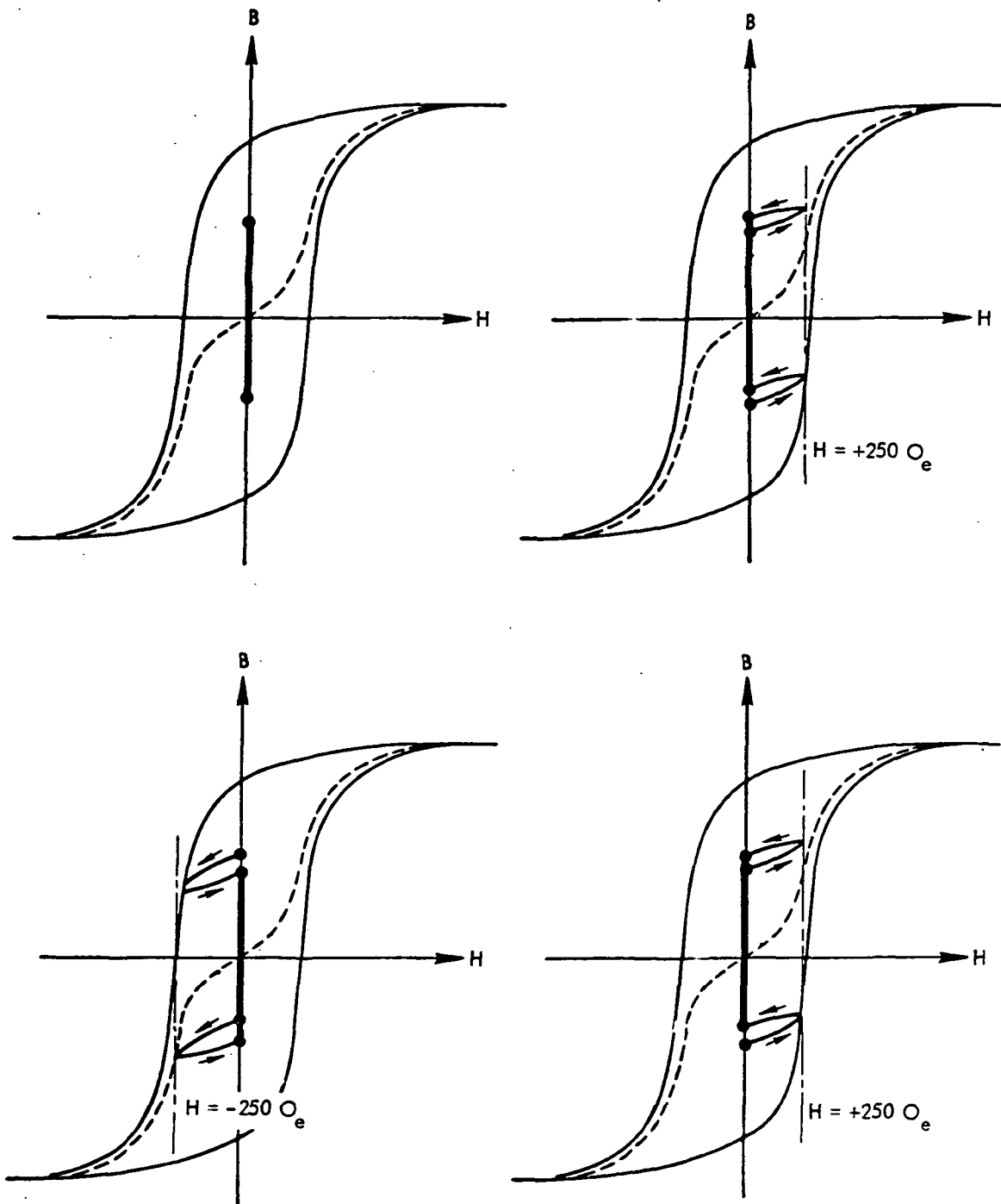


Figure 10-11. Distortion and Erasure of a 6 DB-Below-Saturation Recording by an Alternating Field of Strength  $\pm 250 \text{ O}_e$

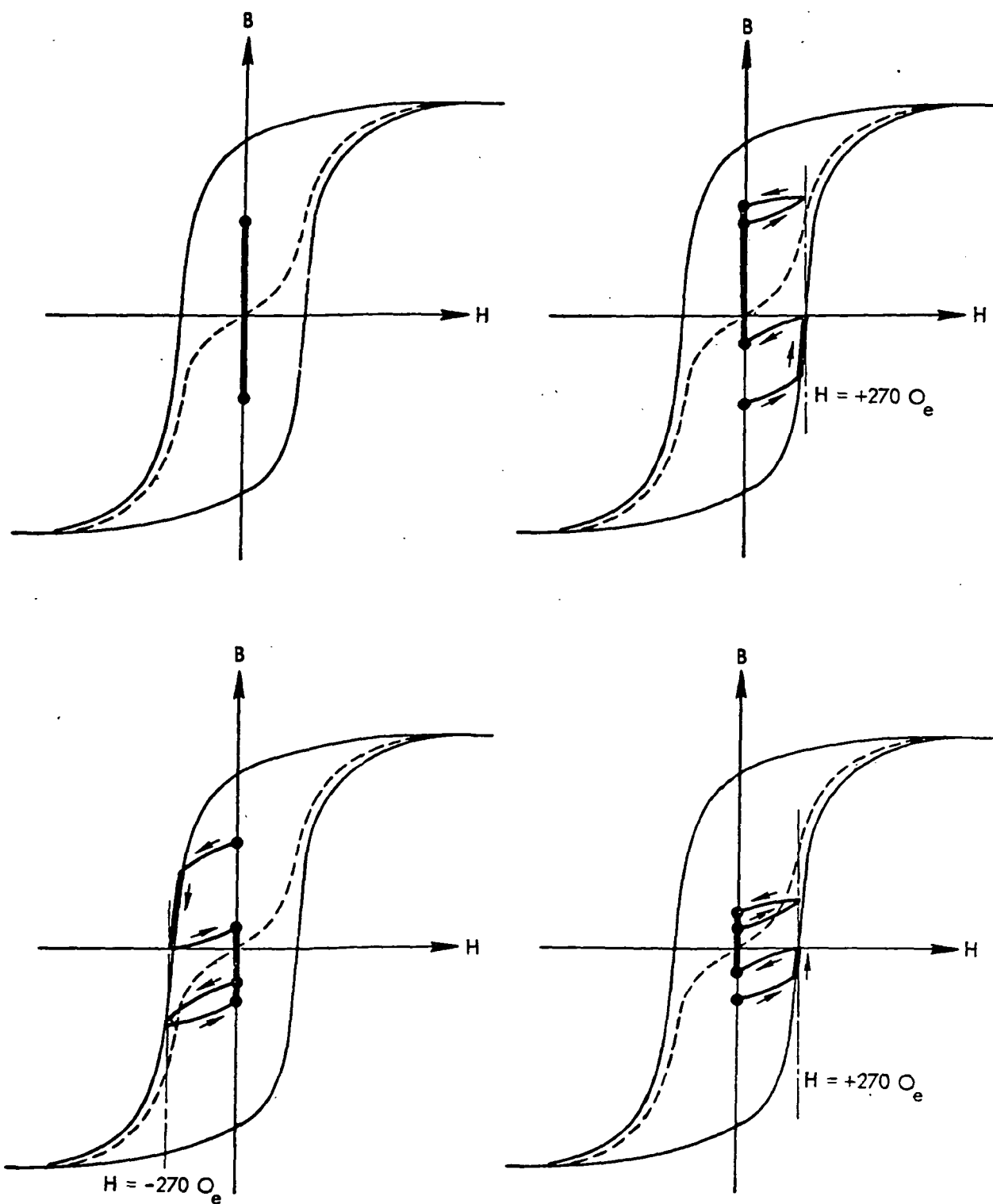


Figure 10-12. Distortion and Erasure of a 6 DB-Below-Saturation Recording by an Alternating Field of Strength  $\pm 270 \text{ O}_e$

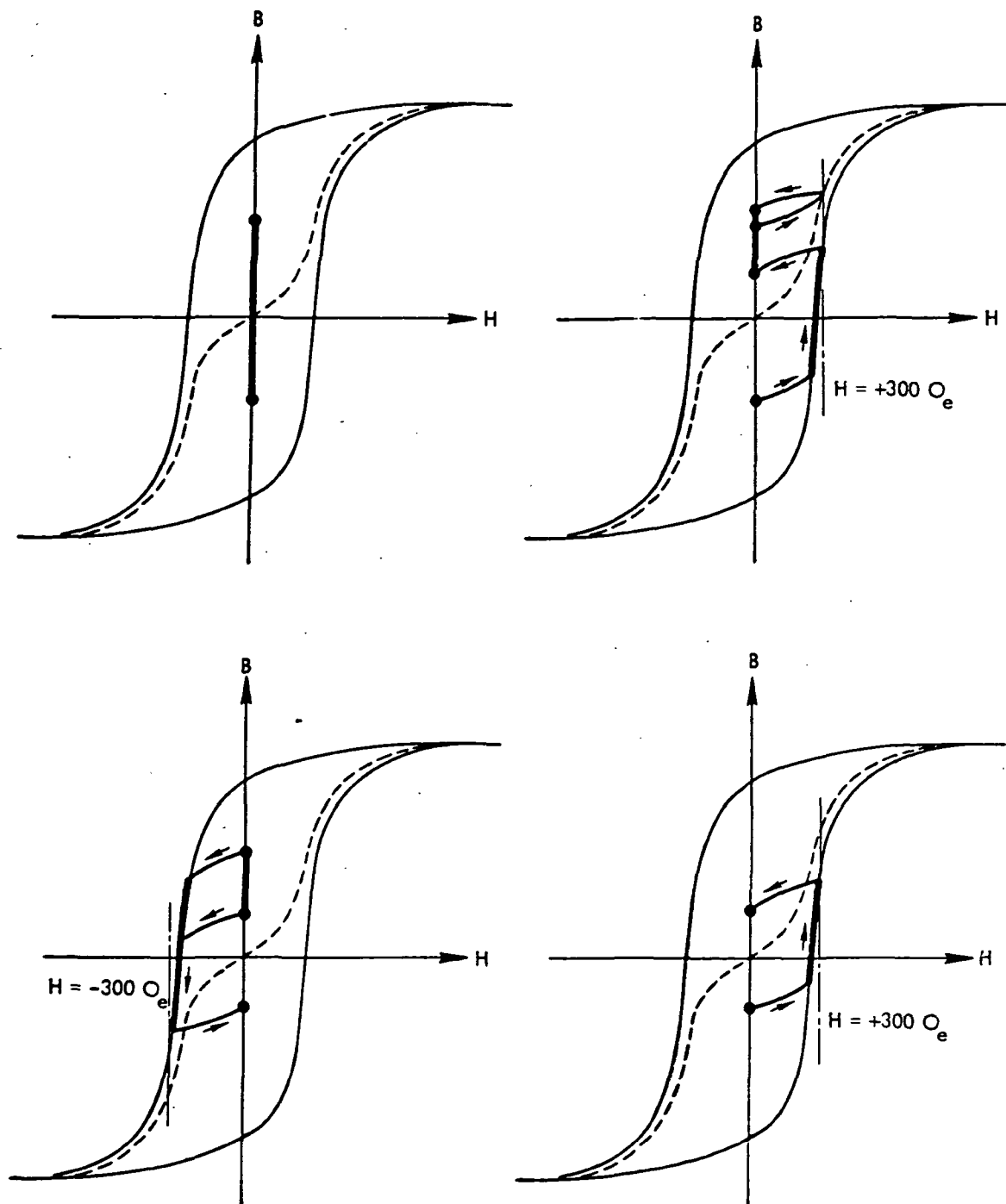


Figure 10-13. Distortion and Erasure of a 6 DB-Below-Saturation Recording by an Alternating Field of Strength  $\pm 300 \text{ O}_e$

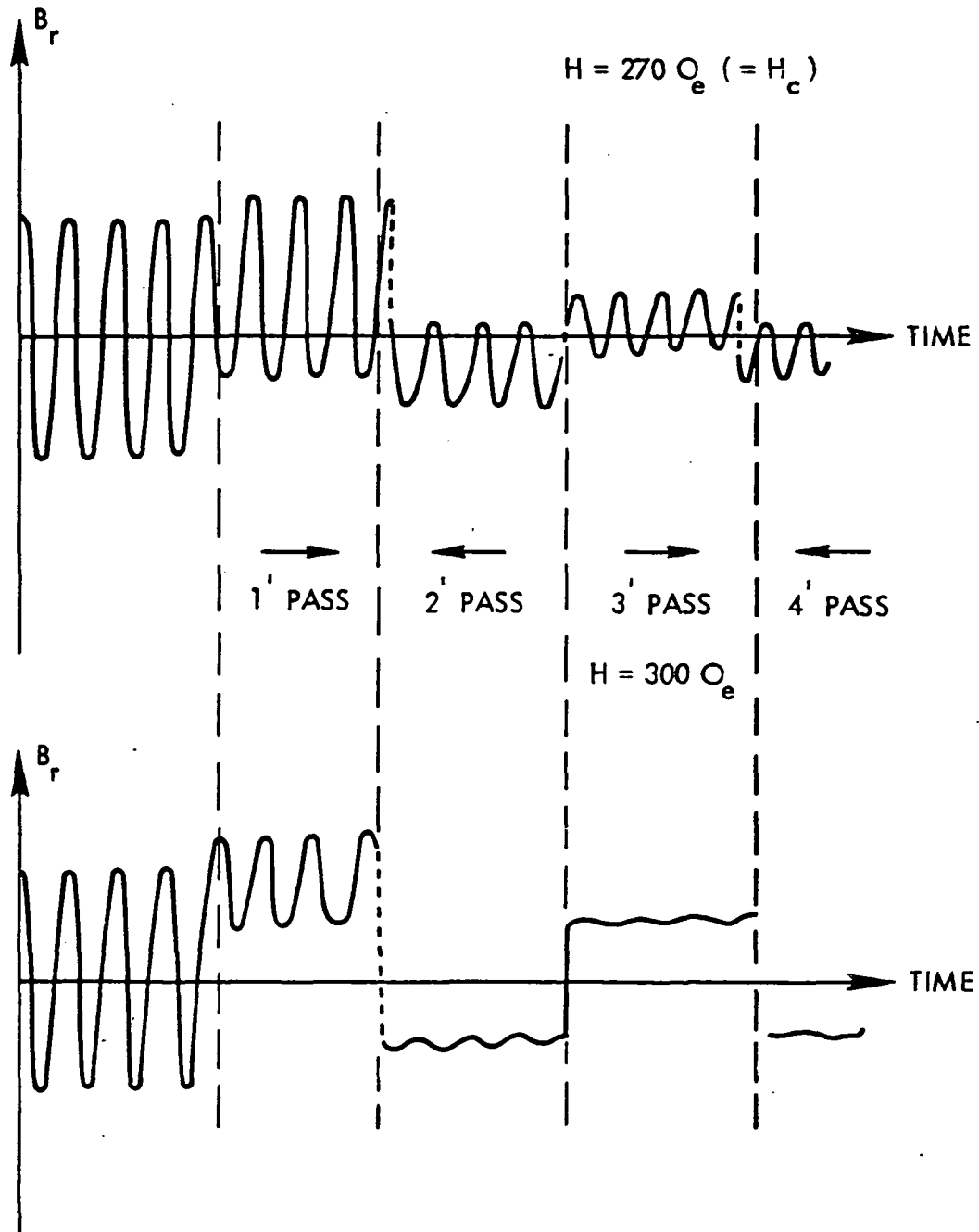


Figure 10-14. Distortion and Erasure of a 6 DB-Below-Saturation Recording by an Alternating Field

We can hence conclude, that a 6db - below - saturation recording will be affected at field strengths of 50 - 100 gauss, and will be severely erased above 300 gauss. This field strengths can be focussed by magnetic heads located in external fields of 10 times less magnitude. We can therefore expect signal degradation of prerecorded data at 5 - 10 gauss, and severe erasure at 30 gauss and above.

#### 10.3.3 Recording of Magnetic Tapes in the Presence of an External Magnetic Field

Most digital recorders operate with saturation recordings, while newer, high packing density units utilize AC-bias during recording. (The subject A-E tape recorder uses AC-bias).

The transfer curves for the two techniques are shown in Figure 10-15. It is evident that the AC bias technique is extremely sensitive to even a small biasing (superimposed) dc field, while saturation recording is relatively insensitive to fields less than 100 gauss.

A 6db-below saturation recording is made with a data field of  $\pm 50$  gauss. The recording will be totally asymmetrical for a DC-bias field of 50 gauss.

A 5 Oe external field will therefore be sufficient to affect the recording, since this field is focussed to 10 times in the record head.

#### 10.3.4 Recording of DC-Magnetized Tapes

The external fields can saturate the magnetic tape in the  $-B_s$  or  $+B_s$  direction when it passes over the erase head (which actually records the external field onto the tape).

This magnetized tape will present a DC flux at the record head and will cause a DC offset (or bias) of the transfer curve with resulting distortion. It is difficult to assess the field value that will cause

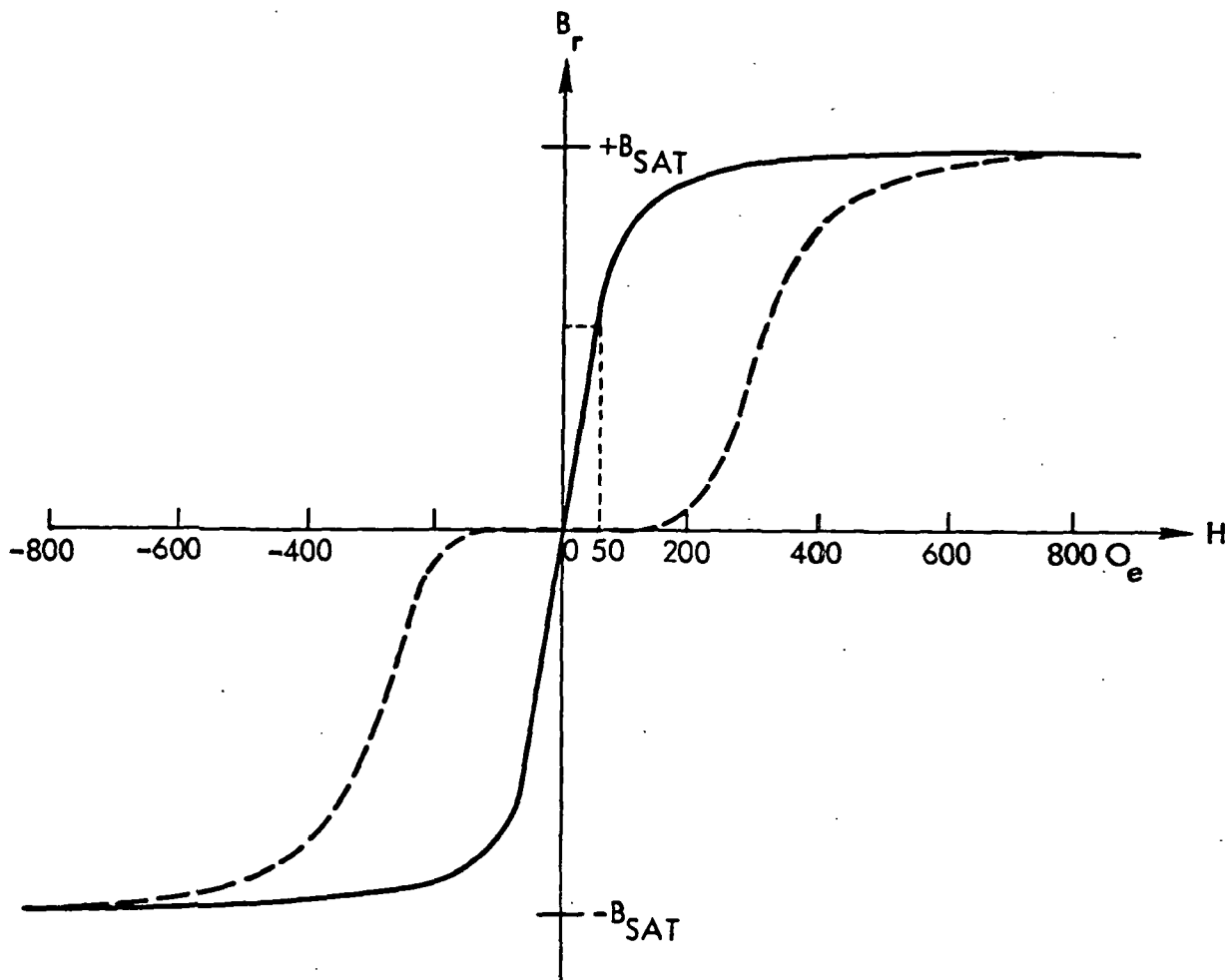


Figure 10-15. Saturation Recording Transfer Curve ----, and AC-Bias Transfer Curve ———

trouble, since the tape remanence will be too low to affect the recording field, but strong enough to "re-record" itself with resulting distortion. This distortion will, during playback, cause zero-crossing (and phase) shift which can cause bit errors.

#### 10.3.5 Experiments

Verification of the predictions from paragraphs 10.3.2, 10.3.3 and 10.3.4 were carried out by an experiment with instrumentation as shown in Figure 10-15.

The recorder was identical to the unit shown in Figures 10-1 and 10-2. The packing density was 6 KbpI, which is identical to the HEAO requirement. Recording speed was 4 IPS and playback speed 32 IPS.

##### 10.3.5.1 Playback of Pre-Recorded Tape

The recorder contained a pre-recorded ATP tape which allowed us to make the first test a determination of signal deterioration of a pre-recorded signal.

The field in the center of the coil was measured with a Hall element probe, prior to insertion of the recorder. All following field readings were made with the probe located as shown in Figure 10-16.

As the field strength was increased a degradation of the playback signal was observed at 5 - 7 gauss. At 28 Oersteds, errors showed up and at 35 Oersteds the errors were in abundance and the played back data a total loss.

The unit was oriented for the worst case field orientation, front-to-back. The playback signal was monitored on an oscilloscope, prior to limiting. Signal degradation was observed as an erasure, starting at 5 - 7 gauss and increasing linearly with added field strength. At 28 - 30 Oersteds erasure of short wavelengths became very noticeable, at which point the phase distortion became severe with resulting high bit error rates.



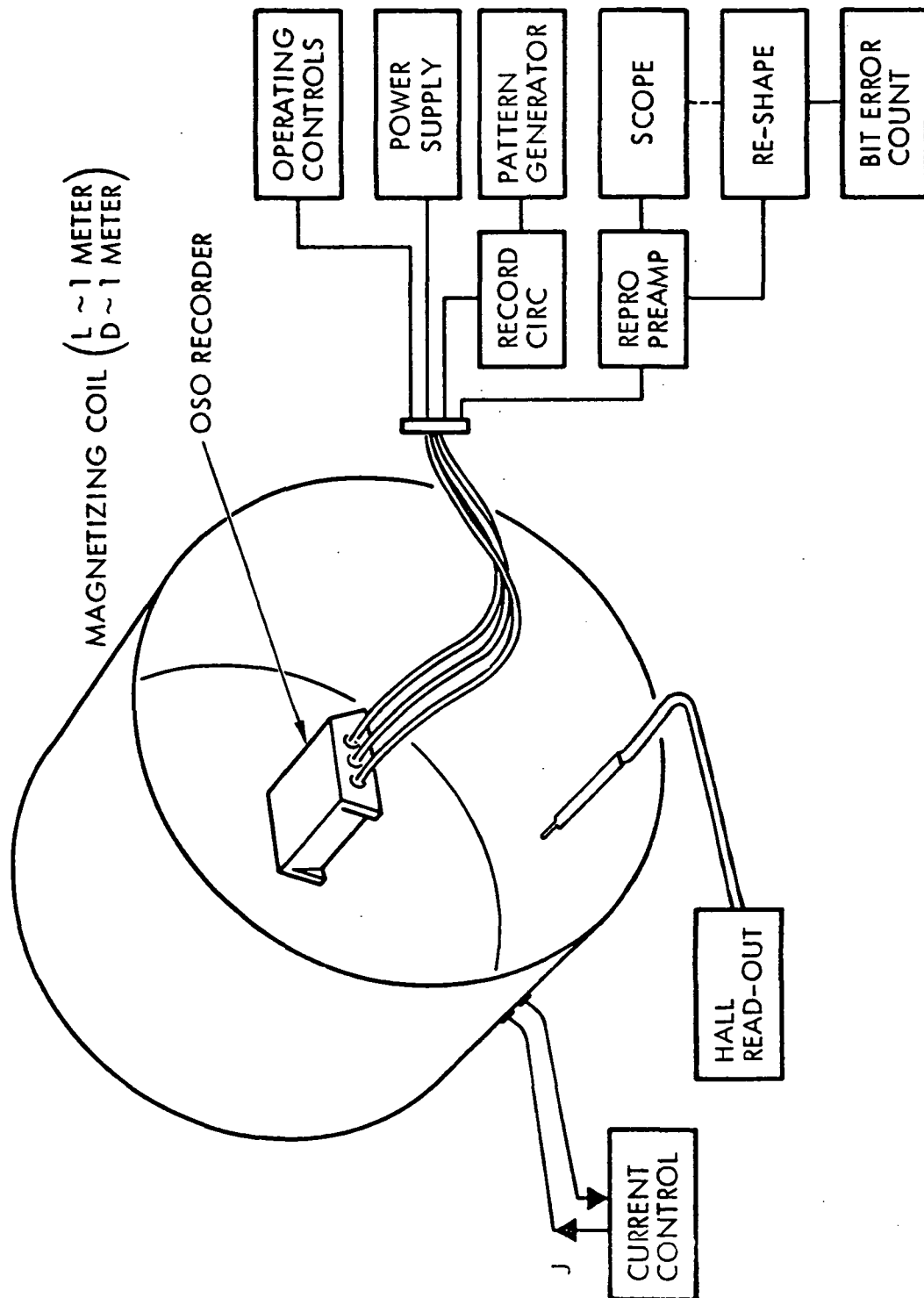


Figure 10-16. Instrumentation for Measurement of Tape Recorder Performance in an External Magnetic Field

#### 10.3.5.2 Record Data in External Field, Playback without Field

In this test a combination of magnetized tape and DC-biasing of the record field was tested. Signal degradation was noticed at 10 - 14 gauss and at 30 gauss the playback signal was a total loss.

#### 10.3.5.3 Record and Playback in an External Field

All degrading effects of the external field are acting in this test: DC-magnetized tape, a DC-biased record field and partial erasure of the recorded tape.

Again, we observed signal erasure at about 5 gauss, and at 25 gauss the playback was a total loss.

#### 10.3.5.4 Effect of Field Orientation

The recorder was sensitive to all field directions except one: perpendicular (as predicted, Figure 10-3). This preferred orientation all allowed recording and playback in the maximum possible field, 160 gauss. The playback level was only reduced 1 db, and there were no errors.

However, this orientation was very critical. By turning the recorder only a few degrees signal deterioration started rapidly. Since the direction of the anticipated field in the HEAO spacecraft will shift in magnitude and orientation as well, advantage can not be taken of this particular recorder orientation.

#### 10.3.5.5 Effect of Magnetic Field on other Elements in the Recorder

During orientation experiments an interesting effect was discovered: Worst case field was front-to-back, with the field entering the recorder front, as shown in Figure 10-5.

This was caused by field disturbance in the magnetic tachometer unit utilized in the Odetics recorder. The affect was severe enough to cause loss of motor speed synchronization, which was noticeable at 30 gauss with complete loss of phase lock at 34 gauss.

#### 10.3.5.6 Remanent Magnetization of Recorder Unit

The magnetization of the recorder was measured before and after test, shown in Figures 10-17 and 10-18. The curves show the magnetic field from the recorder during a 360° rotation, with a field probe located .5, .7 and 1.0 meters from the center of the unit.

At a distance of .5 meters the maximum field was .002 gauss prior to test, and .011 gauss after. This is largely attributed to DC magnetization of the tape packs.

#### 10.3.6 Conclusions

An unshielded tape recorder is susceptible to external magnetic fields. Predicted and measured degradation of the record and playback signal correlate, and ranks as follows:

- 5 Gauss field strength: Amplitude of recorded data is reduced without any bit errors occurring
- 25 Gauss field strength during record and playback: Loss of digital playback
- 30 Gauss field strength during record only: Loss of digital playback
- 35 Gauss field strength, clean, pre-recorded tape: Loss of digital playback.

#### 10.4 Transponder Test Results and Analysis

During the HEAO proposal phase, TRW and Motorola conducted magnetic field susceptibility tests on the ERTS transponder. TRW supplied a specially built coil and power supplies capable of producing a center field flux density in excess of 500 gauss. The coil would have fit over the ERTS transponder, but since only flight units were available it was decided to use the Block II PC-1 unit for the tests since they were essentially equivalent to the ERTS unit in design concept.

##### 10.4.1 Conduct of Test

Block II PC-1 was set up on the STE and baseline data taken as follows:

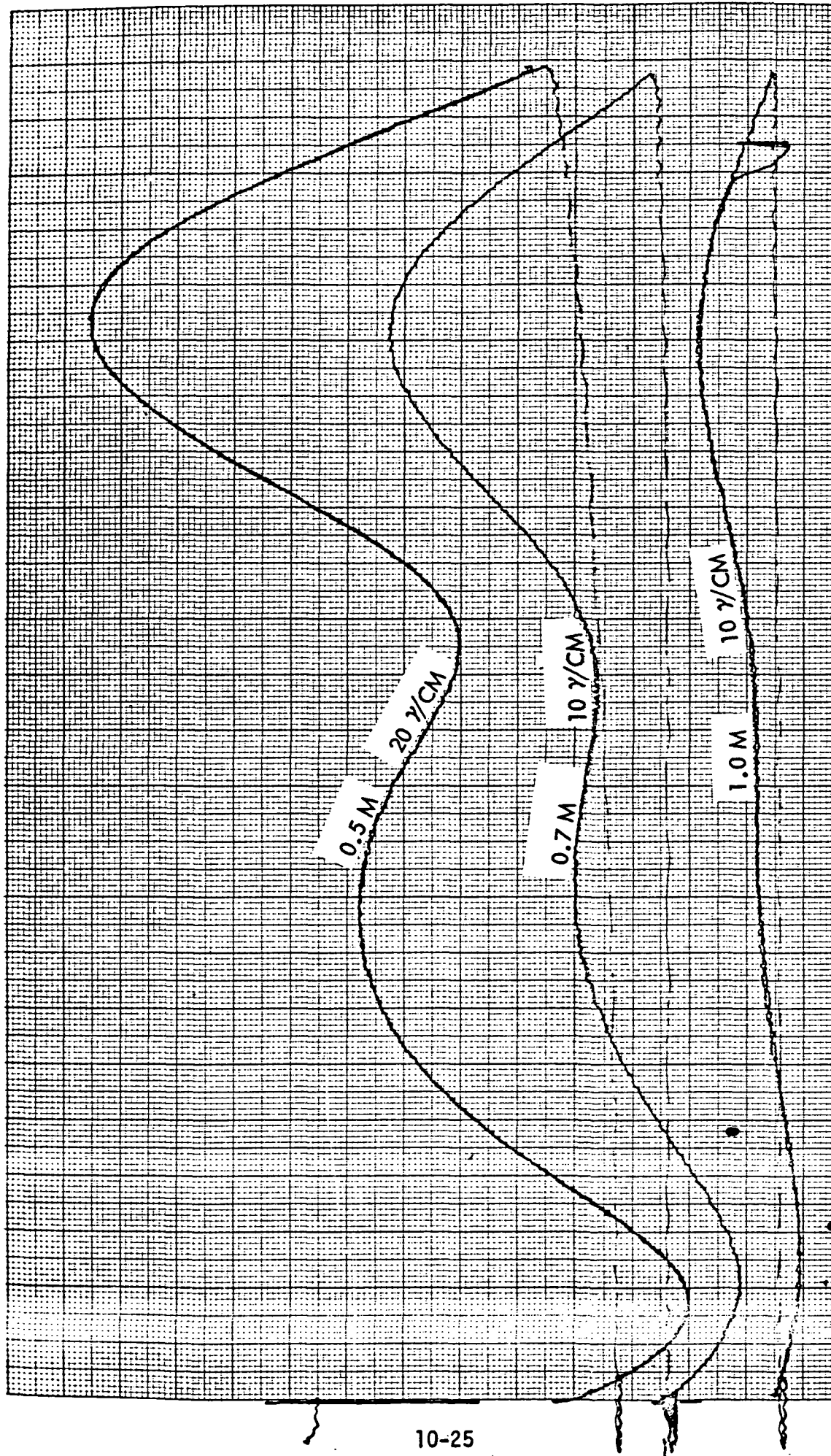


Figure 10-17. Residual Magnetization of Recorder Prior to Tests

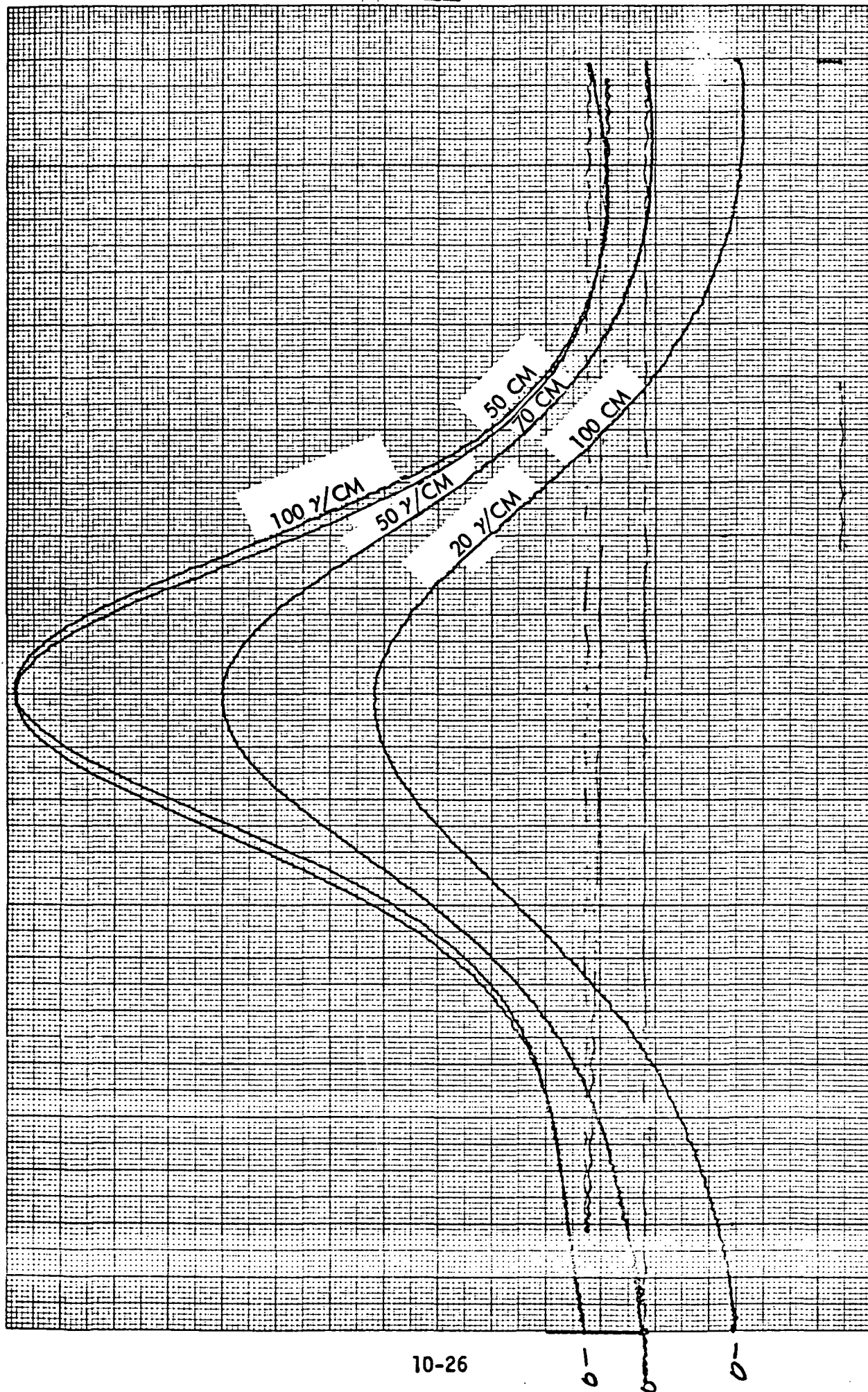


Figure 10-18. Residual Magnetization of Recorder After Test

PM, FM Power Output  
 Power Input  
 FM Frequency  
 AGC Display Voltage (-50, -100 dBm)  
 SPE Test Voltage  
 Subcarrier Output Voltage  
 Demodulated 1.024MHz Subcarrier  
 Threshold Signal Level  
 Aux. Osc. Frequency  
 Phase Noise

All readings appeared to be normal on both sides of the transponder.

The transponder was oriented to produce a field as shown in Figure 10-19.

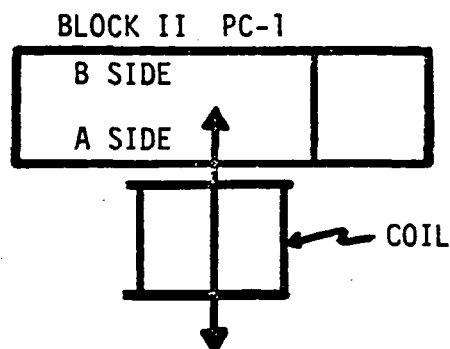


Figure 10-19. Transponder Test Setup A

Baseline data was continually monitored where possible and re-recorded at levels of 30, 105 and 155 gauss. These values were computed values at the center of the "A" module stack. The only delta of any significance proved to be an increase in PM power output of 0.1 dB at the 155 gauss level. The increase was 0.05 dB at the 105 gauss level.

The transponder was then rotated 90° as shown in Figure 10-20.

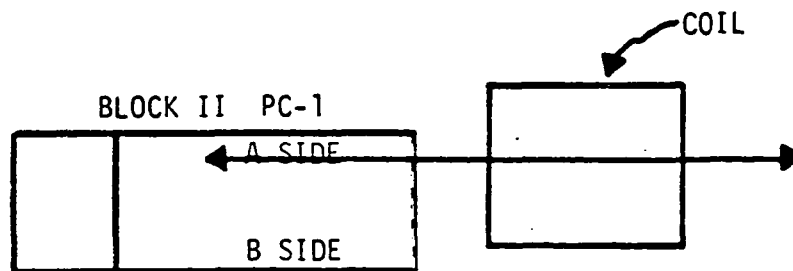


Figure 10-20. Transponder Test Setup B

The field was increased to produce a flux density of 150 gauss at the center of the receiver stack. The only significant delta was a 0.5 dB increase in PM power output. A reversal of the field produced a .15 dB decrease in power output. This orientation produced a computed 25 gauss field at the transmitter isolator. Rotating the transponder 180 degrees from that shown in Figure 10-20 gave similar results.

The transponder was re-oriented per Figure 10-19 but with the handling fixture removed. This permitted closer proximity to the field coil and produced a field of 230 gauss at the center of the "A" transponder stack. Deltas of + .1 dB maximum occurred in PM power output at 110 gauss. Reversing the field produced a -.3 dB delta at 230 gauss.

A test was made at this point during which, while tracking a signal at -135 dBm (1 dB above threshold), the magnetic field was switched on and off at 230 gauss. The receiver did not lose lock.

The transponder was rotated 90° to drive in from the top as shown in Figure 10-21.

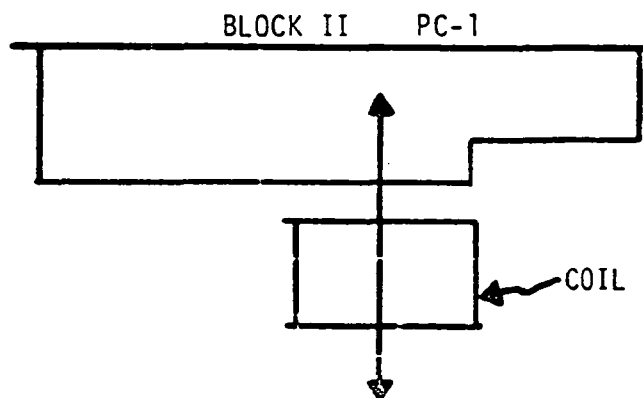


Figure 10-21. Transponder Test Setup C

The computed max field at the edge of the box was 320 gauss and at the center of the receiver, 280 gauss. At max field, the transponder was moved back and forth longitudinally to find the point most sensitive for power output delta. This appeared to be the load isolator and a delta of -.2 dB was recorded.

Elevating the transponder so as to center on the "A" stack produced as much as -.3 dB power delta at max field and -0.15 dB at 140 gauss.

The test setup was then aligned to center the FM isolator on the field. A power delta on the FM output of -0.2 dB was recorded at 280 gauss (at the isolator).

#### 10.4.2 Conclusion

The most critical circuit appeared to be the load isolators with the interfering field at 90° to the plane of the isolators. It was concluded that the USBE will withstand interfering fields up to 25 gauss in any orientation and up to 100 gauss or more in selected orientations without significant degradation.



## 11. THERMAL

The incorporation of electromagnetic torquers alone in place of a hydrazine reaction control system, will result in longer acquisition and re-acquisition times for HEAO. Thermal analyses have been performed for HEAO-A to establish the length of time temperature-sensitive equipment can tolerate off +Z axis sun pointing and random tumbling at reduced power levels associated with acquisition. The thermal control time limits are used to determine maximum allowable acquisition and reacquisition durations. In addition, the thermal analyses results suggest certain measures that can be taken by the observatory to extend allowable acquisition times if required (i.e., increase or decrease internal heat dissipation).

The thermal analysis study has been limited to major observatory units that are felt to be most sensitive to off +Z axis pointing and tumbling. The units selected for analysis are the experiments, batteries, maximum power tracker (MPT) and power control unit (PCU). The following observatory orientation limit conditions were considered for analyses purposes to bound the thermal problem.

I. EXPERIMENTS

- A. CONTINUOUS\* NORMAL SUN ON THE +Y SURFACE EXPERIMENTS  
(FULL SHADE ON THE -Y SURFACE EXPERIMENTS)
- B. CONTINUOUS\* NORMAL SUN ON THE -Y SURFACE EXPERIMENTS  
(FULL SHADE ON THE +Y SURFACE EXPERIMENTS)
- C. CONTINUOUS SHADE ON +Y SURFACE EXPERIMENTS (SURFACES  
ARE NOT EXPOSED TO SUN AT ANY TIME)
- D. CONTINUOUS RANDOM TUMBLING RESULTING IN AVERAGE  $(1/\pi)$   
FULL SUN\* ON +Y SURFACE EXPERIMENTS (EITHER +Y OR -Y  
SURFACE EXPERIMENTS VIEW THE SUN ALL THE TIME)

\*Continuous normal or average sun means the surface views the sun all the time except for normal eclipse periods.

## II. BATTERIES, MPT, AND PCU

- A. CONTINUOUS\* NORMAL SUN ON THE UNIT THERMAL RADIATOR AREA
- B. CONTINUOUS SHADE ON THE UNIT THERMAL RADIATOR AREA (SURFACE NOT EXPOSED TO SUN ANY TIME)
- C. CONTINUOUS RANDOM TUMBLING RESULTING IN AVERAGE ( $1/\pi$ ) FULL SUN\* ON THE UNIT THERMAL RADIATOR AREA

\*Continuous normal or average sun means the surface views the sun all the time except for normal eclipse periods.

A preliminary review of the thermal requirements and capabilities of equipment unique to the magnetic torque control (MTC) system is also presented. The items reviewed were the electromagnets, magnetometer sensor, magnetometer electronics, and possible additional cold gas thruster/valve package.

### 11.1 Experiments

Four observatory orientation limit conditions were considered for analysis purposes to bound the experiment thermal problem. They are discussed individually in the following paragraphs. The first three of these are cases where constant solar orientation conditions are assumed. The possibility of having a constant solar orientation during acquisition or reacquisition is very remote if not impossible. The orientations were analyzed primarily to establish extreme minimum limit times for acquisition in order to bound the problem thermally. For the continuous sun illumination cases (A and B), the experiments exceed maximum operating temperature limits in 2.2 hours if left operating. If turned off, the time limit is extended to 5.5 hours. For the continuous shade case (C), 24 hours in this condition can be tolerated before temperature limits are exceeded.

The continuous random tumbling mode assumed in Case D is the most probable solar orientation time history. Under these conditions, the limiting time is 12 hours if experiments are off and the A-2 LED door is closed.

#### 11.1.1 Continuous Normal Sun on the +Y Surface Experiments (Full Shade on the -Y Surface Experiments)

Figure 11-1 presents experiment temperatures versus time, assuming

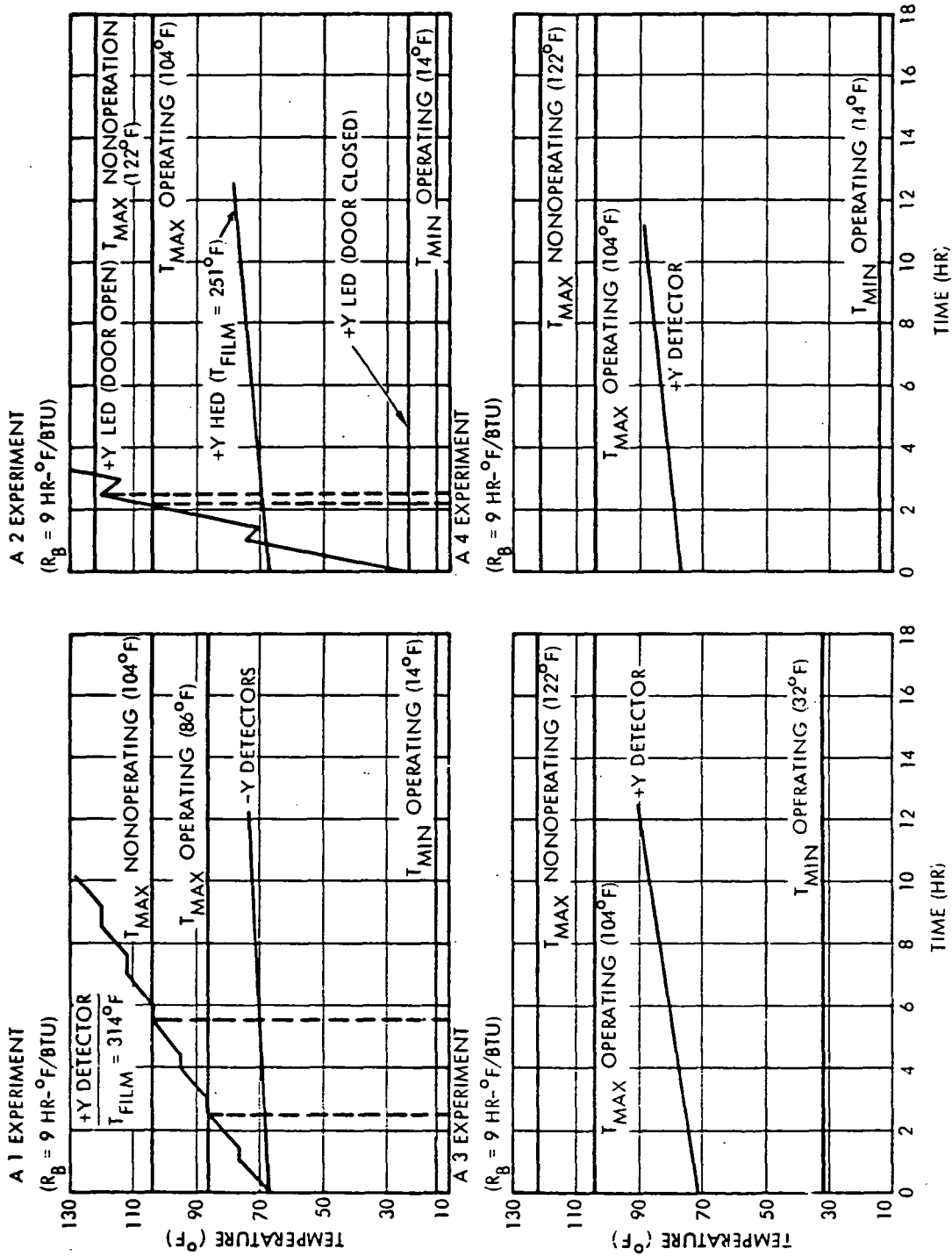


Figure 11-1. Experiment Transient Warm-Up From Hot Steady-State (Exp. On, Continuous +Y Normal Sun)

continuous normal sun on the +Y surface, +Z sun hot case initial temperatures and continued experiment operation.

The A-2 LED will exceed its maximum operating temperature limit (104°F) in 2.2 hours if the LED door is left open. Turning off the A-2 experiment will extend the allowable time to 2.5 hours (maximum non-operating temperature limit = 122°F). If an automatic or ground command is sent to close the A-2 LED door, the A-2 experiment will not exceed the maximum operating temperature in 24 hours.

The A-1 experiment will exceed its maximum operating temperature limit (86°F) in 2.5 hours. Turning off the A-1 experiment will extend the allowable time to 5.5 hours (maximum non-operating temperature limit = 104°F).

As long as an automatic or ground command is sent to close the A-2 LED door and turn off all experiments at loss of acquisition (or at launch for initial acquisition), the experiments can survive for as long as 5.5 hours even with sun continuously on the +Y experiment surfaces which, as stated previously, is a very remote possibility.

#### 11.1.2 Continuous Normal Sun on the -Y Surface Experiments (Full Shade on the +Y Surface Experiments)

Figure 11-2 presents experiment temperatures versus time, assuming continuous normal sun on the -Y surface, +Z sun hot case initial temperatures and continuous experiment operation.

The A-1 experiment will exceed its maximum operating temperature limit (86°F) in 2.2 hours. Turning off the A-1 experiment will extend the allowable time to 5.5 hours (maximum non-operating temperature limit = 104°F).

As long as an automatic or ground command is sent to turn off all experiments at loss of acquisition (or at launch for initial acquisition), the experiments can survive for as long as 5.5 hours even with the sun continuously on the -Y experiment surfaces.

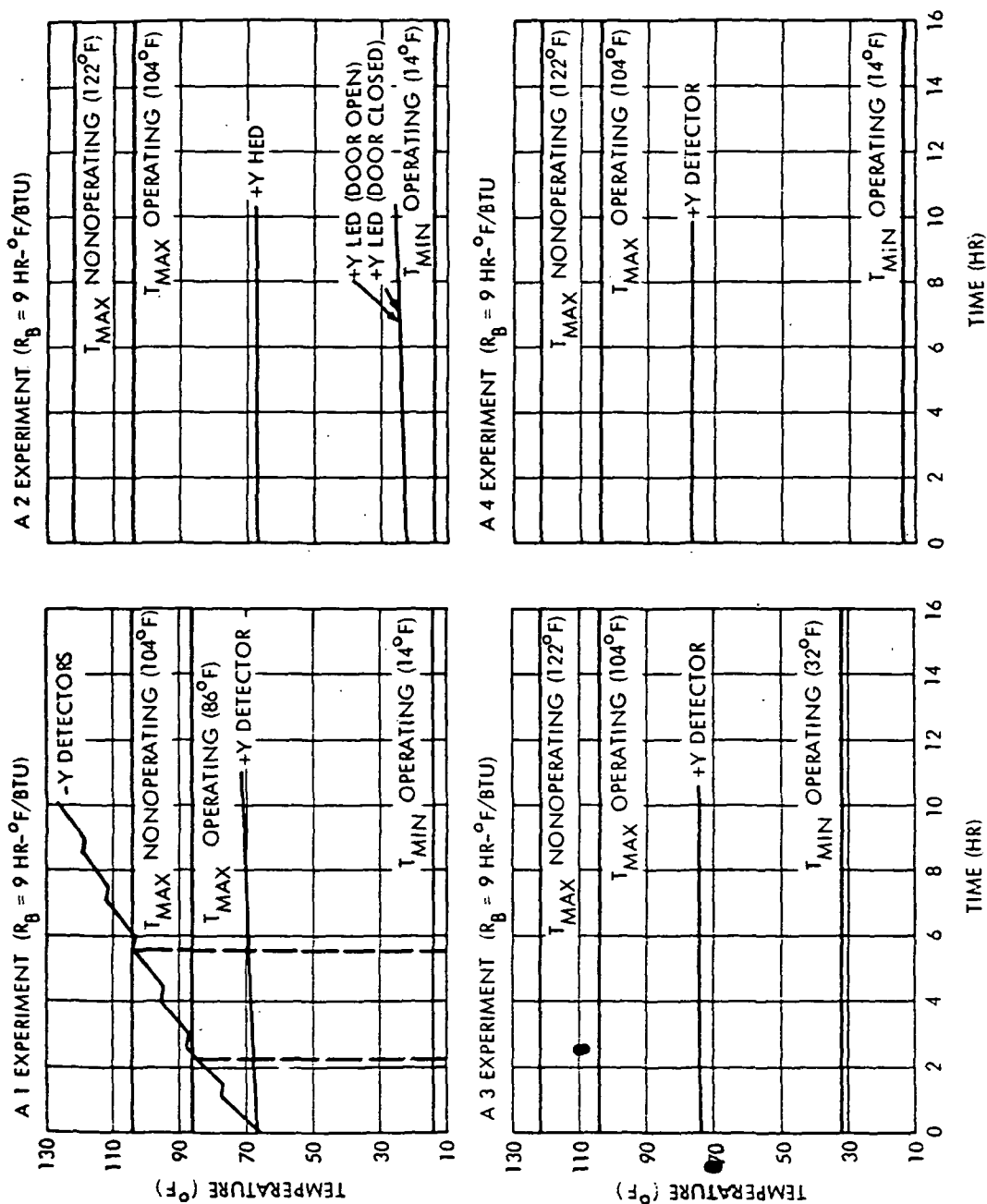


Figure 11-2. Experiment Transient Warm-Up From Hot Steady-State  
(Exp. On, Continuous -Y Normal Sun)

### 11.1.3 Continuous Shade on +Y Surface Experiments (+Y Surfaces are not Exposed to Sun at Any Time)

---

Figure 11-3 presents experiment temperatures versus time assuming continuous shade on the +Y surface experiments, nominal +Z sun cold case initial temperatures and experiments turned off.

None of the experiments exceed minimum survival temperature limits ( $-40^{\circ}\text{F}$ ) in less than 24 hours. If an automatic or ground command is sent to close the A2 LED door, the allowable time can be extended to nearly 48 hours.

### 11.1.4 Continuous Random Tumbling Resulting in Average $(1/\pi)$ Full Sun on +Y Surface Experiments (Either +Y or -Y Surface Experiments View the Sun all the Time)

---

The continuous random tumbling mode is the most probable orientation that the experiment will experience. Figure 11-4 presents experiment temperatures versus time assuming nominal +Z sun hot case initial temperatures and continued experiment operation. The A2 experiment will exceed its maximum operating temperature limit in 6.0 hours. Turning off the A2 experiment will extend the allowable time to 7.5 hours (maximum non-operating temperature limit =  $122^{\circ}\text{F}$ ). If an automatic or ground command is sent to close the A2 LED door, the A2 will not exceed the maximum operating temperature in 24 hours.

The A1 experiment will exceed its maximum operating temperature in 5.5 hours. Turning off the A1 experiment will extend the allowable time to 12 hours (maximum non-operating temperature limit =  $104^{\circ}\text{F}$ ).

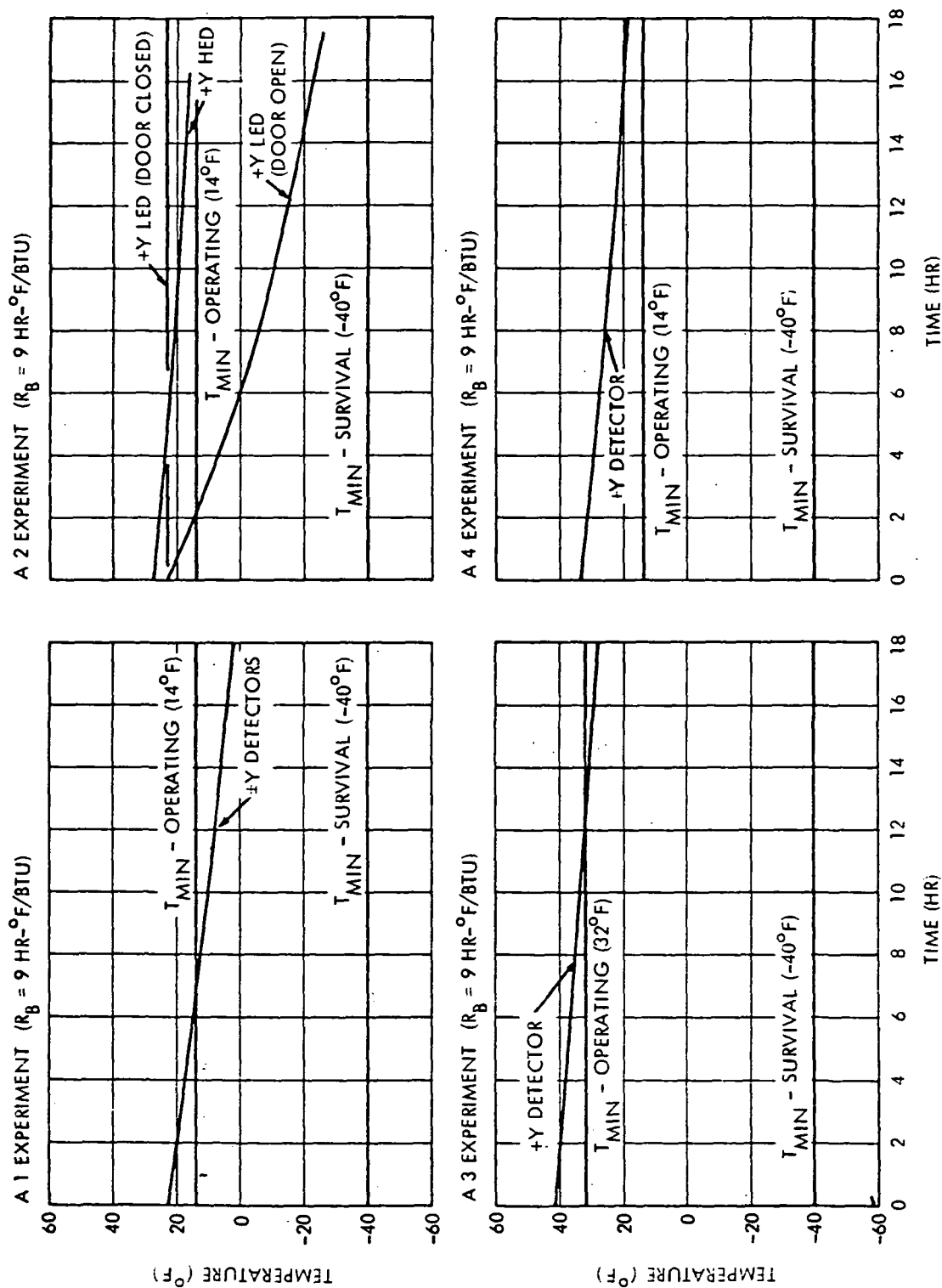


Figure 11-3. Experiment Transient Cooldown  
From Cold Steady-State (Exp. Off, No Solar Input)

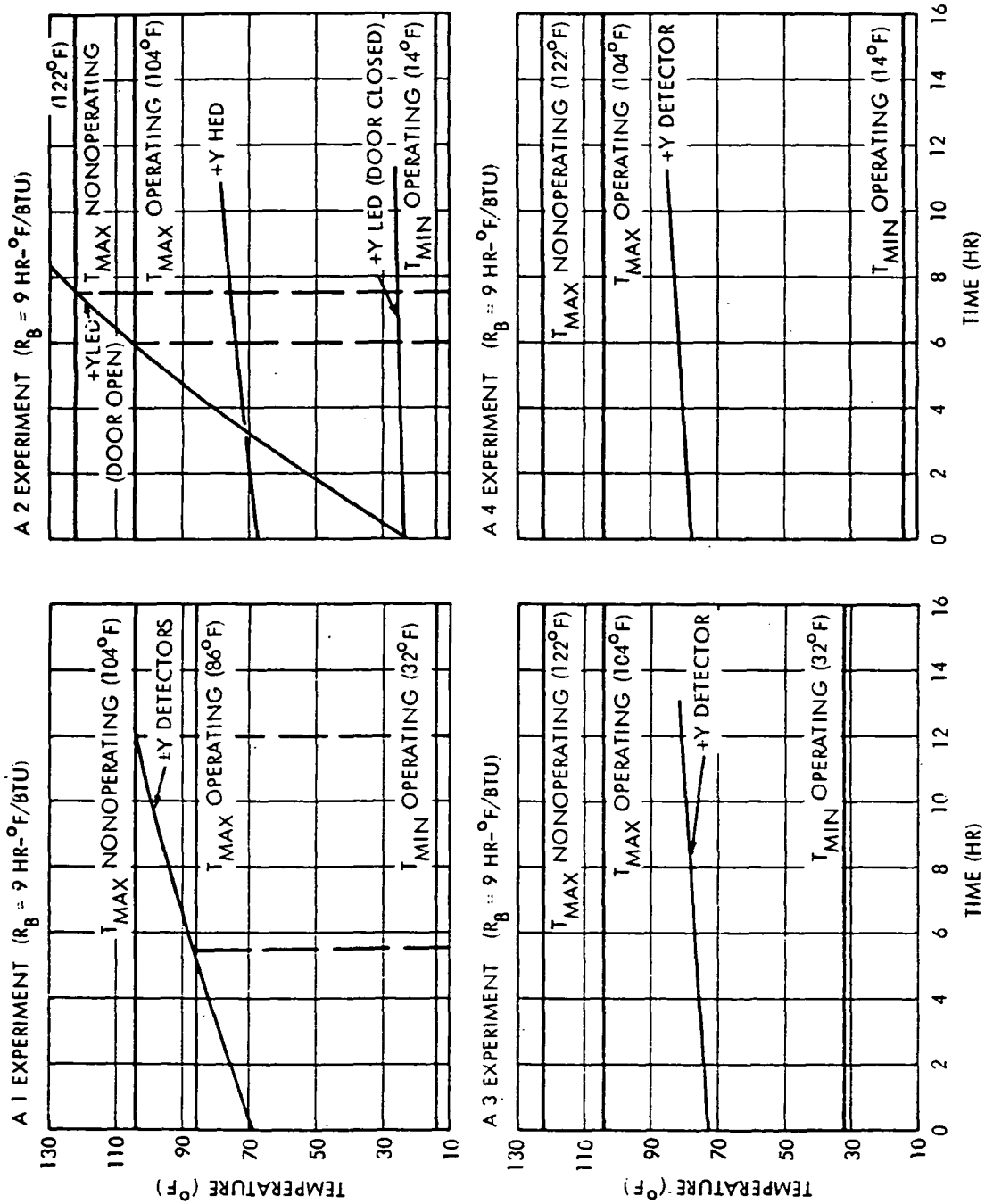


Figure 11-4. Experiment Transient Warm-Up From Hot Steady-State  
(Exp. On, Continuous Random Tumbling)



## 11.2 Battery

Three limiting observatory orientation conditions were considered for analyses purposes to bound the battery thermal problem. They are discussed individually in the following paragraphs. As in the case of the experiments, two of these conditions assume the extremely remote case of constant solar orientations in order to establish very worst case minimum limit times for acquisition. Continuous sun results in a limit time of approximately three hours; continuous shade results in a limit time of 12 hours.

The third case considers a random tumbling mode, which also results in a time limit of 12 hours.

### 11.2.1 Continuous Normal Sun on the Battery Thermal Radiator Area

Figure 11-5A presents three battery operation temperatures versus time assuming nominal +Z hot case initial temperatures. The two limit conditions of battery heat dissipation that were considered to bound the range of possible acquisition power loads were the following:

- a) Maximum battery heat dissipation equivalent to  $2/3$  the nominal eclipse dissipation ( $2/3 \times 35$  watts/battery = 23 watts/battery). This condition assumes the experiments are turned off to conserve power and the solar array does not generate power (i.e., does not see the sun).
- b) Minimum battery heat dissipation equivalent to  $1/3$  the nominal eclipse dissipation ( $1/3 \times 35$  watts/battery = 11.7 watts/battery). This condition assumes the experiments and some non-essential spacecraft equipment are turned off to conserve power and the solar array does not generate power (i.e., does not see the sun).

The maximum battery heat dissipation condition exceeds the maximum allowable short term temperature limit (80°F) in approximately three hours. The minimum battery heat dissipation condition does not exceed maximum allowable short term temperatures. It can be seen in Figure 11-5A that the battery temperatures can be maintained below maximum limits indefinitely if the battery load is maintained below  $1/2$  nominal eclipse conditions.

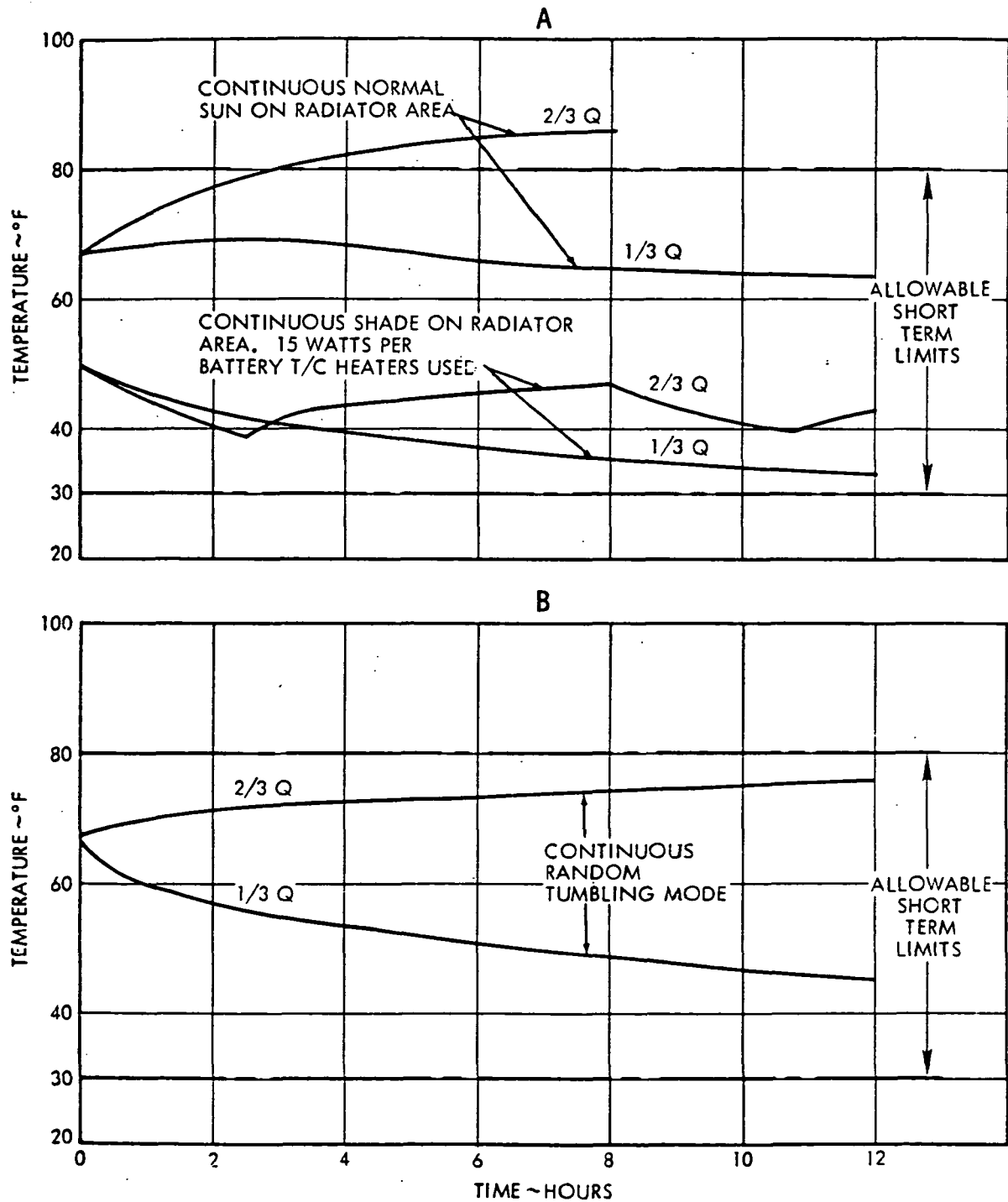


Figure 11-5. Battery Temperatures vs. Time During Loss of Acquisition or Initial Acquisition, Three-Battery Operation Only

### 11.2.2 Continuous Shade on the Battery Thermal Radiator Area

Figure 11-5A presents three-battery operation temperature versus time assuming nominal +Z cold case initial temperatures for the two limit battery heat dissipation conditions described in 11.2.1. Neither the maximum or minimum battery heat dissipation condition exceed minimum allowable short term temperature limits (30°F) within 12 hours. The battery thermal control heaters (15 watts/battery) are utilized for this condition to help maintain acceptable minimum temperatures.

### 11.2.3 Continuous Random Tumbling Resulting in Average (1/π) Full Sun on the Battery Thermal Radiator Area

The continuous random tumbling mode is the most probable orientation that the battery will experience. Figure 11-5B presents three battery operation temperatures versus time assuming nominal +Z hot case initial temperatures for the two limit battery heat dissipation conditions described in 11.2.1. Neither the maximum or minimum battery heat dissipation conditions exceed maximum allowable short term temperature limits (80°F) within 12 hours.

## 11.3 MPT and PCU

Three limiting observatory orientation conditions were considered for analysis purposes to bound the MPT and PCU thermal problem. They are discussed individually in the following paragraphs.

### 11.3.1 Continuous Normal Sun on the MPT and PCU Thermal Radiator Area

The continuous normal sun orientation is possible for the MPT and PCU because magnetic requirements dictate that the units must be located on a +Z -Y equipment panel (22 1/2° off perpendicular to +Z axis). The MPT and PCU are not sensitive to the magnetic field generated by the torquers and are therefore located on a +Z -Y panel near the torquers to make room for sensitive equipment (tape recorders) on -Z +Y panels away

### 11.2.2 Continuous Shade on the Battery Thermal Radiator Area

Figure 11-5A presents three-battery operation temperature versus time assuming nominal +Z cold case initial temperatures for the two limit battery heat dissipation conditions described in 11.2.1. Neither the maximum or minimum battery heat dissipation condition exceed minimum allowable short term temperature limits (30°F) within 12 hours. The battery thermal control heaters (15 watts/battery) are utilized for this condition to help maintain acceptable minimum temperatures.

### 11.2.3 Continuous Random Tumbling Resulting in Average (1/π) Full Sun on the Battery Thermal Radiator Area

The continuous random tumbling mode is the most probable orientation that the battery will experience. Figure 11-5B presents three battery operation temperatures versus time assuming nominal +Z hot case initial temperatures for the two limit battery heat dissipation conditions described in 11.2.1. Neither the maximum or minimum battery heat dissipation conditions exceed maximum allowable short term temperature limits (80°F) within 12 hours.

## 11.3 MPT and PCU

Three limiting observatory orientation conditions were considered for analysis purposes to bound the MPT and PCU thermal problem. They are discussed individually in the following paragraphs.

### 11.3.1 Continuous Normal Sun on the MPT and PCU Thermal Radiator Area

The continuous normal sun orientation is possible for the MPT and PCU because magnetic requirements dictate that the units must be located on a +Z -Y equipment panel (22 1/2° off perpendicular to +Z axis). The MPT and PCU are not sensitive to the magnetic field generated by the torquers and are therefore located on a +Z -Y panel near the torquers to make room for sensitive equipment (tape recorders) on -Z +Y panels away

from the torquers. The MPT and PCU will reach maximum temperatures under  $22\ 1/2^\circ$  off +Z axis sun point orientation conditions (loss of acquisition) when 1) the sun is on the array causing near maximum unit heat dissipations and 2) the sun is normal to the thermal radiator area producing maximum solar heat input.

Figure 11-6 presents maximum orbital steady-state MPT and PCU temperatures versus solar incident angle for a  $2.7\text{ ft}^2$  radiator area. The maximum MPT and PCU temperatures are  $158^\circ\text{F}$  and  $138^\circ\text{F}$ , respectively, for continuous normal sun ( $\phi = 0^\circ$ ) on the radiator area (steady-state). The predicted temperatures are below maximum allowable operating limits for the MPT ( $160^\circ\text{F}$ ) and PCU ( $140^\circ\text{F}$ ). If more temperature margin is required between predicted and allowable, the thermal radiator area can be increased.

#### 11.3.2 Continuous Random Tumbling Resulting in Average ( $1/\pi$ ) Full Sun on the MPT and PCU Thermal Radiator Area

The continuous random tumbling mode is the most probable orientation that will be experienced by the MPT and PCU with loss of acquisition. The unit maximum orbital steady-state temperatures are much less than those discussed in 11.3.1 because 1) the solar heat input to the radiator area would be decreased to  $1/\pi$  of the full normal sun input and 2) the unit heat dissipation would be decreased drastically as electrical power generated in the solar arrays is decreased (30 to 40% of +Z normal sun levels). It is estimated that the unit temperatures would reach orbital steady-state temperatures in the  $40$  to  $60^\circ\text{F}$  range. These temperatures are nearly mid way between the MPT ( $160^\circ\text{F}/-40^\circ\text{F}$ ) and PCU ( $140^\circ\text{F}/-40^\circ\text{F}$ ) maximum and minimum allowable operating temperature limits.

#### 11.3.3 Continuous Shade on the MPT and PCU Thermal Radiator Area (Surface Not Exposed to Sun Anytime)

Continuous thermal radiator shading is remotely possible under loss of acquisition conditions (sun on -Z half of observatory). Such an orientation would produce minimum unit temperatures because 1) the solar heat input to the radiator area would decrease to zero and 2) the unit heat dissipation would decrease to near zero since the solar array would not be generating power (no sun on arrays).

Figure 11-7 presents MPT and PCU temperatures versus time assuming nominal +Z sun hot and cold case initial temperatures (MPT and PCU near zero internal heat dissipation). The MPT and PCU will not reach minimum allowable operating temperature limits ( $-40^{\circ}\text{F}$ ) in 12 hours.

#### 11.4 Interface Requirements for Magnetic Control Equipment

Cold Gas Valve. Thermal requirements for this equipment have been established as 0 to  $200^{\circ}\text{F}$  in similar applications (e.g., Vela Program). The valve is assembled to, and provides support for, the cold gas nozzle. The valve itself would be mounted on the spacecraft central cylinder, and covered by a multi-layer blanket of aluminized Mylar. There is no significant heat dissipation in the valve. Suitable valve temperatures thus depend mostly on availability of mounting locations with temperatures above  $0^{\circ}\text{F}$ . Previous SCM analyses have predicted central cylinder temperatures in the range of 40 to  $70^{\circ}\text{F}$ . No thermal problems are anticipated for the cold gas valve mounted to the SCM central cylinder.

Electromagnets. The three electromagnets are heavy coils with an iron core, contained by an outer shell and potting compound. The weight per electromagnet is 51 pounds, in the form of a cylinder 60 inches long and 3 inches in diameter. Maximum power dissipation per electromagnet is 16 watts each during launch acquisition, and 0.2 watts each during long term operations.

The electromagnets are not known to be particularly temperature-sensitive, having a minimum temperature requirement on the order of  $-58$  to  $-148^{\circ}\text{F}$ , and an upper limit of  $120^{\circ}\text{F}$ . One electromagnet will be mounted outside the spacecraft near the (+Z) axis parallel to the (X) axis. The other two are mounted near or at the -X end of the platform, outside the equipment compartment.

The electromagnets of their own account appear to present no thermal problems; heat leakage from local spacecraft structures and thermal coatings can be utilized to maintain suitably high electromagnet temperatures. Thermal control of external electromagnets thus involves restricting these heat leaks to a low level, so as not to perturb equipment compartment thermal control.

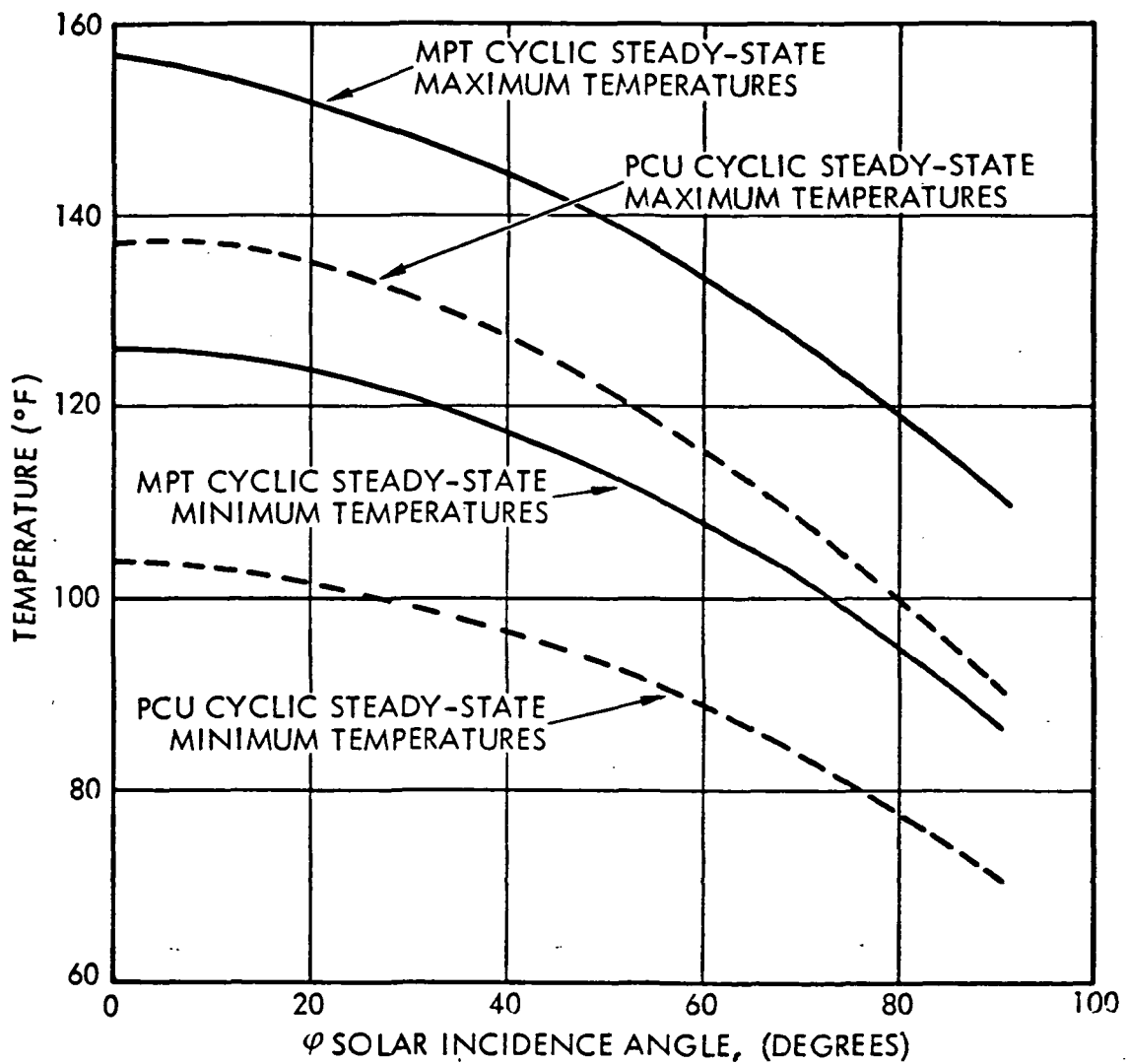
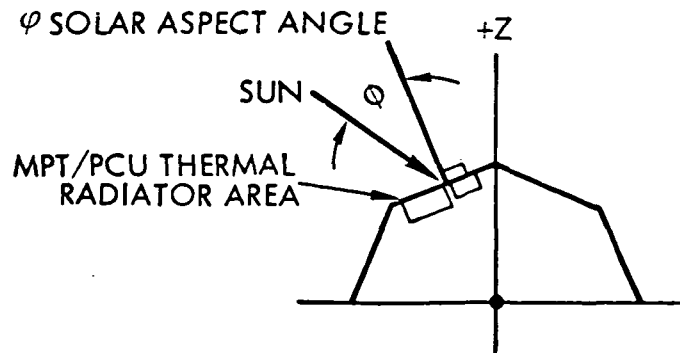


Figure 11-6. MPT and PCU Orbital Cyclic Steady-State Maximum and Minimum Temperatures vs. Solar Aspect Angle

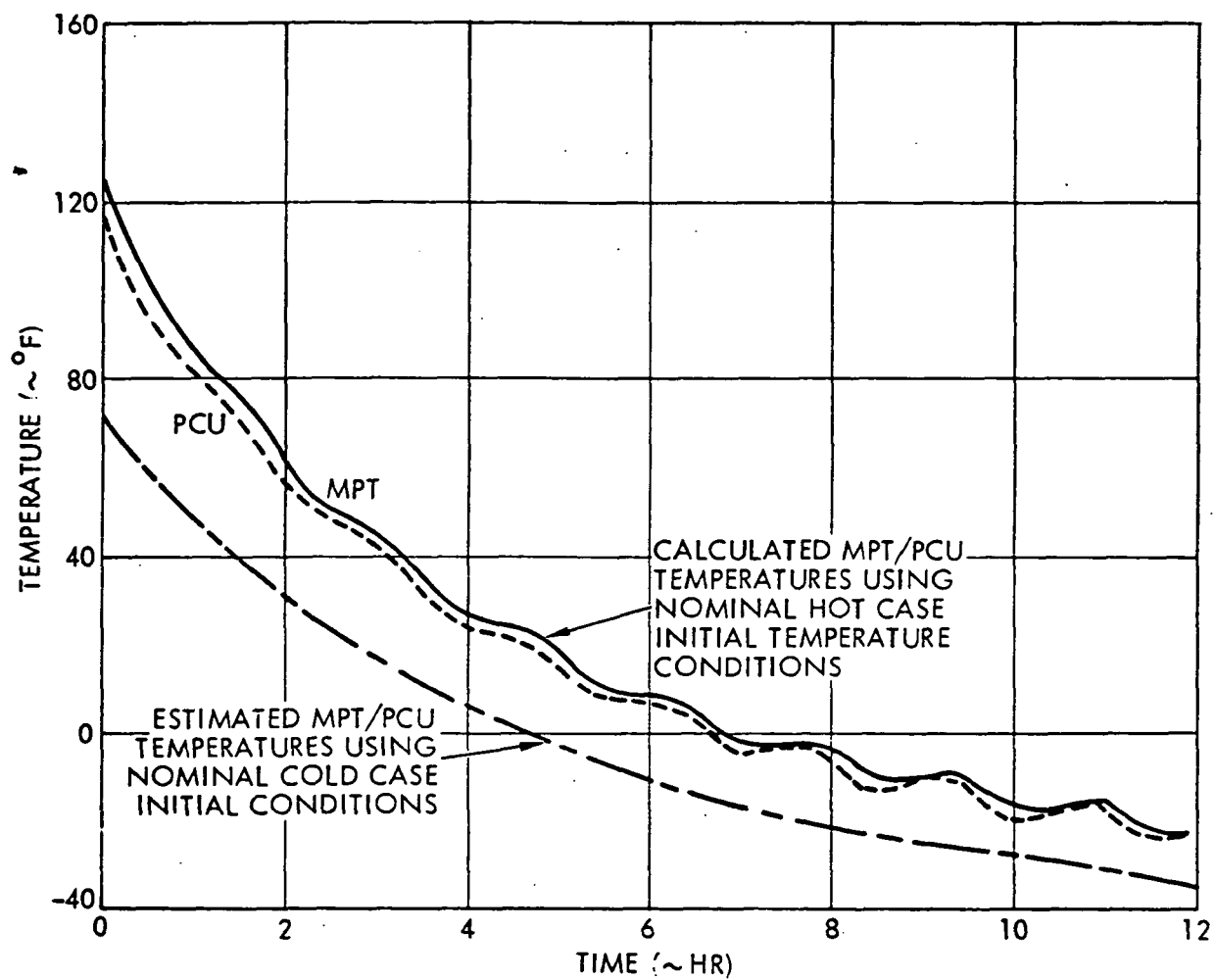


Figure 11-7. MPT and PCU Cooldown for Shaded Radiator Conditions and Near Zero Internal Heat Dissipations (Sun Not on Radiator Area or Solar Array)



High temperatures appear to present no problem. The considerable thermal capacitance of the electromagnets would restrict temperature increases during a six-hour acquisition period to about 30°F. Maximum electromagnet temperature will not exceed 100°F.

Magnetometer Sensor and Electronics. The magnetometer electronics occupy a volume equivalent to a 6-inch cube, dissipate about 1 or 2 watts of energy, and have qualification temperature limits of -10 to 130°F. This unit will be located in the spacecraft equipment module, and no thermal problems are anticipated in that relatively benign environment (40 to 90°F).

The magnetometer sensor will be located on an external support structure. In configuration, it is approximately 5 inches long by 2.5 inches in diameter, weighs about 1.5 pounds, and has negligible internal power dissipation. Its temperature requirements are -10 to 130°F. Approximate calculations indicate that in eclipses of 40 minutes duration, the sensor temperature would drop no more than 30 to 40°F from an initial value near 100°F established by external thermal coatings. If heat losses to the supporting structure are minimized, there is no clear requirement for a sensor heater.

Conclusion. Temperature requirements of the cold gas valve, electromagnets, and magnetometer electronics and sensor, can be met without heaters. In the case of the magnetometer sensor, it is assumed that eclipse durations will not greatly exceed 40 minutes.

## 12. RELIABILITY

The reliability for the three (3) HEAO missions (e.g., A, B, and C), incorporating provisions for electromagnetic reaction control, is estimated below in Table 12-1. Configuration C is the preferred system<sup>(1)</sup>. Calculations are included for several HEAO-A, B, and C spacecraft (S/C) configurations utilizing magnetic control with reaction wheels, together with optional S/C configurations employing cold-gas reaction subsystems which would operate coincident with magnetic control and reaction wheel assemblies. Reliability block diagrams depicting the arrangement of elements comprising the configurations from which analyses were performed are shown in Figures 12-1 and 12-2. Included also are:

- Pertinent study groundrules
- Assumptions regarding;
  - Minimal impact to reliability over baseline configurations,
  - Reaction wheel operation in HEAO-A and C vehicles,
  - Redundancy,
  - Magnetic control subsystem installation and failure characteristics,
  - Intrasystem connectivities for magnetic control and cold-gas subsystems.
- Single-failure suppression
- Reliability trade-offs
- Commonality of HEAO-A, B, and C subsystems employing magnetic control and reaction wheels.

---

(1) Specifically, the C-II configuration as estimated in Table 12-1. C-II provides for initial acquisition maneuvers at minimal impact to current on-board command and attitude control and determination subsystems.

Table 12-1. Reliability Estimate Summary

	I MAGNETIC CONTROL INSTALLATION W/O COLD GAS	II MAGNETIC CONTROL INITIAL ACQUISITION WITH COLD GAS (2)	III MULTIPLE ACQUISITION WITH NON-REDUNDANT THRUSTER BANK (3)	IV MULTIPLE ACQUISITION WITH REDUNDANT THRUSTER BANK (3)
A. All Magnetometers & All Electronics (1) Fully Cross-Strapped HEAO-A HEAO-B	0.944 0.834	0.944 0.834	0.936 0.821	0.941 0.830
B. All Magnetometers Cross-Strapped Plus One (4th) Electronics Subassembly Connected for Standby Service HEAO-A HEAO-B	0.943 0.831	0.943 0.830	0.935 0.817	0.940 0.826
C. Electronics Cross-Strapped Without a Magnetometer Cross-Strap HEAO-A HEAO-B	0.931 0.825	0.930 0.824	0.929 0.823	0.930 0.824
D. Magnetometers Only Cross-Strapped at Transfer Assembly HEAO-A HEAO-B	0.927 0.793	0.926 0.792	0.925 0.791	0.926 0.792
E. No Magnetometer-Transfer Assembly or Electronics Cross-Straps for X,Y,Z, Axes HEAO-A HEAO-B	0.925 0.783	0.924 0.782	0.923 0.781	0.924 0.782

- (1) Electronics essential to electromagnet power and control.  
 (2) Initial acquisition only, thruster bank non-redundant.  
 (3) 1800 acquisition cycles during mission.

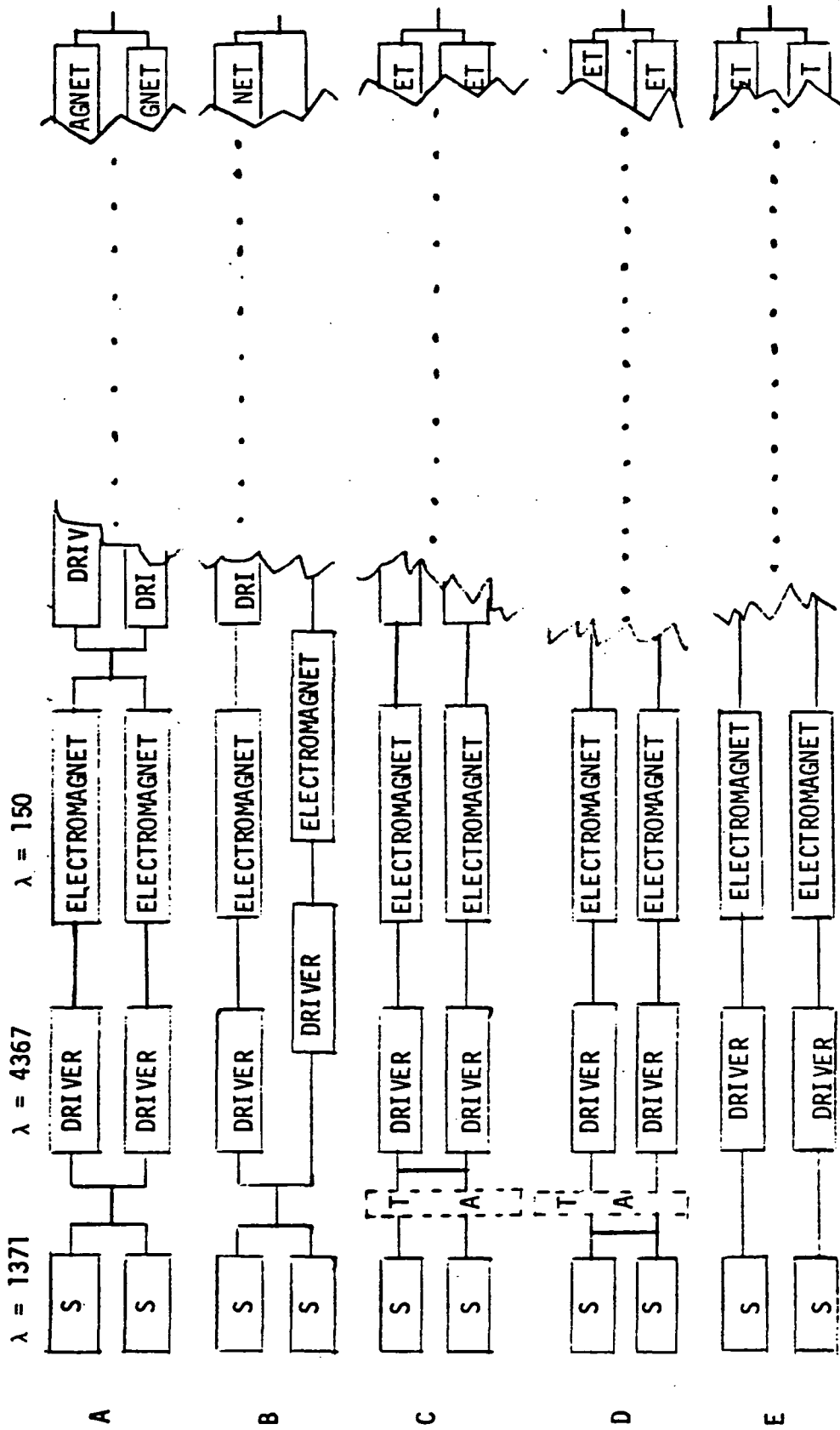


Figure 12-1. Reliability Block Diagrams

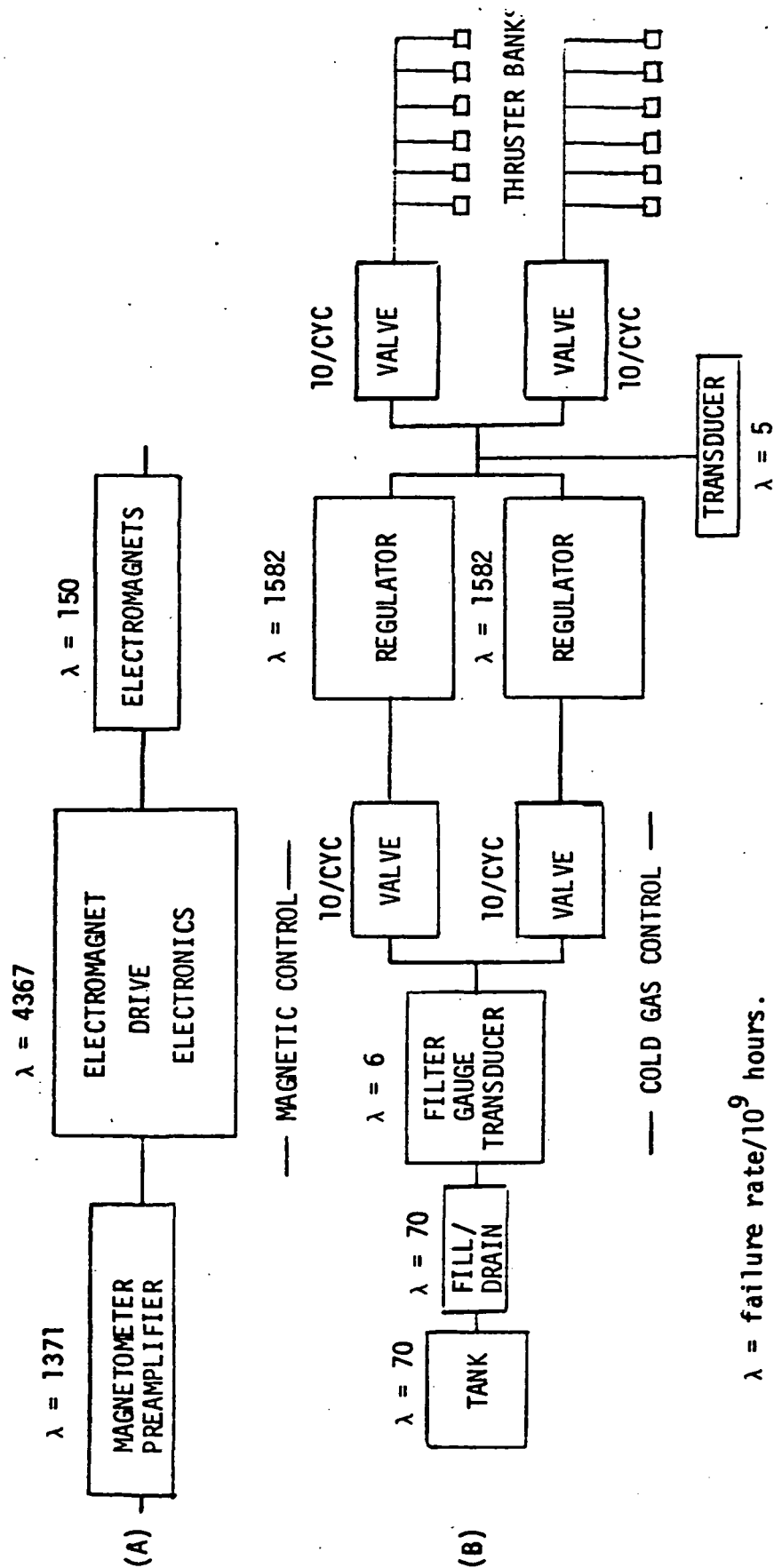


Figure 12-2. Key Reliability Elements of Electromagnet Control (A), and Cold Gas Reaction Control Subsystem (B).

## 12.1 Study Groundrules

Pertinent study groundrules for estimating reliability included:

- full reliance on existing reliability assets for HEAO A, B and C<sup>(2)</sup> missions which reflect current spacecraft (S/C) reliability requirements and goals,
- determination of magnetic and cold-gas subsystem reliability options suitable for all HEAO missions,
- defining the cross-strapping required (if any) to maintain (or improve) established S/C reliability levels,
- the preliminary evaluation of parts, materials, and processes which would foster lower failure-rates for all HEAO missions.

## 12.2 Reliability Assumptions

For study purposes, the assumptions used were:

- Reliability predictions for associative subsystems of HEAO-A, B, and C for 6 and 12 month missions, would require re-examination for any collateral impact to S/C reliability as a result of introducing new reaction control subsystem elements,
- HEAO-A and C S/C would be equipped with HEAO-B type reaction wheel assemblies coincident with the introduction of magnetic control (and cold-gas control) subsystem elements,
- Redundancy would be employed to inhibit single failure modes and increase the reliability of all new independent subsystem elements,

---

(2) Refer to TRW Document HEAO-S-73-632, 3 October 1973, as ammended.

- Installation characteristics and part failure rates employed in the estimating process would be based upon proven engineering practice and upon recent spaceflight experience data in lieu of rough estimates wherever possible,
- Electrical connectivities for new electronic and electro-mechanical assemblies, to accommodate magnetic control, would rely to the maximum extent possible, on existing cross-strapping of command and control elements.

### 12.3 Single-Point Failure Mode Suppression

The proposed subsystem configurations were carefully examined for possible single-point failures whose occurrence could introduce total system failure. (Such configurations are unacceptable for reliability.) In actual design, single-failure mode possibilities will be also eliminated or suppressed by recommending rigid component screening and strict product reliability requirements to reduce failure rates.

### 12.4 Reliability Trade-Offs

Results of preliminary trade studies indicate that electromagnet assemblies having double-wound electromagnets, for back-up operation, afford the best protection against complete failure of the magnetic subsystem for any axis coincident with simplifying the "packaging" of each electromagnet assembly for actual spacecraft installation.

Existing TRW hardware designs for magnetic-field sensing and pre-amplification were deemed appropriate and reliable for HEAO missions without essential modifications. Of the various cross-strapping opportunities available, the cross-strapping of Transfer Assemblies to electromagnet electronics assemblies proved the most suitable scheme inasmuch as attitude control (ACDS) commands to the magnetic control components occur at this system interface in normal operation.

The introduction and use of a cold-gas reaction control subsystem, for initial acquisition, was evaluated and found to present little, if any, real impact upon spacecraft reliability by its incorporation.

The incorporation of a cold-gas reaction control subsystem, for initial acquisition maneuvers, permits additional operating flexibility for full-term magnetic control operations at "no expense" to overall spacecraft reliability requirements.

Special requirements were agreeably introduced for estimating cold-gas reaction control reliability and included:

- 600 thrusting cycles (over a 2-hour term) for initial acquisition maneuvers,
- 1800 thrusting cycles (over a 4380-hour term) for HEAO-A acquisition maneuvers,
- 1800 thrusting cycles (over a 8760-hour term) for HEAO-B acquisition maneuvers.

The introduction of HEAO-B type reaction wheel assemblies (4 each) into the HEAO-A configuration proved acceptable with negligible impact upon overall spacecraft reliability goals (e.g., 0.90).

Results of the trade studies indicate that

- (1) Reliability goals of 0.90 and 0.80 can be met upon incorporation of a Magnetic Controller for both HEAO-A and HEAO-B missions, respectively.
- (2) Cross-strapping of electromagnet electronics and electromagnet assemblies from the output of the Transfer Assemblies provides immediate and active redundancy for reliable X, Y, and Z axis control.



- (3) The intended use of a cold-gas reaction control subsystem will not result in any degradation in system reliability, and will provide added maneuvering flexibility for all HEAO missions equipped with magnetic control provisions.

#### 12.5 Commonality of HEAO-A and HEAO-B Systems Incorporating Magnetic Torquing Provisions

Aside from the introduction of reaction wheel assemblies into the HEAO-A system, coincident with incorporating magnetic control functions, all new components proposed for HEAO-A and B spacecraft were examined for commonality of installation, connection and operation to assure parity of overall reliability estimates.

#### 12.6 Wheels/Magnetics Control System

Candidate subsystem configurations for HEAO-A and HEAO-B have been analyzed, (see Figure 12-1). Estimates of reliability for these configurations have also been calculated and include the addition of reaction wheel provisions for HEAO-A missions, (refer to Column I of Table 12-1). These estimates indicate that HEAO-A and B missions can be accomplished solely using RWA and magnetic control provisions<sup>(3)</sup> in all cases having single-failure mode protection. For the preferred configuration, these estimates are 0.931, and 0.826 for HEAO-A and HEAO-B missions, respectively.

#### 12.7 Wheels/Magnetics/Cold-Gas Control System

Estimates for HEAO-A and B missions having RWA, magnetic control and cold-gas control subsystems have also been calculated, to permit reliability comparisons, (refer to Columns II, III and IV of Table 12-1). Again, the preferred configuration, C, indicates that HEAO-A and B reliability goals can be met for either initial acquisition and multiple acquisitions without redundant thrusters or for multiple acquisitions using fully redundant thruster banks.

---

(3) Based on reliability; not upon operating constraints.

### 13. VERIFICATION AND MISSION OPERATIONS

#### 13.1 Wheels/Magnetics Control System

##### 13.1.1 Observatory Verification

In this approach, the magnetic control system will be incorporated in HEAO-A, -B, and -C and the reaction wheels, baselined for HEAO-B, will also be included on HEAO-A and -C. The following spacecraft/observatory verification activities will be added or deleted:

##### Deleted Tasks

- Installation of RCS
- RCS proof pressure and leak checks
- RCS electrical performance tests
- RCS fueling/pressurizing

The latter is perhaps the most significant deletion since it simplifies the launch site operations of fueling and pressurizing the RCS and deletes the requirement for one of the launch site facilities (Propellant Building in Area ESA-60A) and the observatory movement to and from this facility.

##### Added Tasks

- Installation and test of reaction wheels on HEAO-A and -C
- Installation and test of magnetic control system

The ACDS tests will be modified to incorporate verification of the magnetic control hardware. An end-to-end type verification will be performed by subjecting the magnetometer to a magnetic field and monitoring the resultant electromagnet currents. The field will be applied with several pre-established directions and magnitudes but precise knowledge is not required since the objective of this test will be to verify repeatability and, in particular, to verify that the proper flux polarities are generated by the electromagnets. Additional tests will be performed by injecting into observatory test points, known simulated magnetometer output signals generated by the ACDS test set. The resultant quantitative values of electromagnet current will be verified. The test

parameter values will be established by analysis performed during the development phase. A magnetic field map will be obtained at selected locations on the integrated observatory to determine the field of magnetized objects and critical large-field components.

### 13.1.2 Electrical Support Equipment

This option (Wheels and Magnetic Control) deletes the requirement for the RCS control and monitor unit and changes some of the requirements of the ACDS console. The design changes to the ACDS console can be identified as follows:

- Eliminate the monitoring of the twelve thruster actuation signals.
- Provide a triaxial coil-current device for excitation of the magnetometer-electromagnet system for end-to-end testing. Variable fields would be provided by controlling the current to the coils.
- Provide current control for six magnetometer calibration coils for quantitative magnetometer-electromagnet testing.

### 13.1.3 Mechanical Support Equipment

The reaction control subsystem will be deleted from the observatory for this option which eliminates the need for a propellant and pressurant loading unit (PPLU). The costs for the PPLU will be deleted from the MSE estimates for this option.

A hoist sling will be required to install the electromagnets into the equipment module. Mechanical support equipment personnel will provide support to other disciplines to insure that adequate consideration is given to handling, installation and protection of the electromagnets.

## 13.2 Wheels/Magnetics/Cold Gas System

### 13.2.1 Observatory Verification

This option is different from the wheels/magnetic control option in that a simple cold gas system is incorporated on each observatory in addition to the magnetic system to permit faster sun acquisition after separation.

Deleted Tasks

- Installation of RCS
- RCS proof pressure and leak checks
- RCS electrical performance tests
- RCS fueling/pressurizing

Added Tasks

- Installation and test of reaction wheels on HEAO-A and -C
- Installation and test of magnetic control system
- Cold gas system integration
- Proof pressure and leak checks
- Electrical performance test of cold gas system valves
- Pressurization of cold gas system at launch site

13.2.2 Electrical Support Equipment

This option (wheels, magnetic control and cold gas system) will require changes to both the ACDS console and RCS control and monitor unit. Changes to the ACDS console will consist of reduction of the thruster actuation monitoring from 12 to 6 and also adding the magnetometer electromagnet system test devices as required for the Wheels/Magnetic Control Option.

The cold gas system will require a unit quite similar to the RCS control and monitor unit to include: control of the isolation valves, isolation valve position monitoring and propellant pressure monitoring.

13.2.3 Mechanical Support Equipment

In addition to the mechanical support equipment impact described under 13.1.3, this option has the requirement that a cold gas loading unit be provided for charging the gas storage tanks before launch.

The cold gas loading unit will consist of a bank of standard 6,000 psi gas bottles mounted on a portable, wheeled cart with the associated plumbing and control components. A preliminary concept of the gas loading unit is shown in the schematic in Figure 13-1. All components of the GSU will be stainless steel, except the gas bottles,

and will be capable of delivering gas to the observatory fill valve conforming to MSFC Spec. 234A. The GSU will meet all safety requirements of AFETRM 127-1. All components will be standard commercial equipment.

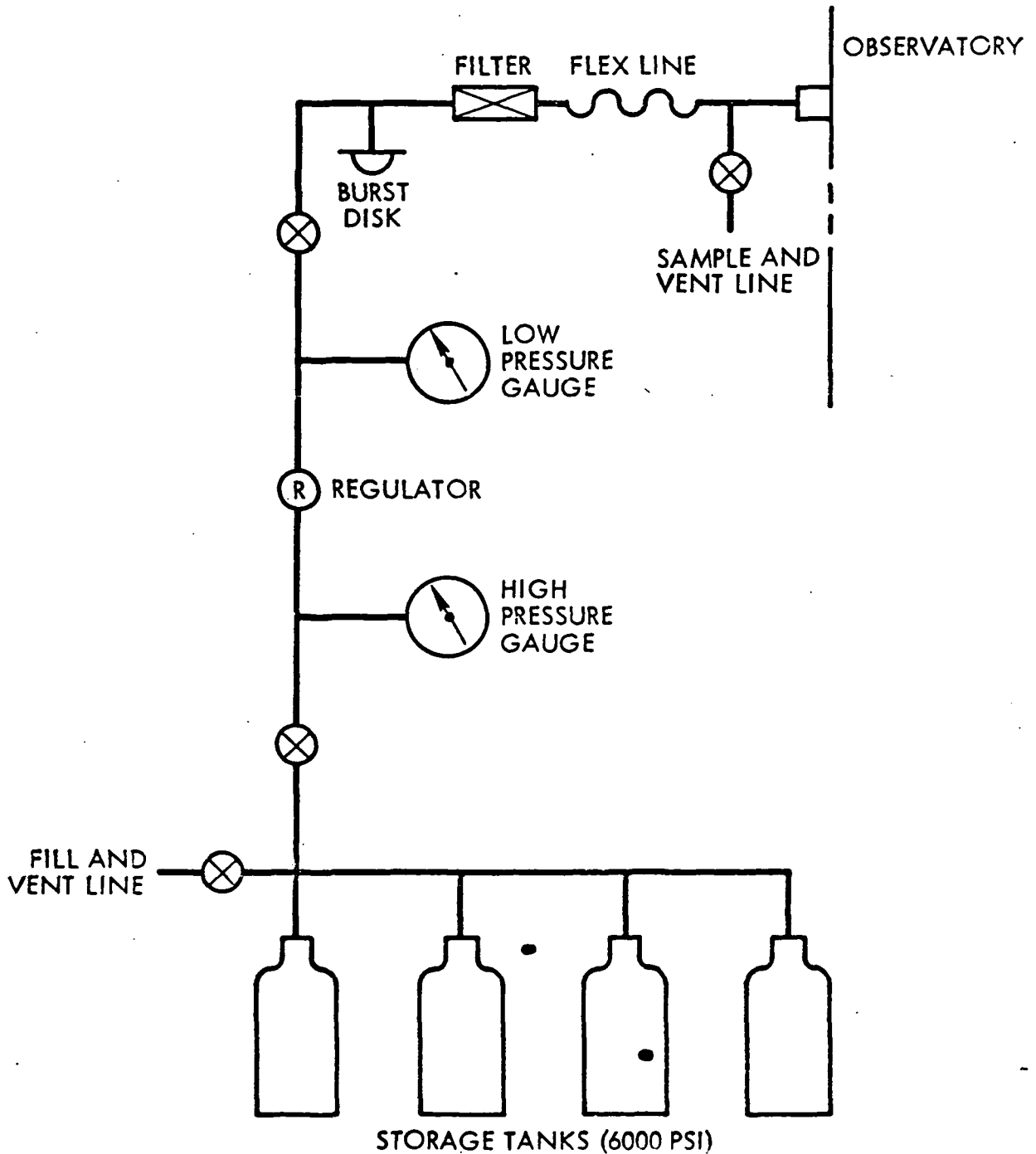


Figure 13-1. Gas Loading Unit Schematic